

**DEVELOPMENT AND ANALYSIS OF RADIOLABELED MAGNETIC NANOPARTICLES FOR POSITRON
EMISSION TOMOGRAPHY AND MAGNETIC RESONANCE IMAGING**

A Dissertation
Presented to
The Academic Faculty

By

Charles R. M. Glaus

In Partial Fulfillment
Of the Requirements for the Degree
Doctor of Philosophy in the
Wallace H. Coulter Department of Biomedical Engineering

Georgia Institute of Technology

December 2008

DEVELOPMENT AND ANALYSIS OF RADIOLABELED MAGNETIC NANOPARTICLES FOR POSITRON
EMISSION TOMOGRAPHY AND MAGNETIC RESONANCE IMAGING

Approved by:

Dr. Gang Bao, Advisor
School of Biomedical Engineering
Georgia Institute of Technology

Dr. Xiaoping P. Hu
School of Biomedical Engineering
Georgia Institute of Technology

Dr. Mark M. Goodman
Division of Radiology
Emory University

Dr. Kurt D. Pennell
School of Civil and Environmental Engineering
Georgia Institute of Technology

Dr. Yadong Wang
School of Biomedical Engineering
Georgia Institute of Technology

Date Approved: October 28, 2008

To my loving wife, Simone

ACKNOWLEDGEMENTS

I would like to acknowledge my advisor, Professor Gang Bao, for the tremendous amount and time and effort he has invested in my training over the past several years. He has skillfully mentored me and helped me to grow as a scientist. Dr. Bao was always available for discussion and advice no matter how busy he was. His patience, generosity, and kindness made the lab a wonderful place to work. This dissertation would not have been possible without Dr. Bao's insight and support.

I would like to thank my family for their support and encouragement during the time I spent in graduate school, especially my loving wife Simone. I could not have done this without her infinite support. I would like to thank the members of the Bao lab present in my early years, such as Yangqing Jason Xu for his mentoring and for introducing me to pertinent biochemical reactions. Jason worked late hours and was always willing to discuss the important things in life after a long day in lab. I would especially like to thank Nitin Nitin for his friendship and the time and effort he spent teaching and training me in the Bao lab (not to mention introducing me to the girl I would eventually marry!). I would like to thank Leslie LaConte for introducing me to many standard lab procedures when I was very green upon arrival. Phil Santangelo was a strong influence on me in my time in the Bao lab. All students present in the Bao lab during Phil's tenure were shaped by his leadership and scholarship. Phil constantly critiqued and improved our experimental approaches. I would like to thank Cindy Glick for her assistance in discussion of my data, for helping to proof documents, for her assistance in and mammalian cell culture techniques. However, I would like to thank Cindy most of all for her genuine friendship. She and Jeremy are dear friends to whom I owe a great debt. I would like to thank Allison Dennis for her friendship throughout my time in the Bao lab. Allison was always eager to help anyone

when help was needed and was willing to watching out for her fellow lab mates. Allison was always available to discuss science and to offer sound advice. I would also like to thank Jeff Stirman for his friendship and for making lab a fun a spontaneous place. Jeff would always speak his mind and offer straightforward advice and discussion. I would like to thank Won Jon Rhee for his friendship. Won Jon would always make time for discussion and is a kind and caring person. Sheng Tong for asking insightful questions in group meeting and for bringing his biological skill set to the lab. I would like to thank Sijian Hou for teaching me some basic synthesis techniques and for good discussion. Sijian has a friendly demeanor and often had wise advice on projects. I would like to thank Frances Lennon for her kind disposition, her friendship, and her great sense of humor. Frances has helped me with antibody staining and many other technical questions. I would like to thank Yiyi Zhang for his willingness to help, his friendship, and his good advice. Yiyi is the go-to-guy for almost anything in the lab. His deep skill set has been a resource to everyone in the lab. I would like to thank Steven Dublin for his friendliness, his insightful questions and advice, and for his and positive attitude. I would like to thank Annie Zheng for her skills in managing the lab, her hard work, and for her happy personality. I would like to thank Judy Tang for her help in coordinating lab activities, her pleasant conversation and for handling our forms.

I would like to thank the members of my thesis committee for their time and advice in my growth as an independent scientist. I would like to acknowledge the information I learned from Dr. Hu in his medical imaging systems course and for the advice he has offered me in my thesis work. I would like to acknowledge the advice and encouragement I received from Dr. Goodman. I would like to acknowledge Dr. Wang's willingness to share his lab equipment and for his willingness to offer good advice on topics of particle chemistry. I would like to acknowledge Dr. Pennell's willingness to collaborate and for the many discussions we have had.

I would like to thank Dr. Dardo Ferrara for the time and effort he spent teaching me the *en face* aorta preparation. I would also like to thank him for his friendship and discussion. I would also like to thank Dr. W. Robert Taylor for welcoming me into his lab and supplying me with resource to learn about cardiovascular biology. I would like to thank Johannes Leisen for his assistance with MRI studies. None of the MR work could have happened without Hanno's effort and patience. I would like to thank Jan Pohl for his expertise in peptide chemistry.

I would like to thank Dr. Michael Welch for his assistance, his scientific guidance, and for the financial contributions he made for many of the experiments herein. Dr. Welch's willingness to collaborate and his technical advice were and integral part of this work. I would also like to thank Drs. Raffaella Rossin and Aviv Hagooly for their immense technical expertise and for their assistance with many experiments presented here. I would also like to thank Dr. Yongjian Liu, Dr. Tetsuya Mori, Dr. Monica Shokeen, Susan Adams, Nikki Fettig, Amanda Roth, Margaret Morris, Eileen Cler, and everyone else at Washington University for their assistance and discussion. I would like to thank Dr. O'Farrell for teaching me useful animal techniques and protocols. I would like to thank the excellent undergraduate students that poured their time and energy into helping me get to this point. Specifically, I would like to thank Bobby Beaulieu for countless hours he invested in my work as a PhD student. Bobby was always helpful and he made a big difference to me and to the lab. I would like to thank Auroop Roy for untold hours he sacrificed in aiding my work. Auroop was a team player and was always there for me. These undergrads are shining examples of Georgia Tech's best and brightest. I would also like to thank the faculty of the Biomedical Engineering department for their time and commitment to furthering the education of the next generation of leaders.

I would also like to acknowledge the funding that supported much of this work: NHLBI Program of Excellence in Nanotechnology, grant number: 5U01HL080711.

TABLE OF CONTENTS

ACKNOWLEDGEMENTS.....	IV
LIST OF TABLES.....	XII
LIST OF FIGURES.....	XIII
LIST OF SYMBOLS AND ABBREVIATIONS.....	XVI
SUMMARY.....	XX
CHAPTER 1: DUAL-MODALITY PET/MR IMAGING.....	1
1.1 Introduction.....	1
1.1.1 Molecular Imaging.....	1
1.1.2 Translation of Preclinical Molecular Imaging Technologies.....	4
1.1.3 Molecular Imaging Using Nanoparticle Probes.....	5
1.2 Multimodality PET/MRI.....	6
1.2.1 Hybrid PET/MRI Instrumentation.....	8
1.2.2 Dual Modality Nanoparticle Probes for PET/MRI.....	9
1.3 References.....	13
CHAPTER 2: DEVELOPMENT, OPTIMIZATION, AND APPLICATIONS OF PEGYLATED-PHOSPHOLIPID ENCAPSULATED MAGNETIC NANOPARTICLES.....	18
2.1 Introduction.....	18
2.2 Probe Development and Optimization.....	20
2.2.1 Development of a Rapid, High Temperature Iron Assay For Quantifying Fe ₃ O ₄ Magnetic Nanoparticles.....	20
2.2.2 In Situ Dye Labeling.....	21
2.2.3 Nanoparticle Separation Using Ultracentrifugation.....	23

2.2.4 Nanoparticle Separation Using High Gradient Magnetic Columns	24
2.2.5 PEG-phospholipid Coating of Multisized Nanoparticles.....	26
2.2.6 mMION Detection Level in Blood	27
2.2.7 Magnetic-based <i>In Vivo</i> Stability Assay	28
2.3 Pilot mMION Radiolabeling Studies	30
2.4 Targeting Vascular Epitopes Using Fluorescent mMIONs	33
2.4.1 Biology of Atherosclerosis	33
2.4.2 Two-Photon Microscopy Using Fluorescent mMIONs	35
2.4.3 Materials.....	36
2.4.4 Experimental Procedures	36
2.4.5 Results	40
2.5 Discussion	48
2.6 References.....	51
 CHAPTER 3: IN VIVO EVALUATION OF ⁶⁴ CU-LABELED MAGNETIC NANOPARTICLES: A NOVEL	
PROBE FOR DUAL-MODALITY PET/MR IMAGING	56
3.1 Introduction.....	56
3.2 Experimental Procedures	57
3.2.1 Materials.....	57
3.2.2 Preparation of micelle-coated MIONS.....	58
3.2.3 Iron Concentration Determination.....	59
3.2.4 Relaxation Measurement	59
3.2.6 Radiolabeling of DOTA-mMION with ⁶⁴ Cu	60
3.2.7 Radiochemical Purity	60
3.2.8 Serum Stability of ⁶⁴ Cu-mMION.....	61

3.2.9 Size Determination	61
3.2.10 Transmission Electron Microscopy	62
3.2.11 Biodistribution	62
3.2.12 Small-Animal PET/CT Imaging Studies of ⁶⁴ Cu-mMIONS	63
3.2.13 Phantom Study	63
3.3 Results	64
3.3.1 Nanoparticle Formation and Characterization	64
3.3.2 ⁶⁴ Cu-Radiolabeling of DOTA-mMION	65
3.3.3 Biodistribution Studies	66
3.3.4 Small Animal PET Imaging Studies	68
3.3.5 Phantom Studies	71
3.3.6 Discussion	72
 CHAPTER 4: DEVELOPMENT OF DEXTRAN-COATED MAGNETIC NANOPARTICLES AND INTEGRIN TARGETING SYSTEM.....	
4.1 Introduction	79
4.1.1 Dextran-coated Iron Oxide Magnetic Nanoparticles	81
4.1.2 Magnetic Nanoparticles for Human Use	82
4.2 Nanoparticle Selection and Modification	84
4.2.1 Nanoparticle PEGylation	88
4.3 Development of $\alpha_v\beta_3$ Integrin Targeting System	90
4.3.1 Tumor Angiogenesis and the Role for Molecular Imaging	90
4.3.2 Selection and <i>In Vitro</i> Characterization of Cell Lines for $\alpha_v\beta_3$ Integrin Targeting	92
4.3.3 In Vitro Nanoparticle Targeting to Cell Surface $\alpha_v\beta_3$ Integrin Using Monoclonal Antibodies.....	96

4.3.4 Selection of Integrin Binding RGD Peptide	100
4.3.5 In Vitro Nanoparticle Targeting to Cell Surface $\alpha_v\beta_3$ Integrin Using a Cyclic RGD Peptide	102
4.4 Preparation and Evaluation of Radiolabeled Nanoparticles	108
4.4.1 Radiolabeling and <i>In Vivo</i> Evaluation of ^{64}Cu -labeled PEGylated Dextran-coated Magnetic Nanoparticles.	109
4.5 Tumor Model Selection	114
4.6 Preliminary MRI Studies	117
CHAPTER 5 PET/MR IMAGING OF RGD-TARGETED ^{64}Cu -LABELED MAGNETIC NANOPARTICLES	128
5.1 Introduction.....	128
5.2 Experimental Procedures	128
5.2.1 Materials.....	128
5.2.2 Preparation of PEGylated DOTA–MNP _{PEG} and DOTA–MNP _{PEG} –RGD	129
5.2.3 Nanoparticle Characterization.....	130
5.2.4 Magnetic Nanoparticle Radiolabeling	131
5.2.5 Nanoparticle Phantom Imaging.....	132
5.2.6 Cellular Imaging Studies	133
5.2.7 M21/M21L Cell Uptake Assay	134
5.2.8 Determination of Nanoparticle Biodistribution	134
5.2.9 U87MG Tumor Model	135
5.2.10 M21/M21L Tumor Model.....	135
5.2.11 In Vivo PET/CT Imaging.....	136
5.2.12 In Vivo MR Imaging.....	136
5.3 Results	137

5.3.1 Nanoparticle Conjugation.....	137
5.3.2 Nanoparticle Radiolabeling	138
5.3.3 Phantom Studies	139
5.3.4 Cellular Imaging Studies	140
5.3.5 M21/M21L Cell Uptake Assay	141
5.3.6 Biodistribution of Peptide-targeted Dual PET/MRI Nanoparticles in BALB/c Mice .	142
5.3.7 Biodistribution of Peptide-targeted Dual PET/MRI Nanoparticles in U87MG Tumor-bearing Mice.....	143
5.3.8 Biodistribution of Peptide-targeted Dual PET/MRI Nanoparticles in M21/M21L Tumor-bearing Mice.....	145
5.3.9 In Vivo PET imaging of Nanoparticle Accumulation in U87MG Tumors.....	146
5.3.10 In Vivo MRI of Nanoparticle Accumulation in U87MG Tumors.....	148
5.4 Discussion	150
5.5 References.....	153
CHAPTER 6: SUMMARY AND FUTURE DIRECTIONS	157
6.1 Conclusions and Ongoing Studies.....	157
6.2 Contributions to the Field.....	162
6.3 Future Collaboration	164
6.4 References.....	165
CURRICULUM VITAE.....	167

LIST OF TABLES

Table 1.1: Characteristics of current molecular imaging modalities	3
Table 2.1: Preparation of ferrous ammonium sulfate standard Curve.....	21
Table 4.1: Dextran-coated superparamagnetic iron oxide nanoparticles	82
Table 4.2: Biodistribution of ⁶⁴ Cu-labeled PEGylated dextran-coated superparamagnetic iron oxide nanoparticles in female BALB/c mice.....	114
Table 5.1: Biodistribution of ⁶⁴ Cu-labeled, RGD-functionalized magnetic nanoparticles in female BALB/c mice	143
Table 5.2: Biodistribution of ⁶⁴ Cu-labeled, RGD-functionalized magnetic nanoparticles in U87MG tumor-bearing mice	144
Table 5.3: Biodistribution of ⁶⁴ Cu-labeled, RGD-functionalized magnetic nanoparticles in M21/M21L bilateral tumor-bearing mice.....	146
Table 6.1: Biodistribution of ⁶⁴ Cu-labeled magnetic nanoparticles in female BALB/c mice with peptide and EPR blocking	161
Table 6.2: Biodistribution of ⁶⁴ Cu-labeled magnetic nanoparticles in U87MG tumor-bearing mice with peptide and EPR blocking	161

LIST OF FIGURES

Figure 1.1: Comparison of surface area and volume for different sized particles.	6
Figure 1.2: Current approaches for combined PET/MRI scanners.	8
Figure 1.3: Schematic of trimodality nanoparticle..	9
Figure 1.4: ¹²⁴ I labeled, albumin coated MnFe ₂ O ₄ dual PET/MRI nanoparticle.	10
Figure 1.5: ⁶⁴ Cu labeling of anion dextran sulfate-coated magnetic nanoparticles.	11
Figure 1.6: Polyaspartic acid-coated iron oxide nanoparticles labeled with ⁶⁴ Cu.	11
Figure 1.7: Dual PET/MRI probes	12
Figure 2.1: Synthesis of micelle-coated monocrystalline iron oxide nanoparticles.	19
Figure 2.2: Complexation of Fe ²⁺ with 1,10-Phenanthroline in the rapid, high temperature Fe assay.....	20
Figure 2.3: <i>In situ</i> fluorescent labeling of micelle-coated magnetic nanoparticles.	23
Figure 2.4: Dynamic light scattering of empty micelles.....	24
Figure 2.5: High gradient magnetic separation column.	26
Figure 2.6: Dynamic light scattering of multisized mMIONS.	27
Figure 2.7: mMION detection level in blood.....	28
Figure 2.8: In vivo stability of mMIONS.....	30
Figure 2.9: Chromatography of ⁶⁴ Cu-mMION.	31
Figure 2.10: microPET/CT and post-imaging biodistribution of ⁶⁴ Cu-mMION in C57BL/6 mice....	33
Figure 2.11: Upregulation of vascular cell adhesion molecule 1 by lipopolysaccharide endotoxin.	41
Figure 2.12: Nanoprobes for targeting vascular epitopes.	42
Figure 2.13: Typical VCAM-1 staining pattern of LPS-activated aortic tissue.....	43

Figure 2.14: Imaging depth in the aorta using VCAM-targeted nanoprobe.	45
Figure 2.15: Nanoparticle and peptide-based imaging of VCAM-1 in the aorta.	47
Figure 2.16: Peptide-based imaging of VCAM-1 expression as a function of local flow environment and LPS treatment.	48
Figure 3.1: Design and characterization of ⁶⁴ Cu-labeled mMIONs.	65
Figure 3.2: Biodistribution data of dual-PET/MR ⁶⁴ Cu-mMION in BALB/c mice.	67
Figure 3.3: Coregistered microPET/microCT of BALB/c administered ⁶⁴ Cu-mMIONs	70
Figure 3.4: PET and MR imaging of ⁶⁴ Cu-mMION phantoms.	71
Figure 4.1: Size determination of high-temperature synthesized magnetic nanoparticles.	80
Figure 4.2: Crosslinked iron oxide (CLIO) magnetic nanoparticle.	84
Figure 4.3: Characterization of commercial USPIOs	86
Figure 4.4: Characterization of amino-CLIO.	87
Figure 4.5: The effect of CLIO PEGylation on serum protein absorption.	90
Figure 4.6: Tumor angiogenesis and the role of $\alpha_v\beta_3$ integrin.	91
Figure 4.7: Two-step immunofluorescence staining of $\alpha_v\beta_3$ integrin expression.	93
Figure 4.8: Comparison of U87MG and MCF-7 $\alpha_v\beta_3$ integrin expression level by flow cytometry.	95
Figure 4.9: Reaction scheme for conjugating antibody fragments with aminated dextran-coated magnetic nanoparticles.	97
Figure 4.10: Imaging $\alpha_v\beta_3$ integrin using nanoparticles targeted with antibody fragments.	99
Figure 4.11: Lactam-cyclized RGD variant used for targeting magnetic nanoparticles to $\alpha_v\beta_3$ integrin.	101
Figure 4.12: Chromatograms of c(RGDyK) reaction with maleimide–Alexa Fluor 488.	104
Figure 4.13: Mass spectrum of c(RGDyK)–Alexa Fluor 488 conjugate.	105

Figure 4.14: Flow cytometry analysis of fluorescent cyclo-RGD and cyclo-RAD peptides binding to $\alpha_v\beta_3$ integrin on U87MG cells.....	106
Figure 4.15: Biodistribution ^{64}Cu -labeled PEGylated Dextran-Coated Superparamagnetic Iron Oxide Nanoparticles.....	113
Figure 4.16: Immunofluorescent staining of newly formed blood vessels in LLC tumors.....	115
Figure 4.17: U87MG tumor growth chart.....	116
Figure 4.18: Schematic of M21/M21L bilateral tumor model.....	117
Figure 4.19: MR imaging difficulties.....	118
Figure 4.20: Intra-tumor injection of magnetic nanoparticle.....	120
Figure 5.1: Development of $\alpha_v\beta_3$ integrin-targeted dual PET/MRI nanoparticles.....	138
Figure 5.2: Characterization of ^{64}Cu -MNP _{PEG} -RGD.....	140
Figure 5.3: Live cell nanoparticle imaging.....	141
Figure 5.4: M21/M21L cell uptake of peptide-targeted magnetic nanoparticles.....	142
Figure 5.5: Tumor/tissue ratios.....	145
Figure 5.6: MicroPET/CT imaging ^{64}Cu -MNP _{PEG} -RGD (A, B) and ^{64}Cu -MNP _{PEG} (C, D) in U87MG tumor-bearing mice at 24 hr post-injection.....	147
Figure 5.7: Alternate microPET/CT images of ^{64}Cu -MNP _{PEG} -RGD (A, C) and ^{64}Cu -MNP _{PEG} (B, D) in U87MG tumor-bearing mice at 24 hr post-injection.....	148
Figure 5.8: MR Imaging of Cu-MNP _{PEG} -RGD and Cu-MNP _{PEG} in tumor-bearing mice at before and 24 hr after injection.....	149
Figure 5.9: Quantitative evaluation of mean tumor T2 before and 24 hr after injection with ^{64}Cu -MNP _{PEG} -RGD or ^{64}Cu -MNP _{PEG}	150

LIST OF SYMBOLS AND ABBREVIATIONS

APD	Avalanche Photo Diode
BSA	Bovine serum albumin
CT	Computed Tomography
CTAB	Cetyltrimethylammonium bromide
DAPI	4',6-diamidino-2-phenylindole
DI	Deionized
DLS	Dynamic Light Scattering
DMEM	Dulbecco's Modified Eagle Medium
DMSO	Dimethyl sulfoxide
DOTA	1,4,7,10-tetraazacyclododecane-1,4,7,10-tetraacetic acid
DSPE	1,2-Distearoyl-sn-Glycero-3-Phosphoethanolamine
DTPA	Diethylene triamine pentaacetic acid
ECM	Extracellular Matrix
EDTA	Ethylenediaminetetraacetic Acid
FBS	Fetal Bovine Serum
FPLC	Fast Protein Liquid Chromatography
HCl	Hydrochloric acid
HGMF	High Gradient Magnetic Field
HPLC	High Performance Liquid Chromatography
IACUC	Institutional Animal Care and Use Committee
IC ₅₀	Inhibitory Concentration-50%
IO	IronOxide

IP	Intraperitoneal
IR	Infrared
IV	Intravenous
Kd	Dissociation Constant
kD	Kilo Dalton
LPS	Lipopolysaccharide
LSO	Lutetium oxyorthosilicate
MEA	Mercaptoethylamine
MION	Monocrystalline iron oxide nanoparticle
mMION	Micelle-coated monocrystalline iron oxide nanoparticle
MNP	Magnetic Nanoparticle
MRI	Magnetic Resonance Imaging
MW	Molecular Weight
NA	Numerical Aperture
NaOAc	Sodium Acetate
NBF	Neutral Buffered Formalin
NH ₄ OAc	Ammonium Acetate
NIR	Near Infrared
NMR	Nuclear Magnetic Resonance
NO	Nitric Oxide
NP	Nanoparticle
PBS	Phosphate Bufferes Saline
PE	Phosphoethanolamine
PEG	Polyethylene Glycol

PET	Positron Emission Tomography
PMT	Photomultiplier Tube
QD	Quantum Dot
RES	Reticuloendothelial System
RGD	Arginine-Glycine-Aspartic Acide
SDS	Sodium dodecyl sulfate
SEC	Size Exclusion Chromatography
SMCC	Succinimidyl-4-(N-maleimidomethyl)cyclohexane-1-carboxylate
SNR	Signal to Noise Ratio
SPDP	N-succinimidyl 3-(2-pyridyldithio)propionate
SPECT	Single Photon Emission Computed Tomography
SPIO	Superparamagnetic Iron Oxide
SQ	Subcutaneous
T	Tesla
T1	Longitudinal relaxation time T1
T2	Transverse relaxation time T2
TCEP	Tris[2-carboxyethyl] phosphine
TEM	Transmission Electron Microscopy
TETA	1,4,8,11-Tetraazacyclododecane-1,4,8,11-tetraacetic acid
TF	Tissue Factor
TLC	Thin Layer Chromatography
TPE	Two-Photon Excitation
US	Ultrasound
USPIO	Ultrasmlal Superparamagnetic Iron Oxide

VCAM

Vascular Cell Adhesion Molecule

SUMMARY

Multimodality imaging is the combination of two or more distinct, standalone imaging modalities that leverages the respective strengths and weaknesses of each imaging technology. The result of this combination is often greater than the sum of its parts. The combination of anatomical and functional imaging modalities, such as positron emission tomography/computed tomography (PET/CT), has produced the most useful multimodality imaging systems. PET/CT is currently the gold standard in oncologic imaging. However, CT exposes patients and experimental animals to substantial doses of ionizing radiation. Magnetic resonance imaging uses no ionizing radiation and provides superior soft tissue contrast at high spatial resolution, a particularly important feature for oncologic imaging because of the epithelial origin of many cancers. Positron emission tomography, the most sensitive human molecular imaging modality, produces whole body images for functional and molecular information. Combining PET with the functional, spectroscopic, and contrast enhanced abilities of MRI would produce a breakthrough in the detection and monitoring of disease.

Nanoparticles possess unique characteristics that make them well suited as probes for molecular imaging. Particles can be synthesized in a systematic fashion with tight control over nanoparticle diameter producing particles with narrow size distributions. As particles become smaller, their surface area to volume ratio increases immensely. Engineering nanoparticle surface chemistry allows the immense surface area to be decorated with therapeutic molecules, imaging agents, targeting ligands, and nucleic acids. Nanoparticles can be conjugated with large numbers of targeting ligands, thus increasing the affinity of the nanoparticle to its biological target through a phenomenon known as multivalency. High loading of reporter molecules (e.g. fluorophores, radionuclides) increases signal in imaging application. Different ligands and

reporters can be attached to a single particle to allow multiplexing and multi-functionality (i.e. single nanoparticle carrying an imaging reported, a targeting ligand, and a therapeutic molecule).

Contrary to gadolinium-based MRI contrast agents, nanoparticle contrast agents circulate in the blood for long periods of time, offer higher sensitivity, and exhibit little to no known toxicity. The unique qualities of nanoparticles are also well suited to the design of PET probes. Because of their large surface area, nanoparticles can be labeled to a high specific activity, further increasing the sensitivity of detection as well as the payload of therapeutic isotopes and targeting ligands. Unlike small molecule PET tracers, radiolabeled nanoparticles can circulate for long periods of time. The work presented in this dissertation focuses on the development and biological application of combined PET/MRI nanoparticles for multimodal imaging.

In chapter one we describe molecular imaging, its role in current biomedical research, and its potential impact on public health. The sensitivity, resolution, cost, and advantages of current imaging modalities are presented. The advantages of nanoparticle imaging agents are outlined and several properties unique to nanoparticles are illustrated. Combined PET/MRI and its potential benefits are described. Remarks are made on hardware and instrumentation considerations for combination scanners. Finally, the few existing published reports of PET/MRI nanoparticles are discussed.

In chapter two the development, optimization, and application of PEGylated-phospholipid encapsulated magnetic nanoparticles is presented. Here we describe the work performed to advance this class of nanoparticle well beyond its original state. The creation of a rapid, high temperature assay for nanoparticle iron content is explained. New techniques for *in situ* dye labeling, ultracentrifugal and high gradient magnetic separation of mMIONs are outline

in detail. In all, the time taken to coat, purify, and obtain the iron concentration of mMION was lowered from \approx 35 hours to 3 – 5 hours. The adaptation of lipid-PEG coating to multisized nanoparticle cores is also explained. Targeting of vascular epitopes using mMION was explored using an *en face* aorta preparation from LPS-activated mice. The performance of mMION in this regard was compared to quantum dot nanocrystals. Measurement of mouse blood T2 after injection with mMIONS was conducted to determine the circulation half-life of mMIONS, marking the first *in vivo* experiments ever performed in our laboratory. Pilot radiolabeling studies of mMION were performed to determine the potential of this nanoparticle as a PET/MRI contrast agent. Appropriate labeling conditions were determined and high purity, yield, and specific activity labeling was achieved. Preliminary organ biodistribution of ^{64}Cu -mMION was measured in to determine the nanoparticle pharmacokinetics and microPET/CT imaging was performed.

In chapter 3 we expanded on the tools produced in chapter 2 to produce novel, high quality PET/MR nanoparticle contrast agents. To ensure a uniform particle population was used, the particles were characterized for their size by dynamic light scattering and transmission electron microscopy. The magnetic properties were evaluated and the particles were radiolabeled at high purity and specific activity. After determining that the particles were stable in mouse serum, a comprehensive organ biodistribution was performed at several time points. Along with multi-timepoint PET/CT, we determined the pharmacokinetics of this novel PET/MRI nanoparticle. This data is essential in determining the potential of a nanoparticle for *in vivo* imaging applications. PET and MR imaging studies were performed using imaging phantoms.

In chapter 4 a second class of magnetic nanoparticle is studied. This class of nanoparticle, USPIO was investigated for its surface chemical reactivity. The particle selected is a stable variant of an FDA-approved nanoparticle. Nanoparticles were modified with bio-inert

polyethylene glycol (PEG) and made more resistant to serum protein absorption. The biodistribution was measured and the particle was confirmed to have desirable pharmacokinetic. An *in vitro* integrin targeting system was developed and particles were targeted to an angiogenesis marker using small peptides. Multiple tumor models were constructed in immune-deficient mice. The tumors and particles were tested in a newly acquired MRI scanner.

In chapter 5 we tested the tumor-targeting ability of our dual modality particles. PET and MR imaging was performed and imaging phantoms were evaluated. Two different tumor models were examined. *In vivo* PET/MR contrast was achieved using our peptide-targeted particle. We also discovered limitations to our probe. The presence of targeting peptides significantly altered the pharmacokinetics. This observation is of value to all researchers conducting *in vivo* studies using ligand-targeted nanoparticles.

In chapter 6 we present experiments performed to study the mechanism of ligand-altered pharmacokinetics observed by our particles. Future studies are also outlined.

CHAPTER 1

DUAL-MODALITY PET/MR IMAGING

1.1 Introduction

Disease has traditionally been detected when anatomical and functional changes to tissue and organs appear. Existing imaging technologies used to detect disease generally rely on gross physical changes to distinguish pathological tissue from normal tissue. Molecular imaging, a rapidly developing and interdisciplinary field, produces visualization of cellular and molecular processes within living organisms. Molecular imaging allows pathological irregularities in genomic and proteomic pathways to be identified and monitored, allowing earlier disease detection as well as observation of treatment efficacy (1). The emergence of molecular imaging technology is due to tremendous progress made in molecular biology, transgenic animals and animal imaging instrumentation, and most importantly the creation of novel imaging probes.

1.1.1 Molecular Imaging

Molecular imaging can be defined as the representation, characterization, or quantization of biological phenomena at the cellular and molecular levels inside living organisms. The information gathered by molecular imaging is a direct analysis of in vivo mechanisms of disease occurring within the framework of biologically authentic environments. It is a highly multidisciplinary field, involving biologists, biochemists and chemical engineers, electrical engineers, biophysicists, and medical scientists.

There are two primary reasons why interest and investment in molecular imaging is rapidly escalating. The first is the recent accumulation of biological knowledge and technology denoted as the “genomic age.” The past decade has witnessed a vast outpouring of biological

knowledge due to new technologies, such as those occurring in mass spectrometry, proteomics, genomic sequencing and gene chip analysis, and through transgenic and knock-out small animal models. Entirely new fields such as biomedical engineering, molecular pharmacology, and bioinformatics are offspring of this revolutionary era. Drugs and imaging agents can now be tailored to disease- and patient-specific biomarkers.

The second reason for the emergence of molecular imaging is the growing need to replace the anatomy-based modalities that form the backbone of current medical imaging. Present imaging technologies rely mostly on nonspecific, macroscopic physical and physiological changes that differentiate pathological from normal tissue rather than identifying the specific molecular events (e.g., gene expression) responsible for disease. Molecular imaging on the other hand exploits specific molecular probes as the source of image contrast. This change in emphasis from a nonspecific to a specific approach represents a significant paradigm shift, the impact of which is that imaging can now provide the potential for earlier detection and characterization of disease, evaluation of treatment, and insight into basic biology. A comparison of common molecular imaging modalities is shown in Table 1.1.

The world's growing healthcare burden stands to gain much from the implementation of molecular imaging. In many cases, particularly in cancer, disease is only detected at an advanced stage in which the options for pharmacological therapy or surgical intervention are of limited success. The end result is a paradigm where the majority of healthcare dollars are spent delivering end-of-life critical care. Molecular imaging has the potential to help lessen this economic burden by providing earlier detection and high fidelity monitoring of treatment.

Table 1.1: Characteristics of current molecular imaging modalities (adapted from Massoud et al (1))

Imaging technique	Portion of EM radiation spectrum used for image generation	Spatial resolution ^a	Depth	Temporal resolution ^b	Sensitivity ^c	Type of molecular probe ^d	Amount of molecular probe used	Quantitative degree	Ability to scale to large animal imaging	Perturbation of biological system	Principal use	Advantages	Disadvantages	Cost ^e
Positron emission tomography (PET)	high-energy γ rays	1-2 mm	no limit	10 sec to minutes	10^{-11} - 10^{-12} mole/L	Radiolabeled, direct or indirect	nanograms	+++	yes	no	metabolic, reporter/gene expression, receptor/ligand, enzyme, cell targeting	high sensitivity, isotopes can substitute naturally occurring atoms, can image multiple translatable research	PET cyclotron or generator needed, relatively low spatial resolution, radiation to subject	\$\$\$\$
Single photon emission computed tomography (SPECT)	lower-energy γ rays	1-2 mm	no limit	minutes	10^{-10} - 10^{-11} mole/L	radio-labeled, direct or indirect	nanograms	++	yes	no	reporter/gene expression, receptor/ligand	many molecular probes available, can image multiple probes simultaneously, not subject to background to clinical imaging systems	relatively low spatial resolution because of sensitivity, collimation, radiation	\$\$\$
Optical bioluminescence imaging	visible light	3-5 mm ^f	1-2 cm	seconds to minutes	not well-characterized possibly 10^{-15} - 10^{-17} mole/L	activatable, indirect ^g	micrograms to milligrams	+ to ++	yes but limited	yes if necessary to give mass quantity of molecular probe	reporter/gene expression, cell trafficking	highest sensitivity, quick, easy, low-cost, relative high-throughput	low spatial resolution, 2D imaging only, relatively surface-weighted, limited functional research	\$\$
Optical fluorescence imaging	visible light or near-infrared	2-3 mm ^h	<1 cm ^b	seconds to minutes	not well characterized, likely 10^{-9} - 10^{-12} mole/L	activatable, direct or indirect	micrograms to milligrams	+ to ++	yes but limited	yes if necessary to give mass quantity of molecular probe	reporter/gene expression, cell trafficking	high sensitivity, detects fluorochrome in live and dead cells	relatively low spatial resolution, surface-weighted	\$-\$\$
Magnetic resonance imaging (MRI)	radio waves	25-100 μ m	no limit	minutes to hours	10^{-1} - 10^{-5} mole/L	activatable, direct or indirect	micrograms to milligrams	++	yes	yes if necessary to give mass quantity of molecular probe	morphological reporter/gene expression, receptor/ligand if many receptors	highest spatial resolution, can image morphological and functional imaging	relatively low sensitivity, long processing time, mass quantity of probe may be needed	\$\$\$\$
Computed tomography (CT)	X-rays	50-200 μ m	no limit	minutes	not well characterized	may be possible (see text)	not applicable	not applicable	yes	as MRI, and also if excessive radiation dose	morphological	bone and tumor imaging, anatomical imaging	limited "molecular" applications, limited soft tissue resolution	\$\$
Ultrasound	high-frequency sound	50-500 μ m	millimeters to centimeters	seconds to minutes	not well characterized	limited, activatable, direct	micrograms to milligrams	+	yes	no	morphological	real-time, low cost	limited spatial resolution, mostly morphological	\$\$

1.1.2 Translation of Preclinical Molecular Imaging Technologies

Pharmaceutical companies are increasingly incorporating “preclinical” molecular imaging studies in small animals to accelerate the search for active chemical species and biological therapeutics. The noninvasive nature of molecular imaging allows for longitudinal studies that decrease cost and experimental variability. Many preclinical imaging strategies are based on optical imaging such as fluorescence and bioluminescence. Unfortunately, several of these techniques require the use of toxic probes (e.g. quantum dots) or the presence of enzyme-encoding transgenes. Neither of these scenarios can be translated to clinical practice. Additionally, most optically-based preclinical methods rely on superficial lesions and lesion sizes that are clinically irrelevant.

Modalities such as magnetic resonance imaging and positron emission tomography are sometimes referred to as “mouse-to-man” modalities. The basic physics of these imaging modalities are, to a great extent, independent of lesion depth or tissue density. The result is very little attenuation of signal from even the deepest regions of the body. Preclinical studies on small animals using depth-independent modalities offer the best opportunity to translate imaging agents to clinical application; because of this we have chosen to use probes that operate by way of MRI and PET. We have also considered toxicity issues when selecting out dual-modality nanoparticles. The iron oxide in our magnetic nanoparticles is relatively harmless at low doses, while the phospholipid-PEG coating is biocompatible and biodegradable. The dextran-coated iron oxide particles we have chosen to use are comparable to dextran particles that have received FDA approval for cancer imaging. The copper-64 tracer used for PET imaging is present only in low amounts and in a chelated form, making it less able to partake in side reactions. Copper-64 has been used in human studies (2) and has shown no acute toxicity in preclinical rodent models (3) when used at concentrations applicable to PET imaging. The cyclic chelator DOTA is used for chelating gadolinium in FDA-approved MRI contrast agents.

1.1.3 Molecular Imaging Using Nanoparticle Probes

Nanoparticles possess unique characteristics that make them well suited as probes for molecular imaging, particularly in cancer imaging where the past several years has witnessed a sharp rise in innovation and funding (4, 5). Liposomes have been studied for many years as imaging and drug delivery systems (6). Modern approaches to nanoparticle synthesis can produce particles in a systematic fashion, with tight control over nanoparticle diameter and narrow size distributions. For example, the ability to tune nanoparticle size allows one to shift the emission spectra of quantum dots (7) as well as the relaxivity of magnetic nanoparticles(8). Another key feature of nanoparticles is their large surface area. As particles become smaller, their surface area to volume ratio increases (Figure 1.1). For example, one gram of iron oxide (Fe_3O_4) would form a sphere of approximately 0.75 cm with a surface area of 1.77 cm^2 . The same gram of iron oxide, when composed of 20 nm nanoparticles, would have a surface area of approximately 60 m^2 . The surface of nanoparticles can be modified with a diverse array of chemical functional groups. Engineering nanoparticle surface chemistry allows the immense surface area to be conjugated with drug molecules, imaging agents, targeting ligands, and nucleic acids. Functionalized nanoparticles can be conjugated with several targeting ligands, thus increasing the affinity of the nanoparticle to its target through multivalent effects. In terms of imaging applications, multivalency increases signal output via increased binding affinity and subsequent accumulation of reporter molecules (e.g. fluorophores, radionuclides). Additionally, different ligands or imaging reporters can be placed on a single particle to allow multiplexing and multi-functionality (i.e. single nanoparticle carrying an imaging reported, a targeting ligand, and a therapeutic molecule).

Nanoparticles have been employed in magnetic resonance molecular imaging for many years (9-11). Magnetic nanoparticles (MNPs) have been used to study a wide range of biological

phenomena, such stem cell tracking (12-14), cancer detection (15-17), and monitoring atherosclerosis (11, 18, 19). Unlike gadolinium based MRI contrast agents, MNPs persist in circulation for long periods of time, offer greater sensitivity, and exhibit little to no known toxicity. The unique qualities of nanoparticles are also well suited to the design of PET probes. Because of their large surface area, nanoparticles can be labeled to a high specific activity, further increasing the sensitivity of detection as well as the payload of therapeutic isotopes and targeting ligands. Unlike small molecule PET tracers, radiolabeled nanoparticles can circulate for long periods of time. The synthesis and use nanoparticles as PET molecular imaging agents have only recently been explored in detail (20-24).

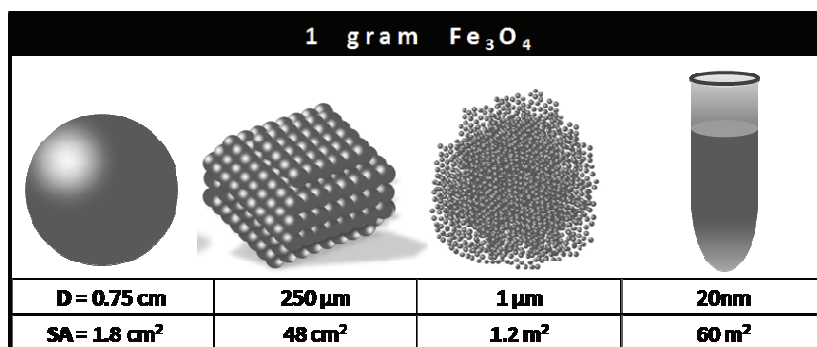


Figure 1.1: Comparison of surface area and volume for different sized particles.

1.2 Multimodality PET/MRI

All imaging modalities have specific resolution, sensitivity, and spatial/temporal dimensions were they operate effectively. A common technique to leverage the power of multiple imaging modalities is to combine two modalities in a complimentary fashion, simultaneously reducing the drawbacks and enhancing the strengths of both modalities. Optical/MRI (16, 25-27), Optical/PET (28, 29), and PET/CT are common multimodality imaging methods employed in pre-clinical research.

Following its creation in the mid-1970s (30), positron emission tomography became an essential diagnostic imaging modality in the early and mid-1990s. The combination of PET with computed tomography (CT) in the late 1990s (31) merged sensitive detection with anatomical orientation and lead to improved cancer staging and restaging accuracies over PET or CT alone. PET/CT has now become the most vital imaging tool in oncology (32). Unfortunately, CT is associated with sizeable radiation exposure to experimental animals and patients. This has lead to concerns regarding longitudinal imaging procedures such as cancer restaging and therapy monitoring (33).

MRI, on the other hand, is suitable for longitudinal imaging and provides soft tissue contrast that is superior to that of CT. In recent years research focusing on combining PET with MRI has surged (34-38), and it is often suggested that combined PET/MRI may surpass PET/CT as the diagnostic imaging modality of choice (39-41). PET/MRI would incorporate the functional and spectroscopic abilities of MRI while delivering better soft tissue contrast than CT without the associated radiation exposure. MRI, when used in conjunction with molecularly targeted magnetic nanoparticles, can generate exceptional high-resolution images of even minuscule tumors.

Nanoparticle-based MRI imaging, however, often requires *a priori* knowledge of the location of the tumor in order to position coils, set up a field of view, and obtain images (42). This drawback could be remedied by using magnetic nanoparticles labeled with a positron-emitting isotope. The PET feature would provide highly sensitive identification of tumors in unknown locations over a large region of interest while the MRI feature would provide high resolution images of nanoparticle-bound structures at tumor site.

1.2.1 Hybrid PET/MRI Instrumentation

Many technical hurdles must be overcome to combine PET and MR scanners (**Figure 1.2**). The detector elements of PET scanners contain photomultiplier tubes (PMT) to produce electrical signals from scintillation events occurring within the lutetium oxyorthosilicate (LSO) crystal blocks. The applied magnetic field used to align protons in MR scanners (as well as gradient fields) would exert a strong Lorentz force on electrons within the vacuum of the PMT. This force alters the electron trajectory and effectively renders the PMT useless.

Conversely, the introduction of nuclear imaging electronics in the MR scanner can negatively influence the field homogeneity, linearity of the gradient fields, can produce susceptibility artifacts, and can cause radiofrequency interference (39). Space constraints are also a challenge for producing combined scanners.

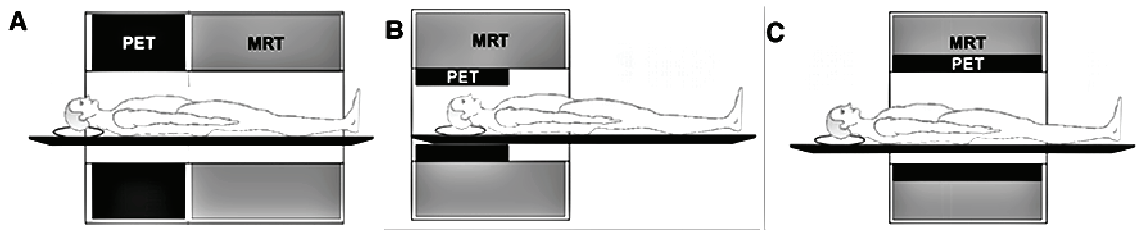


Figure 1.2: Current approaches for combined PET/MRI scanners (adapted from (43)). (A) An in-line set-up adopting the orientation of current PET/CT scanners. (B) Head-only system being released commercially. (C) Fully integrated set-up (currently in development).

Groups from several institutions have developed differing instrumentation approaches to overcome the abovementioned instrumentation issues: University of Tübingen, University of California – Davis, and the University of Cambridge. Siemens and GE Healthcare have commercial models in production. The general approach to overcoming these issues has been to replace the PMT with semiconductor light detectors (avalanche photo diodes, APDs), which are not affected by the magnetic field. APDs are also considerably smaller than PMTs and can aid

in producing a compact integrate scanner. The drawback to APDs is their low gain, which requires placement of preamplifiers, to amplify the low amplitude analog signals, within the magnetic field. These components can be protected using copper (i.e. nonmagnetic) shielding. The development of smaller and more effective instrumentation for combined PET/MRI is an active area of development (34, 36, 43-46).

1.2.2 Dual Modality Nanoparticle Probes for PET/MRI

At the time of writing, relatively few dual-modality probes have been developed for PET/MRI. Nahrendorf et al used untargeted ^{64}Cu -labeled CLIO to image uptake by macrophages in inflammatory plaques in a mouse model of atherosclerosis (47) (Figure 1.3). PET and MRI were performed separately and the images produced were not coregistered. Also, animal groups either received ^{64}Cu -labeled magnetic nanoparticles for PET (at 1.5 mg Fe/kg body weight) or unlabeled (i.e. "cold") versions of the same magnetic nanoparticle for MR imaging (30 mg Fe/kg body weight). No single animals underwent both PET and MRI in this study. Also of note, the chelator used to attach ^{64}Cu was the acyclic diethylene triamine pentaacetic acid (DTPA). Use of this chelator is curious, as its affinity for ^{64}Cu is lower than the more commonly used cyclic chelators (e.g. DOTA, TETA).

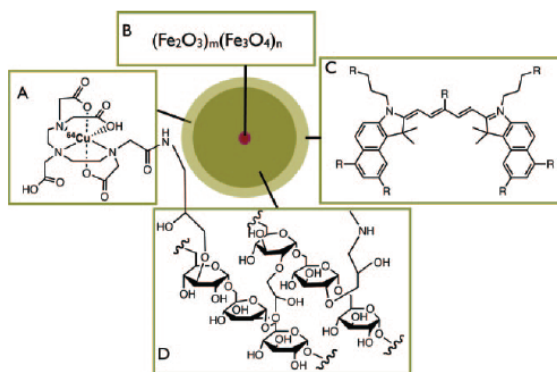


Figure 1.3: Schematic of trimodality nanoparticle (47). This nanoparticle features ^{64}Cu chelated by DTPA (A), and iron oxide core (B), a near IR dye (C), and a cross-linked dextran coating.

Choi et al used ^{124}I to label magnetic nanoparticles for combined PET/MRI (48). High temperature organometallic synthesis was used to produce monodisperse 15nm MnFe_2O_4 nanoparticles (particles are doped with manganese to enhance MR contrast effect (49)). The MnFe_2O_4 cores were coated with serum albumin to allow solubility in water (Figure 1.4). The exchange of nanoparticle surface ligands with protein is an older approach to nanoparticle coating and it is unclear why the authors chose this method. Nevertheless, ^{124}I labeling was achieved and the resultant particles produced PET and MR contrast.



Figure 1.4: ^{124}I labeled, albumin coated MnFe_2O_4 dual PET/MRI nanoparticle (48).

To test the particles in a biological environment, untargeted particles were injected into rat forepaws. At one hour post injection PET and MR imaging was performed. Resulting images were coregistered by means of custom made fiducial markers. The injected particles gathered in the brachial and axillary lymph nodes, which were visible in post PET and MRI. The authors did not state what the circulation half-life of the nanoparticle. The early imaging time point (1 hr postinjection) indicates the nanoparticles have a short blood (ca. < 2hr) half-life. The accumulation in brachial and axillary lymph nodes was unilateral (i.e. restricted to the side possessing the forepaw receiving the injection, in this case the right side of the body). The unilateral accumulation indicates that particles were not systemically available, presumably due to a short blood half-life. The systemic uptake of long circulating magnetic nanoparticles has been well studied (50-52).

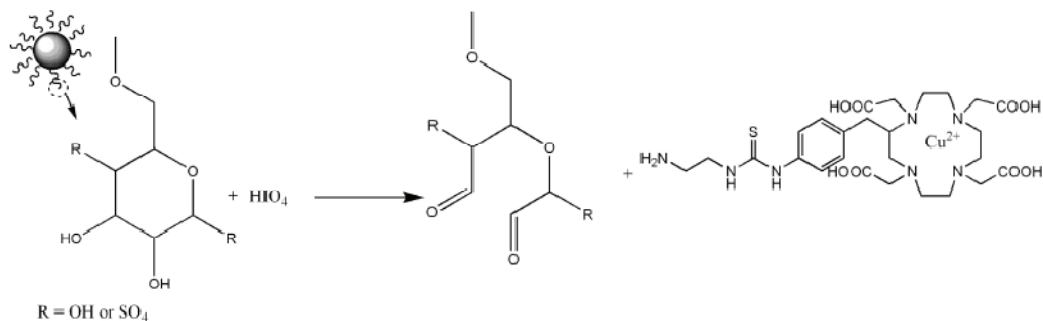


Figure 1.5: ⁶⁴Cu labeling of anion dextran sulfate-coated magnetic nanoparticles (53).

Jarrett et al used ⁶⁴Cu to label anionic dextran sulfate coated iron oxide (ADIO) nanoparticles (53) (Figure 1.5). No PET or MR imaging was performed in this study. The surface of ADIO was modified to contain aldehyde groups to allow conjugation with amine-activated DOTA. Strangely, the authors reported that ADIO functionalized with DOTA could not be labeled with ⁶⁴Cu. The authors claimed that charge effects were the cause. Successful labeling was only reported when ⁶⁴Cu was chelated by DOTA prior to attachment to the nanoparticle surface. After personal discussion with the author it was determined that the author failed to use the correct pH during the labeling step. Additionally, the aldehyde particles were treated with ethylenediamine to generate amine functional groups on the particle surface. The use of bifunctional ethylenediamine will undoubtedly lead to some degree of undesired nanoparticle crosslinking.



Figure 1.6: Polyaspartic acid-coated iron oxide nanoparticles labeled with ⁶⁴Cu (54). Nanoparticles were targeted to tumors using an RGD peptide.

Lee et al used ^{64}Cu to label polyaspartic acid-coated iron oxide nanoparticles (PASP-IO) (54) (Figure 1.6). The PASP-IO particles were synthesized by coprecipitation of iron salts in the presence of PASP. The nanoparticles had a 5 nm core and were 45 ± 10 nm in diameter after coating with PASP. The nanoparticles were conjugated with RGD peptide and target to integrins in a mouse tumor model. PET and MRI was performed but not coregistered. The authors failed to show pre- and post-injection MR images of the same animals. The MR images that were shown were of poor quality and low resolution. Pre- and post-injection PET images were shown and specific targeted was achieved.

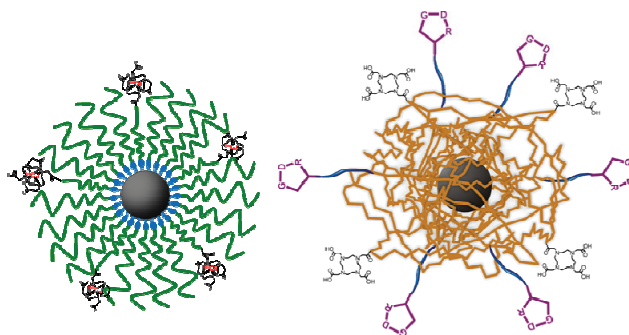


Figure 1.7: Dual PET/MRI probes developed in this work. (Left) A ^{64}Cu -labeled, PEG-lipid coated iron oxide nanoparticle (55). The iron core is shown in grey, mPEG2000 and mPEG5000 polymers are shown in green. DOTA- ^{64}Cu complex shown in black/red. (Right) Cyclic-RGD targeted dual PET/MRI nanoparticle. The particle core (grey) is surrounded by crosslinked dextran (orange). Cyclo(RGDyC) peptides (purple) are conjugated to PEG polymers (blue). The chelator DOTA (black) used to radiolabel the particles with ^{64}Cu is linked to the dextran coating. This particle was targeted to integrins in tumor-bearing mice (56).

Our studies evaluated two radiolabeled nanoparticles for PET/MR imaging. The first was a ^{64}Cu -labeled iron oxide nanoparticle with a PEG-lipid coating. We reported detailed synthesis and radiolabeling studies. Phantom studies showing PET/MRI contrast were performed. Multi-organ, multi-time point biodistribution was performed as well as multi-time point PET imaging. The second study we performed used RGD-targeted magnetic nanoparticles. The MNPs had a

crosslinked dextran coating and were radiolabeled with ^{64}Cu . Phantom PET and MRI studies were performed. PET and MR imaging was performed in tumor-bearing mice. Specific accumulation was observed in PET images. We feel that this work contributes to the field and extends the understanding of dual PET/MRI nanoparticles.

1.3 References

1. Massoud, T. and S. Gambhir, *Molecular imaging in living subjects: seeing fundamental biological processes in a new light*. Genes & Development, 2003. **17**(5): p. 545-580.
2. Anderson, C.J., F. Dehdashti, P.D. Cutler, S.W. Schwarz, R. Laforest, L.A. Bass, J.S. Lewis, and D.W. McCarthy, *^{64}Cu -TETA-octreotide as a PET imaging agent for patients with neuroendocrine tumors*. J Nucl Med, 2001. **42**(2): p. 213-21.
3. Lewis, J.S., J.M. Connett, J.R. Garbow, T.L. Buettner, Y. Fujibayashi, J.W. Fleshman, and M.J. Welch, *Copper-64-pyruvaldehyde-bis(N(4)-methylthiosemicarbazone) for the prevention of tumor growth at wound sites following laparoscopic surgery: monitoring therapy response with microPET and magnetic resonance imaging*. Cancer Res, 2002. **62**(2): p. 445-9.
4. Service, R.F., *MATERIALS AND BIOLOGY: Nanotechnology Takes Aim at Cancer*. Science, 2005. **310**(5751): p. 1132-1134.
5. Ferrari, M., *Cancer nanotechnology: opportunities and challenges*. Nature Reviews Cancer, 2005. **5**(3): p. 161-171.
6. Torchilin, V.P., *Multifunctional nanocarriers*. Adv Drug Deliv Rev, 2006. **58**(14): p. 1532-55.
7. Chen, C.C., A.B. Herhold, C.S. Johnson, and A.P. Alivisatos, *Size Dependence of Structural Metastability in Semiconductor Nanocrystals*. Science, 1997. **276**(5311): p. 398-401.
8. Hyeon, T., S.S. Lee, J. Park, Y. Chung, and H.B. Na, *Synthesis of highly crystalline and monodisperse maghemite nanocrystallites without a size-selection process*. J Am Chem Soc, 2001. **123**(51): p. 12798-801.
9. Josephson, L., C.H. Tung, A. Moore, and R. Weissleder, *High-efficiency intracellular magnetic labeling with novel superparamagnetic-Tat peptide conjugates*. Bioconjug Chem, 1999. **10**(2): p. 186-91.
10. Lewin, M., N. Carlesso, C.H. Tung, X.W. Tang, D. Cory, D.T. Scadden, and R. Weissleder, *Tat peptide-derivatized magnetic nanoparticles allow in vivo tracking and recovery of progenitor cells*. Nat Biotechnol, 2000. **18**(4): p. 410-4.

11. Wickline, S.A. and G.M. Lanza, *Nanotechnology for molecular imaging and targeted therapy*. Circulation, 2003. **107**(8): p. 1092-5.
12. Kraitchman, D.L., A.W. Heldman, E. Atalar, L.C. Amado, B.J. Martin, M.F. Pittenger, J.M. Hare, and J.W. Bulte, *In vivo magnetic resonance imaging of mesenchymal stem cells in myocardial infarction*. Circulation, 2003. **107**(18): p. 2290-3.
13. Walczak, P., J. Ruiz-Cabello, D.A. Kedziorek, A.A. Gilad, S. Lin, B. Barnett, L. Qin, H. Levitsky, and J.W. Bulte, *Magneto-electroporation: improved labeling of neural stem cells and leukocytes for cellular magnetic resonance imaging using a single FDA-approved agent*. Nanomedicine, 2006. **2**(2): p. 89-94.
14. Walczak, P., D.A. Kedziorek, A.A. Gilad, B.P. Barnett, and J.W. Bulte, *Applicability and limitations of MR tracking of neural stem cells with asymmetric cell division and rapid turnover: the case of the shiverer dysmyelinated mouse brain*. Magn Reson Med, 2007. **58**(2): p. 261-9.
15. Winter, P.M., S.D. Caruthers, A. Kassner, T.D. Harris, L.K. Chinen, J.S. Allen, E.K. Lacy, H. Zhang, J.D. Robertson, S.A. Wickline, and G.M. Lanza, *Molecular imaging of angiogenesis in nascent Vx-2 rabbit tumors using a novel alpha(nu)beta3-targeted nanoparticle and 1.5 tesla magnetic resonance imaging*. Cancer Res, 2003. **63**(18): p. 5838-43.
16. Montet, X., K. Montet-Abou, F. Reynolds, R. Weissleder, and L. Josephson, *Nanoparticle imaging of integrins on tumor cells*. Neoplasia, 2006. **8**(3): p. 214-22.
17. Lee, J.H., Y.M. Huh, Y.W. Jun, J.W. Seo, J.T. Jang, H.T. Song, S. Kim, E.J. Cho, H.G. Yoon, J.S. Suh, and J. Cheon, *Artificially engineered magnetic nanoparticles for ultra-sensitive molecular imaging*. Nat Med, 2007. **13**(1): p. 95-9.
18. Winter, P.M., A.M. Morawski, S.D. Caruthers, R.W. Fuhrhop, H. Zhang, T.A. Williams, J.S. Allen, E.K. Lacy, J.D. Robertson, G.M. Lanza, and S.A. Wickline, *Molecular imaging of angiogenesis in early-stage atherosclerosis with alpha(v)beta3-integrin-targeted nanoparticles*. Circulation, 2003. **108**(18): p. 2270-4.
19. Nahrendorf, M., F.A. Jaffer, K.A. Kelly, D.E. Sosnovik, E. Aikawa, P. Libby, and R. Weissleder, *Noninvasive vascular cell adhesion molecule-1 imaging identifies inflammatory activation of cells in atherosclerosis*. Circulation, 2006. **114**(14): p. 1504-11.
20. Rossin, R., D. Pan, K. Qi, J.L. Turner, X. Sun, K.L. Wooley, and M.J. Welch, *⁶⁴Cu-labeled folate-conjugated shell cross-linked nanoparticles for tumor imaging and radiotherapy: synthesis, radiolabeling, and biologic evaluation*. J Nucl Med, 2005. **46**(7): p. 1210-8.
21. Sun, X., R. Rossin, J.L. Turner, M.L. Becker, M.J. Joralemon, M.J. Welch, and K.L. Wooley, *An assessment of the effects of shell cross-linked nanoparticle size, core composition, and surface PEGylation on in vivo biodistribution*. Biomacromolecules, 2005. **6**(5): p. 2541-54.

22. Fukukawa, K., R. Rossin, A. Hagooley, E.D. Pressly, J.N. Hunt, B.W. Messmore, K.L. Wooley, M.J. Welch, and C.J. Hawker, *Synthesis and characterization of core-shell star copolymers for in vivo PET imaging applications*. *Biomacromolecules*, 2008. **9**(4): p. 1329-39.
23. Rossin, R., S. Muro, M.J. Welch, V.R. Muzykantov, and D.P. Schuster, *In vivo imaging of ⁶⁴Cu-labeled polymer nanoparticles targeted to the lung endothelium*. *J Nucl Med*, 2008. **49**(1): p. 103-11.
24. Sun, G., A. Hagooley, J. Xu, A.M. Nystrom, Z. Li, R. Rossin, D.A. Moore, K.L. Wooley, and M.J. Welch, *Facile, efficient approach to accomplish tunable chemistries and variable biodistributions for shell cross-linked nanoparticles*. *Biomacromolecules*, 2008. **9**(7): p. 1997-2006.
25. Sosnovik, D.E., M. Nahrendorf, N. Deliolanis, M. Novikov, E. Aikawa, L. Josephson, A. Rosenzweig, R. Weissleder, and V. Ntzichristos, *Fluorescence tomography and magnetic resonance imaging of myocardial macrophage infiltration in infarcted myocardium in vivo*. *Circulation*, 2007. **115**(11): p. 1384-91.
26. Trehin, R., J.L. Figueiredo, M.J. Pittet, R. Weissleder, L. Josephson, and U. Mahmood, *Fluorescent nanoparticle uptake for brain tumor visualization*. *Neoplasia*, 2006. **8**(4): p. 302-11.
27. Kircher, M.F., U. Mahmood, R.S. King, R. Weissleder, and L. Josephson, *A multimodal nanoparticle for preoperative magnetic resonance imaging and intraoperative optical brain tumor delineation*. *Cancer Res*, 2003. **63**(23): p. 8122-5.
28. Cai, W., K. Chen, Z.B. Li, S.S. Gambhir, and X. Chen, *Dual-function probe for PET and near-infrared fluorescence imaging of tumor vasculature*. *J Nucl Med*, 2007. **48**(11): p. 1862-70.
29. Chen, K., Z.B. Li, H. Wang, W. Cai, and X. Chen, *Dual-modality optical and positron emission tomography imaging of vascular endothelial growth factor receptor on tumor vasculature using quantum dots*. *Eur J Nucl Med Mol Imaging*, 2008.
30. Phelps, M.E., E.J. Hoffman, N.A. Mullani, and M.M. Ter-Pogossian, *Application of annihilation coincidence detection to transaxial reconstruction tomography*. *J Nucl Med*, 1975. **16**(3): p. 210-24.
31. Beyer, T., D.W. Townsend, T. Brun, P.E. Kinahan, M. Charron, R. Roddy, J. Jerin, J. Young, L. Byars, and R. Nutt, *A combined PET/CT scanner for clinical oncology*. *J Nucl Med*, 2000. **41**(8): p. 1369-79.
32. Czernin, J., M. Allen-Auerbach, and H.R. Schelbert, *Improvements in cancer staging with PET/CT: literature-based evidence as of September 2006*. *J Nucl Med*, 2007. **48 Suppl 1**: p. 78S-88S.

33. Boone, J.M., O. Velazquez, and S.R. Cherry, *Small-animal X-ray dose from micro-CT*. Mol Imaging, 2004. **3**(3): p. 149-58.
34. Catana, C., Y. Wu, M.S. Judenhofer, J. Qi, B.J. Pichler, and S.R. Cherry, *Simultaneous acquisition of multislice PET and MR images: initial results with a MR-compatible PET scanner*. J Nucl Med, 2006. **47**(12): p. 1968-76.
35. Higuchi, T., S.G. Nekolla, A. Jankaukas, A.W. Weber, M.C. Huisman, S. Reder, S.I. Ziegler, M. Schwaiger, and F.M. Bengel, *Characterization of normal and infarcted rat myocardium using a combination of small-animal PET and clinical MRI*. J Nucl Med, 2007. **48**(2): p. 288-94.
36. Pichler, B.J., M.S. Judenhofer, C. Catana, J.H. Walton, M. Kneilling, R.E. Nutt, S.B. Siegel, C.D. Claussen, and S.R. Cherry, *Performance test of an LSO-APD detector in a 7-T MRI scanner for simultaneous PET/MRI*. J Nucl Med, 2006. **47**(4): p. 639-47.
37. Ruf, J., E. Lopez Hanninen, M. Bohmig, I. Koch, T. Denecke, M. Plotkin, J. Langrehr, B. Wiedenmann, R. Felix, and H. Amthauer, *Impact of FDG-PET/MRI image fusion on the detection of pancreatic cancer*. Pancreatology, 2006. **6**(6): p. 512-9.
38. Seemann, M.D., G. Meisetschlaeger, J. Gaa, and E.J. Rummeny, *Assessment of the extent of metastases of gastrointestinal carcinoid tumors using whole-body PET, CT, MRI, PET/CT and PET/MRI*. Eur J Med Res, 2006. **11**(2): p. 58-65.
39. Cherry, S.R., *The 2006 Henry N. Wagner Lecture: Of mice and men (and positrons)--advances in PET imaging technology*. J Nucl Med, 2006. **47**(11): p. 1735-45.
40. Gaa, J., E.J. Rummeny, and M.D. Seemann, *Whole-body imaging with PET/MRI*. Eur J Med Res, 2004. **9**(6): p. 309-12.
41. Seemann, M.D., *Whole-body PET/MRI: the future in oncological imaging*. Technol Cancer Res Treat, 2005. **4**(5): p. 577-82.
42. Hu, G., M. Lijowski, H. Zhang, K.C. Partlow, S.D. Caruthers, G. Kiefer, G. Gulyas, P. Athey, M.J. Scott, S.A. Wickline, and G.M. Lanza, *Imaging of Vx-2 rabbit tumors with alpha(nu)beta3-integrin-targeted 111In nanoparticles*. Int J Cancer, 2007. **120**(9): p. 1951-7.
43. Pichler, B.J., H.F. Wehrl, A. Kolb, and M.S. Judenhofer, *Positron emission tomography/magnetic resonance imaging: the next generation of multimodality imaging?* Semin Nucl Med, 2008. **38**(3): p. 199-208.
44. Catana, C., D. Procissi, Y. Wu, M.S. Judenhofer, J. Qi, B.J. Pichler, R.E. Jacobs, and S.R. Cherry, *Simultaneous in vivo positron emission tomography and magnetic resonance imaging*. Proc Natl Acad Sci U S A, 2008. **105**(10): p. 3705-10.
45. Judenhofer, M.S., H.F. Wehrl, D.F. Newport, C. Catana, S.B. Siegel, M. Becker, A. Thielscher, M. Kneilling, M.P. Lichy, M. Eichner, K. Klingel, G. Reischl, S. Widmaier, M.

- Rocken, R.E. Nutt, H.J. Machulla, K. Uludag, S.R. Cherry, C.D. Claussen, and B.J. Pichler, *Simultaneous PET-MRI: a new approach for functional and morphological imaging*. Nat Med, 2008. **14**(4): p. 459-65.
46. Pichler, B.J., M.S. Judenhofer, and H.F. Wehrl, *PET/MRI hybrid imaging: devices and initial results*. Eur Radiol, 2008. **18**(6): p. 1077-86.
47. Nahrendorf, M., H. Zhang, S. Hembrador, P. Panizzi, D.E. Sosnovik, E. Aikawa, P. Libby, F.K. Swirski, and R. Weissleder, *Nanoparticle PET-CT imaging of macrophages in inflammatory atherosclerosis*. Circulation, 2008. **117**(3): p. 379-87.
48. Choi, J.S., J.C. Park, H. Nah, S. Woo, J. Oh, K.M. Kim, G.J. Cheon, Y. Chang, J. Yoo, and J. Cheon, *A hybrid nanoparticle probe for dual-modality positron emission tomography and magnetic resonance imaging*. Angew Chem Int Ed Engl, 2008. **47**(33): p. 6259-62.
49. Lee, J., Y. Huh, Y. Jun, J. Seo, J. Jang, H. Song, S. Kim, E. Cho, H. Yoon, and J. Suh, *Artificially engineered magnetic nanoparticles for ultra-sensitive molecular imaging*. Nature Medicine, 2006. **13**: p. 95-99.
50. Harisinghani, M.G., J. Barentsz, P.F. Hahn, W.M. Deserno, S. Tabatabaei, C.H. van de Kaa, J. de la Rosette, and R. Weissleder, *Noninvasive detection of clinically occult lymph-node metastases in prostate cancer*. N Engl J Med, 2003. **348**(25): p. 2491-9.
51. Harisinghani, M.G., S. Saini, R. Weissleder, P.F. Hahn, R.K. Yantiss, C. Tempany, B.J. Wood, and P.R. Mueller, *MR lymphangiography using ultrasmall superparamagnetic iron oxide in patients with primary abdominal and pelvic malignancies: radiographic-pathologic correlation*. AJR Am J Roentgenol, 1999. **172**(5): p. 1347-51.
52. Weissleder, R., G. Elizondo, J. Wittenberg, A.S. Lee, L. Josephson, and T.J. Brady, *Ultrasmall superparamagnetic iron oxide: an intravenous contrast agent for assessing lymph nodes with MR imaging*. Radiology, 1990. **175**(2): p. 494-8.
53. Jarrett, B.R., B. Gustafsson, D.L. Kukis, and A.Y. Louie, *Synthesis of ⁶⁴Cu-labeled magnetic nanoparticles for multimodal imaging*. Bioconjug Chem, 2008. **19**(7): p. 1496-504.
54. Lee, H.Y., Z. Li, K. Chen, A.R. Hsu, C. Xu, J. Xie, S. Sun, and X. Chen, *PET/MRI dual-modality tumor imaging using arginine-glycine-aspartic (RGD)-conjugated radiolabeled iron oxide nanoparticles*. J Nucl Med, 2008. **49**(8): p. 1371-9.
55. Glaus, C.R.M., R. Rossin, M.J. Welch, and G. Bao, *In vivo evaluation of ⁶⁴Cu-labeled Magnetic Nanoparticles: A Novel Probe for Dual-Modality PET/MR Imaging in submission*.
56. Glaus, C.R.M., A. Hagooly, M.J. Welch, and G. Bao, *PET/MR Imaging of Tumors Using RGD-targeted ⁶⁴Cu-labeled Magnetic Nanoparticles in submission*.

CHAPTER 2

DEVELOPMENT, OPTIMIZATION, AND APPLICATIONS OF PEGYLATED-PHOSPHOLIPID ENCAPSULATED MAGNETIC NANOPARTICLES

2.1 Introduction

Magnetic nanoparticles must possess a surface coating that provides sufficient stability *in vivo*. Our laboratory was one of the first to apply a phospholipid-polyethylene glycol-based coating method to produce water-soluble magnetic nanoparticles containing chemical functional groups as sites for bioconjugation (1, 2) (micelle-coated monocrystalline iron oxide nanoparticles, mMION). The iron oxide crystals that form the magnetic nanoparticle core are produced using standard high temperature synthesis techniques (3, 4). The particles are nucleated in organic solvent with the aid of surfactant molecules such as oleic acid. The surfactant molecules remain on the surface of the particles, and the particles are stored in an organic solvent such as toluene. Coating the hydrophobic cores (outlined in Chapter 3) is achieved by combining PEGylated lipids in excess with iron oxide cores in chloroform in a round bottomed flask. Chloroform is removed by rotary evaporation and heating, creating a thin film of iron oxide cores and PEGylated lipid on the walls of the flask. The film is then hydrated with water, forcing the alkyl chains of the lipid to interdigitate into the oleic acid surfactant molecules on the surface of the iron oxide particles (Figure 2.1). The PEGylated-lipid coating, in this case DSPE-PEG-2000 (1,2-distearoyl-sn-glycero-3-phosphoethanolamine-N-[methoxy(polyethylene glycol)-2000]), provides a biocompatible and functional surface that is modular in nature.

We have since refined the coating methodology and bioconjugation and optimized the purification process. We have developed an ultracentrifugation procedure to efficiently separate coated nanoparticles from empty micelles, a prerequisite for controlling the reaction

stoichiometry of bioconjugations. Ultracentrifugation procedures had to be developed empirically to balance the length of the centrifugation run with the rigidity of the pellet formed. In addition to centrifugation techniques, a magnetic-based separation was applied to the purification of mMIONS from empty micelles, dyes, and biomolecules, reducing the time to purify mMION samples from ≈ 20 hours to 30 minutes.

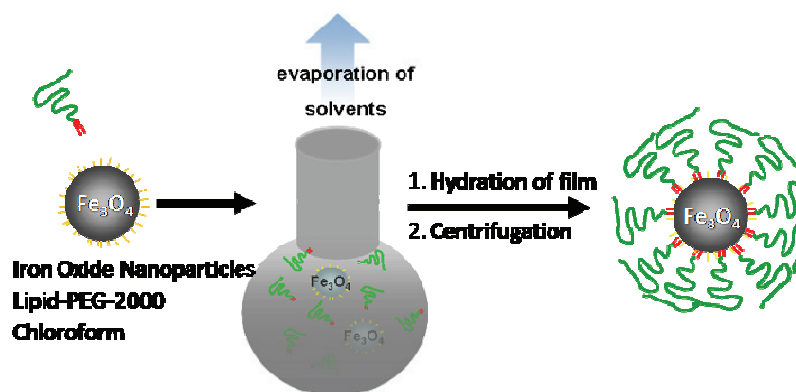


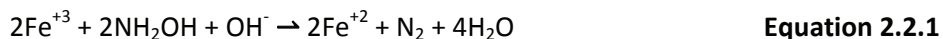
Figure 2.1: Synthesis of micelle-coated monocrystalline iron oxide nanoparticles.

Multiple functional groups have also been incorporated into a single nanoparticle coating. Production scale of the PEGylated-lipid coating has been increased to tens of milligrams of iron at a 100mL volume, some thirty three times greater than previously achieved (5). A new assay was developed to determine the amount of iron in nanoparticle sample which reduces assay time from ≈ 24 hours to ≈ 2 hours. Additionally, the coating method has been generalized to accommodate larger iron oxide core sizes. We have gone to great lengths to optimize the coating procedure. Several types of separation media have been evaluated for their propensity to physically absorb lipid-PEG coated magnetic particles. Size exclusion chromatography (SEC) using successfully employed to purify bioconjugated mMIONS. Filtering particle solutions is a critical step in most conjugation reactions, therefore it was imperative to identify filter material with small pore size (ideally 100 nm), adequate hydrophilicity, and minimal hold-up volume.

2.2 Probe Development and Optimization

2.2.1 Development of a Rapid, High Temperature Iron Assay For Quantifying Fe₃O₄ Magnetic Nanoparticles

In previous iron measurements of mMIONs (2, 6, 7), nanoparticles were incubated in mercaptoacetic acid (MEA) overnight to dissolve the iron oxide core and release ionic iron. The necessary overnight incubation of this method considerably slows the work flow of mMION conjugations. Additionally, MEA has a strong unpleasant odor and is readily oxidized by air. To circumvent these shortcomings, a high-temperature assay was developed by modifying methods used by Yu et al (8). This protocol uses concentrated hydrochloric acid (HCl) with heating to dissolve iron oxide cores in 10 minutes as opposed to overnight in MEA.



18 μL of dilute nanoparticles is combined with 17 μL of 6 M hydrochloric acid in a PCR tube. The tube is incubated in a thermocycler for 10 minutes at 100°C. 10 μL of hydroxylamine hydrochloride (10 mg/mL) is added to the dissolved mMIONs. Hydroxylamine is used to ensure iron ions are in the ferrous state (i.e. +2 oxidation state), according to Equation 2.1.

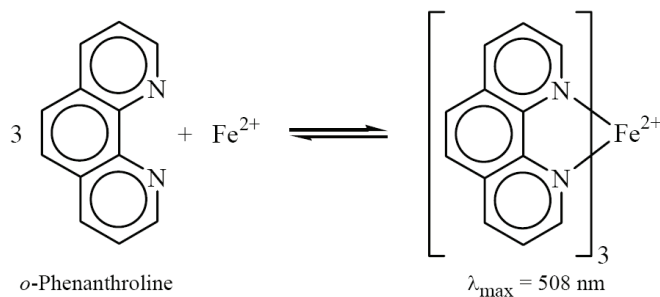


Figure 2.2: Complexation of Fe²⁺ with 1,10-Phenanthroline in the rapid, high temperature Fe assay (9).

Sodium acetate (NaOAc, 855 μL of 125 mg/mL) is then added, followed by of 100 μL of 1,10-phenanthroline (1 mg/mL). Iron ions are allowed to complex with phenanthroline for ≈ 10 minutes before reading the absorbance of samples at 510 nm using a microplate reader (Figure 2.2). The sample absorbance values are then compared to a standard curve. A standard curve of iron-containing solution for was prepared using ferrous ammonium sulfate hexahydrate (Iron(II) ammonium sulfate, Mohr's salt): $(\text{NH}_4)_2(\text{Fe})(\text{SO}_4)_2 \cdot 6\text{H}_2\text{O}$ (Table 2.1). A 5 mg Fe/L standard solution was prepared from DI water and 15 μL of sulfuric acid. The entire assay now requires approximately 1 hour perform.

Table 2.1: Preparation of ferrous ammonium sulfate standard curve

Fe Standard (μL)	DI Water (μL)	NaOAc (μL)	Hydroxylamine (μL)	1,10-Phenanthroline (μL)
500	0	390	10	100
250	250	390	10	100
100	400	390	10	100
50	450	390	10	100
10	490	390	10	100

2.2.2 In Situ Dye Labeling

Traditionally, mMIONs are labeled with fluorescent dyes by conjugating reactive dyes (e.g. amine-reactive NHS-esters) to functional groups on the ends of the PEG-lipid molecules which form the nanoparticle coating. Unfortunately, this “*post-synthesis*” dye insertion inevitably leads to presence unreacted dye along with the fluorescent conjugate, requiring time consuming purification steps which decrease yield. If one desires to have unreacted PEG-lipids after dye labeling, one must either be careful not to consume all functionalized PEG-lipids (accomplished through trial and error). Afterwards it is necessary to determine the number of remaining functional PEG-lipids available prior and downstream reactions so that appropriate

reaction ratios can be determined. Alternatively, multiple PEG-lipid species have orthogonal reactive groups can be used to initially coat the nanoparticles. One functional group would then be available for dye labeling while the other would be available for downstream reactions. This approach adds extra complexity and cost.

A solution to the limitations above is achieved through *in situ* dye labeling (Figure 2.3). That is, labeling of the nanoparticles during the coating step. *In situ* dye labeling of mMIONs is achieved by the addition of fluorescent lipids to the PEG-lipid mixture used to coat hydrophobic iron oxide cores. To achieve a high degree of dye labeling, 1 – 5 mole % of 2-Dioleoyl-sn-Glycero-3-Phosphoethanolamine-N-(Lissamine Rhodamine B Sulfonyl) (18: 1 Lissamine Rhodamine PE) was added to the DSPE-PEG-2000 PEGylated-lipid coating mixture. Rhodamine has a red emission ($\lambda_{\text{abs}} = 550 \text{ nm}$, $\lambda_{\text{em}} = 590 \text{ nm}$, $\epsilon = 100,000 \text{ M}^{-1}\text{cm}^{-1}$), making it favorable for cellular imaging. Also, the lipid-dye is less susceptible to photo-bleaching because its location in the lipid portion of the micelle coating helps to exclude water and therefore destructive oxygen radicals.

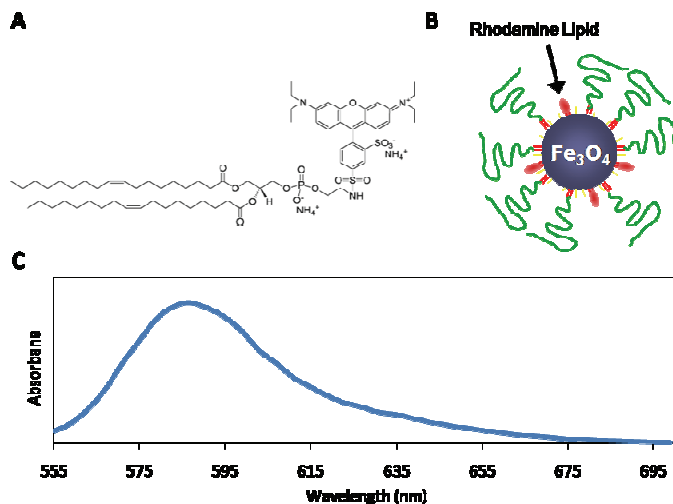


Figure 2.3: *In situ* fluorescent labeling of micelle-coated magnetic nanoparticles. (A) Rhodamine-phosphoethanolamine (PE) conjugate. (B) Schematic showing the insertion of rhodamine-lipid into the lipid portion of the micelle coating. (C) Emission of rhodamine-PE labeled mMIONs in solution.

2.2.3 Nanoparticle Separation Using Ultracentrifugation

The mMION samples used in previous studies were mixtures of empty micelles and micelle-coated nanoparticles, with empty micelles far outnumbering coated nanoparticles (2, 6). As such, conjugations performed with unpurified samples produce empty PEG-lipid micelles labeled with dyes, peptides, etc. Proper purification of mMIONs is required to obtain accurate results.

We have developed an ultracentrifugation procedure to efficiently separate coated nanoparticles from empty micelles. Ultracentrifugation procedures had to be developed empirically to balance the length of the centrifugation run with the rigidity of the pellet formed. Tests were performed using Beckman Coulter Optima XL-100K. Initial studies evaluated the separation of nanoparticles at 30,000 rpm for 18 – 20 hours at 4 °C. Separation at this speed and duration results in a soft pellet with a small amount of nanoparticles remaining in the supernatant. Separation at 41,000 rpm for 6 – 8 hours results in adequate separation, which a more rigid pellet and more clear supernatant. In both cases it is imperative to spin the sample

on a table top centrifuge at 8,000 – 10,000 rpm for 3 – 5 minutes to remove any large iron aggregates. Doing so will keep such aggregates from collecting the pellet produced by ultracentrifugation. Figure 2.4 shows the hydrodynamic diameter of the supernatant solution after ultracentrifugation. The hydrodynamic diameter of the supernatant was found to be 10.0 ± 1.4 nm, which is in agreement with previously reported values of the size of DSPE-PEG-2000 micelles (10-13).

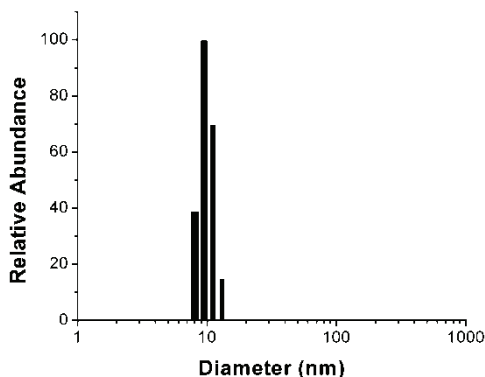


Figure 2.4: Dynamic light scattering of empty micelles. The supernatant following ultracentrifugation was subjected to DLS to measure the size of any remaining material. The supernatant was clear and free from iron. The hydrodynamic diameter of empty micelles was found to be 10.0 ± 1.4 nm.

2.2.4 Nanoparticle Separation Using High Gradient Magnetic Columns

In addition to ultracentrifugation separation techniques, a magnetic-based column separation was applied to the purification of mMIONs from empty micelles, dyes, and biomolecules. To understand this technique, we must first be aware of the nature of the magnetic force exerted on ultras-small superparamagnetic iron oxide nanoparticles (USPIOs) when placed in an external magnetic field. Because the Fe_3O_4 core of mMIONs is superparamagnetic the magnetic volume susceptibility (χ) is ≈ 1 . When an iron oxide nanoparticle in solution is placed in a magnetic field

is experiences a force that aligns its magnetic moment to that of the field, and the energy of such a particles is defined by:

$$U = -\frac{1}{2} \mathbf{m} \cdot \mathbf{B} = -\frac{\chi'V}{2\mu_0} |\mathbf{B}|^2 \quad \text{Equation 2.2}$$

with \mathbf{m} representing the magnetic moment, \mathbf{B} representing the magnetic field, V representing the volume of the nanoparticle, μ_0 representing the permeability of free space, and χ' representing the difference in magnetic susceptibility between the nanoparticle and its surrounding. The force acting on USPIOs is given by:

$$\mathbf{F} = -U = \nabla \left[\frac{\chi'V}{2\mu_0} |\mathbf{B}|^2 \right] = \chi'V \nabla \left[\frac{|\mathbf{B}|^2}{2\mu_0} \right] \quad \text{Equation 2.3}$$

Here we can see that the force exerted on mMIONS is proportional to the gradient of the applied magnetic field. Magnetic separation of USPIOs using standard macroscopic magnetic is often difficult because of the generally low gradient field produced, therefore a high gradient magnetic field (HGMF) separation is generally required (14-18). This is typically achieved using a column filled with small fibers or micron-size beads of a ferromagnetic nature (i.e. magnetizable) (Figure 2.5A) (18, 19). The beads are coated to prevent oxidation and contamination of samples. The column is then placed in an external field. Due to their extreme curvature, a strong magnetic field gradient is produced at the bead surface (Figure 2.5B). To achieve separation, an impure mMION solution of passed over the column. mMIONS are retained in the column and empty micelles, unreacted fluorophores and biomolecules, etc. are removed by washing the column several times with buffer. The column is then removed from

the applied external field and the purified mMION sample is eluted. The entire separation process takes \approx 30 minutes.

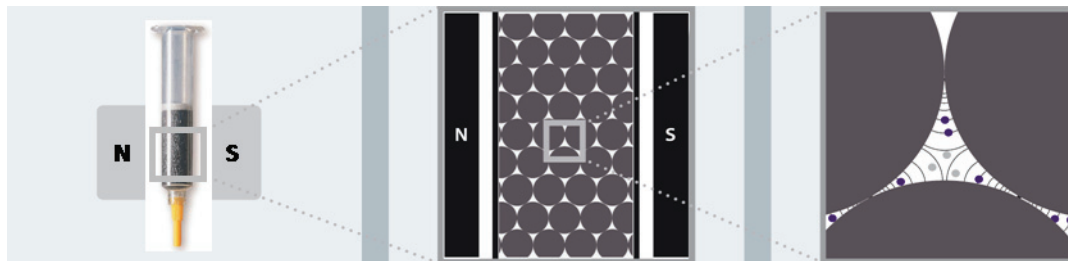


Figure 2.5: High gradient magnetic separation column. Left, column placed into an external magnetic field. Center, ferrous beads stacked inside column. Right, magnetized beads with dense surface gradients (mMIONs are depicted as small blue dots). *Adapted from Miltenyi Biotech GmbH (20).*

2.2.5 PEG-phospholipid Coating of Multisized Nanoparticles

We have also adapted the PEG-phospholipid encapsulation procedure to accommodate different sizes of iron oxide cores. It had previously been thought that nanoparticles needed to be approximately the same as the inner diameter of micelles formed by DSPE-PEG (21). It is now clear that the coating is a physical absorption of PEGylated lipids onto particles is due to a hydrophobic interaction between cetyltrimethylammonium bromide capping ligands on the nanoparticle surface and acyl chains of phospholipids (22, 23). This coating method exploits the hydrophobic interaction between capping ligands on the nanoparticle surface and acyl chains of PEGylated phospholipids, leaving the PEG moieties exposed to confer water solubility and reduce protein absorption.

To investigate the coating of larger magnetic nanoparticles, 5, 15, and 25 nm Fe_3O_4 nanoparticles with oleic acid capping ligands were acquired from Ocean NanoTech, LLC (Fayetteville, AR). Separately, the nanoparticle samples were mixed with DSPE-PEG-200 and chloroform in a round-bottomed flask and placed in a rotary evaporator. Chloroform was

evaporated, the sample was heated at 60 °C for 30 minutes, and the nanoparticle/DSPE-PEG-2000 was film hydrated using deionized water. Empty PEG-phospholipid micelles were separated from coated particles and the purified solution was filtered at 0.1 μm. Triplicate DLS measurements were made on each sample. The hydrodynamic diameters 5, 15, and 25 nm mMIONS was found to be 18.6 ± 3.0 , 29.3 ± 1.9 , and 40.6 ± 3.3 nm, respectively (Figure.

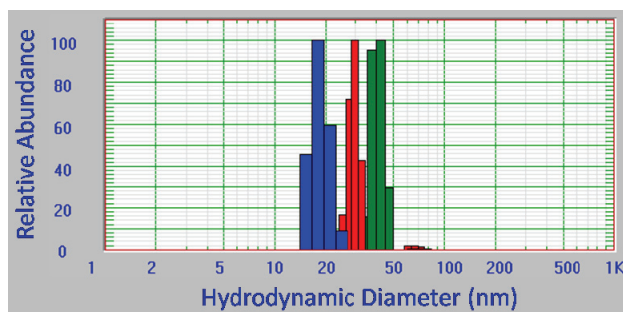


Figure 2.6: Dynamic light scattering of multisized mMIONS. The hydrodynamic diameters 5, 15, and 25 nm mMIONS was found to be 18.6 ± 3.0 , 29.3 ± 1.9 , and 40.6 ± 3.3 nm, respectively.

2.2.6 mMION Detection Level in Blood

To investigate the application of lipid-PEG magnetic nanoparticles as *in vivo* contrast agents, we have measured the ability of lipid-PEG magnetic particles to decrease the T2 relaxation time in blood. Because blood contains high levels of lipids, lipid-binding proteins, opsinizing proteins, and endogenous iron, it was an important "proof of concept" experiment to see if the lipid-PEG-coated nanoparticles would remain stable and produce measurable contrast when incubated with blood. Amounts of mMION solution (0.5, 1, 5, 10, and 20 μL) were added to 500 μL of fresh, heparinized rat blood. A control was prepared by adding PBS to 500 μL of rat blood in equal amounts. Samples were placed in NMR tubes and lowered into the bore of a 0.47 T mq20 Minispec Analyzer (Bruker BioSpin).

Transverse magnetization decay curves were acquired using a Carr-Purcell-Meiboom-Gill sequence. Curves were fit by the mq20 Minispec Analyzer software to obtain T2 time constants. The results of this experiment are shown in Figure 2.7. It can clearly be observed that the PEG-lipid magnetic nanoparticles are still able to decrease T2 relaxation times when incubated in blood. The mean T2 of control blood was found to be 411 ± 14 ms. The mean T2 from blood doped with 0.5, 1, 5, 10, and 20 μL of mMIONs was found to be 360.6 ± 2.3 , 292.4 ± 4.3 , 139.7 ± 0.6 , 88.4 ± 0.1 , and 50.9 ± 0.1 ms, respectively. All mMION measurements were found to be statistically significant ($P < 0.05$) by the Student's t-test.

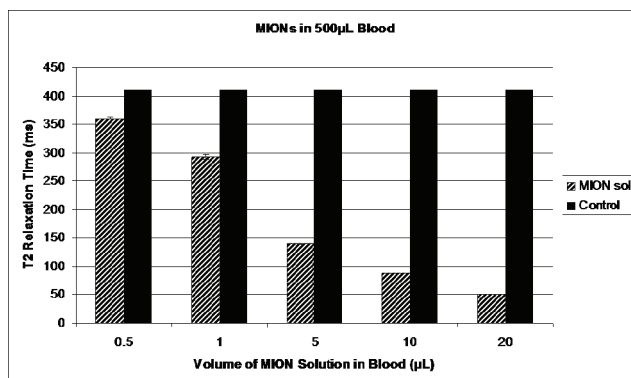


Figure 2.7: mMION detection level in blood. Mean blood T2 was measured after addition of 0.5, 1, 5, 10, or 20 μL mMION solution, and compared to mean T2 of blood with PBS added as a control. The decrease in mean blood T2 can be seen in increasing concentration.

2.2.7 Magnetic-based *In Vivo* Stability Assay

The initial studies of mMION circulation were performed by measuring the T2 of blood from mice injected with iron oxide nanoparticles. These studies evaluated the ability of mMIONs to persist in circulation and produce contrast in the *in vivo* environment. Additionally, this study helped to determine the blood half-life of mMION. All animal studies adhered to guidelines set forth by the Emory University Institutional Animal Care and Use Committee (IACUC).

Male C57BL/6 mice (25 g) aged 32 – 36 week received retro-orbital iv injections with 25 μ L of DPSE-mPEG-2000 coated iron oxide particles at a dose of 10 mg Fe/kg body weight. Control animals were injected with 25 μ L of saline. At 2 min, 30 min, 1 hr, and 4 hr post injection the mice ($n = 3$ per time point) were euthanized by CO₂ asphyxiation. The mice were immediately immobilized in the supine position and the sternum, rib cage, diaphragm, and lungs were quickly removed to expose the contracting heart. The left ventricle was pierced with a heparinized 25G needle and 200 μ L of blood was obtained. The collected blood was then transferred to heparinized tubes.

The T2 relaxation time of 200 μ L blood samples was then measured using a 4.7 T horizontal bore MRI scanner (Oxford Magnet Technology). Samples were measured 15 – 20 minutes after cardiac blood draw. Figure 2.8 shows that as the particles are eliminated from circulation, the T2 relaxation time slowly returns to that of the control blood. The mean blood T2 immediately post-injection, 30 min, 1 hr, and 4 hr post injection was 8.2 ± 1.0 , 9.5 ± 1.5 , 35.1 ± 8.2 , and 54.6 ± 4.6 ms, respectively. The mean T2 of control blood was measured to be 71.2 ± 1.5 ms ($P < 0.01$ for all time points). The blood half-life of mMION is estimated to be 104 ± 17 min. This value is in general agreement with similar PEG-lipid coated nanoparticles (24, 25).

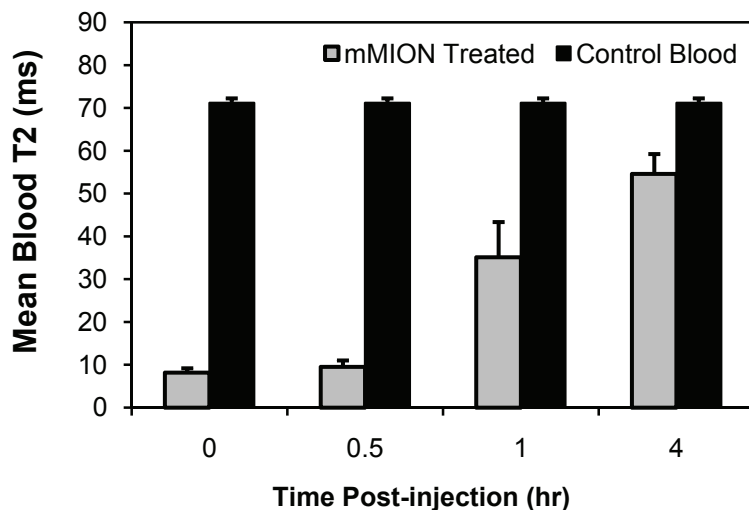


Figure 2.8: In vivo stability of mMIONS. Mice ($n = 3$) were injected with 25 μL of DPSE-mPEG-2000 coated iron oxide particles at a dose of 10 mg Fe/kg body weight. The mean blood T2 was measured immediately post-injection, 30 min, 1 hr, and 4 hr post injection. The blood half-life of mMION is estimated to be 104 ± 17 min. ($P < 0.01$ for all time points)

2.3 Pilot mMION Radiolabeling Studies

We have successfully radiolabeled PEG-lipid magnetic nanoparticles with positron-emitting copper-64. In general, DOTA-mMIONS were labeled with ^{64}Cu and analyzed according to Rossin et al (26), with further details given in Chapter 4. This initial labeling study was performed as a “proof of concept” experiment to evaluate the feasibility of nanoparticle radiolabeling, as well as to evaluate the mMION biodistribution. To bind ^{64}Cu to mMIONS, the cyclic chelator 1,4,7,10-tetraazacyclododecane-1,4,7,10-tetraacetic acid (DOTA) was conjugated to amine-functionalized PEG-lipid magnetic nanoparticles. The DOTA-containing particles were labeled with ^{64}Cu in 0.1 M ammonium acetate (NH_4OAc), pH 5.5 at 37°C with constant mixing in a thermomixer (5,000 rpm) for 1 hr. Radiolabeling in 0.1 M pH 5.5 acetate buffer was found to be superior to labeling in 0.1 mM ammonium citrate buffer, pH 5.5. Nonspecifically bound ^{64}Cu was removed by adding 5 μL of 10 mM of the acyclic chelator diethylenetriaminepentaacetic acid (DTPA) to the labeling

mixture and incubating for 5 min at room temperature. Free ^{64}Cu and ^{64}Cu -DTPA was separated from ^{64}Cu -mMIONS using size exclusion (SEC) column.

The radiochemical purity was measured following the DTPA challenge. TLC plates (Pall ITLC 56) were spotted with the labeled nanoparticle solution, developed in methanol:10% ammonium acetate (v/v, 1:1) mobile phase. The TLC plate was then scanned using a Bioscan 200 imaging scanner and analyzed using Win-Scan v2.2. The ^{64}Cu -labeled magnetic nanoparticles remained at the origin spot and the ^{64}Cu -DTPA complex migrated with the solvent front (Figure 2.9, left) ($R_f = 0$ for ^{64}Cu -MNP and $R_f = 1$ for ^{64}Cu -EDTA and ^{64}Cu -acetate). FPLC analysis was performed using a Superose 12 gel filtration column (Amersham) with 20 mM HEPES and 150 mM NaCl (pH 7.3) at a flow rate of 0.5 mL/min. UV absorption was measured at 280 nm and the radioactivity was monitored by an in-line Beckman radio-detector (Figure 2.9, right). All samples injected into animals were in excess of 95% radiochemical purity.

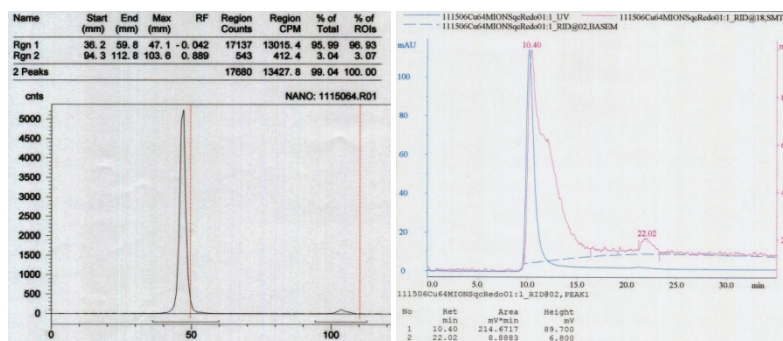


Figure 2.9: Chromatography of ^{64}Cu -mMION. Left, Radio-thin layer chromatograph showing ^{64}Cu -mMION at 47 mm, and ^{64}Cu -DTPA at 103 mm. Right, Radio-fast protein liquid chromatograph of ^{64}Cu -mMION showing UV₂₈₀ (blue) and radioactivity (red). The ^{64}Cu -mMION elutes at 10.4 min (visible in both UV and radioactivity traces), while ^{64}Cu -DTPA elutes at 22 min (visible only in radioactivity trace).

Two female C57BL/6 mice were used to measure the biodistribution of DSPE-PEG-coated magnetic nanoparticles and for PET imaging studies. The ^{64}Cu -labeled magnetic nanoparticles were sterile filtered through a 0.2 μm filter prior to injection. Mice were

anesthetized with 1-2% isoflurane and injected with labeled particles in 100 μ L of saline containing 100 μ Ci at a dose of 10 mg Fe/kg body weight via the tail vein. MicroPET and CT imaging (Figure 2.10, A-C) was performed using a microPET Focus 120 at 10 min, 1 hr, 4 hr, and 24 hr post-injection with mice immobilized in a supine position. MicroPET collection time for the 1 hr and 4hr time points was 10 min, while the collection time for the 24 hr time point was 20 min. Mice were scanned on a microCAT II immediately after microPET. Coregistration of microPET and microCT images was performed using fiducial markers in the animal transfer bed and the Amira software package.

Biodistribution and blood clearance were measured at 24 hr post injection (Figure 2.10, D, E). After sacrifice of anesthetized mice by cervical dislocation, the animals were dissected and the organs of interest were weighed and placed in a gamma counter to measure the activity present in each organ. Standard doses were prepared and measured along with the samples to calculate the percentage of injected dose per gram of tissue (%ID/g) and the percentage of injected dose per organ (%ID/organ). The following organs were harvested: blood, lung, liver, spleen, kidney, fat, heart, brain, and bone. At 1 hr post-injection the heart can easily be identified, indicating a large amount of ^{64}Cu -mMION still circulating in the blood. We observed prominent uptake by organs of the reticuloendothelial system (RES) such as the liver and spleen. At 4 hr post-injection we see diminished heart uptake. By 24 hr post-injection there is virtually no activity in the heart, indicating that nearly all ^{64}Cu -mMION have been cleared from the blood by the organs of the RES. Widespread activity can also be observed in gastrointestinal (GI) tract. This activity is an indication that ^{64}Cu -mMIONS (and their metabolic products) sequestered in the liver at earlier time points undergo biliary excretion into the GI tract to be eliminated in the feces. Some renal clearance also occurred, apparent from the activity present in the urinary bladder.

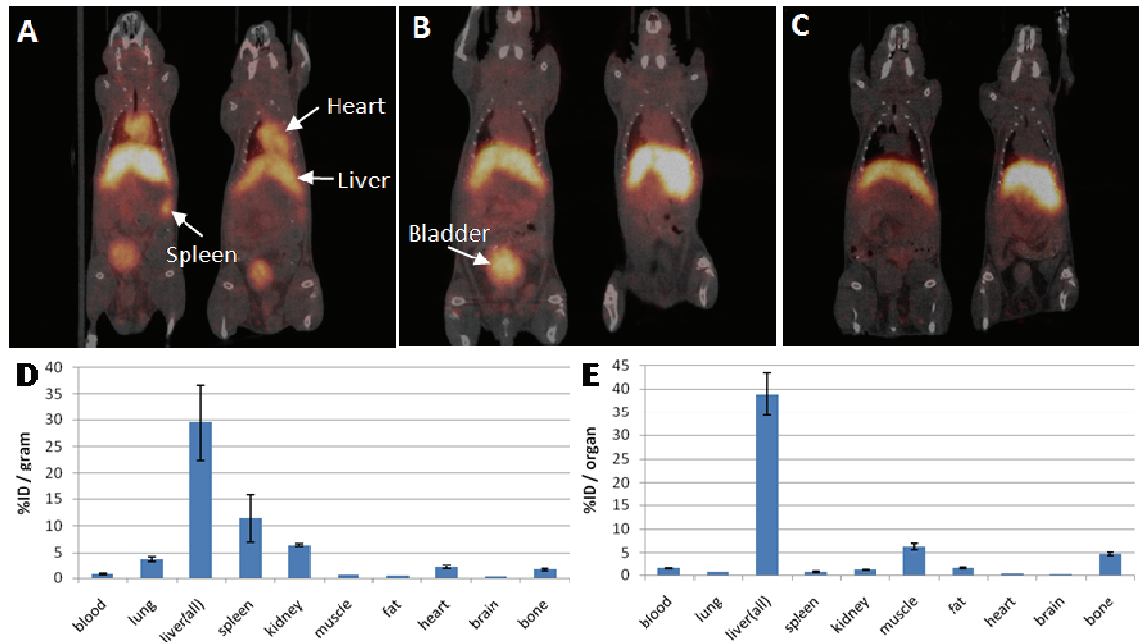


Figure 2.10: microPET/CT and post-imaging biodistribution of ^{64}Cu -mMION in C57BL/6 mice. (A) PET/CT at 1 hr post-injection. The heart can easily be identified, indicating a large amount of ^{64}Cu -mMION is still circulating in the blood. (B) 4 hr post-injection. (C) 24 hr post-injection. (D) Post-imaging biodistribution at 24 hr post-injection. Data presented as percent injected dose per gram of tissue. (E) Post-imaging biodistribution at 24 hr post-injection, with data presented as percent injected dose per organ.

2.4 Targeting Vascular Epitopes Using Fluorescent mMIONS

2.4.1 Biology of Atherosclerosis

Atherosclerosis is a chronic inflammatory disease of medium and large arteries. A remarkable increase in knowledge of the mechanisms of atherosclerosis has occurred in the previous two decades, and extensive reviews summarizing these findings have been published (27, 28).

The earliest recognized stage of atherosclerosis is a pure inflammatory lesion (i.e. fatty streak) consisting of monocyte-derived macrophages and T lymphocytes. It is also known that molecular events occurring at the endothelium contribute significantly to these intimal cellular accumulations. The endothelium is continuously exposed to atherogenic factors such as hyperlipidemia (29), the diabetic milieu, and altered shear stress (30). Endothelial expression of

adhesion molecules such as vascular cell adhesion molecule-1 (VCAM-1), which is involved in leukocyte recruitment, play a critical role in the earliest stages of atherogenesis in lesion-prone regions of the vascular system.

This early atherosclerotic plaque localization is highly correlated with areas exposed to low and oscillatory shear stress. Inflamed and dysfunctional endothelial cells are found in these areas. Nitric oxide (NO) is a potent vasodilator produced by the endothelium. The dysfunction of endothelial nitric oxide synthase (eNOS) is thought to play an important role in early endothelial damage (31). Additionally, monocyte recruitment is enhanced by chemokines secreted by smooth muscle cells such as monocyte chemoattractant protein-1 (MCP-1). Atherosclerotic plaque progression continues through accumulation of various lipids, inflammatory cells, and proliferating smooth muscle cells that produce increased amounts of extracellular matrix (ECM). These recruited cells eventually necrose, releases in toxic cellular byproducts and reactive species.

Plaque erosion with endothelial denudation and eventual plaque rupture are typical mechanisms leading to acute coronary syndromes. These mechanisms expose thrombogenic subendothelial components and the lipid core to members of the coagulation cascade. Atherosclerotic plaques express increased amounts of tissue factor (TF), a critical initiator of the coagulation cascade. Several studies have reported higher TF levels in plaques from patients with unstable coronary syndromes as opposed to patients with stable lesions. This suggests that TF may contribute to plaque growth, instability, and ultimate lethality. The cellular origin of this molecule is thought to be necrotic "foam cells." As of yet, there is little data suggesting endothelial-specific sources of TF are important in vascular inflammation and atherosclerosis (32).

To investigate the ability of mMION to targeted cell inflammation-related surface markers, we used an *en face* preparation of mouse aorta treated with LPS. Treatment with LPS results in systemic upregulation of VCAM-1 expression in the mouse vasculature (33). The imaging of low-abundance receptors such as vascular cell adhesion molecular 1 (VCAM-1) requires high sensitivity and background signal. Fluorescence-based detection using near-infrared mMIONS offers a high degree of sensitivity necessary to visually sparse epitopes.

2.4.2 Two-Photon Microscopy Using Fluorescent mMIONS

Two-photon excitation (TPE) laser scanning microscopy offers many improvements over traditional single-photon microscopy (34). Two-photon excitation occurs when two low-energy photons (i.e. red-shifted, longer wavelengths) arrive at the fluorophore almost simultaneously (on the order of femtoseconds). The fluorophore then populates an excited state via an electronic transition corresponding to twice the energy of each individual single photon. The amount of two-photon excitation is proportional to the square of the incident illumination intensity. This high intensity only occurs in the volume immediately surrounding the focal point. This unique property of two-photon excitation improves resolution through the spatial restriction of the excitation volume (35, 36). Out of focus incident light never reaches the required intensity for two-photon excitation to occur and therefore results in no fluorescence. The lack of fluorescence emission outside the focal volume greatly reduced the photobleaching of biological samples. The lack of out of focus fluorescence eliminates the need for a pinhole in confocal set-ups. Additionally, incident photons with long wavelengths scatter less in biological environments and therefore achieve deeper imaging in tissues.

We have recently described a sensitive, yet easy-to-use fluorescence IHC *en face* method using nanoparticle-bioconjugates and TPE microscopy to investigate endothelial

changes in relatively thin blood vessels such as mouse aortas (37, 38). This method been used to obtain accurate multicolored labeling, reliable fluorescence quantitation of low-abundance antigens and 3D visualization of the vascular endothelium (39).

2.4.3 Materials

Primary monoclonal rat anti-mouse VCAM-1 was purchased from BD Pharmingen. Qdot 655 goat anti-rat (Fab')₂ was provided by Quantum Dot Corporation (Invitrogen). The VCAM-1 binding peptide (40) CVHSPNKKCGGSKGKC (cyclized about C1 and C8) was synthesized with the assistance of Jan Pohl at the Emory University Microchemical and Proteomics Core Facility. Lipopolysaccharide (*E. coli* serotype 055:B5) was purchased from BioChemika. Slo-Fade Gold anti-fading mounting agent was acquired from Molecular Probes (Invitrogen). Angled forceps, scissors, and other microdissection tools were provided by World Precision Instruments, Inc. Microscope slides, #1.5 borosilicate coverglasses, and Microcon centrifugal separators were from Fisher Scientific. Hoechst 33258 was acquired from Sigma.

2.4.4 Experimental Procedures

Iron oxide nanoparticles having a 6 nm core (41) (kindly provided by Dr. Charles O'Connor, University of New Orleans) were suspended in toluene prior to coating. Transmission electron microscopy of uncoated particles was performed using a Hitachi H-7500 electron microscope. Iron oxide nanoparticles in toluene were added to a mixture of DSPE-PEG 2000 (1,2-distearoyl-*sn*-glycero-3-phosphoethanolamine-*N*-[methoxy-(poly(ethylene glycol))-2000]) and DSPE-PEG 2000-Amine (1,2-Distearoyl-*sn*-Glycero-3-Phosphoethanolamine-*N*-[Amino(Polyethylene Glycol)2000]) in chloroform. Organic solvent was removed from the mixture using a rotary evaporator with heating. The resulting film was hydrated with deionized water, sonicated, and

filtered using a 100nm syringe filter. A clear solution of water-soluble micelle-coated superparamagnetic iron oxide nanoparticles was obtained (2). A Beckman Coulter Optima XL-100K ultracentrifuge was used to remove empty micelles from mMIONS.

For antibody-based targeting, rat anti-mouse VCAM-1 IgG was conjugated to Alexa Fluor 647-labeled amine-mMIONS ($\lambda_{\text{abs}} = 650 \text{ nm}$, $\lambda_{\text{em}} = 665 \text{ nm}$) using the heterobifunctional crosslinkers N-succinimidyl 3-(2-pyridyldithio)propionate (SPDP) and sulfosuccinimidyl-4-(*N*-maleimidomethyl)cyclohexane-1-carboxylate (sulfo-SMCC). The conjugation strategy used was to thiol-functionalize mMIONS and to modify the antibody with thiol-reactive maleimide groups, allowing the two to be conjugated together. Thiol functionalization of amino-mMIONS was accomplished using SPDP, while water soluble sulfo-SMCC was used to modify anti-VCAM-1 IgG with thiol-reactive maleimide functional groups (the water soluble form of SMCC was used to modify IgG to prevent protein precipitation).

For thiol functionalization of amino-mMIONS, SPDP was dissolved in DMSO at a concentration of 1 mM. An aliquot of SPDP was then added to amino-mMIONS, allowing the NHS-ester functionality of SPDP to react with amine groups on the nanoparticle coating. The mixture reacted at room temperature for 30 min. After 30 min the reaction mixture was added to a 100 Kilo Dalton (KD) microcon centrifugal separation device and repeatedly washed to remove unreacted SPDP and DMSO. To produce a free-thiol on the particle surface, the disulfide bond within SPDP was cleaved using a reducing agent. The reducing agent tris[2-carboxyethyl] phosphine (42) was dissolved in DI water at 1 mM along with 10 mM EDTA (to prevent metal-catalyzed oxidation of newly formed thiols). An aliquot was added to mMION-SPDP and allowed to react for 30 min at room temperate. TCEP reduced the disulfide bond within SPDP, leaving the mMIONS with a thiol-functionalized state (mMION-SH). It was not

necessary to remove TCEP upon completion of the reaction because it does not interfere with thiol-maleimide chemistry at low concentrations (43).

To functionalize anti-VCAM-1 IgG with thiol-reactive maleimide groups, sulfo-SMCC was dissolved in 10 mM PBS at a concentration of 1mM. An aliquot of sulfo-SMCC was then added to VCAM-1 IgG and reacted at room temperature for 30 min with constant shaking. In this step the NHS-ester functionality of sulfo-SMCC reacts with a small portion of amines in solvent-exposed lysine residues on the antibody ($\approx 1 - 3$ sulfo-SMCC conjugated per antibody, assuming a 25 – 33 % reaction efficiency (43). The maleimide modified antibody (IgG-Mal) was washed 2 times with 10 mM PBS using a 100 kD microcon to remove unreacted sulfo-SMCC.

IgG-Mal was combined with mMION-SH at a molar ratio of 2:1 and allowed to react overnight at 4 °C. This low molar ratio ensures that nearly all IgG-Mal is consumed by mMION-SH in the reaction. In the reaction solution, the concentration of –SH is much greater than the concentration of –Mal. The large excess of thiol groups on mMION-SH relative to the low number maleimide groups on IgG-Mal also helps prevent crosslinking of multiple mMION via an IgG bridge. Near IR dye-labeling of the VCAM-1 binding peptide was performed using Alexa Fluor 647-Maleimide (Invitrogen). The reaction was carried out in 10 mM PBS (pH 6.5) in the presence of 10 mM EDTA, 4 °C overnight. The product was purified using HPLC by Jan Pohl at the Emory University Microchemical and Proteomics Core Facility.

All animal studies adhered to guidelines set forth by the Emory University Institutional Animal Care and Use Committee (IACUC). Male C57BL/6 mice (Jackson Laboratories) aged 32-36 weeks were used for all imaging experiments. Widespread upregulation of vascular cell adhesion molecule 1 (VCAM-1) was produced by administering (intraperitoneal) 100 μ g of lipopolysaccharide (LPS). LPS is a bacterial toxin that is known to induce an inflammation response when given systemically (33).

Animals were euthanized by CO₂ inhalation 5 hours after injection of LPS. The mice were then immediately immobilized in the supine position and the sternum, rib cage, diaphragm, and lungs were quickly removed to expose the contracting heart. A 25 gauge needle from a scalp vein set (Baxter) was used to pierce the left ventricle. The heart was then pressurized with saline and the vena cava was cut, allowing rapid perfusion tissues. After 5 min of saline perfusion, 3-way valve was used to perfuse with 10% neutral buffered formalin (NBF). Perfusion with 10% NBF was allowed for 5 min, followed by another 5 min perfusion with saline.

The heart and liver were removed to expose the thoracic descending aorta. Using a dissecting microscope and microdissection tools, the aorta was severed near the renal arteries, followed by cutting away of all the intercostal arteries. The aorta was then cut longitudinally from the bottom up to near the beginning of the aortic arch. The aorta was removed and pinned onto a black silicone elastomer and fat was removed from either side of the aorta (male mice have considerably more fat surrounding the aorta than females).

Aortas were placed in wells of a 24-well plate washed with PBS for 15 min on an orbital shaker. PBS was removed from the wells and 5% goat serum in PBS was added to block the tissue. Blocking was performed at room temperature for 1 h on an orbital shaker. Staining with primary antibodies (1 µg/mL), VCAM-1 targeted mMIONs (350 nM), or VCAM-1 binding peptide (350 nM) was performed overnight at 4 °C. The samples were then washed for 15 min in a nutator mixer (Becton-Dickinson) to remove primary antibodies, nanoparticles, or peptides. For QD staining, QD-secondary antibody conjugates were incubated with aorta samples for 1 hr, followed by washing. Hoechst staining was applied to all samples for 15 min to stain the cell nuclei. The aortas were then laid flat onto glass slides to expose their inside surface. The samples were mounted using Slo-Fade Gold and covered with a #1.5 borosilicate coverglass.

LPS-activated aorta tissues were imaged using a Zeiss LSM 510 inverted confocal microscope equipped with a META detector. Two-photon excitation of Hoechst and Qdot 655 was achieved using a Mira 900 Ti:Sapphire laser (Coherent) mode-locked at 750nm. Alexa 647-labeled mMIONs were excited using a 633 nm He:Ne laser. An oil-immersion, 1.3 NA (numerical aperture), 40X Plan-Neofluor objective was used to collect emitted fluorescence.

2.4.5 Results

The imaging of low-abundance receptors such as vascular cell adhesion molecular 1 (VCAM-1) requires high sensitivity and background signal. Fluorescence-based detection offers a high degree of sensitivity. Additionally, fluorescent labels such as near infrared (NIR) fluorophore-labeled mMIONs and NIR quantum dots (QDs) are emit light with a wavelength in the 650-675 nm range. Most tissue auto-fluorescence emission is in the 500 – 525 nm range (i.e. green light). The far-red emission of our probes can easily be separated from green light, allowing data acquisition of complex tissues and with low background. The aorta tissue contains a layer of endothelial cells (EC), smooth muscle, and elastic lamina containing a dense layer of ECM proteins. Normally a complex multilayer tissue such as the aorta would produce considerable auto-fluorescence; however this is mitigated through the use of NIR probes and TE excitation.

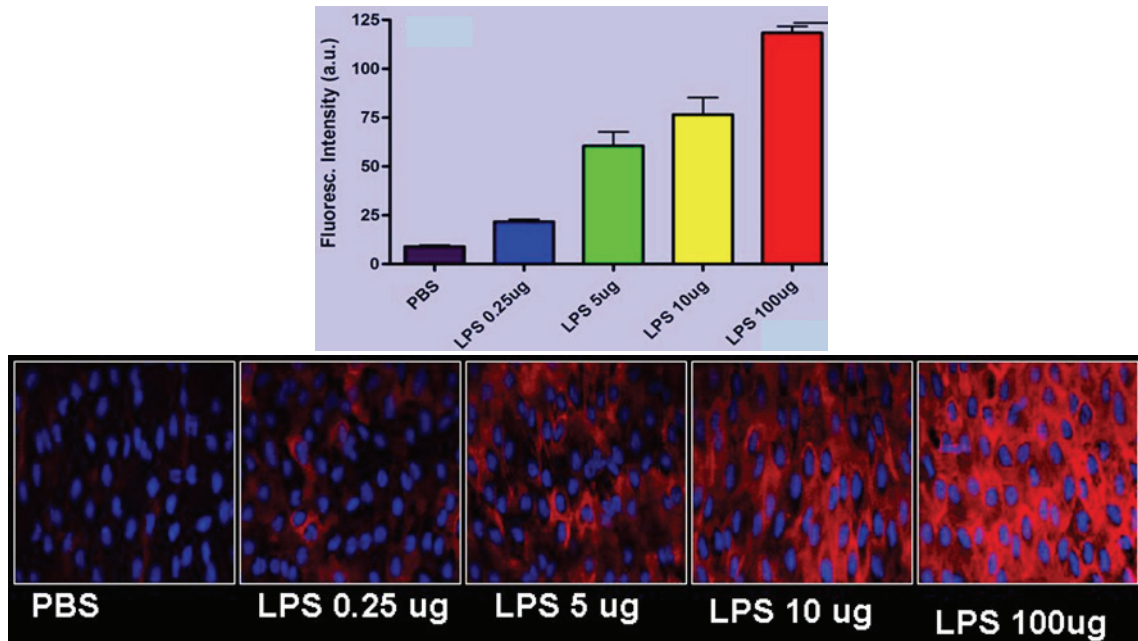


Figure 2.11: Upregulation of vascular cell adhesion molecule 1 by lipopolysaccharide endotoxin⁽³⁷⁾. Top, Quantification of VCAM-1 expression by aortic endothelial cells. Quantification was possible because aortas were stained using NIR quantum dots (very low photobleaching) and imaged using a TPE system (little to no background). Bottom, Images of aortic endothelial cells treated with increasing amounts of LPS. Endothelial cell (nuclei in blue) expression of VCAM-1 (red channel) responds to LPS in a dose-dependent manner.

In this study the ability of mMION to targeted cell inflammation-related surface markers, we used an *en face* preparation of mouse aorta treated with LPS. Treatment with LPS results in a dose-dependent upregulation of VCAM-1 expression by mouse aortic endothelial cells (Figure 2.11). The imaging of low-abundance receptors such as vascular cell adhesion molecular 1 (VCAM-1) requires high sensitivity and background signal. Fluorescence-based detection using near-infrared mMIONs offers a high degree of sensitivity necessary to visualize sparse vascular epitopes.

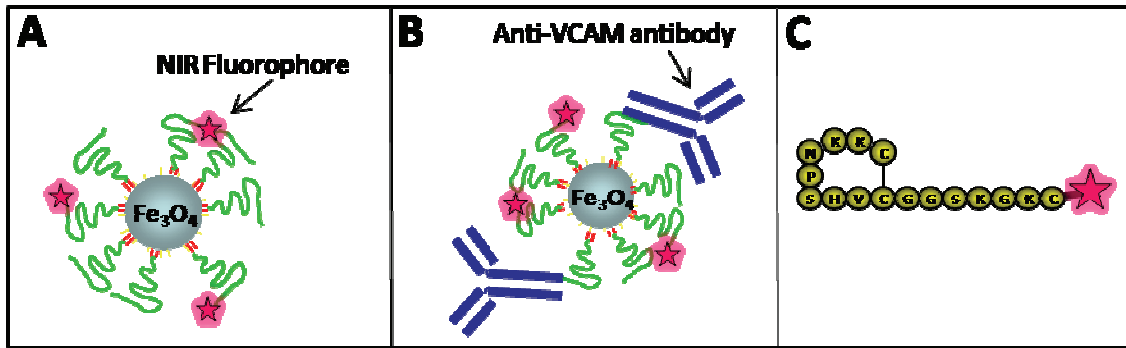


Figure 2.12: Nanoprobes for targeting vascular epitopes. (A) mMIONS were labeled with the near infrared fluorophore Alexa Fluor 647 ($\lambda_{abs} = 650 \text{ nm}$, $\lambda_{em} = 665 \text{ nm}$), a, was conjugated to mMIONS. (B) Anti-VCAM monoclonal antibodies were conjugated to NIR-labeled mMIONS to allow nanoparticle targeting on aorta tissues. (C) Alexa Fluor 647-labeled VCAM-1 binding peptide (CVHSPNKKCGGSKGKC, cyclized about C1 and C8) (40) was also evaluated for its potential to bind VCAM-1 on LPS treated aortic tissue.

The far-red emitting Alexa Fluor[®] 647 fluorescent dye was conjugated to micelle-coated magnetic nanoparticles (Figure 2.12A). An anti-VCAM-1 antibody was then conjugated to the dye-labeled magnetic particles to allow imaging of VCAM-1 (Figure 2.12B). A VCAM-1 binding peptide (40) was tagged with Alexa Fluor[®] 647 to investigate its binding in our *en face* model of LPS-stimulated VCAM-1 expression by aortic endothelial cells (Figure 2.12C). Two-step immunofluorescence was performed using a rat anti-mouse VCAM-1 antibody in conjunction with goat anti-rat Qdot 655 (Fab')₂ a positive control for mMION and peptide binding of VCAM-1.

The animal model selected for this study was the C57BL/6 mouse with an intraperitoneal injection of LPS. This model provides rapid (5 hour) systemic expression of endothelial VCAM-1. The endothelial inflammatory marker VCAM-1 was upregulated in C57BL/6 mice using a 100 μ g intraperitoneal injection of lipopolysaccharide (LPS) 5 hours prior to euthanasia. Animals were euthanized by CO₂ inhalation, perfused with 0.9% NaCl, followed by fixation with 10% formalin. The thoracic descending aortas were dissected, carefully sectioned,

and washed in PBS. Aorta sections were blocked in 2% BSA in PBS overnight at 4°C and stained with targeted or control particles at room temperature for 1 hour. Following staining with anti-VCAM-1 antibody-conjugated dye-labeled magnetic particles, goat anti-mouse Qdot 655 (Fab')₂, or dye-labeled VCAM-1 binding peptide. Aorta sections were washed in PBS 3 times for 15 minutes each at room temperature. The sections were then mounted on glass slides using anti-fade mounting media. Two-step IHC using a Qdot[®] 655 goat (Fab')₂ anti-rat IgG conjugate and rat anti-mouse VCAM-1 IgG was also performed as a positive control. A Zeiss LSM 510 META two-photon microscope with a Mira[®] 900 Ti:Sapphire laser tuned and mode-locked at 750 nm was used for Hoechst and Qdot 655 excitation. A 633nm HeNe was used to excite Alexa Fluor[®] 647-labeled particles and VCAM-1 binding peptide. Images were collected at 40X using an inverted Zeiss Axiovert 100 microscope.

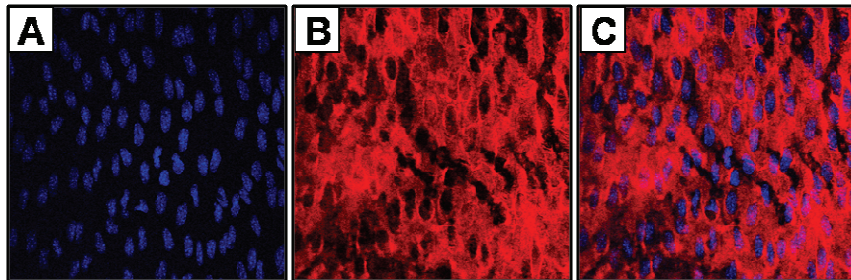


Figure 2.13: Typical VCAM-1 staining pattern of LPS-activated aortic tissue. (A) Aortic endothelial cell nuclei labeled with Hoechst stain and imaged using two-photon excitation (TPE). This image only shows the signal from the blue channel (Hoechst stain). Endothelial cells were generally observed to orientate in the direction of flow (from top to bottom in this image). (B) Red channel showing Qdot 655 staining of endothelial VCAM-1 using TPE. The expression observed was generally a diffuse/feathered pattern across the entire endothelial surface. (C) Red and blue channel showing cell nuclei (blue) and VCAM-1 expression (red) on the cell surface.

VCAM-1 is expressed on the surface of aortic endothelial cells where it recruits circulating monocytes to locations of inflammation. The nanoprobe used in this experiment (mMION and

Qdot) produced strong signal at the luminal surface of aortic endothelial cells from LPS treated animals (Figure 2.13).

We were able to perform optical sectioning in the z-direction due to the confocal imaging set-up used in this experiment (Figure 2.14). As we looked beneath the luminal endothelial to the layer of smooth muscle cells found in the tunica media. We did not observe signal originating from the smooth muscle later of from any other tissue beneath the endothelial layer (Figure 2.14B). One reason for the lack of signal is that there is no VCAM-1 expression beneath the endothelial layer. Additionally, we believe that the nanoprobe do not significantly diffuse into deeper aorta layers due to the formalin fixation of the tissue. Therefore, the *en face* aorta preparation outlined here is most useful when vascular epitopes of interest are of endothelial origin only (we did not examine axial tissue slices in this study). Beneath the smooth muscle cells of the tunica media lay the external elastic lamina and the tunica adventitia. When viewed in an epifluorescent microscope, strong autofluorescence is produced by the dense connective tissue and the elastin, collagen, and other ECM proteins found therein (Figure 2.14C).

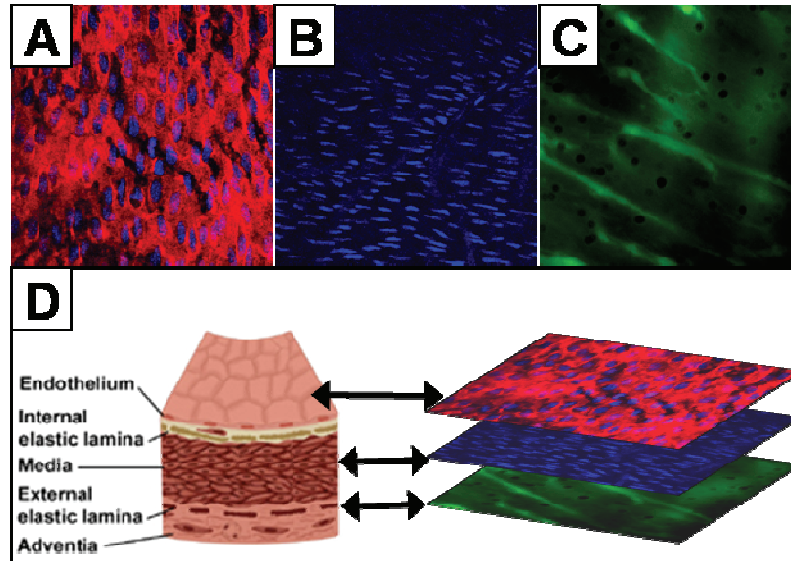


Figure 2.14: Imaging depth in the aorta using VCAM-targeted nanoprobes. (A) Qdot 655 bound to VCAM-1 (red channel) expressed by endothelial cells of the descending aorta after LPS treatment. The nuclei, stained with Hoechst (blue channel) are generally aligned with the direction of blood flow. (B) Beneath the endothelium are the smooth muscle cells of the tunica media (nuclei shown in blue channel). Smooth muscle cells are generally perpendicular to the direction of flow. (C) Under the tunica media is external elastic lamina and the tunica adventitia, rich in ECM proteins which produce strong autofluorescence. Imaged here in an epifluorescent set-up (Axiovert 100, 100X objective lens, GFP filter set), dense layers of elastin and collagen in the elastic lamina and adventitia show prominent autofluorescence in green wavelengths.

To investigate the ability of mMION to targeted cell inflammation-related surface markers, we used an *en face* preparation of mouse aorta treated with LPS. LPS has been shown to cause upregulation of VCAM-1 expression throughout the vasculature (33). The aorta was chosen as an endothelial region of interest because it is a common site for the development of atherosclerotic lesions that lead to cardiac events (e.g. aneurism, plaque rupture and thrombosis). Upon treatment with LPS we observed an increase in VCAM-1 expression in the normally VCAM-free areas of the descending thoracic aorta as well as increased expression in the areas surrounding intercostal branches. The general pattern of VCAM-1 staining was observed with mMION and with dye-labeled VCAM-1 binding peptide.

The images produced by the anti-VCAM-mMION (Figure 2.15, C) and VCAM-binding peptide (Figure 2.15, D) are of lower signal intensity than that of the Qdot (Figure 2.15, A). There are two reasons for the large difference in signal intensity between the Qdot images and those from the mMION and the peptide. The first reason is that quantum dots have an exceedingly large molar extinction coefficient compared to organic dyes like Alexa Fluor 647. This makes quantum dots much brighter than traditional dyes. The second reason is because the Qdot images were produced using 2-step immunofluorescence which provides amplification of signal due to multiple 2° antibodies binding a single 1° antibody. Aorta samples stained with mMION happened to exhibit a large amount of rippled surface topology which sometimes results from formalin fixation of tissues. Only the luminal (top) “ridges” of the endothelial layer were in the imaging plane. Z-stack images are available which show that the mMION signal is continuous across the endothelial layer.

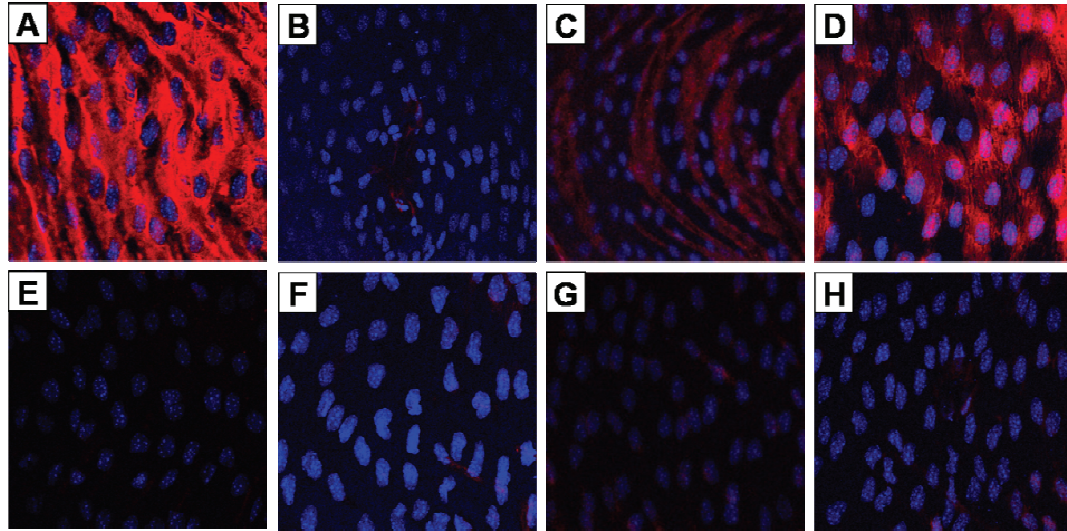


Figure 2.15: Nanoparticle and peptide-based imaging of VCAM-1 in the aorta. Tissue from LPS-treated tissue is shown in A-D, while untreated tissue is shown in E-H. (A, E) Qdot 655 (Fab')₂ imaging of VCAM-1 after application of rat anti-mouse anti-VCAM-1 antibody. A clear pattern of VCAM-1 expression is observed in LPS treated tissue (A) but not in untreated tissue (E). Particularly strong signal is observed from quantum dot-treated samples because (1) relative to organic dyes QDs have a large molar extinction coefficient when excited with short wavelengths, and (2) the QD images were produced using 2-step immunofluorescence which provides amplification of signal due to multiple 2° antibodies binding a single 1° antibody. (B, F) Virtually no signal was observed from NIR-labeled mMIONs without anti-VCAM-1 antibodies. (C, G) Antibody-targeted mMIONs bound to VCAM-1 on the endothelium of LPS-treated tissue (C) but not on untreated tissue (G). Aorta sample shown here exhibited a large amount of “wavy” surface topology which sometimes results from formalin fixation of tissues. Only the luminal (top) “ridges” of the endothelial layer were in the imaging plane. Z-stack images are available which show that the mMION signal is continuous across the endothelial layer. (D, H) The NIR-labeled peptide produced a strong VCAM-1 staining pattern in LPS-treated tissue (D).

In its native state, the descending thoracic aorta of C57BL/6 mice lacks appreciable expression of VCAM-1. The exception to this is the small regions of VCAM-1 expression exist in areas immediately surrounding the intercostal artery branches (i.e. ostia). These areas are also naturally prone to lesion development due to perturbed flow at these locations. We imaged areas in the descending thoracic aorta (no appreciable VCAM-1 expression) as well as intercostal artery ostia (VCAM-1 expression) with and without LPS treatment. VCAM-1 expression

surrounding intercostal branches remained higher than that of the descending aorta with LPS treatment (Figure 2.16).

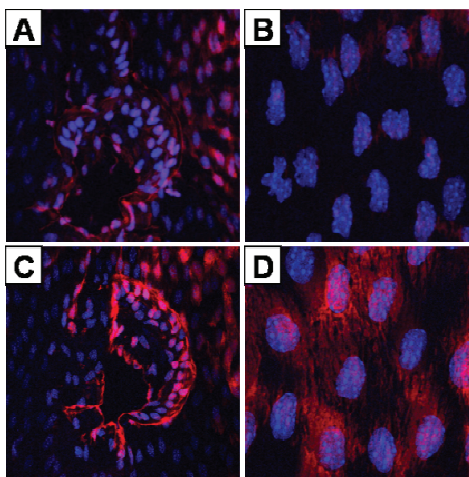


Figure 2.16: Peptide-based imaging of VCAM-1 expression as a function of local flow environment and LPS treatment. on intercostal artery ostia. Aorta sections from untreated (A, B) and LPS-treated (C, D) animals. In untreated animals, endogenous VCAM-1 expression can be observed in intercostals branches (A), due to disturbed flow, while little endogenous VCAM-1 expression is detected in non-branching areas of the descending aorta (B). Treatment with LPS leads to an increase in VCAM-1 expression around intercostal artery ostia (C) and on the smooth areas of the descending aorta (D). While VCAM-1 expression increased in both regions, the intensity from areas of disturbed flow (C) remained greater than that of smooth regions (D).

2.5 Discussion

Lipid-PEG micelles have been successfully used to deliver hydrophobic proteins, drugs, and imaging agents to tumors (44-47). It stands to reason that the same can be achieved with hydrophobic nanoparticles. Lipid-PEG coatings, due to their biocompatible nature and easy of fabrication, have the potential to enjoy wide range of applications in disease detection and monitoring. DSPE-PEG micelles have been used to deliver quantum dots *in vivo* (21, 24, 48), however most studies have not assessed the circulation lifetime or biodistribution of such

probes. The studies performed here have bridged this gap by providing detailed biodistribution of micelle-coated nanoparticles.

The stability of lipid-PEG coatings is of notable concern. DSPE-PEG forms micelles in solution, and all micelles will become unstable when their concentration falls below the *critical micelle concentration* (CMC) (49). Micelles will dissociate to monomers when below the CMC; the CMC for DSPE-PEG is sub-micromolar (47). However, concerns about the CMC may be less of a problem for DSPE-PEG-coated nanoparticles. It is highly likely that the coating surrounding the iron oxide core is in fact not a micelle in the classical sense. The inner diameter of DSPE-PEG micelles is known to be approximately 3nm (50). Dubertret, et al (21) chose quantum dots of this size so that only a single QD would fill the core of the DSPE-PEG micelle. However we, and others (51), have found that particles of a much larger size (as large as 40nm) can be coated with DSPE-PEG. This finding suggests a direct interaction between capping layer of surfactant on the surface of the nanoparticle and the alkyl chains of the DSPE. This interaction is expected to significantly stabilize the coating molecules against exchange at low concentrations.

We believe that micelle coating iron oxide nanoparticles with PEGylated lipids offers advantages to polymer coatings. Most polymer coatings are bulky and significantly increase the hydrodynamic diameter of the hydrophobic nanoparticles being coated. For optical nanoparticles (quantum dots, organic-dye loaded silica particles, etc) this increased distance prevents the coated particles from participating in fluorescent resonance energy transfer reaction. For magnetic nanoparticles, bulky coatings push water further away and reduce the amount of water protons that are affected by the magnetic moment of the nanoparticle. Finally, tagging proteins with small nanoparticles is less likely to perturb the protein's native biological behavior.

The number and identity of functional groups on micelle-coated nanoparticles can be easily changed by using headgroup-modified lipids and termini-modified PEG-lipids. Incorporation of these groups is easily achieved by adding functionalized lipids to the initial coating solution. This addition does not affect the coating procedure, unlike some polymer coating schemes where different monomers must be used to impart new functionality and the entire polymer must be resynthesized and analyzed. Many functionalized lipids and PEG-lipids are commercially available and contain chemical groups commonly used in bioconjugations (e.g. -NH₂, -COOH, -SH, -Maleimide, -NHS ester).

The micelle-coated iron oxide nanoparticles used in these studies have a 6.6 ± 0.7 nm iron oxide core, with a phospholipid-PEG coating of $\approx 4-7$ nm in thickness. The circulation half-life of these probes was determined by *ex vivo* mean T2 measurements to be ~ 2 hours. We functionalized mMIONs for targeting vascular cell adhesion molecule-1 (VCAM-1) in a mouse model of atherosclerosis. VCAM-1, a known early marker of atherosclerosis, mediates the adhesion of circulating monocytes to areas of activated vascular endothelium. The expression of VCAM-1 during initial lesion development, as well as its prominent endothelial localization, make VCAM-1 an attractive target for detection and monitoring by circulating imaging probes. For targeting and fluorescence reporting, end-functionalized phospholipid-PEG was used to conjugate anti-VCAM-1 antibody, Alexa Fluor® 647 fluorophores. After increasing the expression level of VCAM-1 in mice with lipopolysaccharide (LPS) treatment, aortas were dissected and probed with functionalized mMIONs. Specific targeting of antibody-conjugated nanoparticles to VCAM-1 in *ex vivo* aorta samples from LPS-treated mice was observed using fluorescence.

The potential of mMIONs to be used as dual-modality imaging agents for PET/MRI was evaluated by radiolabeling mMIONs using copper-64. The particles were successfully

conjugated with the cyclic chelator DOTA and labeled at high specific activity. The radiochemical purity (RCP) of ^{64}Cu -mMIONs was measured by radio-thin layer chromatography (radio-TLC) and radio-fast protein liquid chromatography (radio-FPLC). The RCP of ^{64}Cu -mMIONs was found to be > 95%, and the particles maintained monodispersity after radiolabeling. Pilot small animal PET/CT imaging with ^{64}Cu -mMION was performed in female C57BL/6 weighing \approx 20g. The nanoparticle dose tested was 10 mg/kg mouse body weight, with 100 μCi of radioactivity administered per animal.

Pharmacokinetic information on blood clearance and RES uptake was gathered through microPET imaging of mice at 1 hr, 4 hr, and 24 hr post-injection. MicroPET images were coregistered with computed x-ray tomograms using the Amira software package. Post-imaging organ biodistribution at 24 hr post injection was used to measure the accumulation of ^{64}Cu -mMION in organs of interest. ^{64}Cu -mMION displayed a high blood concentration at the 1 hr imaging time point. A precipitous decline in blood concentration was observed by 4 hr post-injection, as nanoparticles were cleared from the blood stream by the liver and spleen. At 24 hours roughly 1% of the initial dose remained in circulation. The kinetics of this probe make it best suited for high affinity ligands that can bind rapidly, or situations when fast washout is desired. The addition of targeting ligand onto the nanoparticle surface may further reduce the blood half-life of ^{64}Cu -mMION by increasing opsonization and subsequent RES uptake, and may limit the utility of mMION for ligand-targeting applications *in vivo*. Further derivatization of mMION may be required to ensure stability and successful targeting in the *in vivo* environment.

2.6 References

1. DeCuyper, M., P. Müller, H. Lueken, and M. Hødenius, *Synthesis of magnetic Fe_3O_4 particles covered with a modifiable phospholipid coat*. Journal of Physics: Condensed Matter, 2003. **15**(15): p. S1425-S1436.

2. Nitin, N., L.E. LaConte, O. Zurkiya, X. Hu, and G. Bao, *Functionalization and peptide-based delivery of magnetic nanoparticles as an intracellular MRI contrast agent*. J Biol Inorg Chem, 2004. **9**(6): p. 706-12.
3. Hyeon, T., S.S. Lee, J. Park, Y. Chung, and H.B. Na, *Synthesis of highly crystalline and monodisperse maghemite nanocrystallites without a size-selection process*. J Am Chem Soc, 2001. **123**(51): p. 12798-801.
4. Sun, S., H. Zeng, D.B. Robinson, S. Raoux, P.M. Rice, S.X. Wang, and G. Li, *Monodisperse MFe₂O₄ (M = Fe, Co, Mn) nanoparticles*. J Am Chem Soc, 2004. **126**(1): p. 273-9.
5. Nitin, N., *Optical and MR Molecular Imaging Probes and Peptide-based Cellular Delivery for RNA Detection in Living Cells*, in *Biomedical Engineering*. 2005, Georgia Institute of Technology: Atlanta. p. 258.
6. LaConte, L.E., N. Nitin, O. Zurkiya, D. Caruntu, C.J. O'Connor, X. Hu, and G. Bao, *Coating thickness of magnetic iron oxide nanoparticles affects R2 relaxivity*. J Magn Reson Imaging, 2007. **26**(6): p. 1634-41.
7. Zurkiya, O., A.W. Chan, and X. Hu, *MagA is sufficient for producing magnetic nanoparticles in mammalian cells, making it an MRI reporter*. Magn Reson Med, 2008. **59**(6): p. 1225-31.
8. Yu, Z., M. Grafe, H. Meyborg, E. Fleck, and Y. Li. *In Vitro Characterization of Magnetic Resonance Imaging Contrast Agents for Molecular Imaging*. in *ASH Annual Meeting Abstracts*. 2006.
9. Harris, D.C., *Quantitative Chemical Analysis*. 7 ed. 2006, New York: W. H. Freeman. 1008.
10. Arleth, L., B. Ashok, H. Onyuksel, P. Thiyagarajan, J. Jacob, and R. Hjelm, *Detailed structure of hairy mixed micelles formed by phosphatidylcholine and PEGylated phospholipids in aqueous media*. Langmuir, 2005. **21**(8): p. 3279-90.
11. Ashok, B., L. Arleth, R. Hjelm, I. Rubinstein, and H. Onyuksel, *In vitro characterization of PEGylated phospholipid micelles for improved drug solubilization: Effects of PEG chain length and PC incorporation*. JOURNAL OF PHARMACEUTICAL SCIENCES, 2004. **93**(10): p. 2476-2487.
12. Johnsson, M., P. Hansson, and K. Edwards, *Spherical Micelles and Other Self-Assembled Structures in Dilute Aqueous Mixtures of Poly (Ethylene Glycol) Lipids*. JOURNAL OF PHYSICAL CHEMISTRY B, 2001. **105**(35): p. 8420-8430.
13. Lukyanov, A. and V. Torchilin, *Micelles from lipid derivatives of water-soluble polymers as delivery systems for poorly soluble drugs*. Advanced Drug Delivery Reviews, 2004. **56**(9): p. 1273-1289.

14. Melville, D., F. Paul, and S. Roath, *High gradient magnetic separation of red cells from whole blood*. *Magnetics, IEEE Transactions on*, 1975. **11**(6): p. 1701-1704.
15. Molday, R. and D. MacKenzie, *Immunospecific ferromagnetic iron-dextran reagents for the labeling and magnetic separation of cells*. *J Immunol Methods*, 1982. **52**(3): p. 353-67.
16. Owen, C. and J. Lindsay, *Ferritin as a label for high-gradient magnetic separation*. *Biophysical Journal*, 1983. **42**(2): p. 145-150.
17. Owen, C.S., *High gradient magnetic separation of erythrocytes*. *Biophys. J.*, 1978. **22**(2): p. 171-178.
18. U. Jeong, X.T., Y. Wang, H. Yang, Y. Xia,, *Superparamagnetic Colloids: Controlled Synthesis and Niche Applications*. *Advanced Materials*, 2007. **19**(1): p. 33-60.
19. Miltenyi, S., W. Muller, W. Weichel, and A. Radbruch, *High gradient magnetic cell separation with MACS*. *Cytometry*, 1990. **11**(2): p. 231-8.
20. *MACS[®] Column Selection Guide*. 2006, Miltenyi Biotech GmbH: Bergisch Gladbach, Germany. p. 3.
21. Dubertret, B., P. Skourides, D.J. Norris, V. Noireaux, A.H. Brivanlou, and A. Libchaber, *In vivo imaging of quantum dots encapsulated in phospholipid micelles*. *Science*, 2002. **298**(5599): p. 1759-62.
22. Mulder, W., R. Koole, R. Brandwijk, G. Storm, P. Chin, G. Strijkers, C. de Mello Donegá, K. Nicolay, and A. Griffioen, *Quantum dots with a paramagnetic coating as a bimodal molecular imaging probe*. *Nano Lett*, 2006. **6**(1): p. 1-6.
23. Mulder, W.J., G.J. Strijkers, G.A. van Tilborg, A.W. Griffioen, and K. Nicolay, *Lipid-based nanoparticles for contrast-enhanced MRI and molecular imaging*. *NMR Biomed*, 2006. **19**(1): p. 142-64.
24. Duconge', F., T. Pons, C. Pestourie, L. He'rin, B. The'ze', K. Gombert, B. Mahler, F. Hinnen, B. Kühnast, and F. Dolle', *Fluorine-18-Labeled Phospholipid Quantum Dot Micelles for in Vivo Multimodal Imaging from Whole Body to Cellular Scales*. *Bioconjug Chem*, 2008.
25. van Schooneveld, M., E. Vucic, R. Koole, Y. Zhou, J. Stocks, D. Cormode, C. Tang, R. Gordon, K. Nicolay, and A. Meijerink, *Improved Biocompatibility and Pharmacokinetics of Silica Nanoparticles by Means of a Lipid Coating: A Multimodality Investigation*. *Nano Lett*, 2008.
26. Shokeen, M., N.M. Fetting, and R. Rossin, *Synthesis, in vitro and in vivo evaluation of radiolabeled nanoparticles*. *Q J Nucl Med Mol Imaging*, 2008. **52**(3): p. 267-77.
27. Libby, P., *Inflammation in atherosclerosis*. *Nature*, 2002. **420**(6917): p. 868-74.

28. Falk, E., *Pathogenesis of atherosclerosis*. J Am Coll Cardiol, 2006. **47**(8 Suppl): p. C7-12.
29. Khan, B.V., S.S. Parthasarathy, R.W. Alexander, and R.M. Medford, *Modified low density lipoprotein and its constituents augment cytokine-activated vascular cell adhesion molecule-1 gene expression in human vascular endothelial cells*. J Clin Invest, 1995. **95**(3): p. 1262-70.
30. Nerem, R.M., R.W. Alexander, D.C. Chappell, R.M. Medford, S.E. Varner, and W.R. Taylor, *The study of the influence of flow on vascular endothelial biology*. Am J Med Sci, 1998. **316**(3): p. 169-75.
31. Forstermann, U. and T. Munzel, *Endothelial nitric oxide synthase in vascular disease: from marvel to menace*. Circulation, 2006. **113**(13): p. 1708-14.
32. Steffel, J., T.F. Luscher, and F.C. Tanner, *Tissue factor in cardiovascular diseases: molecular mechanisms and clinical implications*. Circulation, 2006. **113**(5): p. 722-31.
33. Henninger, D.D., J. Panes, M. Eppihimer, J. Russell, M. Gerritsen, D.C. Anderson, and D.N. Granger, *Cytokine-induced VCAM-1 and ICAM-1 expression in different organs of the mouse*. J Immunol, 1997. **158**(4): p. 1825-32.
34. Zipfel, W.R., R.M. Williams, and W.W. Webb, *Nonlinear magic: multiphoton microscopy in the biosciences*. Nat Biotechnol, 2003. **21**(11): p. 1369-77.
35. Denk, W., J.H. Strickler, and W.W. Webb, *Two-photon laser scanning fluorescence microscopy*. Science, 1990. **248**(4951): p. 73-6.
36. Rubart, M., *Two-photon microscopy of cells and tissue*. Circ Res, 2004. **95**(12): p. 1154-66.
37. Ferrara, D., C. Glaus, and W. Taylor, *Targeting Vascular Epitopes Using Quantum Dots*, in *Nanoparticles in Biomedical Imaging: Emerging Technologies and Applications*, J.W.M. Bulte and M.M.J. Modo, Editors. 2007, Springer: New York. p. 543.
38. Glaus, C., D.E. Ferrara, W.R. Taylor, and G. Bao, *Micelle-coated Superparamagnetic Iron Oxide Nanoparticles as an MRI Contrast Agent for Plaque Detection*, in *Fifth Annual Meeting of The Society for Molecular Imaging*. 2006, BC Decker Inc: Kona, Hawaii.
39. Ferrara, D.E., D. Weiss, P.H. Carnell, R.P. Vito, D. Vega, X. Gao, S. Nie, and W.R. Taylor, *Quantitative 3D fluorescence technique for the analysis of en face preparations of arterial walls using quantum dot nanocrystals and two-photon excitation laser scanning microscopy*. Am J Physiol Regul Integr Comp Physiol, 2006. **290**(1): p. R114-23.
40. Kelly, K.A., J.R. Allport, A. Tsourkas, V.R. Shinde-Patil, L. Josephson, and R. Weissleder, *Detection of vascular adhesion molecule-1 expression using a novel multimodal nanoparticle*. Circ Res, 2005. **96**(3): p. 327-36.

41. Seip, C.T. and C.J. O'Connor, *The fabrication and organization of self-assembled metallic nanoparticles formed in reverse micelles*. Nanostructured Materials, 1999. **12**(1-4): p. 183-186.
42. Burns, J.A., J.C. Butler, J. Moran, and G.M. Whitesides, *Selective reduction of disulfides by tris(2-carboxyethyl)phosphine*. J. Org. Chem., 1991. **56**(8): p. 2648-2650.
43. Hermanson, G., *Bioconjugate Techniques*. 2008: Academic Press.
44. Lizano, C., V. Weissig, V.P. Torchilin, P. Sancho, A.I. Garcia-Perez, and M. Pinilla, *In vivo biodistribution of erythrocytes and polyethyleneglycol-phosphatidylethanolamine micelles carrying the antitumour agent dequalinium*. Eur J Pharm Biopharm, 2003. **56**(2): p. 153-7.
45. Lukyanov, A.N., Z. Gao, L. Mazzola, and V.P. Torchilin, *Polyethylene glycol-diacyllipid micelles demonstrate increased acculamation in subcutaneous tumors in mice*. Pharm Res, 2002. **19**(10): p. 1424-9.
46. Torchilin, V.P., A.N. Lukyanov, Z. Gao, and B. Papahadjopoulos-Sternberg, *Immunomicelles: targeted pharmaceutical carriers for poorly soluble drugs*. Proc Natl Acad Sci U S A, 2003. **100**(10): p. 6039-44.
47. Weissig, V., K.R. Whiteman, and V.P. Torchilin, *Accumulation of protein-loaded long-circulating micelles and liposomes in subcutaneous Lewis lung carcinoma in mice*. Pharm Res, 1998. **15**(10): p. 1552-6.
48. Stroh, M., J.P. Zimmer, D.G. Duda, T.S. Levchenko, K.S. Cohen, E.B. Brown, D.T. Scadden, V.P. Torchilin, M.G. Bawendi, D. Fukumura, and R.K. Jain, *Quantum dots spectrally distinguish multiple species within the tumor milieu in vivo*. Nat Med, 2005. **11**(6): p. 678-82.
49. Voet, D., J. Voet, I. Geis, J. Woolsey, B. Woolsey, and P. Lane, *Biochemistry*. 1990: Wiley New York.
50. Johnsson, M., P. Hansson, and K. Edwards, *Spherical Micelles and Other Self-Assembled Structures in Dilute Aqueous Mixtures of Poly(Ethylene Glycol) Lipids*. J. Phys. Chem. B, 2001. **105**(35): p. 8420-8430.
51. Grancharov, S.G., H. Zeng, S. Sun, S.X. Wang, S. O'Brien, C.B. Murray, J.R. Kirtley, and G.A. Held, *Bio-functionalization of monodisperse magnetic nanoparticles and their use as biomolecular labels in a magnetic tunnel junction based sensor*. J Phys Chem B Condens Matter Mater Surf Interfaces Biophys, 2005. **109**(26): p. 13030-5.

CHAPTER 3

IN VIVO EVALUATION OF ^{64}Cu -LABELED MAGNETIC NANOPARTICLES: A NOVEL PROBE FOR DUAL-MODALITY PET/MR IMAGING

3.1 Introduction

Multimodality imaging combines two or more distinct imaging modalities in a way that leverages the respective strengths and weaknesses of each imaging technology. The result of this combination is often superior to both modalities operating in standalone fashion. PET/CT is currently the gold standard in oncologic imaging. However, CT exposes patients and experimental animals to substantial doses of ionizing radiation. Magnetic resonance imaging uses no ionizing radiation and provides superior soft tissue contrast at high spatial resolution, a particularly important feature for oncologic imaging because of the epithelial in origin of many cancers. Positron emission tomography, the most sensitive human molecular imaging modality, produces whole body images for functional and molecular information. Combining PET with the functional, spectroscopic, and contrast enhanced abilities of MRI would produce a breakthrough in the detection and monitoring of disease.

Nanoparticles possess unique characteristics that make them well suited as probes for molecular imaging. Particles can be synthesized in a systematic fashion with tight control over nanoparticle diameter producing particle with narrow size distributions. Contrary to gadolinium-based MRI contrast agents, nanoparticle contrast agents circulate in the blood for long periods of time, offer higher sensitivity, and exhibit little to no known toxicity. The unique qualities of nanoparticles are also well suited to the design of PET probes. Because of their large surface area, nanoparticles can be labeled to a high specific activity, further increasing the sensitivity of detection as well as the payload of therapeutic isotopes and targeting ligands.

Unlike small molecule PET tracers, radiolabeled nanoparticles can circulate for long periods of time.

We report the development of a novel dual-modality nanoparticle for PET/MR imaging. The probe in this work has an iron oxide core with a micelle coating composed of functionalized PEGylated lipids. The nanoparticles were modified with DOTA to allow chelation of copper-64 for PET imaging. The nanoparticles were labeled at high specific activity and produced strong PET and MRI contrast. The pharmacokinetics of this novel probe was measured using microPET/CT and organ biodistribution.

3.2 Experimental Procedures

3.2.1 Materials

Magnetic iron oxide (Fe_3O_4) nanoparticles (MION) (kindly provided by Dr. Charles O'Connor, University of New Orleans) were synthesized using a reverse micelle process (1, 2). 1,2-distearoyl-*sn*-glycero-3-phosphoethanolamine-N-[amino(polyethylene glycol)2000] (DSPE-PEG2000-amine) and 1,2-distearoyl-*sn*-glycero-3-phosphoethanolamine-N-[methoxy(polyethylene glycol)-5000] (DSPE-mPEG5000) were purchased from Avanti Polar Lipids Inc. (Alabaster, AL). 1,4,7,10-Tetraazacyclododecane-1,4,7,10-tetraacetic acid mono(*N*-hydroxysuccinimide ester) (DOTA-NHS) was purchased from Macrocyclics Inc. (Dallas, TX). ^{64}Cu was produced on a Washington University Medical School Cyclotron (Model CS-15, Cyclotron Corp.) by the $^{64}\text{Ni}(p,n)^{64}\text{Cu}$ reaction with the nuclide having a specific activity of 50-200 mCi/ μg at the end of bombardment, as previously described (3). All buffers used for ^{64}Cu labeling were passed through a Chelex 100 column before use. Water was deionized to 18 M Ω •cm using an E-Pure water filtration system (Barnstead International, Dubuque, IA). Wiretrol II capillary micropipets were purchased from the Drummond Scientific Company (Broomall, PA). Chelex

100 resin (50–100 mesh), hydrochloric acid, hydroxylamine hydrochloride, ferrous ammonium sulfate hexahydrate, 1,10-phenanthroline, ethylenediaminetetraacetic acid (EDTA), 10 mM phosphate buffered saline (PBS), chloroform, and mouse serum were purchased from Sigma-Aldrich Inc. (St. Louis, MO).

3.2.2 Preparation of micelle-coated MIONs

Micelle-coated MIONs (mMIONs) were prepared as previously described (4) with slight modifications. DSPE-PEG2000-amine and DSPE-mPEG5000 were individually dispersed in chloroform at 25 mg/mL and stored at -20 °C prior to the coating procedure. To prepare amino-functionalized mMIONs, DSPE-PEG2000-amine (9 μmol) and DSPE-mPEG5000 (34 μmol) were added to 24 mL chloroform in a round-bottomed flask. Uncoated MIONs (20 mg Fe) were then added to the flask and the mixture was placed in a rotary evaporator. Pressure was slowly reduced to 10 mTorr to remove all solvents, resulting in a dry film of nanoparticles and PEG-phospholipids. The physical absorption of PEGylated lipids onto particles is due to a hydrophobic interaction between cetyltrimethylammonium bromide capping ligands on the nanoparticle surface and acyl chains of phospholipids. The film was heated at 60 °C for 30 minutes under vacuum. Next, the flask was removed from vacuum and the film hydrated using deionized water with gentle agitation followed by sonication, producing a clear, brown solution of mMIONs. Empty PEG-phospholipid micelles were separated from mMIONs by ultracentrifugation (Optima XL-100K; Beckman Coulter Inc., Fullerton, CA) for 10 hrs at 280,000 g (4 °C). The supernatant containing empty micelles was removed and the nanoparticle pellet was resuspended in PBS to 10 mg Fe/mL and passed through a 0.1 μm Anotop syringe filter (Whatman International Ltd., UK).

3.2.3 Iron Concentration Determination

Iron concentrations of DOTA-mMION solutions were determined using a 1,10-phenanthroline assay (5, 6). Solutions of hydroxylamine hydrochloride (10 mg/mL), sodium acetate (125 mg/mL), 1,10-phenanthroline (1 mg/mL) and hydrochloric acid (6 M) were freshly prepared using deionized water. In a 200 μ L PCR tube, 17 μ L of hydrochloric acid was added to 18 μ L of dilute nanoparticles and incubated in a thermocycler at 100°C for 10 minutes. The resulting solution of dissolved mMIONS was combined with 10 μ L of hydroxylamine hydrochloride and 855 μ L of sodium acetate, followed by addition of 100 μ L 1,10-phenanthroline. After 10 minutes the absorbance of the sample at 510 nm was measured using a Safire microplate reader (Tecan Group Ltd., Männedorf, Switzerland) and compared to the absorbance of a standard curve created using a ferrous ammonium sulfate hexahydrate solution.

3.2.4 Relaxation Measurement

Relaxation measurements were performed according to previous studies (4). Measurements were carried out using a 0.47 T Minispec mq20 (Bruker Optics, Billerica, MA). Briefly, transverse magnetization decay curves were acquired using a Carr-Purcell-Meiboom-Gill sequence, while longitudinal magnetization recovery curves were acquired using an inversion-recovery sequence. Curves were fit using Origin 6 analysis software (OriginLab Corp., Northampton, MA) to obtain T1 and T2 time constants. Relaxivity values (R_1 and R_2) were calculated using T1 and T2 time constants and the iron concentration of measured samples.

3.2.5 Conjugation of mMIONS with DOTA-NHS-Ester

DOTA-NHS-ester was reacted with 1 mL of 10 mg Fe/mL amino-functionalized mMIONS at 1 mM in PBS (pH 7.5) overnight at 4 °C. The product, DOTA-mMION conjugate, was separated from

excess DOTA-NHS-ester by dialysis using a 100 kD Float-A-Lyzer (Spectrum Laboratories, Inc., Rancho Dominguez, CA) against 2L of phosphate buffer for 48hrs at 4 °C with a total of 8 buffer changes.

3.2.6 Radiolabeling of DOTA-mMION with ^{64}Cu

In general, DOTA-mMIONS were labeled with ^{64}Cu and analyzed according to Rossin et al (7). DOTA-mMIONS (5mg in 610 μL) were incubated with $^{64}\text{CuCl}_2$ (3 mCi in 2.2 μL , 0.1 M HCl) in 0.1 M ammonium acetate buffer (pH 5.5) at 37 °C for 1 hr in a thermomixer. The solution was then challenged with 5 μL of 10 mM EDTA or DTPA at 37 °C for 5 min with mixing to remove nonspecifically bound ^{64}Cu , followed by purification using a centrifugal desalting column (Pierce Biotechnology, Inc., Rockford, IL). Labeling yield was determined by radiochemical thin layer chromatography (radio-TLC). A small amount of the of the ^{64}Cu -labeled mMION (^{64}Cu -mMION) solution was applied to an ITLC-SG plate (Pall Corporation, East Hills, NY) and developed using a 1:1 mixture (v/v) of 10% (w/v) ammonium acetate and methanol. The TLC plate was then measured using a Bioscan 200 imaging scanner (Bioscan Inc., Washington DC).

3.2.7 Radiochemical Purity

Radiochemical purity (RCP) of ^{64}Cu -mMION was evaluated by radio-fast protein liquid chromatography (radio-FPLC) using an Amersham Biosciences ÄKTA FLPC system (GE Healthcare, Piscataway, NJ) equipped with a UV detector (280nm) and fitted with an in-line Model 170 radioisotope detector (Beckman Coulter Inc., Fullerton, CA). A 100 μL sample of dilute ^{64}Cu -mMION was applied to a Superose 12 gel filtration column (GE Healthcare, Piscataway, NJ) and eluted with 20 mM HEPES and 150 mM NaCl at a flow rate of 0.8 mL/min.

The RCP of ^{64}Cu -labeled mMION was found to be > 95%. The nanoparticle solution was then diluted with PBS to obtain doses suitable for biodistribution and imaging studies.

3.2.8 Serum Stability of ^{64}Cu -mMION

The serum stability of ^{64}Cu -mMION was tested by incubated labeled nanoparticles in mouse serum at 37 °C with shaking for 24 hr with constant shaking. The samples were then subjected to radioTLC analysis after 0, 1, 3, 6, and 24 hr incubation to measure the amount of activity dissociated from ^{64}Cu -mMIONs.

3.2.9 Size Determination

Dynamic light scattering (DLS) was used to measure the hydrodynamic diameter of uncoated MIONs and DOTA-mMIONs using a NICOMP 380 ZLS Submicron Particle Sizer (Particle Sizing Systems, Inc., Santa Barbara, CA) equipped with a 632.8 nm He-Ne laser and an Avalanche Photodiode detector at a fixed 90° scattering angle. DLS measurements were performed on DOTA-mMION samples chelated with “cold” (i.e. stable) isotopes of copper (Cu-DOTA-mMION) according to the same procedure used for radiolabeling with copper-64. DLS of uncoated, hydrophobic MIONs was performed in toluene. Dilute nanoparticle samples (0.4 mL) were placed in prewashed cylindrical optical cells and incident laser light was adjusted using a neutral density filter to obtain a scattering intensity of 300 KHz. Samples were scanned at 23 °C for 30 min in a temperature-controlled sample chamber and data are reported as the volume-weighted hydrodynamic diameter.

3.2.10 Transmission Electron Microscopy

Uncoated MIONs were stored in toluene prior to surface modification and were analyzed using transmission electron microscopy (TEM) to ensure monodispersity. TEM micrographs were produced by applying dilute MION samples to copper TEM grids allowing the organic solvent to evaporate. Grids were then imaged using a Hitachi H-7500 TEM. Micrographs were analyzed for particle size and distribution using ImageJ (NIH).

3.2.11 Biodistribution

All animal studies were performed in compliance with guidelines set by the Washington University Animal Studies Committee. Female BALB/c mice (Charles River Laboratories, Inc., Wilmington, MA) weighing approximately 20 g were anesthetized using 1-2 % isoflurane and given tail vein injections of 100 μCi of ^{64}Cu -mMION at a dose of 10 mg Fe/kg body weight. Mice ($n = 4$ per time point) were sacrificed by cervical dislocation at 10 min, 1 hr, 4 hr, and 24 hr post injection and organs of interest were collected, blotted dry, weighed, and assessed for radioactivity by counting for one minute in a Gamma 8000 scintillation counter (Beckman Coulter Inc., Fullerton, CA). A standard dose was prepared and measured along with the samples to allow calculation of the percentage injected dose (%ID) for the various tissues and organs. Data were corrected for ^{64}Cu decay and the percentage injected dose per gram of tissue (%ID/g) and the percentage injected dose per organ (%ID/ organ) were calculated according to the following equations:

$$\%ID/g = \frac{(\text{cpm in sample} - \text{background}) \times 10^2}{(\text{decay correction factor}) \times (\text{sample weight}) \times (\text{cpm in standard dose})} \quad \text{Equation 3.1}$$

$$\%ID/organ = \frac{(cpm \text{ in sample} - \text{background}) \times 10^2}{(\text{decay correction factor}) \times (cpm \text{ in standard dose})} \quad \text{Equation 3.2}$$

3.2.12 Small-Animal PET/CT Imaging Studies of ⁶⁴Cu-mMIONS

MicroPET imaging scans were performed using a microPET Focus 120 and (Siemens Medical Solutions USA, Inc., Malvern, PA). Female BALB/c mice (20-25 g) were anesthetized using 1-2 % isoflurane and given tail vein injections with 100 μ Ci of ⁶⁴Cu-mMION (10 mg Fe/kg body weight) in 100 μ L PBS. Mice were reanesthetized and imaged in the supine position at 1 hr, 4 hr, and 24 hr post injection. PET scan acquisition time for the 10 min, 1 hr, and 4 hr images was 10 min, while the PET scan acquisition time for the 24 hr image was 20 min. Mice were scanned on a microCAT II (Siemens Medical Solutions USA, Inc., Malvern, PA) immediately after microPET. Analysis of microPET images was accomplished using vendor software (ASIPro, Siemens Medical Solutions USA, Inc.) on decay-corrected images. Coregistration of microPET and microCT images was performed using fiducial markers in the animal transfer bed and the Amira software package (Mercury Computer Systems, Inc., Chelmsford, MA).

3.2.13 Phantom Study

To demonstrate the ability of mMIONS to function as a dual imaging agent, we prepared a microfuge tube of ⁶⁴Cu-mMIONS for PET and MR imaging. Radiolabeled nanoparticles were added to a tubes containing PBS to a final concentrations of 10 and 25 μ g Fe/mL. The tubes were placed upright in the bed of a Focus 120 microPET and scanned for 10 minutes. After a sufficient amount of time to allow ⁶⁴Cu to decay, the samples were then imaged in a 7.0-T Pharmascan magnet (Bruker BioSpin, Billerica, MA). A T2-weighted proton density scan was obtained using a multi-slice multi-echo sequence (MSME-PD-T2, Bruker Paravision 4) using the

following parameters: 1000 ms repetition time; 180° flip angle, 3cm FOV; 1mm slice thickness, 2 averages.

3.3 Results

3.3.1 Nanoparticle Formation and Characterization

Dual PET/MR nanoparticles (Figure 3.1A) were prepared by first encapsulating monocrystalline superparamagnetic iron oxide nanoparticles (MIONs) in PEG-phospholipid micelles (4, 8, 9). This technique exploits the hydrophobic interaction between capping ligands on the nanoparticle surface and acyl chains of PEGylated phospholipids, leaving the PEG moieties exposed to confer water solubility and reduce protein absorption. MIONs used in this experiment were highly monodisperse (Figure 3.1B), having an average diameter of 6.2 ± 0.5 nm as determined by TEM. Functionalized micelle-coated MION (mMION) was prepared by coating nanoparticles with a 1:5 molar ratio of amino-PEG2000 phospholipids to methoxy-terminated mPEG5000 phospholipids. Empty micelles were separated from mMIONs using ultracentrifugation. The R_2 relaxivity of mMION, measured using a 0.47 T Bruker Minispec, was 209 ± 26 mM⁻¹•sec⁻¹.

Amine-modified mMION was conjugated with DOTA-NHS-ester to allow incorporation of PET imaging isotopes. Dialysis was used to separate DOTA-mMION from excess DOTA-NHS-ester. Dynamic light scattering was used to measure the hydrodynamic diameter of DOTA-mMION (Figure 3.1C). DOTA-mMION has a hydrodynamic diameter of 20.3 ± 1.9 nm as determined by dynamic light scattering, while prior to encapsulation MION had a diameter of 7.1 ± 8 nm.

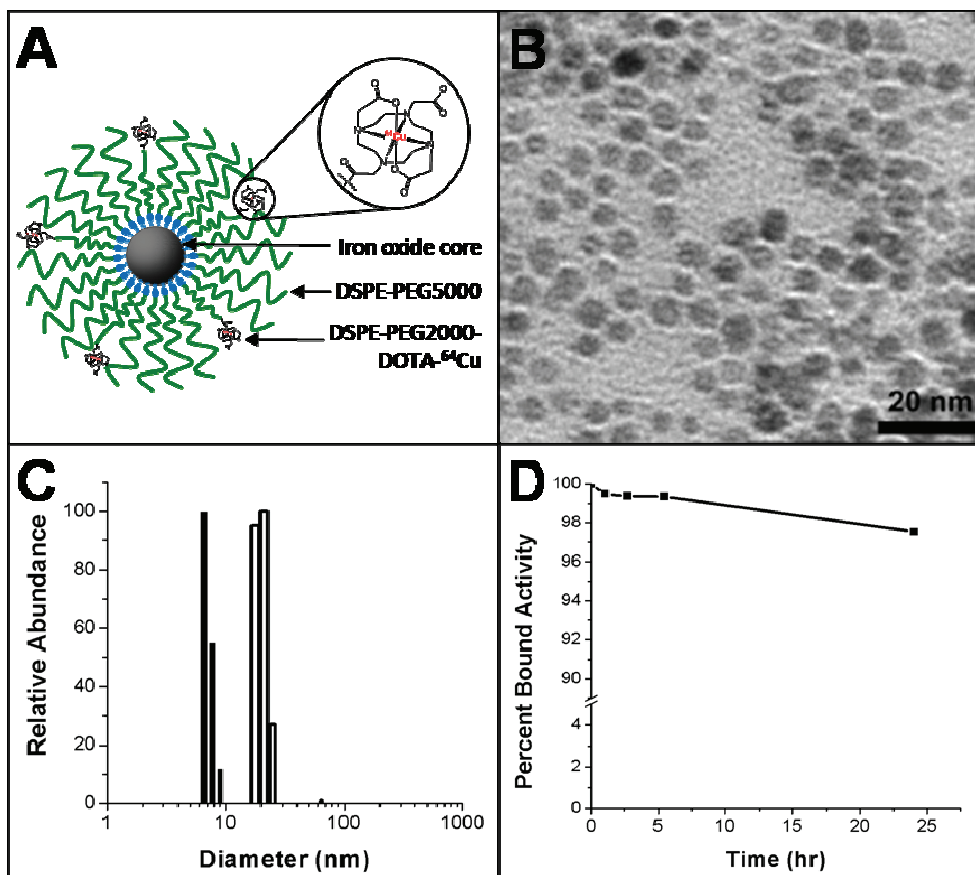


Figure 3.1: Design and characterization of ⁶⁴Cu-labeled mMIONS. (A) Transmission electron micrograph of uniform monocrystalline superparamagnetic iron oxide nanoparticles. (B) Schematic representation dual-modality ⁶⁴Cu-mMION. (C) Dynamic light scattering showing highly monodisperse populations of mMION before (closed bars) and after (open bars) encapsulation in PEGylated lipid micelle. (D) In vitro stability of ⁶⁴Cu-mMION over the course of 24 hr incubation in 37 °C mouse serum.

3.3.2 ⁶⁴Cu-Radiolabeling of DOTA-mMION

The positron-emitting radionuclide ⁶⁴Cu ($t_{1/2} = 12.7$ hr; $\beta^+ = 0.653$ MeV, 17.4%; $\beta^- = 0.578$ MeV, 39%) was used to radiolabel mMIONS to allow small animal PET imaging and biodistribution studies. Copper-64 has is commonly used in PET imaging and radiopharmaceuticals (10) because it can be produce at high specific activity and yield in biomedical cyclotrons (11, 12). Chelation of ⁶⁴Cu to various macrocyclic ligands provides an efficient route for radiolabeling a wide variety of macromolecules and nanoparticles.

Efficient labeling of DOTA-mMION was obtained by incubation with ^{64}Cu at 37 °C for 1 hr in 0.1 M ammonium acetate buffer, pH 5.5 (radiolabeling in acetate buffer was found to be superior to labeling in 0.1 mM ammonium citrate buffer, pH 5.5). DOTA-mMIONs can be labeled to a specific activity of at least 10-20 $\mu\text{Ci}/\mu\text{g}$. Nonspecifically bound ^{64}Cu was removed from ^{64}Cu -mMIONs by addition of excess EDTA following completion of the labeling reaction, and ^{64}Cu -EDTA was separated from ^{64}Cu -mMIONs using a desalting column. The radiochemical purity of the labeled nanoparticles, determined by radio-FPLC, was found to be > 95%. Incubation of ^{64}Cu -MIONs at 37 °C for 24 hr in mouse indicated *in vitro* stability of radiolabeling (Figure 3.1D).

3.3.3 Biodistribution Studies

The pharmacokinetics and biodistribution of dual-PET/MR nanoparticles was studied to evaluate their usefulness as *in vivo* imaging probes. Radiolabeled nanoparticles were administered via tail vein injection and circulation half-life and accumulation in major organs was investigated (Figure 3.2). To allow dual PET/MR imaging with ^{64}Cu -mMIONs, the dose of particles administered must be within the detection limits of both modalities. Positron emission tomography is more sensitive than MRI (13) therefore the amount of administered iron oxide was the limiting factor when formulating animal doses. Mice ($n = 4$) weighing approximately 20 g were injected with a 10 mg Fe/kg dose of ^{64}Cu -mMIONs, a typical amount of iron oxide used for *in vivo* magnetic resonance imaging experiments. Each dose of particles were labeled with 100 μCi of ^{64}Cu ($t_{1/2} = 12.7$ hr) to allow imaging to 24 hr post injection. ^{64}Cu -labeled mMIONs exhibited high blood retention at 10 minutes and 1 hr post injection of 47.5 ± 4.6 and 37.3 ± 12.9 %ID/g, respectively. Blood retention of ^{64}Cu -labeled mMIONs decreased to 7.9 ± 0.8 %ID/g at 4 hr post injection and to 1.0 ± 0.05 %ID/g by 24 hr post injection. Accumulation in the heavily vascularized tissues of the heart and lungs generally followed the pattern of blood

retention. The circulation half-life of labeled nanoparticles was 143 ± 21 minutes, substantially longer than ^{64}Cu -DOTA alone which undergoes rapid renal excretion (14, 15).

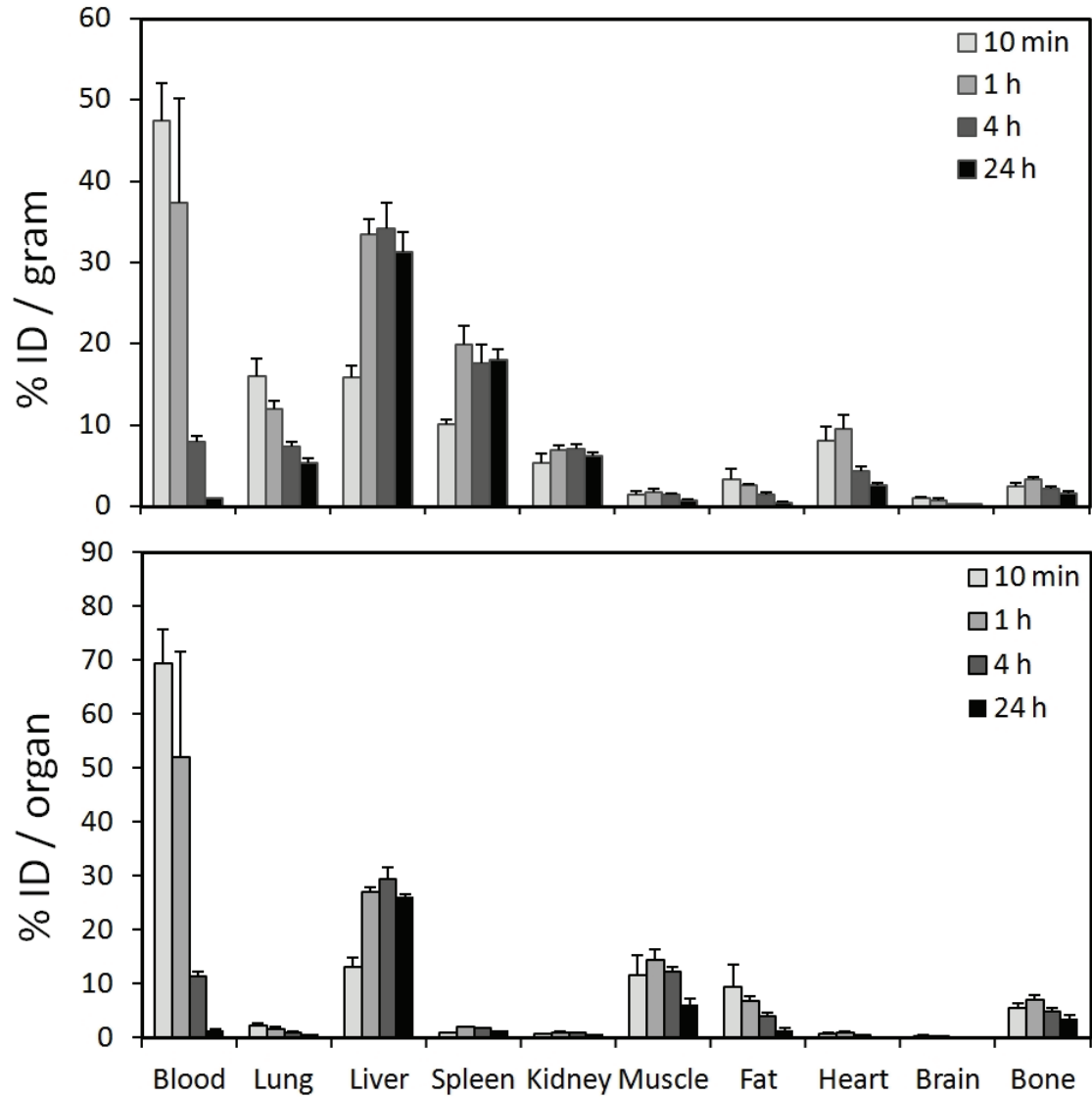


Figure 3.2: Biodistribution data of dual-PET/MR ^{64}Cu -mMION in BALB/c mice. Groups of mice ($n = 4$) were sacrificed at 10 min, 1 hr, 4 hr, and 24 hr and select organs were measured for activity. Animals were injected at a dose of 10 mg Fe/kg body weight (100 μCi). Data are expressed as percent injected dose per gram tissue (%ID/g, top) and percent injected dose per organ (%ID/organ, bottom) \pm one standard deviation.

Organs of the reticuloendothelial system (RES) experienced moderate nanoparticle uptake. The liver and spleen showed a low initial accumulation of 15.8 ± 1.4 and 10.1 ± 0.6 %ID/g, respectively. At 1 hr post injection the liver and spleen uptake reached 33.4 ± 1.8 and 20.0 ± 2.3 %ID/g, respectively, and generally maintained those values for the remainder of the study. It is known that ^{64}Cu dissociated from the ^{64}Cu -DOTA complex will undergo transchelation by proteins in the liver such as superoxide dismutase, and metallothionein, and ceruloplasmin (16-18). Therefore, while uptake by the liver uptake in later time points is prominent, some contribution is due to the accumulation of disassociated ^{64}Cu .

Kidney uptake remained relatively constant, averaging 5 - 7 %ID/g for all time points. Renal excretion of ^{64}Cu -labeled mMIONs was assessed by measuring urine activity using a metabolism cage. The activity of urine at 4 hr post injection was 1.1 %ID/g at 4 hr post injection and 5.0 %ID/g at 24 hr post injection. While ^{64}Cu -labeled mMIONs are larger than the cut-off for glomerular filtration (19), individual PEGylated lipids would be able to traverse the glomerular pores if disassociated from the nanoparticle surface. All other organs evaluated showed low (muscle, fat, bone) or negligible (brain) uptake. Organs were not perfused prior to counting and a small contribution of activity in harvested organs is due to remaining blood.

3.3.4 Small Animal PET Imaging Studies

The PET imaging capabilities of dual-modality ^{64}Cu -labeled mMIONs was analyzed by small animal microPET imaging performed using a microPET Focus 120. In this study, BALB/c mice were administered tail vein injections with 100 μCi of ^{64}Cu -mMION (10 mg Fe/kg body weight) in 100 μL PBS and imaged at 1 hr, 4 hr, and 24 hr post injection. Accurate comparison of microPET images with *ex vivo* biodistribution data required additional anatomical information which was provided by microCT scans. Mice were scanned on a microCAT II immediately after acquisition

of microPET images and coregistration was accomplished using fiducial landmarks on the animal bed. Examples of coregistered images obtained after administration of ^{64}Cu -mMION are shown in Figure 3.3.

MicroPET images show a general agreement with the results of the nanoparticle biodistribution studies. High levels of activity are observed in the heart and carotid arteries at 1 hr post injection (Figure 3.3A, 3.3B), indicating a large amount of nanoparticles in circulation. The strong presence of circulating nanoparticles was also detected in the descending abdominal aorta, aortic bifurcation, and common iliac arteries. Less activity was observed in the heart at 4 hr post injection (Figure 3.3C, 3.3D). The absence of activity in the heart indicates a marked decrease in circulating nanoparticles relative to levels at 1 hr post injection, corresponding well to the decrease in blood activity observed from the 1 hr to 4 hr *ex vivo* biodistribution. Uptake of ^{64}Cu -mMIONs by the liver is also clearly apparent, indicating significant amounts of nanoparticles are sequestered by the RES systems by 4 hr post injection.

By 24 hr post injection microPET images show little activity heart (Figure 3.3E, 3.3F), corresponding to negligible amounts of circulating nanoparticles. While the liver and spleen show high uptake at 24 hr, widespread activity can also be observed in gastrointestinal (GI) tract. This activity is an indication that ^{64}Cu -mMIONs (and their metabolic products) present in the liver at earlier time points undergo biliary excretion into the GI tract to be eliminated in the feces.

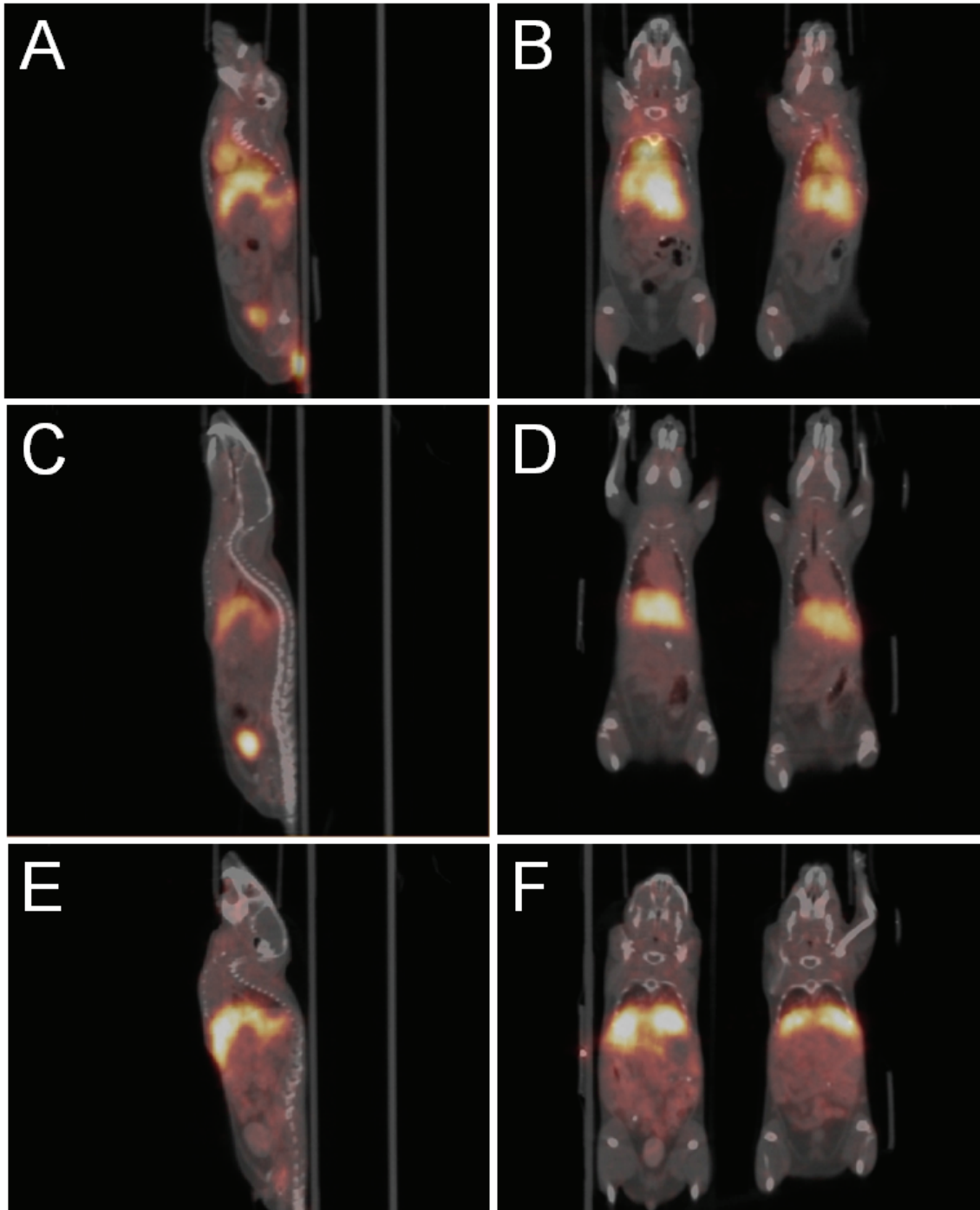


Figure 3.3: Coregistered microPET/microCT of BALB/c administered 100 μ Ci of 64 Cu-mMIONS (10 mg Fe/kg body weight, 100 μ L injection volume). Whole body sagittal (A-E) and coronal (B-F) PET images are decay corrected and scaled by min/max frame: (A, B) 1 hr; (C, D) 4 hr; and (E, F) 24 hr post injection.

3.3.5 Phantom Studies

To verify the dual imaging capability of ^{64}Cu -mMIONS, nanoparticle samples underwent PET and MR scans using standard techniques. Figure 4 shows T2-weighted and microPET images of 10 and 25 $\mu\text{g Fe/mL}$ samples of labeled magnetic nanoparticles. Iron oxide cores in ^{64}Cu -mMION produce a characteristic darkening at increasing iron concentrations, seen in Figure 3.4A. A strong PET signal is produced from ^{64}Cu chelated to PEG-phospholipid micelle coating (Figure 3.4B)

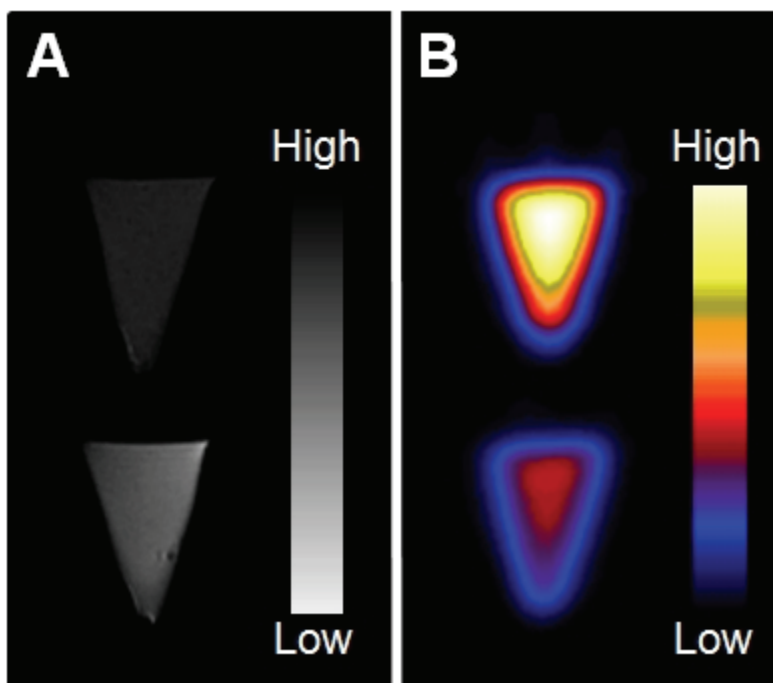


Figure 3.4: Pet and MR imaging of ^{64}Cu -mMION phantoms. (A) T2-weight proton density image of 25 $\mu\text{g Fe/mL}$ (top) and 10 $\mu\text{g Fe/mL}$ (bottom) of ^{64}Cu -labeled magnetic nanoparticles (scale bar corresponds to high and low iron concentration). (B) Decay-corrected microPET image of 25 $\mu\text{g Fe/mL}$ (top) and 10 $\mu\text{g Fe/mL}$ (bottom) of ^{64}Cu -labeled magnetic nanoparticles (scale bar corresponds to high and low copper-64 concentration).

3.3.6 Discussion

The combination of positron emission tomography (PET) with magnetic resonance imaging (MRI) offers many opportunities (20-23). PET is a highly sensitive imaging modality that provides quantitative, whole-body imaging. Magnetic resonance produces high resolution images of soft tissue as well as functional and spectroscopic information. Interest in combining PET with MRI has surged (24-27), and structured nanomaterials have emerged as possible a platform for the development of dual-PET/MR imaging agents. The unique qualities of nanoparticles are well suited to the design of PET probes. Because of their large surface area, nanoparticles can be labeled to a high specific activity, further increasing the sensitivity of detection as well as the payload of therapeutic isotopes and targeting ligands. The synthesis and use nanoparticles as PET molecular imaging agents have only recently been explored in detail (28-31). Alternatively, magnetic nanoparticles have been used extensively for MRI to study a wide range of biological phenomena, such stem cell tracking, cancer detection, and monitoring atherosclerosis .

We report the development and *in vivo* evaluation of a novel dual-PET/MR nanoparticle composed of a monocrystalline iron oxide core (MION) and a physically absorbed layer of PEGylated lipids. High magnetic field gradients surround the surface of the iron oxide core, allowing sensitive detection by high resolution MRI. The PEGylated micelle coating, formed by the hydrophobic interaction between capping ligands on the particle surface and acyl chains of phospholipids, permits ample labeling with radioisotopes for sensitive detection using PET imaging. The micelle-coated MIONS (mMIONS) used in this study had a 6.2 nm Fe₃O₄ core (Figure 3.1A), a hydrodynamic diameter of approximately 20 nm (Figure 3.1C), and a R₂ relaxivity of 209 ± 26 mM⁻¹•sec⁻¹.

Encapsulation of magnetic nanoparticles in micelles of PEGylated lipids has many advantages over traditional polymer- and carbohydrate-based approaches. Due to the modular nature of this coating scheme, tuning nanoparticle surface chemistry with multiple lipid species and alternative chemical groups on PEG termini is achieved *in situ* by simply adjusting the stoichiometry of the initial lipid solution, unlike polymeric encapsulation. Several functionalized PEG-phospholipids are commercially available and inexpensive. Additionally, polymer coatings commonly applied to nanoparticles are relatively bulky and possess surface chemistry that result in nanoparticles which experience high RES uptake (15). Carbohydrate coatings traditionally used in precipitation-based nanoparticle synthesis limit core size that can be encapsulated (32) and generally require post-synthesis surface functionalization. PEGylated lipid coatings have been applied to nanoparticles ranging from 3 (33) to 35 nm (34) using a multiple chemical functionalities (9, 35).

In this work, successful radiolabeling of DOTA-conjugated mMION with ^{64}Cu was achieved. ^{64}Cu -mMIONs produced strong MR and PET signal (Figure 3.4) and were found to be stable in serum for 24 hr (Figure 3.1D). The potential of this nanoparticle as novel imaging agent was investigated by *ex vivo* biodistribution and *in vivo* PET imaging. Biodistribution results high initial blood retention with moderate liver uptake (Figure 3.2). ^{64}Cu -mMION had a circulation life time of 143 minutes, a value that compares well with previous reports of quantum dots and silica nanoparticles with PEGylated lipid coatings (34, 36). This result suggests that the circulation profile is dominated by the coating, and that the lipid-PEG coating can be generalized to other classes of nanoparticles with differing surface chemistries

PET/CT imaging showed high levels of activity in several regions. In general, microPET imaging correlated well with biodistribution findings. The heart and carotid arteries are clearly visible at early time points, indicating a high level up ^{64}Cu -mMION blood retention (Figure 3.3A,

3.3B). While the liver and spleen show high uptake at 24 hr, widespread activity can also be observed in gastrointestinal (GI) tract (Figure 3.3E, 3.3F). This activity is an indication that ^{64}Cu -mMIONs (and their metabolic products) sequestered in the liver at earlier time points undergo biliary excretion into the GI tract to be eliminated in the feces. Iron oxide has been used in animals and humans with little observed (37, 38). ^{64}Cu has also been used in patients (39) and showed little toxicity.

The few published reports of dual-modality PET/MRI nanoparticles have used either dextran-based (40, 41) or protein-based (42, 43) coatings. In this study, we present the results of a novel dual-PET/MRI nanoparticle with a flexible coating composed of PEGylated phospholipids. The physical and magnetic properties of ^{64}Cu -mMION were characterized, and the potential as a dual-modality imaging was evaluated using quantitative *ex vivo* biodistribution and *in vivo* microPET/CT imaging. We are currently investigating this and other dual-PET/MRI nanomaterials and their application to disease detection and treatment in models of atherosclerosis and cancer.

3.4 References

1. Feltin, N. and M.P. Pileni, *New technique for synthesizing iron ferrite magnetic nanosized particles*. Langmuir, 1997. **13**(15): p. 3927-3933.
2. Seip, C.T. and C.J. O'Connor, *The fabrication and organization of self-assembled metallic nanoparticles formed in reverse micelles*. Nanostructured Materials, 1999. **12**(1-4): p. 183-186.
3. McCarthy, D.W., R.E. Shefer, R.E. Klinkowstein, L.A. Bass, W.H. Margeneau, C.S. Cutler, C.J. Anderson, and M.J. Welch, *Efficient production of high specific activity ^{64}Cu using a biomedical cyclotron*. Nucl Med Biol, 1997. **24**(1): p. 35-43.
4. Laconte, L.E., N. Nitin, O. Zurkiya, D. Caruntu, C.J. O'Connor, X. Hu, and G. Bao, *Coating thickness of magnetic iron oxide nanoparticles affects $R(2)$ relaxivity*. J Magn Reson Imaging, 2007. **26**(6): p. 1634-41.

5. Yu, Z., *In vitro Characterization of Magnetic Resonance Imaging Contrast Agents for Molecular Imaging in Cardiology*. 2006, Charité Universitätsmedizin Berlin: Berlin. p. 60.
6. Yu, Z., M. Grafe, H. Meyborg, E. Fleck, and Y. Li, *In Vitro Characterization of Magnetic Resonance Imaging Contrast Agents for Molecular Imaging*. ASH Annual Meeting Abstracts, 2006. **108**(11): p. 3944-.
7. Rossin, R., D. Pan, K. Qi, J.L. Turner, X. Sun, K.L. Wooley, and M.J. Welch, *⁶⁴Cu-labeled folate-conjugated shell cross-linked nanoparticles for tumor imaging and radiotherapy: synthesis, radiolabeling, and biologic evaluation*. J Nucl Med, 2005. **46**(7): p. 1210-8.
8. van Tilborg, G., W. Mulder, N. Deckers, G. Storm, C. Reutelingsperger, G. Strijkers, and K. Nicolay, *Annexin A5-functionalized bimodal lipid-based contrast agents for the detection of apoptosis*. Bioconjug Chem, 2006. **17**(3): p. 741-9.
9. Nitin, N., L.E. LaConte, O. Zurkiya, X. Hu, and G. Bao, *Functionalization and peptide-based delivery of magnetic nanoparticles as an intracellular MRI contrast agent*. J Biol Inorg Chem, 2004. **9**(6): p. 706-12.
10. Sun, X. and C. Anderson, *Production and applications of copper-64 radiopharmaceuticals*. Methods Enzymol, 2004. **386**: p. 237-61.
11. McCarthy, D., R. Shefer, R. Klinkowstein, L. Bass, W. Margeneau, C. Cutler, C. Anderson, and M. Welch, *Efficient production of high specific activity ⁶⁴Cu using a biomedical cyclotron*. Nuclear Medicine and Biology, 1997. **24**(1): p. 35-43.
12. McCarthy, D., L. Bass, P. Cutler, R. Shefer, R. Klinkowstein, P. Herrero, J. Lewis, C. Cutler, C. Anderson, and M. Welch, *High purity production and potential applications of copper-60 and copper-61*. Nuclear Medicine and Biology, 1999. **26**(4): p. 351-358.
13. Frangioni, J., *New Technologies for Human Cancer Imaging*. Journal of Clinical Oncology, 2008. **26**(24): p. 4012.
14. Jones-Wilson, T., K. Deal, C. Anderson, D. McCarthy, Z. Kovacs, R. Motekaitis, A. Sherry, A. Martell, and M. Welch, *The in vivo behavior of copper-64-labeled azamacrocyclic complexes*. Nuclear Medicine and Biology, 1998. **25**(6): p. 523-530.
15. Schipper, M.L., Z. Cheng, S.W. Lee, L.A. Bentolila, G. Iyer, J. Rao, X. Chen, A.M. Wu, S. Weiss, and S.S. Gambhir, *microPET-based biodistribution of quantum dots in living mice*. J Nucl Med, 2007. **48**(9): p. 1511-8.
16. Bass, L., M. Wang, M. Welch, and C. Anderson, *In Vivo Transchelation of Copper-64 from TETA-Octreotide to Superoxide Dismutase in Rat Liver*. BIOCONJUGATE CHEMISTRY, 2000. **11**(4): p. 527-532.
17. Woodin, K., K. Heroux, C. Boswell, E. Wong, G. Weisman, W. Niu, S. Tomellini, C. Anderson, L. Zakharov, and A. Rheingold, *Kinetic Inertness and Electrochemical Behavior*

of Copper (II) Tetraazamacrocyclic Complexes: Possible Implications for in Vivo Stability. EUROPEAN JOURNAL OF INORGANIC CHEMISTRY, 2005. **23**: p. 4829.

18. Mirick, G., R. O'Donnell, S. DeNardo, S. Shen, C. Meares, and G. DeNardo, *Transfer of copper from a chelated ⁶⁷Cu-antibody conjugate to ceruloplasmin in lymphoma patients.* Nuclear Medicine and Biology, 1999. **26**(7): p. 841-845.
19. Choi, H., W. Liu, P. Misra, E. Tanaka, J. Zimmer, B. Ipe, M. Bawendi, and J. Frangioni, *Renal clearance of quantum dots.* Nature Biotechnology, 2007. **25**(10): p. 1165.
20. Seemann, M.D., *Whole-body PET/MRI: the future in oncological imaging.* Technol Cancer Res Treat, 2005. **4**(5): p. 577-82.
21. Cherry, S.R., *The 2006 Henry N. Wagner Lecture: Of mice and men (and positrons)-- advances in PET imaging technology.* J Nucl Med, 2006. **47**(11): p. 1735-45.
22. Ruf, J., E. Lopez Hanninen, M. Bohmig, I. Koch, T. Denecke, M. Plotkin, J. Langrehr, B. Wiedenmann, R. Felix, and H. Amthauer, *Impact of FDG-PET/MRI image fusion on the detection of pancreatic cancer.* Pancreatology, 2006. **6**(6): p. 512-9.
23. Seemann, M.D., G. Meisetschlaeger, J. Gaa, and E.J. Rummeny, *Assessment of the extent of metastases of gastrointestinal carcinoid tumors using whole-body PET, CT, MRI, PET/CT and PET/MRI.* Eur J Med Res, 2006. **11**(2): p. 58-65.
24. Catana, C., D. Procissi, Y. Wu, M.S. Judenhofer, J. Qi, B.J. Pichler, R.E. Jacobs, and S.R. Cherry, *Simultaneous in vivo positron emission tomography and magnetic resonance imaging.* Proc Natl Acad Sci U S A, 2008. **105**(10): p. 3705-10.
25. Judenhofer, M.S., H.F. Wehrl, D.F. Newport, C. Catana, S.B. Siegel, M. Becker, A. Thielscher, M. Kneilling, M.P. Lichy, M. Eichner, K. Klingel, G. Reischl, S. Widmaier, M. Rocken, R.E. Nutt, H.J. Machulla, K. Uludag, S.R. Cherry, C.D. Claussen, and B.J. Pichler, *Simultaneous PET-MRI: a new approach for functional and morphological imaging.* Nat Med, 2008. **14**(4): p. 459-65.
26. Pichler, B.J., M.S. Judenhofer, and H.F. Wehrl, *PET/MRI hybrid imaging: devices and initial results.* Eur Radiol, 2008. **18**(6): p. 1077-86.
27. Pichler, B.J., H.F. Wehrl, A. Kolb, and M.S. Judenhofer, *Positron emission tomography/magnetic resonance imaging: the next generation of multimodality imaging?* Semin Nucl Med, 2008. **38**(3): p. 199-208.
28. Fukukawa, K., R. Rossin, A. Hagooley, E.D. Pressly, J.N. Hunt, B.W. Messmore, K.L. Wooley, M.J. Welch, and C.J. Hawker, *Synthesis and characterization of core-shell star copolymers for in vivo PET imaging applications.* Biomacromolecules, 2008. **9**(4): p. 1329-39.

29. Rossin, R., S. Muro, M.J. Welch, V.R. Muzykantov, and D.P. Schuster, *In vivo imaging of ⁶⁴Cu-labeled polymer nanoparticles targeted to the lung endothelium*. J Nucl Med, 2008. **49**(1): p. 103-11.
30. Sun, G., A. Hagooly, J. Xu, A.M. Nystrom, Z. Li, R. Rossin, D.A. Moore, K.L. Wooley, and M.J. Welch, *Facile, efficient approach to accomplish tunable chemistries and variable biodistributions for shell cross-linked nanoparticles*. Biomacromolecules, 2008. **9**(7): p. 1997-2006.
31. Sun, X., R. Rossin, J.L. Turner, M.L. Becker, M.J. Joralemon, M.J. Welch, and K.L. Wooley, *An assessment of the effects of shell cross-linked nanoparticle size, core composition, and surface PEGylation on in vivo biodistribution*. Biomacromolecules, 2005. **6**(5): p. 2541-54.
32. Jarrett, B., M. Frendo, J. Vogan, and A. Louie, *Size-controlled synthesis of dextran sulfate coated iron oxide nanoparticles for magnetic resonance imaging*. NANOTECHNOLOGY, 2007. **18**(3): p. 35603.
33. Dubertret, B., P. Skourides, D. Norris, V. Noireaux, A. Brivanlou, and A. Libchaber, *In Vivo Imaging of Quantum Dots Encapsulated in Phospholipid Micelles*. 2002. p. 1759-1762.
34. van Schooneveld, M., E. Vucic, R. Koole, Y. Zhou, J. Stocks, D. Cormode, C. Tang, R. Gordon, K. Nicolay, and A. Meijerink, *Improved Biocompatibility and Pharmacokinetics of Silica Nanoparticles by Means of a Lipid Coating: A Multimodality Investigation*. Nano Lett, 2008.
35. Mulder, W., R. Koole, R. Brandwijk, G. Storm, P. Chin, G. Strijkers, C. de Mello Donegá, K. Nicolay, and A. Griffioen, *Quantum dots with a paramagnetic coating as a bimodal molecular imaging probe*. Nano Lett, 2006. **6**(1): p. 1-6.
36. Duconge', F., T. Pons, C. Pestourie, L. He'rin, B. The'ze', K. Gombert, B. Mahler, F. Hinnen, B. Kühnast, and F. Dolle', *Fluorine-18-Labeled Phospholipid Quantum Dot Micelles for in Vivo Multimodal Imaging from Whole Body to Cellular Scales*. Bioconjug Chem, 2008.
37. Anzai, Y., K. Blackwell, S. Hirschowitz, and J. Rogers, *Initial Clinical Experience with Dextran-coated Superparamagnetic Iron Oxide for Detection of Lymph Node Metastases in Patients with Head and Neck Cancer'*. Radiology, 1994. **192**: p. 709-715.
38. Heesakkers, R., A. Hövels, G. Jager, H. van den Bosch, J. Witjes, H. Raat, J. Severens, E. Adang, C. van der Kaa, and J. Fütterer, *MRI with a lymph-node-specific contrast agent as an alternative to CT scan and lymph-node dissection in patients with prostate cancer: a prospective multicohort study*. Lancet Oncology, 2008.
39. Anderson, C.J., F. Dehdashti, P.D. Cutler, S.W. Schwarz, R. Laforest, L.A. Bass, J.S. Lewis, and D.W. McCarthy, *⁶⁴Cu-TETA-octreotide as a PET imaging agent for patients with neuroendocrine tumors*. J Nucl Med, 2001. **42**(2): p. 213-21.

40. Nahrendorf, M., H. Zhang, S. Hembrador, P. Panizzi, D.E. Sosnovik, E. Aikawa, P. Libby, F.K. Swirski, and R. Weissleder, *Nanoparticle PET-CT imaging of macrophages in inflammatory atherosclerosis*. *Circulation*, 2008. **117**(3): p. 379-87.
41. Jarrett, B.R., B. Gustafsson, D.L. Kukis, and A.Y. Louie, *Synthesis of ⁶⁴Cu-labeled magnetic nanoparticles for multimodal imaging*. *Bioconjug Chem*, 2008. **19**(7): p. 1496-504.
42. Choi, J.S., J.C. Park, H. Nah, S. Woo, J. Oh, K.M. Kim, G.J. Cheon, Y. Chang, J. Yoo, and J. Cheon, *A hybrid nanoparticle probe for dual-modality positron emission tomography and magnetic resonance imaging*. *Angew Chem Int Ed Engl*, 2008. **47**(33): p. 6259-62.
43. Lee, H.Y., Z. Li, K. Chen, A.R. Hsu, C. Xu, J. Xie, S. Sun, and X. Chen, *PET/MRI dual-modality tumor imaging using arginine-glycine-aspartic (RGD)-conjugated radiolabeled iron oxide nanoparticles*. *J Nucl Med*, 2008. **49**(8): p. 1371-9.

CHAPTER 4

DEVELOPMENT OF DEXTRAN-COATED MAGNETIC NANOPARTICLES AND INTEGRIN TARGETING SYSTEM

4.1 Introduction

Modern techniques used to synthesize magnetic nanoparticles involve high-temperature decomposition of organometallic precursors. The precursors are heated in the presence of organic coordinating ligands, nucleation occurs, and crystal growth is allowed for a prescribed duration to yield nanoparticles of a controlled, narrow size (1).

We investigated high temperature nanoparticle synthesis using the two most commonly cited methods (Figure 4.1A). The necessary equipment (heating mantle, temperature controller, etc.) and performed the synthesis with the assistance of Sijian Hou. One method produces iron nanoparticles by the high temperature decomposition of iron pentacarbonyl ($\text{Fe}(\text{CO})_5$) (2). We synthesized nanoparticles and dispersed them in toluene. The particle size was measured using transmission electron microscopy to be 11 – 17 nm and had a somewhat size distribution. The particles were then subjected to sizing by dynamic light scattering (DLS) in toluene using a Nicomp 380 ZLS manufactured by Particles Sizing Systems (Santa Barbara, CA). The nanoparticles had a diameter of 13.1 ± 2.5 nm.

The other method for high temperature synthesis of magnetic nanoparticles that we evaluated uses the reduction of iron(III) acetylacetonate (AcAc) in the presence of oleic acid and oleyamine (3) (Figure 4.1B). Using this procedure we were able to produce small, monodisperse Fe_3O_4 nanoparticles. We dissolved the particles in toluene measured their size using TEM. The nanoparticle diameter was $\approx 4 - 5$ nm and had a narrow size distribution (note: nanoparticles of this size approach the resolution limit for the Hitachi H-7500 transmission electron microscope

used for characterization, leading to low-quality images). The particles were then subjected to sizing by DLS in toluene and had a diameter of 6.3 ± 0.6 nm.

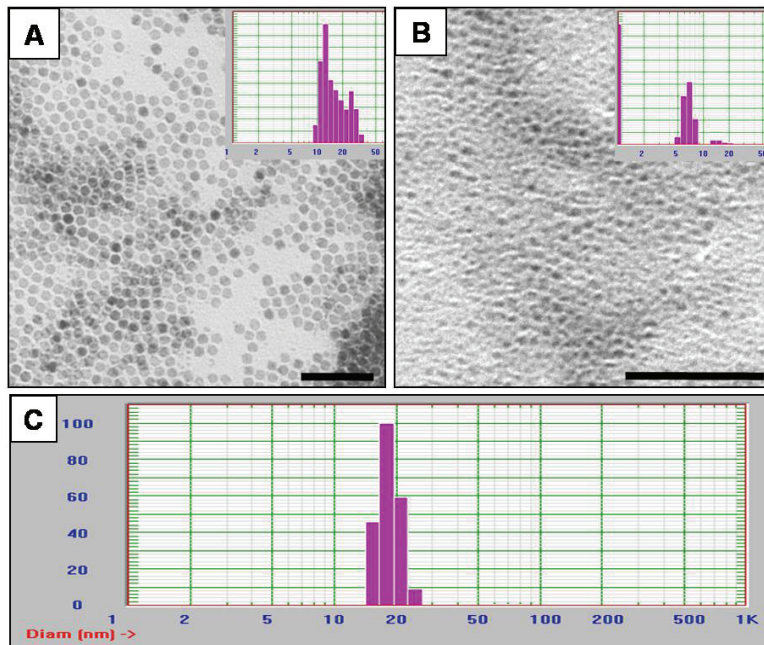


Figure 4.1: Size determination of high-temperature synthesized magnetic nanoparticles. (A) TEM image of Fe₃O₄ nanoparticles synthesized from iron pentacarbonyl. Scale bar is 50 nm. Particle size ranged from 11-17 nm. Inset shows DLS of particles in toluene, showing particles to have an average diameter of 13.1 ± 2.5 nm. (B) High magnification TEM image of Fe₃O₄ nanoparticles synthesized from iron(III) AcAc. Scale bar is 50 nm. Particle size ranged from 4-5 nm. DLS inset shows an average diameter of 6.3 ± 0.6 nm. Particles of this size are approaching the resolution limit of the instrument used. (C) DLS of PEG-lipid coated iron(III) AcAc nanoparticles (hydrodynamic diameter = 18.6 ± 3 nm).

All nanoparticles synthesized through high temperature methods and coated with organic surface ligands. As such they are only soluble in organic solvent. Magnetic nanoparticles used in biomedical applications must first be transferred into aqueous solution through secondary coatings or ligand exchange reactions. This represents a major drawback of high temperature nanoparticle synthesis, as producing robust coating schemes can be technically challenging. We were able to coated nanoparticles produced from the reduction of iron(III) AcAc using our

micelle encapsulation procedure. Nanoparticles were successfully coated with DPSE-mPEG2000 and characterized by DLS (Figure 4.1C). The coated particles had a hydrodynamic diameter of 18.6 ± 3 nm. Other approaches to coat hydrophobic with elaborate polymer coatings were briefly explored. It was determined that pursuing such strategies lies outside the main scope of the thesis: to produce nanoparticles capable of dual modality PET/MR imaging and to evaluate them for *in vivo* imaging. A decision was made to pursue this objective using magnetic nanoparticles (MNPs) produced through the coprecipitation of iron salts in an emulsion of dextran. These particles, referred to as USPIOs, are more well understood have been extensively studied.

4.1.1 Dextran-coated Iron Oxide Magnetic Nanoparticles

Dextran-coated monocrystalline iron oxide nanoparticles (MION) are the most prevalent form of ultrasmall superparamagnetic iron oxide (USPIO) magnetic nanoparticle (4, 5). First synthesized by Molday et al (4), these magnetic nanoparticles (MNPs) are produced through the coprecipitation of iron salts in an emulsion of dextran. Dextran is a polysaccharide formed from branched glucose molecules. Dextran is biocompatible and has uses as an anti-thrombogenic and as lubricant in eye drops. The MION iron oxide core has an inverse spinel crystal structure with each cubic unit containing $(\text{Fe}^{3+}(\text{Fe}^{2+})\text{Fe}^{3+}\text{O}_4)_8$ (6). This crystalline form of iron oxide is commonly referred to as magnetite. Each cubic unit is $\approx 8.4 \text{ \AA}$ in length (7), and the core diameter ranges from 4 – 7 nm (4.6 nm average size). The iron oxide core is coated with 25 ± 6 dextran molecules (10 kD each), and the final particle is 27% iron and 57% dextran by weight (respectively) (6). The hydrodynamic diameter in aqueous solution is ≈ 20 nm, while in nonaqueous media the diameter is ≈ 8 nm, indicating that the dextran coat surrounding the core is considerably hydrated and exhibits a high degree of flexibility.

Table 4.1: Dextran-coated superparamagnetic iron oxide nanoparticles (adapted from Sosnovik et al⁽⁸⁾)

Short Circulating	
Ferumoxides (Feridex)	Approved liver imaging agent. Experimental stem cell labeling
Long Circulating	
Ferumoxtran (Combidex)	Completed phase 3 trials for lymph node imaging, development currently halted Experimental imaging of human plaque macrophages
Experimental Particles	
Ferumoxytol	Experimental iron replacement therapeutic (NDA submitted Dec. 2007)
MION-47	Experimental nanoparticle highly similar to Ferumoxtran, used extensively in animal models
MION-48	Experimental nanoparticle similar to MION-47, extremely high transverse relaxivity (R2)
CLIO	Experimental nanoparticle, developed for targeted imaging

In general, SPIOs and to a lesser extent USPIOs are cleared from the circulation by mononuclear phagocytic cells within the organs of the reticuloendothelial system (RES) and accumulate in the liver, spleen, bone and lymph nodes (9). The thick, flexible dextran coating on MIONs helps to reduce the absorption of plasma proteins (i.e. opsonins), leading to decreased recognition by phagocytic cells and reduced accumulation in RES tissues.

4.1.2 Magnetic Nanoparticles for Human Use

Two generations of dextran coated magnetic nanoparticles have used for human studies. The first class to be FDA approved was the heterogeneous SPIO sold under the trade name Feridex I.V., introduced in 1996. Feridex I.V is 80 – 120 nm in diameter and has multiple 4 – 5 nm non-stoichiometric magnetite cores (FeO_{1.44}). Feridex I.V. (generic name is ferumoxides) is manufactured by AMAG Pharmaceuticals, Inc. and distributed by Bayer Healthcare. Feridex is taken up by phagocytic cells in the liver where it leads to a decrease in signal intensity in T2-

weighted MRI. Areas of the liver with decreased function, presumably due to a pathological lesion, retain their signal intensity and are easily discerned from the surrounding healthy tissue.

The second generation of dextran-coated magnetic nanoparticle developed for human use was the USPIO Combidex (ferumoxtran-10). Combidex is a 20 – 30 nm MNP with a single iron oxide crystalline core surrounded by a thick dextran layer. Unlike Feridex I.V., Combidex exhibits extended blood circulation and reduced RES uptake. Combidex has been used for the differentiation of lymph nodes in patients with pelvic cancers, including metastatic cancer of the prostate (10). Combidex has also had limited human use for imaging inflamed atherosclerotic plaques (11). At the time of writing, Combidex has not received FDA approval because it has failed to provide sufficient statistical demonstration of the efficacy and has requested additional clinical trials to obtain approval. AMAG Pharmaceuticals, Inc. currently has no plans to sponsor additional clinical studies of Combidex (12) (Table 4.1).

Another formulation of dextran USPIO has been heavily utilized in preclinical imaging. Known as cross-linked iron oxide (CLIO) nanoparticles (13), this formulation features a highly stabilized dextran coating (Figure 4.2). The crosslinked coating prevents dissociation of dextran from the nanoparticles core and increases the blood half-life (14). The particles can be further derivatized using ammonia to produce amine groups on crosslinked coating, allow a site for conjugation of various targeting and reporter molecules (15).

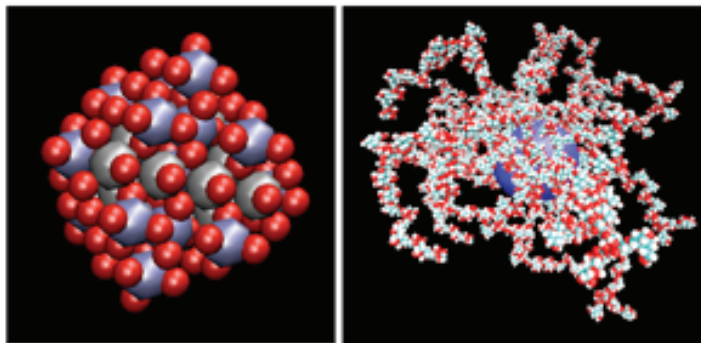


Figure 4.2: Crosslinked iron oxide (CLIO) magnetic nanoparticle⁽¹⁶⁾. Right. The iron oxide core ($[\text{Fe}_2\text{O}_3]_m[\text{Fe}_3\text{O}_4]_n$), shown on the left, is an inverse spinel structured crystal with a diameter ranging from 4 – 5 nm in diameter. Left. The crystalline core is coated with 27 ± 6 crosslinked dextran molecules (10 kD each), making the final particle 27% iron and 57% dextran by weight (respectively).

Crosslinked iron oxide nanoparticles have notable disadvantages in terms of potential human use. The compound used to crosslink dextran molecules on the particle coat is the reactive epoxide epichlorohydrin, a highly toxic compound and a known carcinogen. Another drawback is the extreme persistence of the crosslinked stabilized dextran coating. The iron oxide core of CLIO will eventually be dissolved *in vivo*, however a nondegradable crosslinked dextran shell will remain (17). These characteristics prevent CLIO from being used in human subjects and limit its application to pre-clinical *in vivo* molecular imaging studies.

4.2 Nanoparticle Selection and Modification

We chose to go forward with dextran-coated USPIO for the development of dual modality nanoparticles for PET/MRI due to their stability, variety, commercial availability, and their widespread use in the literature. The nanoparticle platform originally chosen was a dextran coated USPIO manufactured by Micromod Partikeltechnologie GmbH (Rostock-Warnemünde, Germany). Micromod produces magnetic nanoparticles with a variety of sizes (20 nm to micron-sized) and surface functionalities including functional groups ($-\text{COOH}$, $-\text{NH}_2$, $-\text{C18}$) and

biomolecules (streptavidin, biotin, protein A). Additionally, Micromod magnetic nanoparticles have been cited widely in the relevant literature (18-22). Attempts were made to dye label both amine and carboxyl functionalized 20 and 50 nm USPIOs from Micromod Partikeltechnologie. No dye labeling was observed in either case (Figure 4.3B). The reactive dye itself was not responsible for the lack of labeling, as verified through successful labeling of bovine serum albumin protein labeling. The particles were then subjected to zeta potential measurement to evaluate the presence of charged amino and carboxylic acid functional groups (Figure 4.3A). Zeta potential measurements were performed using a Nicomp 380 ZLS manufactured by Particles Sizing Systems (Santa Barbara, CA). Carboxylic acid-functionalized beads from Invitrogen (FluorSpheres) were used as a positive control.

Micromod Partikeltechnologie research scientist Dr. Cordula Gruettner was contacted to discuss the lack of charge and reactive potential of their USPIOs. Zeta potential measurements showing the lack of charge on Micromod USPIOs were sent to Dr. Gruettner. Dr. Gruettner sent additional USPIO samples, free of charge, to Georgia Tech. Unfortunately these particles also lacked surface charge and ability to conjugate with proteins and dyes. At this point a decision was made to abandon Micromod Partikeltechnologie USPIOs and pursue other magnetic nanoparticle sources.

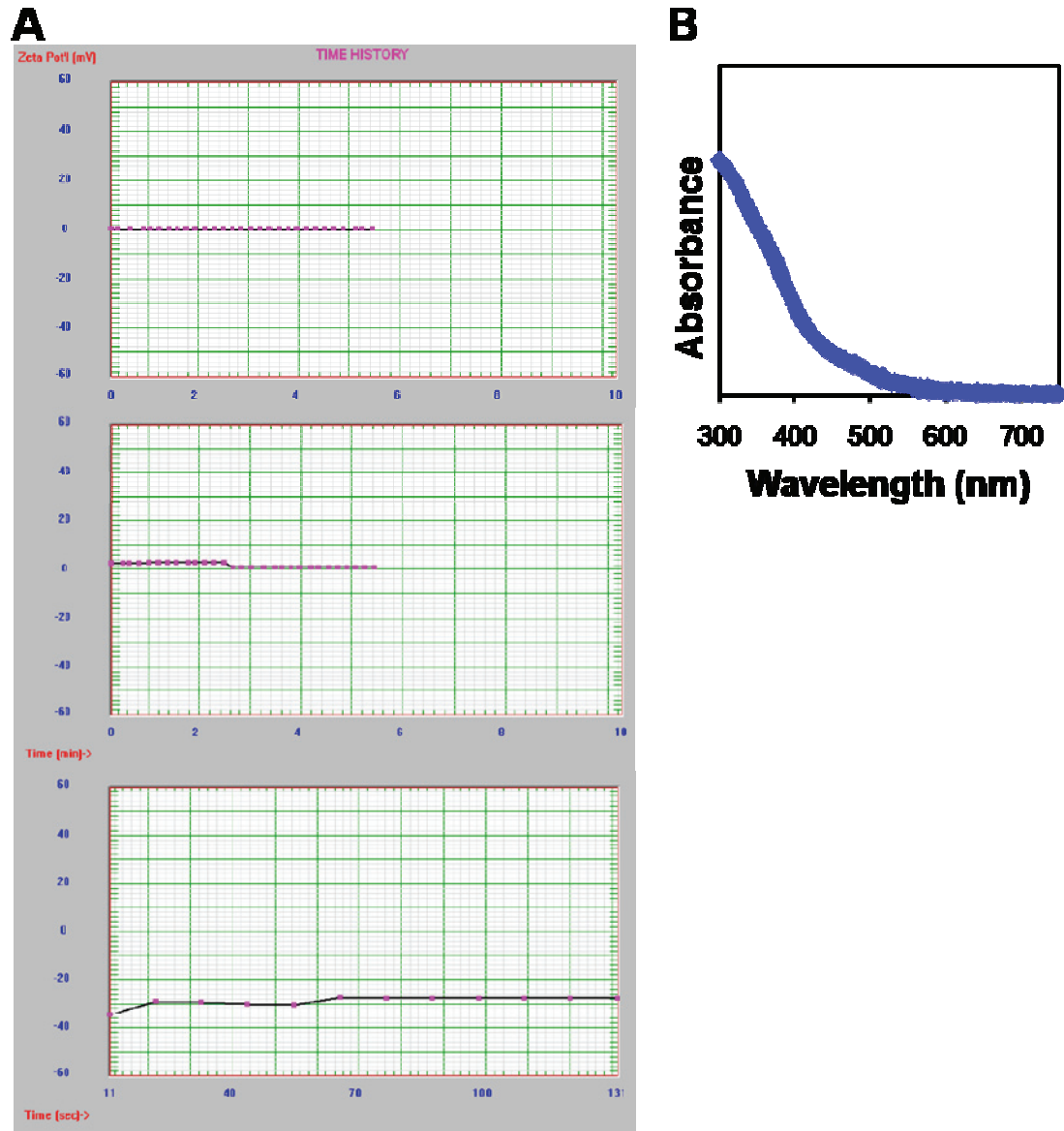


Figure 4.3: Characterization of USPIOs from Micromod Partikeltechnologie GmbH. (A) Zeta potential measurement of 20 nm carboxyl (top) and amine (middle) functionalized UPSIOs, as well as carboxyl-functionalized beads (bottom) used as a control. (B) Failure of Micromod 20 nm amino-USPIO to label with amine reactive NHS-ester Alexa Fluor 488 ($Abs_{max} = 493 \text{ nm}$)

Amine-functionalized crosslinked iron oxide (CLIO) nanoparticles were purchased from BioPAL, Inc. The particle is a Molday-type superparamagnetic iron oxide nanoparticles that has been crosslinked with epichlorohydrin and aminated with ammonia. The particles have a hydrodynamic diameter of 25 – 30 nm. The particles were tested for surface amines using the

ninhydrin assay and by conjugation with an amine-reactive dye. The surface potential of amino-CLIO in solution was measured using the NICOMP 380 phase analysis light scattering (PALS) module. Electrophoretic mobility (μ) was measured and ξ -potential was calculated using the Smoluchowski equation. Amino-CLIO was found to have a zeta potential of ≈ 35 mV (Figure 4.4C). The particles were evaluated for their ability to react with fluorophores under standard bioconjugation conditions. Particles were able to label with various levels of near infrared dye (Figure 4.4A). Also, particles could be labeled at multiple concentrations with multiple dyes (Figure 4.4B). These experiments established BioPAL amino-CLIO as useful nanoparticle platform for bioconjugations, with the ability to link multiple species to the particle coating.

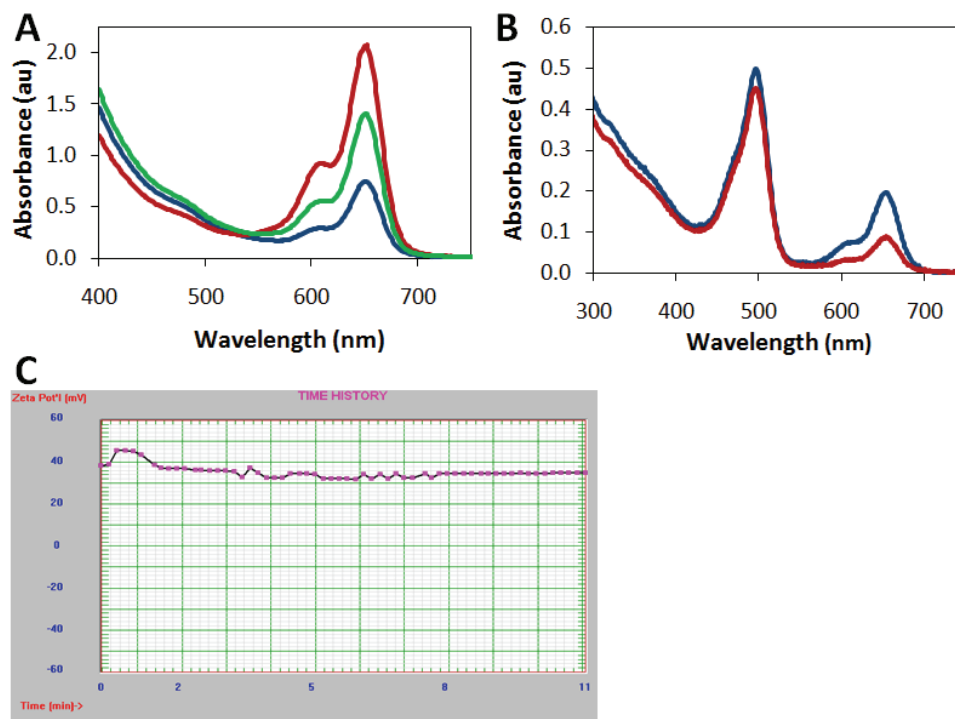


Figure 4.4: Characterization of amino-CLIO. (A) Amino-CLIO could be conjugated with varying amounts of NIR dye (Alexa Fluor 647) in a controlled fashion. Dye labeling is shown for 3 concentrations (high, red; medium, green; low, blue) (B) Amino-CLIO could be labeled with multiple fluorescent dyes at different concentrations (Alexa 488, Abs = 493 nm; Alexa 647, Abs = 651 nm; high concentration, blue; low concentration, red). This shows that multiple moieties can be linked the particle coating (necessary for linking both binding ligands and radiolabel chelators to the same nanoparticle).

4.2.1 Nanoparticle PEGylation

When nanoparticles are administered intravenously, circulating blood proteins (known as opsonins) bind to the surface of the nanoparticles. Opsonins generally bind to nanoparticles in a nonspecific fashion. The binding is often due to the presence of charge or hydrophobic features on the nanoparticle surface. When circulating nanoparticles are bound by opsonins, they are removed from the blood by organs of the reticuloendothelial system (e.g. liver, spleen). The rapid removal of nanoparticles from circulation has deleterious effect on the ability of particles to target biological molecules of interest.

A common method to mitigate this behavior is modification of nanoparticles with polyethylene glycol. Polyethylene glycol (PEG) is highly flexible and hydrophilic. PEG is known to prevent the adsorption of protein by shielding surfaces through steric crowding (i.e. physical exclusion). When nanoparticles (e.g. liposomes, quantum dots, superparamagnetic iron oxide) are coated with PEG a marked extension in the circulation half-life is observed. This occurs because opsonins are prevented from binding, and nanoparticle clearance by the liver is slowed.

The crosslinked dextran coating on CLIO much works like PEG to reduce RES uptake. The baseline opsonization of CLIO is already lower than most classes of nanoparticles due to the presence of stabilized dextran. Another common use of PEG is to provide a flexible linker for tethering binding ligands. This acts to push the ligand away from the particle surface, decreasing any steric interference with ligand binding caused by the particle. The flexibility also allows free motion of the ligand and increases the number of conformational states (i.e. entropy). The increased freedom of motion more easily allows the ligand to form an encounter complex with its target. Therefore, the primary reason we chose to PEGylate CLIO was to have a flexible linker for the targeting ligand. The secondary reason we chose to modify our

nanoparticle with PEG to slow blood clearance and minimize off-target accumulation in organ such as the liver and spleen.

An experiment was designed to measure the decrease in serum protein absorption onto nanoparticles due to PEGylation (Figure 4.5). Amine-modified cross-linked iron oxide magnetic nanoparticles (MNP) were suspended in 100 mM PBS, pH 8. The near infrared dye Alexa Fluor 647 was used to label MNPs. Lyophilized methoxy-PEG₁₂ NHS-ester (Pierce Biotechnology) was solubilized in DMSO at 250 mM. An aliquot of the PEG solution was added to amino-CLIO-A647 nanoparticles suspended in 100 mM PBS (1000:1 molar ratio) (separately, a portion of dye-labeled amino-CLIO was set aside for comparison and received no PEG). The NHS-ester of the PEG reacted with the amine groups on the surface of the nanoparticles for 1 hr at room temperature. Excess PEG was removed using size exclusion chromatography.

To measure the decrease in serum protein absorption onto nanoparticles due to PEGylation, mouse serum was added to PEGylated or unPEGylated CLIO and incubated at 37 °C for 60 min. An aliquot of each sample was separately ultracentrifuged in 10 – 30% glycerol gradient. During ultracentrifugation, nanoparticles pellet through the gradient more quickly than the mouse plasma proteins. The nanoparticle pellet was recovered from each sample and resuspended in 10 nM PBS. The absorption at 651 nm was measured, and the particle concentration was adjusted so that the PEGylated and non-PEGylated nanoparticles were at the identical concentration. To determine the amount of protein absorbed on to each nanoparticle, an aliquot from each was subjected to protein measurement using a bicinchoninic acid (BCA) assay (Pierce Biotechnology). The results of this assay, shown in Figure 4.5, showed a 44% decrease in protein absorption due to PEGylation.

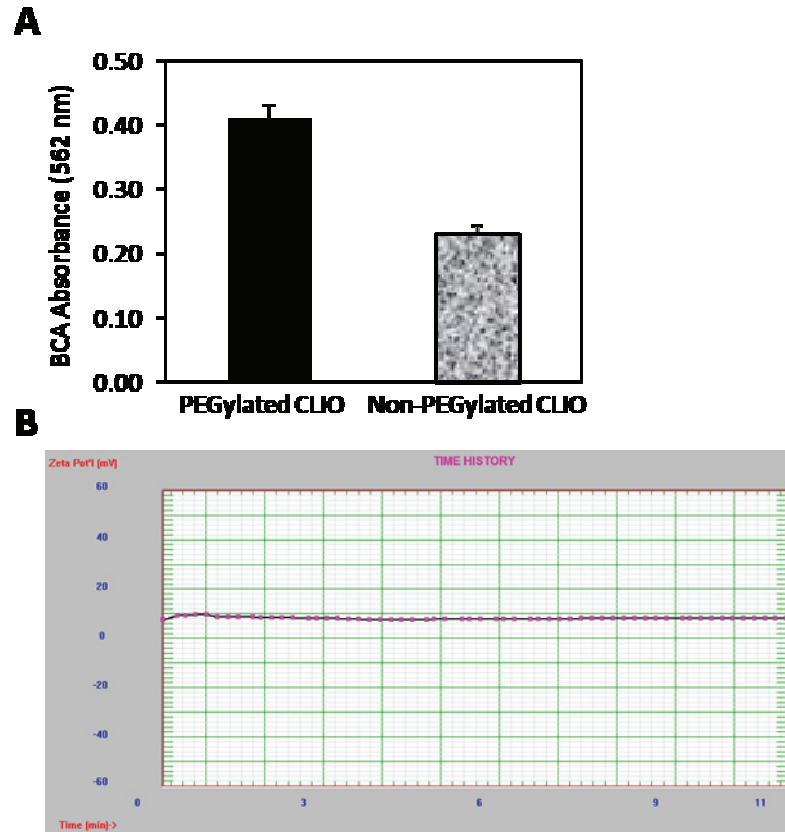


Figure 4.5: The effect of CLIO PEGylation on serum protein absorption. (A) Pegylation of CLIO resulted in a 44% decrease in protein absorption (as measured by microBCA assay) relative to non-pegylated nanoparticles. (B) The surface charge of amino-CLIO dropped from 35 mV to 8 mV upon pegylation.

4.3 Development of $\alpha_v\beta_3$ Integrin Targeting System

4.3.1 Tumor Angiogenesis and the Role for Molecular Imaging

Angiogenesis is the formation of new blood vessels from preexisting vessels and is a hallmark of tumor growth (23). Angiogenesis is controlled primarily by growth factors such as vascular endothelial growth factor, fibroblast growth factor, epidermal growth factor (24). Unlike physiologic angiogenesis, cancer-associated angiogenesis produces irregular vascular growth patterns, altered blood flow and pressure, and increase vascular permeability (25).

Integrins are a family of heterodimeric adhesion molecules consisting of pairs of α and β subunits (26). Integrin signaling plays an important role in angiogenesis and cancer metastasis (27, 28). Angiogenic endothelial cells express integrins. Cancer cells express integrin to allow movement through blood vessels and other tissues by binding to ECM proteins. The $\alpha_v\beta_3$ integrin binds to the arginine-glycine-aspartic acid (RGD) containing ECM proteins vitronectin, fibronectin, and thrombospondin (29).

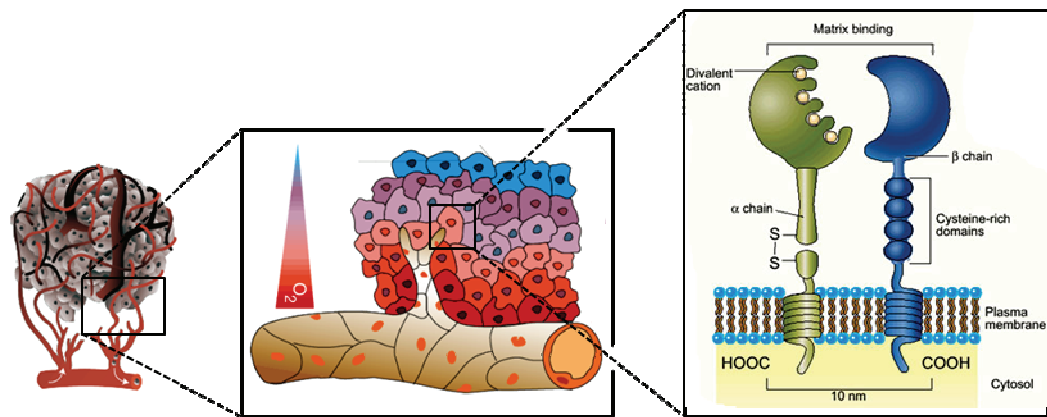


Figure 4.6: Tumor angiogenesis and the role of $\alpha_v\beta_3$ integrin. (Left) Newly formed (angiogenic) form to support the growing tumor mass. (Center) The interior of tumors is generally a low-oxygen environment. This prompts tumor cells to release pro-angiogenic growth factors, leading to the formation of new capillaries and vessels. (Right) Integrin $\alpha_v\beta_3$ is found on nascent blood vessels and is present on the surface of many tumors with metastatic potential.

Integrin $\alpha_v\beta_3$ is overexpressed in several human cancers such as glioma (30), ovarian cancer (31), and melanoma (32). Several anti- $\alpha_v\beta_3$ therapeutics exist, such as the humanized monoclonal antibody Abegrin[®] (etaracizumab), and the cyclic RGDfV peptide Cilengitide (EMD 121974) from Merck. Because therapeutics exist, early detection of $\alpha_v\beta_3$ -positive tumors could impact the survival rate for patients. Additionally, $\alpha_v\beta_3$ integrin is one of the most extensively studied integrins. Together, these aspects make $\alpha_v\beta_3$ integrin an attractive target for molecular imaging.

4.3.2 Selection and *In Vitro* Characterization of Cell Lines for $\alpha_v\beta_3$ Integrin Targeting

The $\alpha_v\beta_3$ integrin-overexpressing U87MG human glioblastoma cell line was chosen for *in vitro* assays (33, 34). This cell line has been used extensively for RGD-targeting of $\alpha_v\beta_3$ integrin (30, 35, 36). The MCF-7 human mammary gland adenocarcinoma cell line was chosen as a $\alpha_v\beta_3$ integrin-negative control (37, 38).

We performed immunofluorescence microscopy to confirm the high expression of $\alpha_v\beta_3$ integrin by U87MG as well as the low expression of $\alpha_v\beta_3$ integrin reported for MFC-7. Integrin $\alpha_v\beta_3$ positive U87MG and integrin $\alpha_v\beta_3$ negative MCF7 cells were cultured according to the supplier recommendations in an 8-well LabTek II Chambered #1.5 Coverglass culture plates (Nunc) containing low glucose DMEM (Invitrogen). The growth medium was supplemented with 10% fetal bovine serum (FBS, supplied by ATCC), 100 units/mL penicillin and 100 mg/mL streptomycin (Gibco) in a 5% CO₂ incubator at 37°C.

First, U-87 MG cells and MCF7 cells were treated with the mouse anti-human $\alpha_v\beta_3$ primary monoclonal antibody (clone LM609) by removing supernatant media and replacing it with full growth media containing anti- $\alpha_v\beta_3$ at a 5 $\mu\text{g}/\text{mL}$. The primary antibody was incubated on cells for 30 min at 37°C, followed by 3 five-minute washes with PBS. The cells were then incubated with a 1:100 dilution of goat anti-mouse an Alexa Fluor 647-labeled secondary antibody (Invitrogen) for 30 min at 37°C. The cells were washed 3 times for 5 minutes each with PBS. Phenol red-free OptiMEM imaging media (Invitrogen) was then added to the well to facilitate microscopy imaging. U87MG cells that received the dye-labeled secondary antibody, but not the anti- $\alpha_v\beta_3$ primary antibody, were used as a control. Epifluorescent images were acquired using a Zeiss Axiovert 100 microscope equipped with a Pico CoolSnap cooled CCD camera.

We found that U87MG cells expressed high levels of $\alpha_v\beta_3$ integrin, as determined by immunofluorescent staining (Figure 4.7). Only background fluorescence was observed from cells treated with secondary antibody only. MCF-7 cells expressed no detectable amount of surface $\alpha_v\beta_3$ integrin. The fluorescence of MCF-7 was comparable to that of background fluorescence.

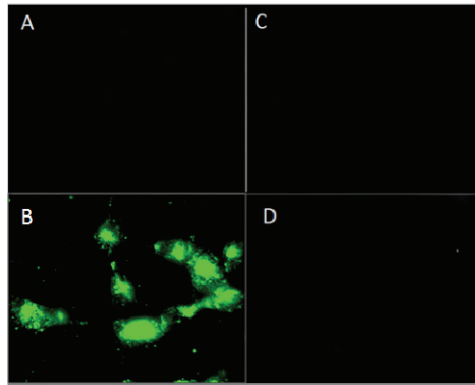


Figure 4.7: Two-step immunofluorescence staining of $\alpha_v\beta_3$ integrin expression. (A, B) U87MG cells were stained with dye-labeled secondary antibody alone (A) or with both primary and dye-labeled secondary antibodies (B). From this we can confirm that U87MG cells express high levels of surface $\alpha_v\beta_3$ integrin. (C, D) MCF7 cells stained with dye-labeled secondary antibody only (C) or primary plus dye-labeled secondary antibody (D) displayed fluorescence above background level, indicating an absence of surface $\alpha_v\beta_3$ integrin expression.

Flow cytometry was performed to allow a quantitative comparison of the surface $\alpha_v\beta_3$ integrin expression level on U87MG and MCF-7 cells. U87MG and MCF-7 cells grown in T-75 flasks using low glucose DMEM, 10% FBS, 100 units/mL penicillin and 100 mg/mL streptomycin in a 5% CO₂ incubator at 37°C. Cells were detached from flasks using a non-enzymatic method (Cell Dissociation Buffer, Gibco) to prevent proteolysis of surface integrins. Detached cells were pelleted, washed twice with PBS containing 2% goat serum, and filtered through a 40 micron nylon mesh. LM609 anti- $\alpha_v\beta_3$ primary antibody was added (10 μ g/mL) and the cells were incubated for on ice for 1 hr. Cells were washed three times with PBS containing 2% goat serum

followed by incubation with a goat anti-mouse Alexa Fluor 647-labeled secondary antibody (1:100 dilution) on ice for 60 minutes. Cells were then washed three times with PBS containing 2% goat serum to remove excess fluorescent secondary antibody. Cells incubated with dye-labeled secondary antibody, but not the anti- $\alpha_v\beta_3$ primary antibody, were used as a control. Cells were counted using a hemocytometer and resuspended at 2.5×10^6 cells/mL.

Samples were analyzed using a BD LSR II digital flow cytometer (BD Biosciences) using a 633 nm laser and emission was collected using a APC bandpass filter (660/20 nm). Scattering from untreated cells (no primary or dye-labeled secondary antibodies added) was also measured. Ten thousand events were scored for each sample.

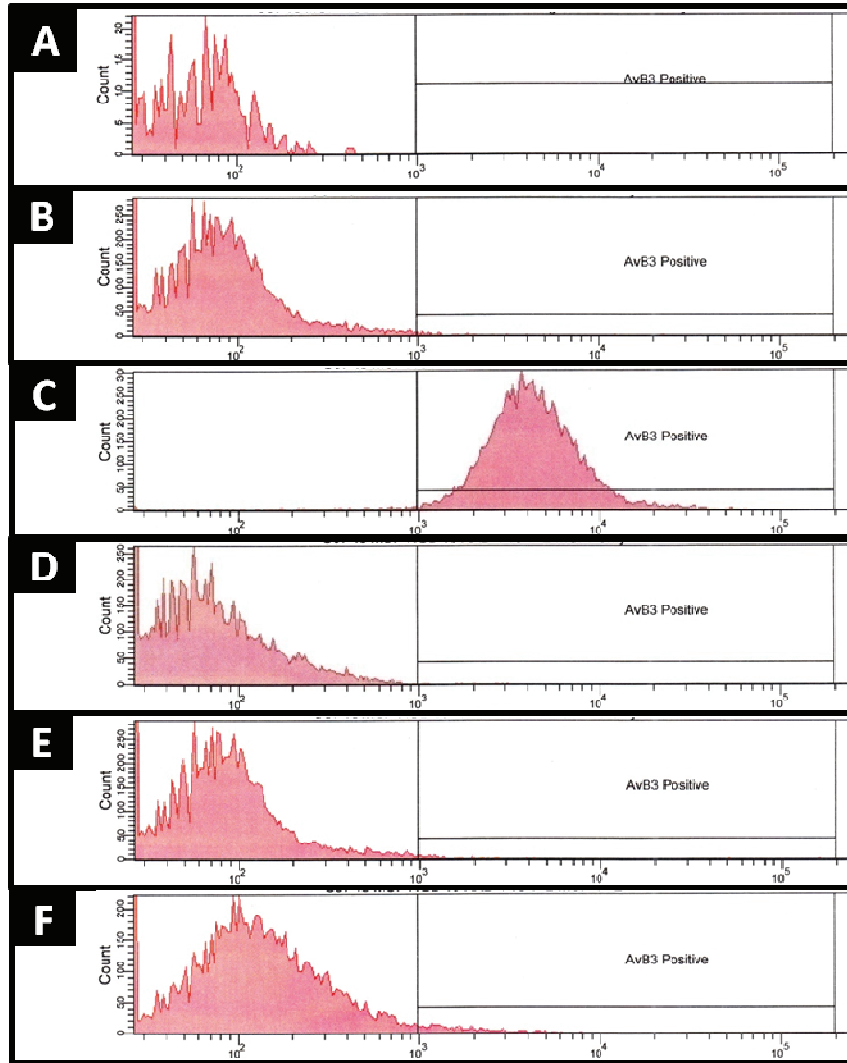


Figure 4.8: Comparison of U87MG and MCF-7 $\alpha_v\beta_3$ integrin expression level by flow cytometry. (A-C) U87MG cells were measured alone (A), after treatment with dye-labeled secondary antibody only (B), and after treatment with anti- $\alpha_v\beta_3$ primary and dye-labeled secondary antibodies (C). A clear shift due to the presence of surface $\alpha_v\beta_3$ integrin is observed. (D-F) MCF-7 cells were measured alone (D), after treatment with dye-labeled secondary antibody only (E), and after treatment with anti- $\alpha_v\beta_3$ primary and dye-labeled secondary antibodies (F). No appreciable amount of $\alpha_v\beta_3$ integrin expression was detected.

Flow cytometry analysis of surface $\alpha_v\beta_3$ integrin expression on U87MG is shown in Figure 4.8, A-C. Addition of a dye-labeled secondary antibody (Figure 4.8B) only shifted 0.6 % of measured scattering events into the high scattering region designated $\alpha_v\beta_3$ integrin positive (relative to the baseline scattering of unlabeled cells, Figure 4.8A). Compared to the natural scattering of

unlabeled cells, treatment with anti- $\alpha_v\beta_3$ primary and dye-labeled secondary antibodies shifted 98.5% of measured scattering events into the $\alpha_v\beta_3$ integrin-positive scattering region (Figure 4.8C). This indicates that nearly all U87MG cells express a high expression level of surface $\alpha_v\beta_3$ integrin. MCF-7 cells (Figure 4.8, D-F) also showed a shift of 0.6 % of measured scattering events into the $\alpha_v\beta_3$ integrin positive scattering region upon treatment with Alexa 647-labeled secondary antibody (Figure 4.8E). Treatment with both anti- $\alpha_v\beta_3$ primary and dye-labeled secondary antibodies shifted 2.4% of measured scattering events into the $\alpha_v\beta_3$ integrin-positive scattering region (Figure 4.8F). This indicates that nearly all MCF-7 cells express a low expression level of surface $\alpha_v\beta_3$ integrin. Furthermore, it is highly likely the 2.4% shift observed is due to nonspecific absorption instead of actual surface $\alpha_v\beta_3$ integrin expression.

4.3.3 In Vitro Nanoparticle Targeting to Cell Surface $\alpha_v\beta_3$ Integrin Using Monoclonal

Antibodies

After differential expression of $\alpha_v\beta_3$ integrin by U87MG and MCF-7 cells was confirmed, a pilot nanoparticle binding experiment was performed. The purpose of the experiment was to ensure that CLIO magnetic nanoparticles could bind to $\alpha_v\beta_3$ integrin in a physiologically authentic *in vitro* environment. Steric effects (i.e. physical crowding) from nanoparticles and their coatings have been known to have deleterious effects in ligand binding. Therefore, we performed these experiments to ensure that our particles could actually bind to their target on the surface of living cells. To achieve targeting, antibody fragments were conjugated to aminated, dextran-coated magnetic nanoparticles according to published procedures (39, 40).

Briefly, 1mg of goat anti-mouse secondary antibody (Sigma) was suspended in 10 mM PBS at a concentration of 10mg/mL. The reducing agent 2-mercaptoethylamine (MEA) was added to the antibody solution at a final concentration of 50 mM. The solution was placed in a

37 °C water bath for 90 minutes. 2-MEA reduces disulfide bonds in the hinge region of antibodies, leaving exposed thiol groups on the fragmented antibodies available bioconjugation. Meanwhile, Alexa Fluor 647-labeled aminated dextran particles (10 mg Fe/mL) were reacted with 10 mM sulfo-SMCC in 100 mM PBS, pH 7.5 for 90 minutes. After the 90 minute incubation, the sulfo-SMCC activated particles and the reduced antibody were separately desalted using spin desalt columns to remove excess sulfo-SMCC and 2-MEA, respectively. The nanoparticles and reduced secondary antibody were combined, antibody fragments being in excess, and allowed to react overnight at 4°C. A diagram of this reaction scheme is shown in Figure 4.9.

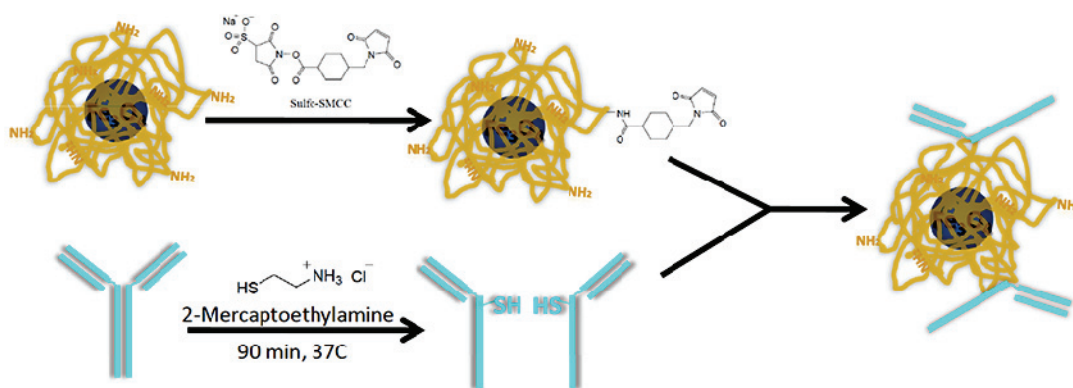


Figure 4.9: Reaction scheme for conjugating antibody fragments with aminated dextran-coated magnetic nanoparticles.

The solution was then applied to a Sephacryl-300 size exclusion chromatography (SEC) column and antibody-conjugated nanoparticles were separated from unreacted antibody fragments using an Aktä Prime FPLC (GE Lifesciences) equipped with a UV detector. The mobile phase used was 10 mM PBS (pH 7.4) with a flow rate of 0.5 mL/min. The antibody-nanoparticle conjugate eluted first, followed by the antibody fragments.

The specificity of the antibody conjugated magnetic particles *in vitro* was then evaluated using live-cell imaging experiments. Integrin $\alpha_v\beta_3$ -positive U87MG and Integrin $\alpha_v\beta_3$ -

negative MCF-7 cells were cultured LabTek II Chambered Coverglass (#1.5) plates containing DMEM (Sigma) with 10% FBS (ATCC), 100 units/mL penicillin and 100 mg/mL streptomycin (Gibco) in a 5% CO₂ incubator at 37°C.

First, U87MG cells and MCF-7 cells were treated with the $\alpha_v\beta_3$ integrin-binding LM609 primary antibody at a 5 $\mu\text{g}/\text{mL}$ concentration 30 min at 37°C. The cells were then washed 3 times with normal culture media. The dye- and antibody-labeled nanoparticle probes were then added to cells at a 200nM dye concentration and allowed to bind for 30 min at 37°C. Excess probe was removed by washing 3 times with normal culture media and the cells were placed in phenol red-free OptiMEM imaging media. Cells that did not receive the primary antibody were used as a control. Epifluorescent images were acquired using a Zeiss Axiovert 200 microscope equipped with a Zeiss AxioCam MRm cooled CCD camera. Nanoparticles conjugated with antibody fragments were able to bind to $\alpha_v\beta_3$ integrin-positive U87MG cells, while $\alpha_v\beta_3$ integrin negative MCF-7 cells treated with nanoparticles produce no signal above background (Figure 4.10).

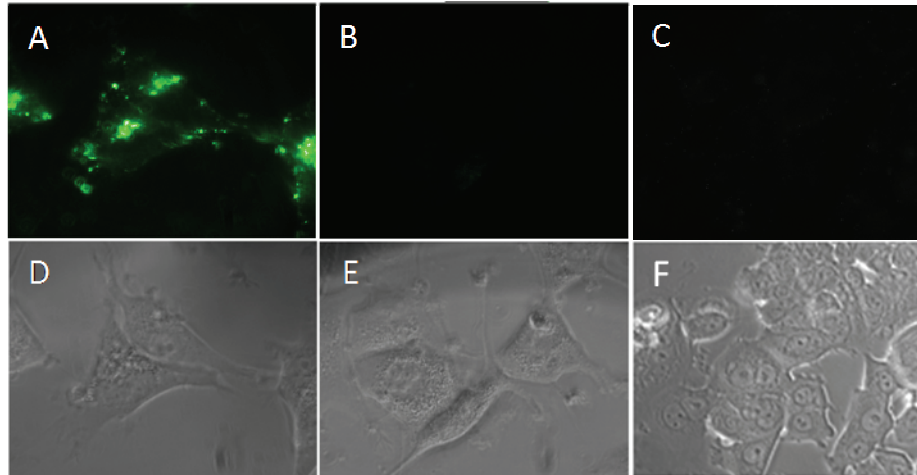


Figure 4.10: Imaging $\alpha_v\beta_3$ integrin using nanoparticles targeted with antibody fragments. (A) U87MG cells imaged using Alexa Fluor 647 labeled nanoparticles conjugated with secondary antibody fragment pretreated with anti- $\alpha_v\beta_3$ primary antibody. Imaging of $\alpha_v\beta_3$ integrin is clearly observed. (B) Cells treated with dye-labeled, secondary antibody-conjugated nanoparticles that did not receive pretreatment with anti- $\alpha_v\beta_3$ primary antibody showed no signal. (C) Fluorescence imaging of $\alpha_v\beta_3$ integrin-negative MCF-7 cells that were treated with anti- $\alpha_v\beta_3$ primary antibody and secondary antibody-conjugated nanoparticles. Bottom row shows corresponding white light images.

LM609 was chosen because for these preliminary studies because it high affinity and specificity for the $\alpha_v\beta_3$ heterodimer (41, 42) as well as clinical relevance: the humanized form of LM609, Abegrin (etaracizumab), is currently in Phase II clinical trials, www.ClinicalTrials.gov (43). Large amounts of antibody (tens of milligrams) are typically required for *in vivo* nanoparticle imaging. Unfortunately the cost of commercially available mouse anti-human $\alpha_v\beta_3$ integrin antibody LM609 is \$3,000/mg (Chemicon). I requested the murine hybridoma to produce LM609 from the ATCC Patent Depository (HB-9537) and was eventually provided with it. The cells had been frozen in 1986 by the inventor (David Cheresch) and were difficult to culture. Dr. Robert Mittler, director of the Yerkes Hybridoma core, was contacted to produce the antibody. The Cheresch hybridoma protocol from ATCC was as follows:

1. DMEM
2. 10% NCTC Medium

3. 1 mM cis-oxaloacetate
4. 0.45 mM Sodium pyruvate
5. 2 mM L-glutamine
6. Penicillin (10,000 units/mL) and streptomycin (10 mg/mL)
7. 20% FBS
8. 20 mM HEPES
9. 1 mM Hypoxanthine
10. 0.3 mM Thymidine
11. Fungizone (250 µg/mL)

(Cell concentration should be kept between 2.5×10^5 and 1.5×10^5 cells/mL)

Unfortunately the first few tries at thawing and culturing the hybridomas proved unsuccessful. Additionally, working with Dr. Mittler was problematical as he was unable to deliver according to the timeline we agreed to. A decision was made to forego use of LM609 to target the nanoparticles, opting to use integrin-binding peptides instead.

4.3.4 Selection of Integrin Binding RGD Peptide

Small peptides containing the arginine-glycine-aspartate (RGD) sequence bind to $\alpha_v\beta_3$ integrin (44-48) and inhibit angiogenesis (27, 28, 49, 50) in several forms of cancer. Several forms of synthetic RGD have been studied including linear RGDS (51-53), RDG peptides cyclized via internal disulfide bonds (i.e. RGD-4C) (54, 55), and RGD peptides formed from lactam-type (head-tail) cyclization (56-59). In general, the binding affinity of structurally constrained head-tail cyclized RGD and RGD-4C to $\alpha_v\beta_3$ integrin (IC_{50} , 1 – 100 nM) is 10 – 100 times greater than that of linear peptides (58, 60-62).

Head-tail cyclized RGD peptides are more chemically stable than peptides with internal disulfide bonds such as RGD-4C, which can be reduced to lower affinity the linear form. Cyclic peptides are more resistant proteolysis by being impervious to hydrolysis by all exopeptidases and most endopeptidases. Additionally, cyclic peptides can be produced using modern, automated peptide synthesis techniques to create large batches at a lower cost. The general structure of these peptides is: cyclo(RGD \mathbf{X} Z) (63, 64), where \mathbf{X} represents a D-stereoisomer of an amino acid, generally the phenyl-containing D-phenylalanine (*f*), or the phenol-containing D-tyrosine (*y*). The \mathbf{Z} position accommodates amino acids with a wide range of hydrophobicity, charge, and polarity. An RGD variant with an N-methylated valine at the \mathbf{Z} position (Cilengitide, EMD 121974) has been developed by Technical University Munich in collaboration with Merck. This variant has the highest affinity for $\alpha_v\beta_3$ integrin and has been evaluated in multiple clinical trials (3 open Phase II/III trials and 14 closed Phase I/II trials) for glioma, lymphoma, androgen-independent prostate cancer, Kaposi's sarcoma, and melanoma (www.ClinicalTrials.gov, (43)). Often residues with side chains containing functional groups are inserted in this position to provide a locus for modification. Common residues selected for the \mathbf{Z} position include lysine and cysteine.

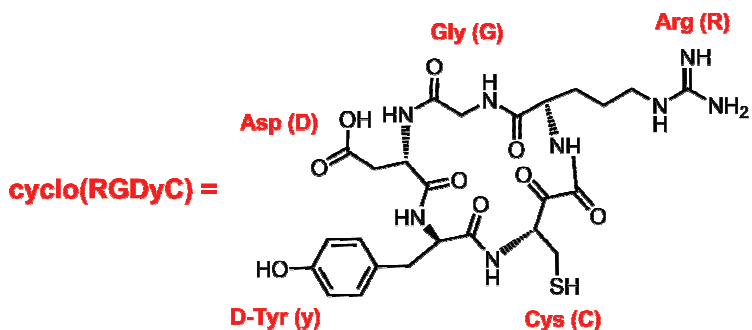


Figure 4.11: Lactam-cyclized RGD variant used for targeting magnetic nanoparticles to $\alpha_v\beta_3$ integrin. This variant is a head-tail cyclized pentapeptide consisting of: cyclo(arginine–glycine–aspartic acid–D-tyrosine–cysteine).

We selected the RGD variant cyclo(arginine–glycine–aspartic acid–D-tyrosine–cysteine) to target our magnetic nanoparticles to $\alpha_v\beta_3$ integrin (Figure 4.11). D-tyrosine was selected for the **X** position because the presence of a hydroxyl group on the phenyl ring of tyrosine makes it significantly less hydrophobic than phenylalanine (hydropathy index of -1.3 for tyrosine vs. +2.8 for phenylalanine). Cysteine was selected for the **Z** position because it contains a highly reactive thiol side chain. The magnetic nanoparticles used in this study possess an amine-modified dextran coating and thiol chemistry is widely used for conjugations of macromolecules with free amines on surface lysine residues (39).

4.3.5 In Vitro Nanoparticle Targeting to Cell Surface $\alpha_v\beta_3$ Integrin Using a Cyclic RGD Peptide

To confirm binding cyclic-RGD binding to $\alpha_v\beta_3$ integrin on U87MG cells, a dye-labeled peptide was synthesized. Cyclo(RGDyK) (Peptides International, Inc.; MW, 619; purity, 98.2%) dissolved in DMSO was reacted with the reactive fluorescent dye Alexa Fluor 488 carboxylic acid, succinimidyl ester (Invitrogen Corp.; MW, 643, mixed isomers). Dye was added to c(RGDyK) at a 10:1 molar ratio in 100 mM PBS (pH 8) with 10 mM EDTA. The reaction proceeded overnight at 4 °C. HPLC purification was used to separate unreacted Alexa Fluor 488 from dye-labeled peptide. HPLC was performed using a 250mm X 4.6mm Phenomenex Jupiter HPLC column with 4 μm beads and 300 Å pores. The solvent system used was A = 0.1% TFA on H₂O, B = 0.1% TFA in acetonitrile, starting at 5% B and ramping to 50% B at 30 min, with a constant 1 mL/min flow rate. A control peptide, cyclo(RADyK) (65), was synthesized in the same fashion.

Figure 4.12 shows chromatograms of unreacted Alexa Fluor 488 succinimidyl ester (top, t_r = 12:10, 13:00), unreacted cyclo(RGDyK) (middle, t_r = 12:50), and the dye-RGD conjugate (bottom, t_r = 15:21, 16:15). The peptide reacted with both dye isomers to yield two products

differing only by the dye isomer conjugated to the peptide. The identity of the product (MW 1136) was verified by mass spectrometry (Figure 4.13).

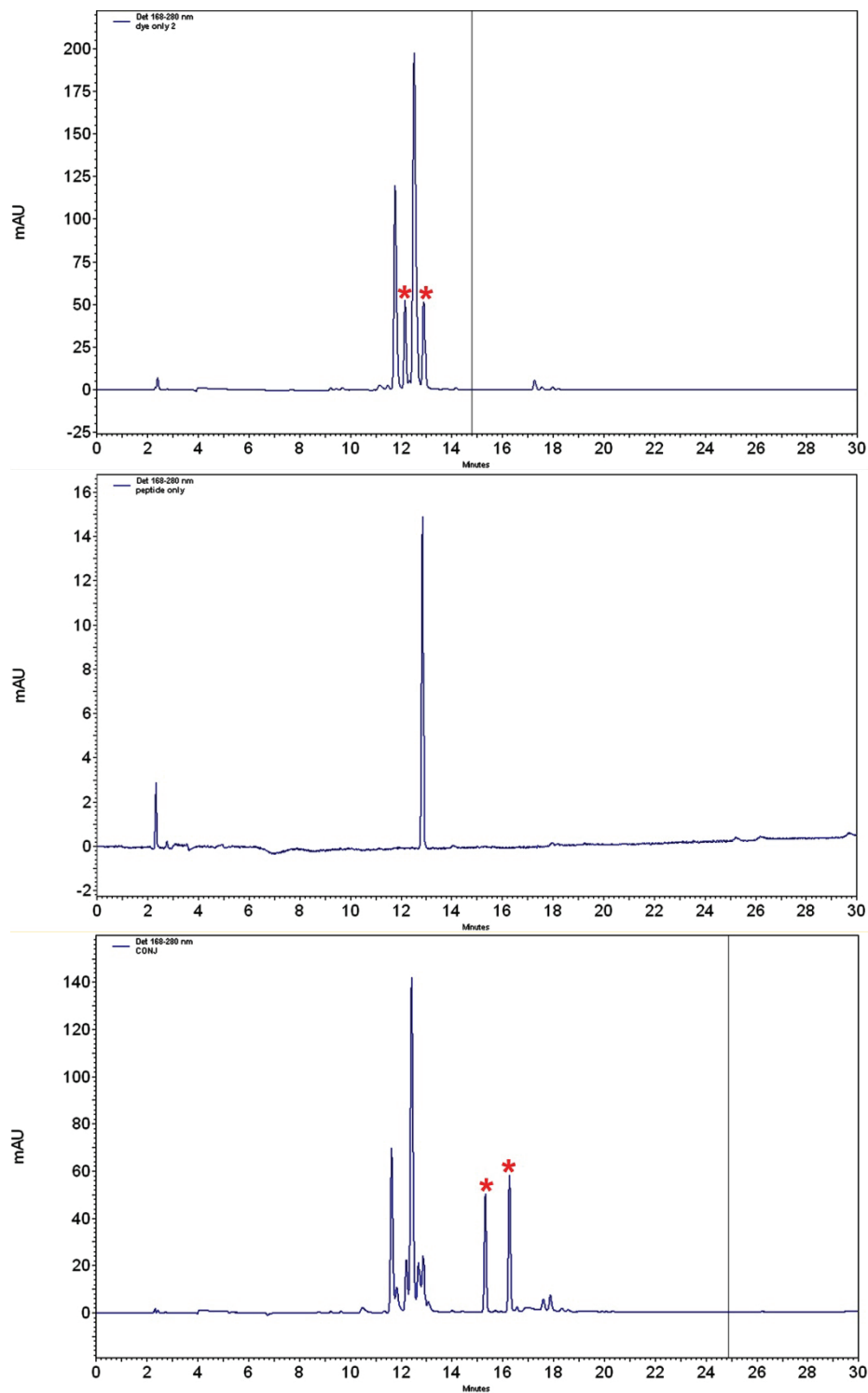


Figure 4.12: Chromatograms of c(RGDyK) reaction with maleimide–Alexa Fluor 488. (Top) Chromatogram of unreacted Alexa Fluor 488 succinimidyl ester. The two reactive dye isomers are indicated with red asterisks. (Middle) Chromatogram of unreacted cyclo(RGDyK). (Bottom) Chromatogram of dye-RGD conjugate. The peptide reacted with both dye isomers to yield two products differing only by the dye isomer conjugated to the peptide.

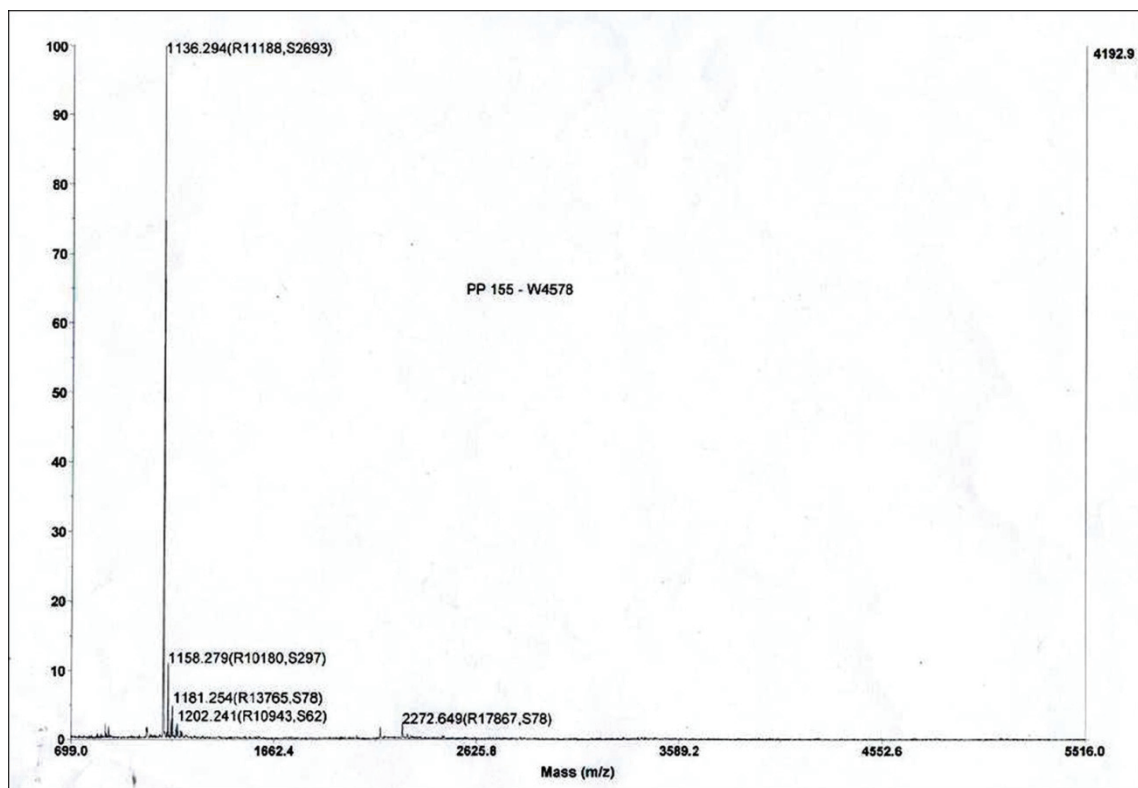


Figure 4.13: Mass spectrum of c(RGDyK)–Alexa Fluor 488 conjugate. c(RGDyK) (MW 619) was reacted with Alexa Fluor 488 succinimidyl ester (MW 643). The molecular weight of the product (minus the NHS leaving group of Alexa Fluor) is 1136.

Flow cytometry was performed to verify cyclic RGD binding to surface $\alpha_v\beta_3$ integrin on U87MG cells. U87MG cells grown in T-75 flasks using low glucose DMEM, 10% FBS, 100 units/mL penicillin and 100 mg/mL streptomycin in a 5% CO₂ incubator at 37°C. Cells were detached from flasks using a non-enzymatic method (Cell Dissociation Buffer, Gibco) to prevent proteolysis of surface integrins. Detached cells were pelleted, washed twice with PBS containing 2% goat serum, and filtered through a 40 micron nylon mesh. Alexa Fluor 488-labeled cyclo(RGDyK) peptide was added to cells (100 nM) and incubated for on ice for 1 hr. Cells were washed three times with PBS containing 2% goat serum. Cells incubated with dye-labeled secondary antibody, but not the anti- $\alpha_v\beta_3$ primary antibody, were used as a control. Cells were counted using a hemocytometer and resuspended at 2.5×10^6 cells/mL. Cells were treated with Alexa Fluor 488-

labeled cyclo(RADyK) as a control. Samples were then analyzed using a BD LSR II digital flow cytometer using a 488 nm laser with a 505 nm long pass dichroic mirror and a FITC bandpass filter (530/30). Scattering from untreated cells (no primary or dye-labeled secondary antibodies added) was also measured. Ten thousand events were scored for each sample.

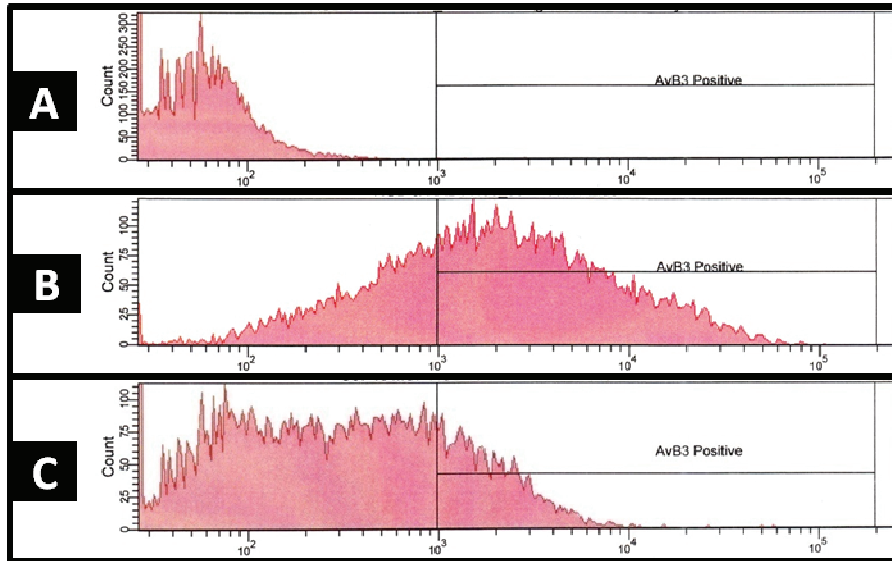


Figure 4.14: Flow cytometry analysis of fluorescent cyclo-RGD and cyclo-RAD peptides binding to $\alpha_v\beta_3$ integrin on U87MG cells. U87MG cells measured alone (A), and after treatment with an Alexa Fluor 488-labeled $\alpha_v\beta_3$ integrin-targeting cyclo(RGDyK) peptide (B). Cyclo(RGDyK) showed binding to U87MG cells, evident by the shift observed relative to untreated cells. (C) U87MG cells were measured after treatment with Alexa Fluor 488-labeled cyclo(RADyK) control peptide. A small shift was still observed using this variant.

Flow cytometry analysis of $\alpha_v\beta_3$ integrin-expressing U87MG is shown in Figure 4.14. Binding of dye-labeled RGD to U87MG cells shifted 68.5 % of measured scattering events into the high scattering region (Figure 4.14B) (relative to the baseline scattering of unlabeled cells, Figure 4.14A). This is lower than the shift produced by LM609 antibody in the previous experiment; however this is to be expected. In the previous experiment $\alpha_v\beta_3$ integrin on the cell surface was bound by the LM609 primary antibody, which was in turn bound by multiple secondary

antibodies, each of which carries ≈ 6 dyes. Therefore the difference in absolute shift observed here is simply due to amplification typical of two-step immunofluorescence.

Surprisingly, treatment with dye-labeled RAD shifted 21.7 % of measured scattering events into the high scattering region (Figure 4.14C). We expected to see a minor shift (e.g. < 5%) due to nonspecific scattering common after the addition of any dye-labeled species. However the 21.7% shift observed here was nearly 1/3 the change produced by the specific probe. After much examination of the literature it was learned that RAD-based peptides have sometimes been reported as possessing a level of residual binding affinity for $\alpha_v\beta_3$ integrin but does not always inhibit the function of the integrins. Specifically, cyclic peptides containing the RAD domain have been found to inhibit platelet aggregation *ex vivo*, whereas linear peptides with the identical sequence produced no effect (66). In a similar study of paramagnetic liposomes targeted to $\alpha_v\beta_3$ integrin in tumor-bearing mice using cyclic RGD or cyclic RAD. Both peptides showed equal tumor accumulation in tumors (67). Others have reported linear GRGDSPK blocked $\alpha_5\beta_1$ integrin binding to fibronectin, inhibited HT1080 adhesion to fibronectin, and decreased HT1080 cell wound healing in a scratch assay, but that GRADSPK produced no such effects (68). It appears that while conformational restriction via cyclization of RGD and RAD sequences increases their affinity for $\alpha_v\beta_3$ integrin, it may also increase the likelihood of off-target binding. This makes cyclic RGD a promiscuous ligand of many integrin heterodimers. The effect of cyclization on RAD peptides may increase the affinity for $\alpha_v\beta_3$ integrin enough to promote physical association but not enough to cause receptor activation. This behavior may classify cyclic RAD as a possible $\alpha_v\beta_3$ integrin partial agonist (69).

4.4 Preparation and Evaluation of Radiolabeled Nanoparticles

Noncovalent radiolabeling of nanoparticles has many advantages. Cyclic chelators (e.g. DOTA, TETA) can be conjugated to nanoparticles and stored for later use, allowing for rapid radiolabeling on demand. Unlike conventional covalent techniques where specific atoms must be substituted, chelators can be linked to a variety of functional groups commonly found on nanoparticles (e.g. carboxyl, amine, thiol).

Radiolabeling nanoparticles with ^{64}Cu has many benefits. Copper-64 is a positron emitter (β^+ decay, 17.4%; $E_{\text{max}} = 0.653$ MeV) used for PET imaging. This isotope has been used for imaging a broad array of nanoparticles, including polymer nanostructures (70-73), quantum dots (74-76), magnetic nanoparticles (77-82), and carbon nanotubes (83). With a 12.7 hour half-life, ^{64}Cu can be used to image particles *in vivo* for up to 48 hr and can be evaluate the *ex vivo* biodistribution for 72 hours or more. In addition to positron emission, ^{64}Cu nuclides undergo β^- decay (39%; $E_{\text{max}} = 0.578$ MeV) making it a useful isotope for radiotherapy.

It is critical to avoid contamination of nanoparticle and labeling solutions with heavy metals, as most macrocyclic radioligands are avid chelators of metals (particularly divalent cations). Methods to reduce metal contaminants in conjugation and labeling reactions were recently published by Wadas et al (84). The inclusion of a spacer between the chelator and nanoparticle surface is useful for radiolabeling particles with a highly charged surface. Conversely, if the particle and radiometal ion have opposite charges, removal of electrostatically absorbed radiometals from the particle surface using competing chelators (i.e. DTPA/EDTA challenge) is necessary. Also, if Cu-binding ligands lie deep within the nanoparticle coating they may not be available to charged radiometals. A recent publication by Shokeen et al provides and extensive overview of the methods involved in radiolabeling nanoparticles (85).

4.4.1 Radiolabeling and *In Vivo* Evaluation of ⁶⁴Cu-labeled PEGylated Dextran-coated Magnetic Nanoparticles.

To produce a nanoparticle capable of producing dual PET/MRI contrast *in vivo*, we first measured the circulation half-life and organ biodistribution of ⁶⁴Cu-labeled PEGylated crosslinked dextran-coated iron oxide magnetic nanoparticles. DOTA-NHS ester was dissolved in 100 mM PBS and pH was adjusted to 7.5 by drop-wise addition of 0.5 M NaOH. An aliquot of the DOTA-NHS solution was immediately added to amino-functionalized cross-linked iron oxide nanoparticles at a molar ratio of 25:1 and the reaction was mixed for 1.5 hr at room temperature. The solution was loaded onto a desalting spin column to separate any unreacted DOTA-NHS from DOTA-conjugated magnetic nanoparticles (DOTA-MNP). NHS-ester methoxy PEG-5000 was dissolved in molecular sieve-treated DMSO and added to DOTA-MNP in 100 mM PBS (pH 7.3) at a molar ration of 1000:1. After reacting overnight at 4 °C the DOTA-magnetic nanoparticles (DOTA-MNP_{PEG}) were purified using spin columns equilibrated with 10 mM PBS, followed by filtration at 0.2 μm and storage at 4 °C. Dynamic light scattering of iron oxide nanoparticles was performed using a Particle Sizing Systems, Inc. NICOMP™ 380 ZLS.

To radiolabel DOTA-MNP_{PEG} with ⁶⁴Cu, nanoparticles were dissolved in 10 mM PBS at 2.5 mg Fe/mL prior to labeling. Nanoparticles were dissolved in 0.1 M ammonium acetate buffer (pH 5.5) and ⁶⁴Cu-acetate was added and nanoparticle samples were incubated at 37 °C for 1 hr with constant mixing. The solution was then challenged with 5 μL of 10 mM EDTA at 37 °C for 5 min with mixing (to remove nonspecifically bound ⁶⁴Cu), followed by purification using a centrifugal desalting column equilibrated with 10 mM PBS . Purity of ⁶⁴Cu-MNP_{PEG} was determined by radiochemical thin layer chromatography (radio-TLC). A small amount of the of the ⁶⁴Cu-labeled MNP solution was applied to an ITLC-SG plate (Pall Corporation, East Hills, NY) and developed using a 1:1 mixture (v/v) of 10% (w/v) ammonium acetate and methanol ($R_f = 0$

for ^{64}Cu -MNP and $R_f = 1$ for ^{64}Cu -EDTA and ^{64}Cu -acetate). The TLC plate was then measured using a Bioscan 200 imaging scanner.

Radiochemical purity (RCP) of ^{64}Cu -MNP_{PEG} was measured by radio-fast protein liquid chromatography (radio-FPLC) using an ÄKTA FLPC system equipped with a UV detector (280nm) and fitted with an in-line radioisotope detector. A 100 μL sample of dilute ^{64}Cu -MNP (ca. 10 μCi) was applied to a Superose 12 gel filtration column and eluted with 20 mM HEPES and 150 mM NaCl (pH 7.3) at a flow rate of 0.8 mL/min. The RCP of ^{64}Cu -MNP_{PEG} was to be >98%. The nanoparticle solution was then diluted in 10 mM PBS (pH 7.4) to obtain doses suitable for imaging and biodistribution studies (ca. 100 μCi).

Sixteen female BALB/c mice weighing approximately 20 g were anesthetized using 1-2 % isoflurane and given tail vein injections of 100 μCi of ^{64}Cu -MNP_{PEG} at a dose of 10 mg Fe/kg body weight. Mice ($n = 4$ per time point) were sacrificed by cervical dislocation at 10 min, 1 hr, 4 hr, and 24 hr post injection and organs of interest were collected, blotted dry, weighed, and assessed for radioactivity by counting for one minute in a gamma counter. A standard dose was prepared and measured along with the samples to allow calculation of the percentage injected dose (%ID) for the various tissues and organs. Data were corrected for ^{64}Cu decay and the percentage injected dose per gram of tissue (%ID/g) and the percentage injected dose per organ (%ID/organ) were calculated according to the following equations:

$$\%ID/g = \frac{(\text{cpm in sample} - \text{background}) \times 10^2}{(\text{decay correction factor}) \times (\text{sample weight}) \times (\text{cpm in standard dose})} \quad \text{Equation 4.1}$$

$$\%ID/\text{organ} = \frac{(\text{cpm in sample} - \text{background}) \times 10^2}{(\text{decay correction factor}) \times (\text{cpm in standard dose})} \quad \text{Equation 4.2}$$

MicroPET imaging scans were carried out using a microPET Focus 120 and. Female BALB/c mice (20-25 g) were anesthetized using 1-2 % isoflurane and given tail vein injections with 100 μ Ci of ^{64}Cu -MNP_{PEG} (10 mg Fe/kg body weight) in 100 μ L PBS. Mice were reanesthetized and imaged supine at 1 hr, 4 hr, and 24 hr post injection. PET scan collection time for the 10 min, 1 hr, and 4 hr images was 10 min, while collection time for the 24 hr image was 20 min. Computed tomography scans were performed immediately after microPET using a microCAT II. Decay-corrected microPET images were analyzed using ASIPro. Coregistration of microPET and microCT images was performed using fiducial markers in the animal transfer bed and the Amira software package.

The biodistribution of ^{64}Cu -MNP_{PEG} is shown in Figure 4.15 and Table 4.2. At ten minutes post injection the particles showed high blood concentration and relatively low uptake in RES organs. By 24 hr post injection the blood concentration remained at a modest 30.2 ± 1.1 %ID/g while liver and spleen uptake climbed to 19.7 ± 2.1 and 18.2 ± 1.3 %ID/g, respectively. From this data we concluded that the particles are able to persist in circulation for long enough to take advantage of the 12.7 hr half life of copper-64. While 30 %ID/g in the blood would produce unacceptable background for imaging at 24 hr, we have the possibility to image at 36 or 48 hrs. More importantly, we anticipated a significant increase in blood clearance upon functionalization of nanoparticles with peptides and other biomolecules. The present of additional surface charge and hydrophobic residues due to decoration of particles with peptides is sure to decrease the blood half life.

The ability to radiolabel MNP_{PEG} at high specific activity and radiochemical purity makes them well suited for PET imaging. The particles are easily conjugated with antibodies and peptides due to the presence numerous amine groups on the coating. The crosslinked surface

and PEG modification allow these nanoparticles to avoid rapid blood clearance and high RES uptake. For these reasons decided to move forward using PEGylated dextran-coated magnetic nanoparticles for dual PET/MR imaging of angiogenesis.

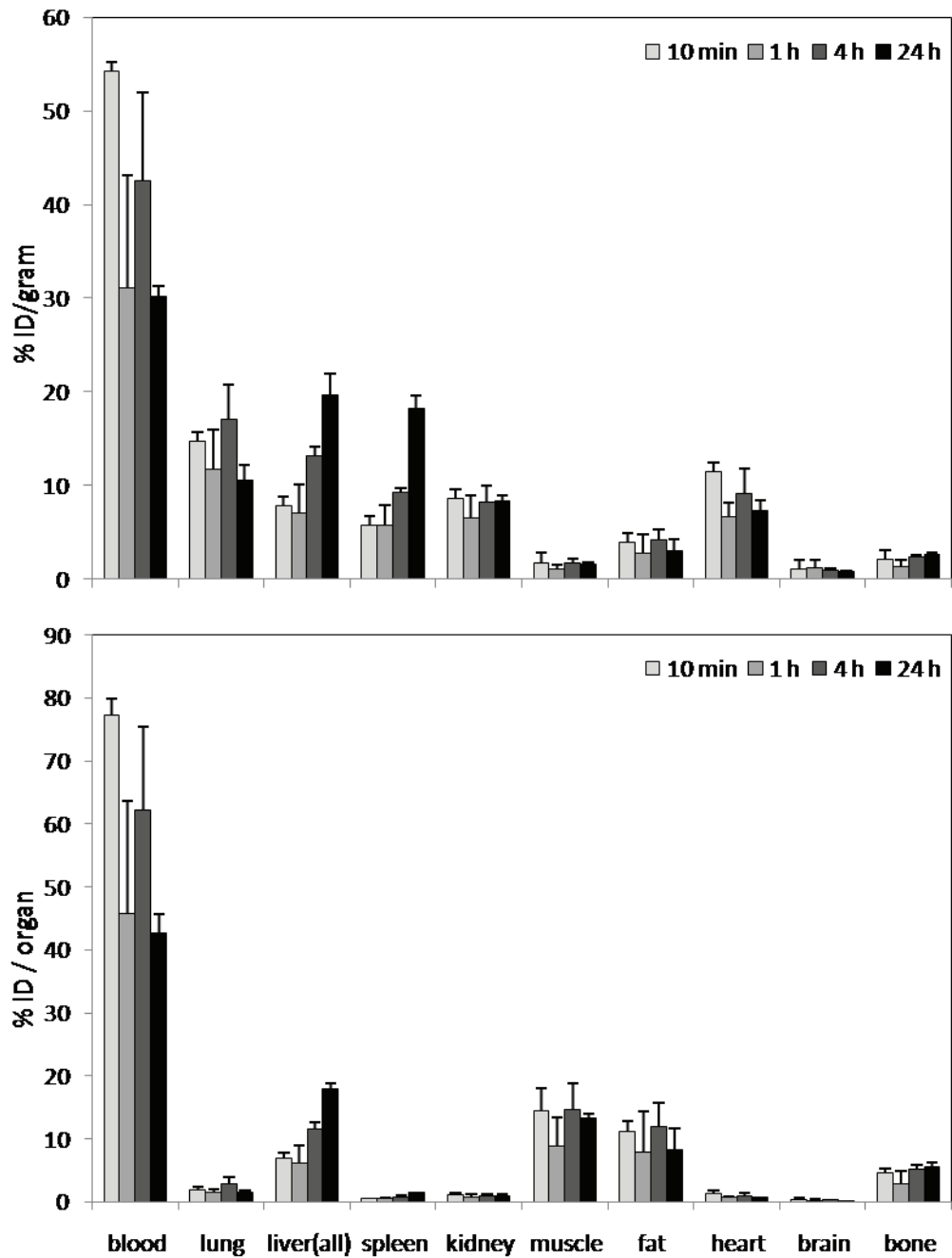


Figure 4.15: Biodistribution ^{64}Cu -labeled PEGylated Dextran-Coated Superparamagnetic Iron Oxide Nanoparticles. Data from 10 min, 1 hr, 4 hr, and 24 hr post injection are shown ($n = 4$ per time point). Data are expressed as percent injected dose per gram tissue (%ID/g, top) and percent injected dose per organ (%ID/organ, bottom) \pm one standard deviation.

Table 4.2: Biodistribution Data of ⁶⁴Cu-labeled PEGylated Dextran-Coated Superparamagnetic Iron Oxide Nanoparticles in Female Balb/C Mice (n = 4)

Biodistribution	%ID/g				%ID/organ			
	10 min	1 hr	4 hr	24 hr	10 min	1 hr	4 hr	24 hr
Blood	54.2 ± 5.5	31.1 ± 12.0	42.5 ± 9.3	30.2 ± 1.1	77.3 ± 2.6	45.8 ± 17.8	62.2 ± 13.3	42.7 ± 3.0
Lung	14.7 ± 1.8	11.7 ± 4.2	17.1 ± 3.6	10.5 ± 1.7	2.0 ± 0.5	1.5 ± 0.5	2.8 ± 1.1	1.5 ± 0.2
Liver	7.8 ± 0.4	7.1 ± 3.0	13.1 ± 1.0	19.7 ± 2.1	7.0 ± 0.8	6.2 ± 2.7	11.6 ± 1.1	17.9 ± 0.8
Spleen	5.7 ± 0.5	5.7 ± 2.1	9.2 ± 0.5	18.2 ± 1.3	0.6 ± 0.1	0.5 ± 0.2	0.9 ± 0.1	1.5 ± 0.1
Kidney	8.6 ± 1.6	6.5 ± 2.4	8.2 ± 1.8	8.3 ± 0.7	1.2 ± 0.2	0.8 ± 0.3	1.0 ± 0.2	1.0 ± 0.1
Muscle	1.7 ± 0.5	1.0 ± 0.5	1.7 ± 0.4	1.6 ± 0.2	14.5 ± 3.6	8.9 ± 4.5	14.7 ± 4.0	13.2 ± 0.8
Fat	3.9 ± 0.3	2.7 ± 2.1	4.1 ± 1.1	3.0 ± 1.3	11.3 ± 1.6	8.0 ± 6.3	11.9 ± 3.7	8.3 ± 3.3
Heart	11.4 ± 3.6	6.6 ± 1.5	9.1 ± 2.7	7.3 ± 1.2	1.3 ± 0.4	0.7 ± 0.1	1.0 ± 0.4	0.7 ± 0.1
Brain	1.1 ± 0.3	1.2 ± 0.8	0.9 ± 0.2	0.7 ± 0.1	0.4 ± 0.1	0.2 ± 0.2	0.4 ± 0.1	0.3 ± 0.1
Bone	2.1 ± 0.4	1.3 ± 0.8	2.3 ± 0.3	2.6 ± 0.2	4.5 ± 0.7	2.9 ± 1.9	5.3 ± 0.6	5.6 ± 0.6

Data are presented as percentage injected dose per gram (%ID/g) and percentage injected dose per organ (%ID/organ) ± SD.

4.5 Tumor Model Selection

The primary requirement for our model was to produce tumors with angiogenesis, and therefore $\alpha_v\beta_3$ integrin. This is easily achieved, as the vast majority of solid tumors undergo angiogenesis. Another consideration for a tumor model is the cell type used and whether it overexpresses $\alpha_v\beta_3$ integrin on the cell surface. Time to produce tumors, potential for metastasis, and cost of host animal are important factors in selecting and producing authentic tumor models for the desired application.

The most commonly used model produces subcutaneous tumors. The frequent use of this model is due to simplicity: tumors are accessible for measurement evaluation, anesthetics are not necessary, and the inoculation procedure is straightforward (86). There are, however, several drawbacks to subcutaneous tumor models in terms of biological relevance and authenticity of lesion pathology. These tumors often have altered surface protein expression profiles compared to lesions normally found in their tissue of origination (87). They typically do not metastasize (88), and often display increased sensitivity to treatments (89). Nevertheless, for imaging purposes (i.e. nontherapeutic) a subcutaneous model is straightforward and robust. Therefore we chose to use subcutaneous tumor to validate our dual modality nanoparticle.

We evaluate three tumor models in this work. The simplest model we studied was that of tumors formed in C57BL/6 mice using Lewis lung carcinoma cells. Lewis lung carcinoma cells (LLC) are mouse cells originally isolated from a spontaneous carcinoma in a C57BL/6 mouse at the Wistar Institute in 1951 and later propagated in culture (90, 91). The LLC line has been used to study metastasis, chemotherapeutics, and angiogenesis. Because this is a mouse cell line it can be grown in immune competent animals, making it cost effective. We grew LLC tumors in mice and examined mouse tissue for the presence of $\alpha_v\beta_3$ integrin. LLC tumors produce intensely angiogenic lesions, with endothelial cells expressing $\alpha_v\beta_3$ integrin, however the cells do not express surface $\alpha_v\beta_3$ integrin (Figure 4.16). We therefore decided to use alternative tumor lines in which express surface $\alpha_v\beta_3$ integrin as well as produce angiogenic blood vessels. Doing so would effectively increase the concentration of $\alpha_v\beta_3$ integrin within the lesion, which in turn would increase the amount of accumulated nanoparticles and maximize signal intensity.

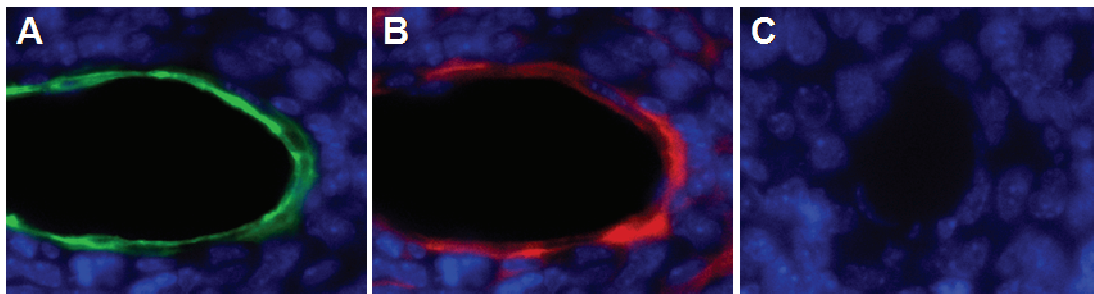


Figure 4.16: Immunofluorescent staining of newly formed blood vessels in LLC tumors. (A) Frozen sections were stained with DAPI (blue), anti-PECAM primary antibody, and Cy3-labeled secondary antibody (green). PECAM expressing endothelial cells of angiogenic blood vessels are shown in green. (B) Anti- β_3 primary antibody and Cy5 secondary antibody (red) show the expression of $\alpha_v\beta_3$ integrin by endothelial cells. (C) Isotype control antibodies produced no fluorescence above background.

A second tumor model we examined was the U87MG human glioblastoma cell line. This line is known to overexpress $\alpha_v\beta_3$ integrin (33, 34) and has been used extensively for RGD-targeting of

$\alpha_v\beta_3$ integrin (30, 35, 36). As this is a human cell line, it must be grown in immune-deficient athymic nude (*nu/nu*) mice. This model was used in conjunction with our collaborators at Washington University School of Medicine. Tumors typically take 3 – 4 weeks to reach approximately 500 mm³, when they are used in experiments. The tumor growth plot can be seen in Figure 4.17 below. At 4 weeks some tumors will show hemorrhaging, and by 5 weeks some animals will have bleeding tumors, making it desirable to use animals at or before 4 weeks.

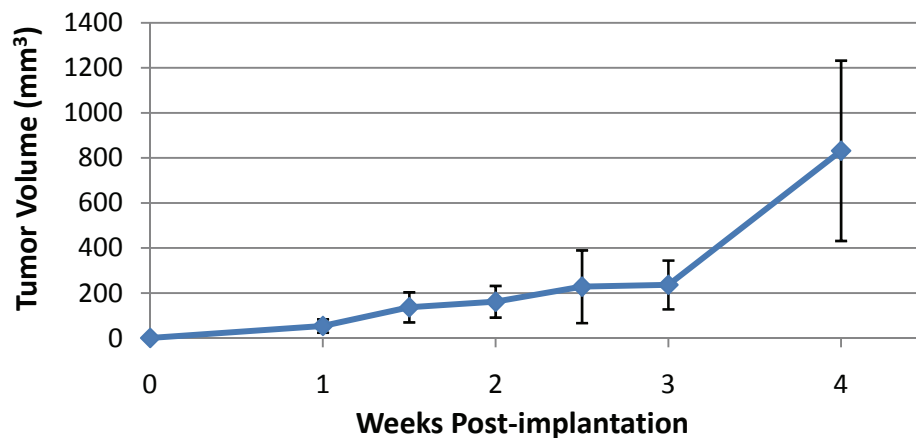


Figure 4.17: U87MG tumor growth plot.

The third and most complex tumor model tested was a bilateral model formed from subcutaneous inoculation with two cell lines. One cell line is the $\alpha_v\beta_3$ integrin-positive M21 line derived from a metastatic human melanoma lesion (92). The accompanying line, M21L, is an $\alpha_v\beta_3$ integrin-negative stable variant derived from the M21 that fails to synthesize α_v subunit mRNA (41). A schematic of this model is shown in Figure 4.18.

In our experience, the M21/M21L bilateral model was considerably problematic. The growth rate of M21 tumors was often different than the growth of M21L tumors, resulting in uneven lesion volumes. At times one tumor would grow and the other would not. Additionally,

the growth rate was typically slower than that of U87MG lesions which slowed the rate of progress. The M21/M21L model was used by our collaborators at Washington University and the M21 and M21L cells were acquired from the laboratory of David Cheresh. This model was not replicated at Georgia Tech.

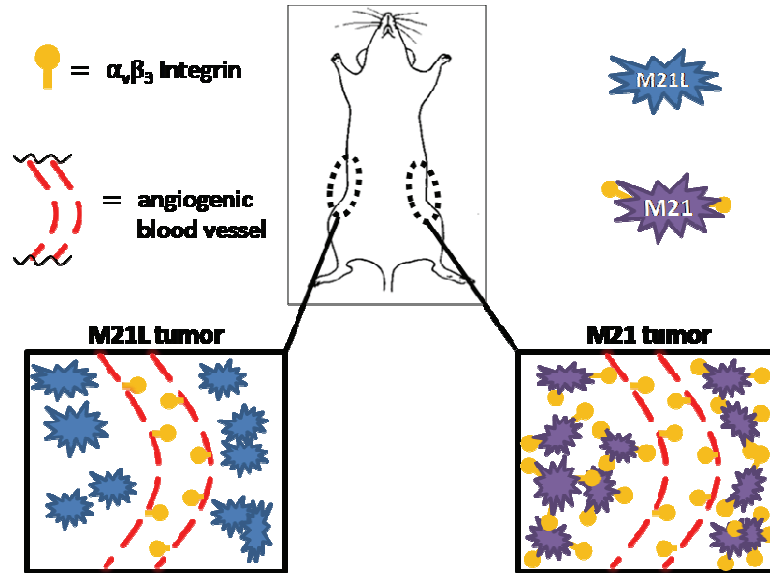


Figure 4.18: Schematic of M21/M21L bilateral tumor model. The animal is inoculated in its right and left rear flanks with M21L and M21 cells, respectively. M21 cells are shown in purple and M21L cells are shown in blue. Integrin $\alpha_v\beta_3$ is represented in yellow while leaky angiogenic blood vessels are shown in red. In the M21 tumor, $\alpha_v\beta_3$ integrin is present on endothelial cells as well as M21 cells. In the M21L tumor, $\alpha_v\beta_3$ integrin is present only on M21L cells.

4.6 Preliminary MRI Studies

The Bao lab has recently acquired a 7.0 T Pharmascan small animal MR scanner (Bruker BioSpin).

The system became operational on April 25th, 2008. Dr. Johannes Leisen, senior research scientist at Georgia Tech NMR Center, was hired to manage the scanner. The system is equipped with an MR-compatible monitoring and gating system (SA Instruments). Cardiac gating was performed by affixing neonatal ECG electrodes (3M Corp.) to the forepaws using conducting electrode cream (Grass Technologies), and respiratory gating was performed by

means of a respiratory pillow (SA Instruments). The system is equipped with a small an isoflurane vaporizer to anesthetize animals. Animal body temperature was maintained using a water-filled blanket fed by a thermostatically controlled heating pump.

The water-filled blanket and ECG leads initially caused a marked decrease in signal to noise ratio (SNR); the first images acquired with the system were low SNR (Figure 4.19A). The method used to heat animals while being imaged consisted of a blanket filled with moving water. This, along with the direction of the ECG leads, lead to significant SNR problems in initial imaging studies. These issues were eventually solved and higher quality images were acquired. The use of a 30 mm mouse-body volume coil certainly limits SNR in our superficial tumor model.

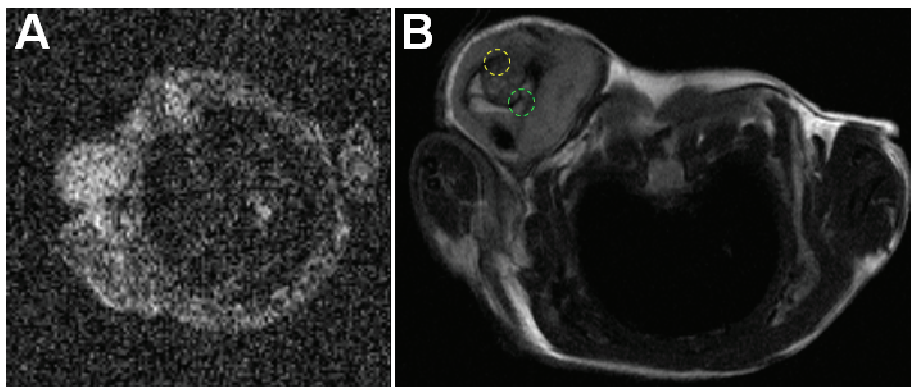


Figure 4.19: Initial imaging difficulties: (A) Initial studies produced images with low signal-to-noise ratio (SNR). The blanket of moving water wrapped around the animal to heat it, as well as the direction of ECG leads, contributed to poor image quality. (B) Several U87MG tumors exhibited sizable inherent T2 variations. For example, the T2 variation for the regions of interest (ROIs) in the tumor is 48 ms (yellow) and 77 ms (yellow). Variation in tumor T2 creates difficulties in discerning nanoparticle induced changes in T2 from the inherent variation in T2.

To obtain images, animals were placed in the prone position on an imaging bed and positioned in the bore of the MRI scanner. Transverse relaxation time (T2) weighed images were obtained using a multi-slice multi-echo sequence with the following parameters: SE TR/(TE), 2000 ms/(12, 24, 36, 48, 60, 72, 84, 96, 108, 120, 132, 144) ms; flip angle, 180°; matrix size, 128 × 128; field of

view, 3 × 3 cm; in-plane resolution, 234 μm; slice thickness, 1 mm; slices acquired, 8; slice orientation, axial; averages, 4; scan time, 17 min 4 s. Tumor ROIs were defined using ParaVision 4 and T2 colormaps were generated using MATLAB.

One of the first observations made was that U87MG tumors exhibited sizable inherent T2 variations. For example, typical T2 variation in some tumors ranges from 25 – 75 ms (generally the variation was within 25 ms). This variation in U87MG tumors may be due to extensive blood vessels and hemorrhaging within the tumor. This drawback was not apparent in microPET imaging. Variation in tumor T2 creates difficulties in discerning nanoparticle induced changes in T2 from the inherent variation in T2. Some animals showed changes in inherent tumor T2 over a 24 hr period. This change would make comparison of images before and 24 hr after nanoparticle injection more complex.

To determine if the decrease in T2 due to nanoparticle accumulation is greater than the natural T2 variation of the tumor, tumors were directly injected with nanoparticle. The concentration of particles used (1 - 10 μM Fe) is the high end of the range of possible expected accumulation. Tumors were injected with nanoparticles (50 μL) suspended in 10 mM PBS. After 30 minutes animals were imaged and ROIs were defined on pre- and post injection images. The T2 of pre-injection ROIs differed by 6.8 ± 2.3 ms (typical range of T2 within a tumor was 5 - 25 ms). Post-injection ROIs showed a difference of 39.6 ± 5.6 ms. In this instance, the difference due to nanoparticles within the tumor was greater than the natural T2 variation. Thus, we decided to continue with *in vivo* nanoparticle targeting experiments.

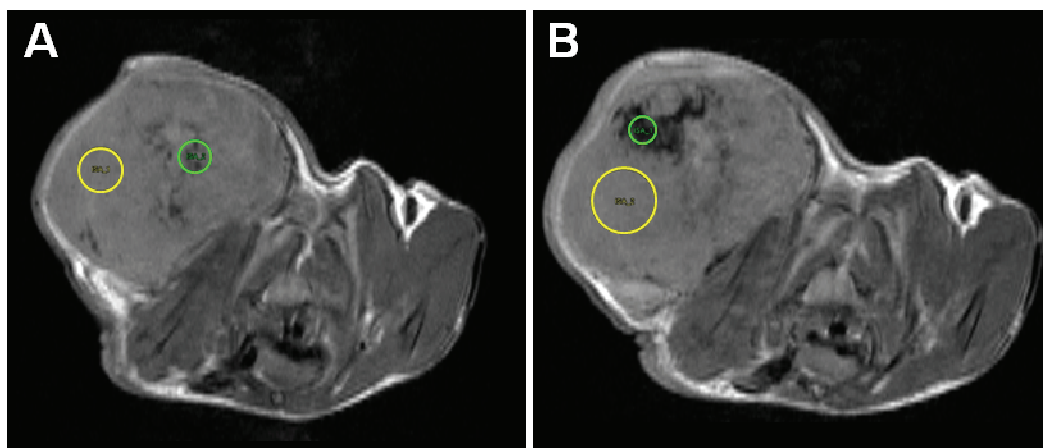


Figure 4.20: Intra-tumor injection of magnetic nanoparticle. (A) Pre-injection ROIs were defined for two regions within the tumor that differed in T2 (yellow, 54.6 ± 1.3 ms; green, 47.8 ± 1.9 ms). (A) Post-injection ROIs showed a difference that was greater than the natural variation in tumor T2 (yellow, 55.7 ± 5.5 ms; green, 16.1 ± 1 ms).

4.6.1 References

1. Sun, S., C. Murray, D. Weller, L. Folks, and A. Moser, *Monodisperse FePt Nanoparticles and Ferromagnetic FePt Nanocrystal Superlattices*. *Science*, 2000. **287**(5460): p. 1989.
2. Hyeon, T., S. Lee, J. Park, Y. Chung, and H. Na, *Synthesis of Highly Crystalline and Monodisperse Maghemite Nanocrystallites without a Size-Selection Process*. *J. Am. Chem. Soc.*, 2001. **123**(51): p. 12798-12801.
3. Sun, S., H. Zeng, D. Robinson, S. Raoux, P. Rice, S. Wang, and G. Li, *Monodisperse MFe_2O_4 ($M = Fe, Co, Mn$) Nanoparticles*. *J. Am. Chem. Soc.*, 2004. **126**(1): p. 273-279.
4. Molday, R.S. and D. MacKenzie, *Immunospecific ferromagnetic iron-dextran reagents for the labeling and magnetic separation of cells*. *J Immunol Methods*, 1982. **52**(3): p. 353-67.
5. Molday, R.S. and L.L. Molday, *Separation of cells labeled with immunospecific iron dextran microspheres using high gradient magnetic chromatography*. *FEBS Lett*, 1984. **170**(2): p. 232-8.
6. SHEN, T., R. WEISSLEDER, M. PAPISOV, A. BOGDANOV, and T. BRADY, *Monocrystalline iron oxide nanocompounds(MION): physicochemical properties*. *Magnetic resonance in medicine*, 1993. **29**(5): p. 599-604.
7. Verwey, E.J.W. and E.L. Heilmann, *Physical Properties and Cation Arrangement of Oxides with Spinel Structures I. Cation Arrangement in Spinels*. *The Journal of Chemical Physics*, 1947. **15**(4): p. 174-180.

8. Sosnovik, D., M. Nahrendorf, and R. Weissleder, *Magnetic nanoparticles for MR imaging: agents, techniques and cardiovascular applications*. Basic Research in Cardiology, 2008. **103**(2): p. 122-130.
9. Weissleder, R., J. Wittenberg, C. Rabito, and H. Bengel, *Ultrasmall Superparamagnetic Iron Oxide: Characterization of a New Class of Contrast Agents for MR Imaging*. Radiology, 1990. **175**: p. 489-493.
10. Harisinghani, M.G., J. Barentsz, P.F. Hahn, W.M. Deserno, S. Tabatabaei, C.H. van de Kaa, J. de la Rosette, and R. Weissleder, *Noninvasive detection of clinically occult lymph-node metastases in prostate cancer*. N Engl J Med, 2003. **348**(25): p. 2491-9.
11. Kooi, M., V. Cappendijk, K. Cleutjens, A. Kessels, P. Kitslaar, M. Borgers, P. Frederik, M. Daemen, and J. van Engelshoven, *Accumulation of Ultrasmall Superparamagnetic Particles of Iron Oxide in Human Atherosclerotic Plaques Can Be Detected by In Vivo Magnetic Resonance Imaging*. 2003, Am Heart Assoc. p. 2453-2458.
12. AMAG Pharmaceuticals, I. *Combidex*. 2008 10, 2008]; Available from: <http://www.amagpharma.com/products/combidex.php>.
13. Wunderbaldinger, P., L. Josephson, and R. Weissleder, *Crosslinked iron oxides (CLIO): a new platform for the development of targeted MR contrast agents*. Acad Radiol, 2002. **9 Suppl 2**: p. S304-6.
14. Stephen, P. and J. Lee, *Synthesis of polysaccharide covered superparamagnetic oxide colloids*, U.S.P. Office, Editor. 1991, Advanced Magnetics, Inc.: USA. p. 17.
15. Lewin, M., N. Carlesso, C. Tung, X. Tang, D. Cory, D. Scadden, and R. Weissleder, *Tat peptide-derivatized magnetic nanoparticles allow in vivo tracking and recovery of progenitor cells*. Nature Biotechnology, 2000. **18**: p. 410-414.
16. CMIR. *Nanotechnology Program*. 2008 10/2008]; Available from: http://cmir.mgh.harvard.edu/nano/nano_main.php?menuID_=222.
17. Gaw, D.A. and L. Josephson, *AMINE FUNCTIONALIZED SUPERPARAMAGNETIC NANOPARTICLES FOR THE SYNTHESIS OF BIOCONJUGATES AND USES THEREFOR*, U.S.P. Office, Editor. 2003: USA.
18. DeNardo, S., G. DeNardo, L. Miers, A. Natarajan, A. Foreman, C. Gruettner, G. Adamson, and R. Ivkov, *Development of Tumor Targeting Bioprobes (111In-Chimeric L6 Monoclonal Antibody Nanoparticles) for Alternating Magnetic Field Cancer Therapy*. Clinical Cancer Research, 2005. **11**(19): p. 7087-7092.
19. DeNardo, S., G. DeNardo, A. Natarajan, L. Miers, A. Foreman, C. Gruettner, G. Adamson, and R. Ivkov, *Thermal Dosimetry Predictive of Efficacy of 111In-ChL6 Nanoparticle AMF-Induced Thermoablative Therapy for Human Breast Cancer in Mice*. Journal of Nuclear Medicine, 2007. **48**(3): p. 437.

20. Simberg, D., T. Duza, J. Park, M. Essler, J. Pilch, L. Zhang, A. Derfus, M. Yang, R. Hoffman, and S. Bhatia, *Biomimetic amplification of nanoparticle homing to tumors*. Proceedings of the National Academy of Sciences, 2007. **104**(3): p. 932.
21. Natarajan, A., C. Gruettner, R. Ivkov, G. DeNardo, G. Mirick, A. Yuan, A. Foreman, and S. DeNardo, *NanoFerrite Particle Based Radioimmunonanoparticles: Binding Affinity and In Vivo Pharmacokinetics*. Bioconjugate Chem, 2008. **19**(6): p. 1211-1218.
22. Natarajan, A., C. Xiong, C. Gruettner, G. DeNardo, and S. DeNardo, *Development of Multivalent Radioimmunonanoparticles for Cancer Imaging and Therapy*. Cancer Biotherapy & Radiopharmaceuticals, 2008. **23**(1): p. 82-91.
23. Bergers, G. and L. Benjamin, *Tumorigenesis and the angiogenic switch*. NATURE REVIEWS CANCER, 2003. **3**: p. 401-410.
24. Ferrara, N., *VEGF and the quest for tumour angiogenesis factors*. Nat Rev Cancer, 2002. **2**(10): p. 795-803.
25. Hanahan, D. and J. Folkman, *Patterns and Emerging Mechanisms of the Angiogenic Switch during Tumorigenesis*. CELL-CAMBRIDGE MA-, 1996. **86**: p. 353-364.
26. Xiong, J., T. Stehle, B. Diefenbach, R. Zhang, R. Dunker, D. Scott, A. Joachimiak, S. Goodman, and M. Arnaout, *Crystal Structure of the Extracellular Segment of Integrin $\alpha_v\beta_3$* . Science, 2001. **294**(5541): p. 339-345.
27. Brooks, P., R. Clark, and D. Cheresh, *Requirement of vascular integrin alpha v beta 3 for angiogenesis*. Science, 1994. **264**(5158): p. 569-571.
28. Hood, J.D. and D.A. Cheresh, *Role of integrins in cell invasion and migration*. Nat Rev Cancer, 2002. **2**(2): p. 91-100.
29. Ruoslahti, E., *RGD AND OTHER RECOGNITION SEQUENCES FOR INTEGRINS*. Annual Reviews in Cell and Developmental Biology, 1996. **12**(1): p. 697-715.
30. Chen, X., R. Park, Y. Hou, V. Khankaldyyan, I. Gonzales-Gomez, M. Tohme, J. Bading, W. Laug, and P. Conti, *MicroPET imaging of brain tumor angiogenesis with ^{18}F -labeled PEGylated RGD peptide*. European Journal of Nuclear Medicine and Molecular Imaging, 2004. **31**(8): p. 1081-1089.
31. Beck, V., H. Herold, A. Bengel, B. Lubber, P. Hutzler, H. Tschesche, H. Kessler, M. Schmitt, H. Geppert, and U. Reuning, *ADAM15 decreases integrin $\alpha_v\beta_3$ /vitronectin-mediated ovarian cancer cell adhesion and motility in an RGD-dependent fashion*. International Journal of Biochemistry and Cell Biology, 2005. **37**(3): p. 590-603.
32. Haubner, R., W.A. Weber, A.J. Beer, E. Vabuliene, D. Reim, M. Sarbia, K.-F. Becker, M. Goebel, R. Hein, #252, diger, H.-J. Wester, rgen, H. Kessler, and M. Schwaiger,

- Noninvasive Visualization of the Activated $\alpha_v\beta_3$ Integrin in Cancer Patients by Positron Emission Tomography and [^{18}F]Galacto-RGD.* PLoS Medicine, 2005. **2**(3): p. e70.
33. Guo, P., L. Xu, S. Pan, R.A. Brekken, S.-T. Yang, G.B. Whitaker, M. Nagane, P.E. Thorpe, J.S. Rosenbaum, H.-J. Su Huang, W.K. Cavenee, and S.-Y. Cheng, *Vascular Endothelial Growth Factor Isoforms Display Distinct Activities in Promoting Tumor Angiogenesis at Different Anatomic Sites.* Cancer Res, 2001. **61**(23): p. 8569-8577.
 34. Ponten, J. and E. Macintyre, *Long term culture of normal and neoplastic human glia.* Acta Pathol Microbiol Scand, 1968. **74**(4): p. 465-86.
 35. Montet, X., M. Funovics, K. Montet-Abou, R. Weissleder, and L. Josephson, *Multivalent effects of RGD peptides obtained by nanoparticle display.* J Med Chem, 2006. **49**(20): p. 6087-93.
 36. Montet, X., K. Montet-Abou, F. Reynolds, R. Weissleder, and L. Josephson, *Nanoparticle imaging of integrins on tumor cells.* Neoplasia, 2006. **8**(3): p. 214-22.
 37. Cai, W., D. Shin, K. Chen, O. Gheysens, Q. Cao, S. Wang, S. Gambhir, and X. Chen, *Peptide-labeled near-infrared quantum dots for imaging tumor vasculature in living subjects.* Nano Lett, 2006. **6**(4): p. 669-676.
 38. Niu, G., Z. Xiong, Z. Cheng, W. Cai, S. Gambhir, L. Xing, and X. Chen, *In Vivo Bioluminescence Tumor Imaging of RGD Peptide-modified Adenoviral Vector Encoding Firefly Luciferase Reporter Gene.* Molecular Imaging and Biology, 2007. **9**(3): p. 126-134.
 39. Hermanson, G., *Bioconjugate Techniques.* 2008: Academic Press.
 40. Xing, Y., Q. Chaudry, C. Shen, K. Kong, H. Zhou, L. Chung, J. Petros, R. O'Regan, M. Yezhelyev, and J. Simons, *Bioconjugated quantum dots for multiplexed and quantitative immunohistochemistry.* Nature Protocols, 2007. **2**(5): p. 1152.
 41. Cheresch, D. and R. Spiro, *Biosynthetic and functional properties of an Arg-Gly-Asp-directed receptor involved in human melanoma cell attachment to vitronectin, fibrinogen, and von Willebrand factor.* Journal of Biological Chemistry, 1987. **262**(36): p. 17703-17711.
 42. Felding-Habermann, B., B. Mueller, C. Romerdahl, and D. Cheresch, *Involvement of integrin alpha V gene expression in human melanoma tumorigenicity.* Journal of Clinical Investigation, 1992. **89**(6): p. 2018.
 43. www.ClinicalTrials.gov. *www.ClinicalTrials.gov*. 2008 [cited 2008; Available from: www.ClinicalTrials.gov].
 44. Pierschbacher, M., E.G. Hayman, and E. Ruoslahti, *Synthetic peptide with cell attachment activity of fibronectin.* Proc Natl Acad Sci U S A, 1983. **80**(5): p. 1224-7.

45. Pierschbacher, M.D. and E. Ruoslahti, *Cell attachment activity of fibronectin can be duplicated by small synthetic fragments of the molecule*. Nature, 1984. **309**(5963): p. 30-3.
46. Pytela, R., M.D. Pierschbacher, and E. Ruoslahti, *A 125/115-kDa cell surface receptor specific for vitronectin interacts with the arginine-glycine-aspartic acid adhesion sequence derived from fibronectin*. Proc Natl Acad Sci U S A, 1985. **82**(17): p. 5766-70.
47. Pytela, R., M.D. Pierschbacher, M.H. Ginsberg, E.F. Plow, and E. Ruoslahti, *Platelet membrane glycoprotein IIb/IIIa: member of a family of Arg-Gly-Asp--specific adhesion receptors*. Science, 1986. **231**(4745): p. 1559-62.
48. Ruoslahti, E. and M.D. Pierschbacher, *New perspectives in cell adhesion: RGD and integrins*. Science, 1987. **238**(4826): p. 491-7.
49. Cheresch, D. and J. Harper, *Arg-Gly-Asp recognition by a cell adhesion receptor requires its 130-kDa alpha subunit*. Journal of Biological Chemistry, 1987. **262**(4): p. 1434-1437.
50. CHERESH, D., J. SMITH, H. COOPER, and V. QUARANTA, *A novel vitronectin receptor integrin($\alpha_v\beta_x$) is responsible for distinct adhesive properties of carcinoma cells*. Cell, 1989. **57**(1): p. 59-69.
51. Straus, A.H., W.G. Carter, E.A. Wayner, and S. Hakomori, *Mechanism of fibronectin-mediated cell migration: dependence or independence of cell migration susceptibility on RGDS-directed receptor (integrin)*. Exp Cell Res, 1989. **183**(1): p. 126-39.
52. Narumiya, S., Y. Abe, Y. Kita, K. Miyake, K. Nakajima, T.X. Watanabe, Y. Oka, H. Sugiyama, H. Yagita, K. Okumura, T. Hamaoka, and H. Fujiwara, *Pre-B cells adhere to fibronectin via interactions of integrin $\{\alpha\}_5/\{\alpha\}_v$ with RGDS as well as of integrin $\{\alpha\}_4$ with two distinct V region sequences at its different binding sites*. Int. Immunol., 1994. **6**(1): p. 139-147.
53. Sanchez-Aparicio, P., C. Dominguez-Jimenez, and A. Garcia-Pardo, *Activation of the alpha 4 beta 1 integrin through the beta 1 subunit induces recognition of the RGDS sequence in fibronectin*. J. Cell Biol., 1994. **126**(1): p. 271-279.
54. Arap, W., R. Pasqualini, and E. Ruoslahti, *Cancer Treatment by Targeted Drug Delivery to Tumor Vasculature in a Mouse Model*. Science, 1998. **279**(5349): p. 377-380.
55. Koivunen, E., W. Arap, D. Rajotte, J. Lahdenranta, and R. Pasqualini, *Identification of Receptor Ligands with Phage Display Peptide Libraries*. J Nucl Med, 1999. **40**(5): p. 883-888.
56. Barker, P., S. Bullens, S. Bunting, D. Burdick, K. Chan, T. Deisher, C. Eigenbrot, T. Gadek, and R. Gantzos, *Cyclic RGD peptide analogs as antiplatelet antithrombotics*. Journal of Medicinal Chemistry, 1992. **35**(11): p. 2040-2048.

57. Cheng, S., W. Craig, D. Mullen, J. Tschopp, D. Dixon, and M. Pierschbacher, *Design and synthesis of novel cyclic RGD-containing peptides as highly potent and selective integrin. alpha. IIb. beta. 3 antagonists*. Journal of Medicinal Chemistry, 1994. **37**(1): p. 1-8.
58. Haubner, R., R. Gratias, B. Diefenbach, S. Goodman, A. Jonczyk, and H. Kessler, *Structural and functional aspects of RGD-containing cyclic pentapeptides as highly potent and selective integrin v 3 antagonists*. J. Am. Chem. Soc, 1996. **118**(32): p. 7461-7472.
59. Thibault, G., P. Tardif, and G. Lapalme, *Comparative Specificity of Platelet {alpha}IIb{beta}3 Integrin Antagonists*. J Pharmacol Exp Ther, 2001. **296**(3): p. 690-696.
60. Aumailley, M., M. Gurrath, G. Muller, J. Calvete, R. Timpl, and H. Kessler, *Arg-Gly-Asp constrained within cyclic pentapeptides. Strong and selective inhibitors of cell adhesion to vitronectin and laminin fragment P1*. FEBS Lett, 1991. **291**(1): p. 50-4.
61. Marion GURRATH, G.M., Horst KESSLER, Monique AUMAILLEY, Rupert TIMPL,, *Conformation/activity studies of rationally designed potent anti-adhesive RGD peptides*. European Journal of Biochemistry, 1992. **210**(3): p. 911-921.
62. Kuhn, K. and J. Eble, *The structural bases of integrin-ligand interactions*. Trends Cell Biol, 1994. **4**(7): p. 256-61.
63. Burke, P., S. DeNardo, L. Miers, K. Lamborn, S. Matzku, and G. DeNardo, *Cilengitide Targeting of $\alpha_v\beta_3$ Integrin Receptor Synergizes with Radioimmunotherapy to Increase Efficacy and Apoptosis in Breast Cancer Xenografts 1*. Cancer Res, 2002. **62**(15): p. 4263-4272.
64. Goodman, S.L., G. Holzemann, G.A. Sulyok, and H. Kessler, *Nanomolar small molecule inhibitors for $\alpha_v(\beta)_6$, $\alpha_v(\beta)_5$, and $\alpha_v(\beta)_3$ integrins*. J Med Chem, 2002. **45**(5): p. 1045-51.
65. Friedlander, M., C.L. Theesfeld, M. Sugita, M. Fruttiger, M.A. Thomas, S. Chang, and D.A. Cheresh, *Involvement of integrins alpha v beta 3 and alpha v beta 5 in ocular neovascular diseases*. Proceedings of the National Academy of Sciences of the United States of America, 1996. **93**(18): p. 9764-9769.
66. CHUNG, J., C. RADER, M. POPKOV, Y.-M. HUR, H.-K. KIM, Y.-J. LEE, and C.F. BARBAS, III, *Integrin {alpha}IIb{beta}3-specific synthetic human monoclonal antibodies and HCDR3 peptides that potently inhibit platelet aggregation*. FASEB J., 2004. **18**(2): p. 361-363.
67. Mulder, W.J.M., G.J. Strijkers, J.W. Habets, E.J.W. Bleeker, D.W.J. van der Schaft, G. Storm, G.A. Koning, A.W. Griffioen, and K. Nicolay, *MR molecular imaging and fluorescence microscopy for identification of activated tumor endothelium using a bimodal lipidic nanoparticle*. FASEB J., 2005. **19**(14): p. 2008-2010.

68. Wei, Y., R. Czekay, L. Robillard, M. Kugler, F. Zhang, K. Kim, J. Xiong, M. Humphries, and H. Chapman, *Regulation of $\alpha 5\beta 1$ integrin conformation and function by urokinase receptor binding*. *The Journal of Cell Biology*, 2005. **168**(3): p. 501.
69. Zhu, B., *Mechanistic explanation for the unique pharmacologic properties of receptor partial agonists*. *Biomedicine & Pharmacotherapy*, 2005. **59**(3): p. 76-89.
70. Rossin, R., S. Muro, M. Welch, V. Muzykantov, and D. Schuster, *In Vivo Imaging of ^{64}Cu -Labeled Polymer Nanoparticles Targeted to the Lung Endothelium*. *Journal of Nuclear Medicine*, 2008. **49**(1): p. 103.
71. Rossin, R., D. Pan, K. Qi, J.L. Turner, X. Sun, K.L. Wooley, and M.J. Welch, *^{64}Cu -labeled folate-conjugated shell cross-linked nanoparticles for tumor imaging and radiotherapy: synthesis, radiolabeling, and biologic evaluation*. *J Nucl Med*, 2005. **46**(7): p. 1210-8.
72. Sun, G., A. Hagooly, J. Xu, A. Nyström, Z. Li, R. Rossin, D. Moore, K. Wooley, and M. Welch, *Facile, Efficient Approach to Accomplish Tunable Chemistries and Variable Biodistributions for Shell Cross-Linked Nanoparticles*. *Biomacromolecules*, 2008. **9**(7): p. 1997-2006.
73. XU, J., G. SUN, R. ROSSIN, A. HAGOOLY, Z. LI, K. FUKUKAWA, B. MESSMORE, D. MOORE, M. WELCH, and C. HAWKER, *Labeling of polymer nanostructures for medical imaging: Importance of cross-linking extent, spacer length, and charge density*. *Macromolecules*, 2007. **40**(9): p. 2971-2973.
74. Cai, W., K. Chen, Z.B. Li, S.S. Gambhir, and X. Chen, *Dual-function probe for PET and near-infrared fluorescence imaging of tumor vasculature*. *J Nucl Med*, 2007. **48**(11): p. 1862-70.
75. Chen, K., Z.B. Li, H. Wang, W. Cai, and X. Chen, *Dual-modality optical and positron emission tomography imaging of vascular endothelial growth factor receptor on tumor vasculature using quantum dots*. *Eur J Nucl Med Mol Imaging*, 2008.
76. Schipper, M.L., Z. Cheng, S.W. Lee, L.A. Bentolila, G. Iyer, J. Rao, X. Chen, A.M. Wu, S. Weiss, and S.S. Gambhir, *microPET-based biodistribution of quantum dots in living mice*. *J Nucl Med*, 2007. **48**(9): p. 1511-8.
77. Choi, J.S., J.C. Park, H. Nah, S. Woo, J. Oh, K.M. Kim, G.J. Cheon, Y. Chang, J. Yoo, and J. Cheon, *A hybrid nanoparticle probe for dual-modality positron emission tomography and magnetic resonance imaging*. *Angew Chem Int Ed Engl*, 2008. **47**(33): p. 6259-62.
78. Nahrendorf, M., H. Zhang, S. Hembrador, P. Panizzi, D.E. Sosnovik, E. Aikawa, P. Libby, F.K. Swirski, and R. Weissleder, *Nanoparticle PET-CT imaging of macrophages in inflammatory atherosclerosis*. *Circulation*, 2008. **117**(3): p. 379-87.
79. Lee, H.Y., Z. Li, K. Chen, A.R. Hsu, C. Xu, J. Xie, S. Sun, and X. Chen, *PET/MRI dual-modality tumor imaging using arginine-glycine-aspartic (RGD)-conjugated radiolabeled iron oxide nanoparticles*. *J Nucl Med*, 2008. **49**(8): p. 1371-9.

80. Jarrett, B.R., B. Gustafsson, D.L. Kukis, and A.Y. Louie, *Synthesis of ⁶⁴Cu-labeled magnetic nanoparticles for multimodal imaging*. *Bioconjug Chem*, 2008. **19**(7): p. 1496-504.
81. Glaus, C.R.M., R. Rossin, M.J. Welch, and G. Bao, *In vivo evaluation of ⁶⁴Cu-labeled Magnetic Nanoparticles: A Novel Probe for Dual-Modality PET/MR Imaging in submission*.
82. Glaus, C.R.M., A. Hagooly, M.J. Welch, and G. Bao, *PET/MR Imaging of Tumors Using RGD-targeted ⁶⁴Cu-labeled Magnetic Nanoparticles in submission*.
83. Liu, Z., W. Cai, L. He, N. Nakayama, K. Chen, X. Sun, X. Chen, and H. Dai, *In vivo biodistribution and highly efficient tumour targeting of carbon nanotubes in mice*. *Nat Nanotechnol*, 2007. **2**(1): p. 47-52.
84. Wadas, T.J. and C.J. Anderson, *Radiolabeling of TETA- and CB-TE2A-conjugated peptides with copper-64*. *Nat Protoc*, 2006. **1**(6): p. 3062-8.
85. Shokeen, M., N. Fettig, and R. Rossin, *Synthesis, in vitro and in vivo evaluation of radiolabeled nanoparticles*. *QJ Nucl Med Mol Imaging*, 2008.
86. Jacob, D. and B. Davis JFang, *Xenograftic tumor models in mice for cancer research, a technical review*. *Gene Ther Mol Biol*, 2004. **8**: p. 213-9.
87. Killion, J., R. Radinsky, and I. Fidler, *Orthotopic Models are Necessary to Predict Therapy of Transplantable Tumors in Mice*. *Cancer and Metastasis Reviews*, 1998. **17**(3): p. 279-284.
88. Fidler, I., *Experimental orthotopic models of organspecific metastasis by human neoplasms*. *Adv Mol Cell Biol*, 1994. **9**: p. 191-215.
89. Fidler, I., C. Wilmanns, A. Staroselsky, R. Radinsky, Z. Dong, and D. Fan, *Modulation of tumor cell response to chemotherapy by the organ environment*. *Cancer and Metastasis Reviews*, 1994. **13**(2): p. 209-222.
90. Bertram, J.S. and P. Janik, *Establishment of a cloned line of Lewis Lung Carcinoma cells adapted to cell culture*. *Cancer Lett*, 1980. **11**(1): p. 63-73.
91. Mayo, J.G., *Biologic characterization of the subcutaneously implanted Lewis lung tumor*. *Cancer Chemother Rep* 2, 1972. **3**(1): p. 325-30.
92. Guilano, A., R.F. Irie, D.L. Morton, and K.P. Rammin, *Proc. Am. Assoc. Cancer Res.*, 1978(19).

CHAPTER 5

PET/MR IMAGING OF RGD-TARGETED ^{64}Cu -LABELED MAGNETIC NANOPARTICLES

5.1 Introduction

Strategies that combine anatomical and functional imaging modalities hold the greatest promise to studying the molecular and cellular processes of disease. Positron emission tomography (PET) is a highly sensitive imaging nuclear imaging modality that provides quantitative, functional information at the whole-body scale. Magnetic resonance imaging (MRI) produces high resolution images of soft tissue as well as functional and spectroscopic information. Interest in combining PET with MRI has surged (1-4), and structured nanomaterials have emerged as possible a platform for the development of dual-PET/MR imaging agents.

To date, few reports of dual-modality PET/MRI nanoparticles have been published (5-8). We report the development and *in vivo* evaluation of a dual-PET/MR nanoparticle target to the angiogenesis molecular marker $\alpha_v\beta_3$ integrin. We produced ^{64}Cu -labeled iron oxide nanoparticles labeled at high specific activity and radiochemical purity. The particles were enveloped by polyethylene glycol polymers tipped with cyclized RGD peptides. Phantom imaging studies measured the PET and MRI contrast generation by ^{64}Cu -labeled iron oxide nanoparticles. Quantitative *ex vivo* biodistribution, *in vivo* microPET/CT and MR imaging was used to assess nanoparticle targeting to tumor $\alpha_v\beta_3$ integrin expression.

5.2 Experimental Procedures

5.2.1 Materials

Chelex 100 resin (50–100 mesh), hydrochloric acid, hydroxylamine hydrochloride, ferrous ammonium sulfate hexahydrate, 1,10-phenanthroline, sodium hydroxide,

ethylenediaminetetraacetic acid (EDTA), dimethyl sulfoxide (DMSO), 10 mM phosphate buffered saline (PBS), chloroform, and mouse serum were obtained from Sigma-Aldrich Inc. (St. Louis, MO). 1,4,7,10-Tetraazacyclododecane-1,4,7,10-tetraacetic acid mono(*N*-hydroxysuccinimide ester) (DOTA-NHS) was provided Macrocylics Inc. (Dallas, TX). Succinimidyl-([*N*-methyl]-dodecaethylene glycol) ester (NHS-mPEG), succinimidyl-([*N*-maleimidopropionamido]-dodecaethylene glycol) ester (NHS-PEG-Maleimide), 100 mM phosphate buffered saline, and desalting spin columns were obtained from Pierce Biotechnology, Inc. (Rockford, IL). Integrin $\alpha_v\beta_3$ targeting peptide c(RGDyC) (cyclo-(Arg-Gly-Asp-D-Tyr-Cys)) was obtained from Peptides International, Inc. (Louisville, KY). Alexa Fluor 647 succinimidyl ester was purchased from Invitrogen (Carlsbad, CA). Copper-64 was produced on a Washington University Medical School Cyclotron (Model CS-15, Cyclotron Corp.) by the $^{64}\text{Ni}(p,n)^{64}\text{Cu}$ reaction with the nuclide having a specific activity of 50-200 mCi/ μg at the end of bombardment (11). Buffers used for ^{64}Cu labeling and all reactions were passed through a Chelex 100 column prior to use. Water was deionized to 18 M Ω •cm using an E-Pure water filtration system (Barnstead International, Dubuque, IA).

5.2.2 Preparation of PEGylated DOTA–MNP_{PEG} and DOTA–MNP_{PEG}–RGD

DOTA-NHS ester was dissolved in 10 mM PBS and pH was adjusted to 7.5 by drop-wise addition of 0.5 M NaOH. An aliquot of the DOTA-NHS solution was immediately added to amino-functionalized cross-linked iron oxide nanoparticles (BioPhysics Assay Laboratory, Inc., Worcester, MA) at a molar ratio of 25:1 and the reaction was mixed for 1.5 hr at room temperature. The solution was loaded onto a desalting spin column to separate any unreacted DOTA-NHS from DOTA-conjugated magnetic nanoparticles (DOTA–MNP). NHS-PEG-Maleimide or NHS-mPEG was dissolved in molecular sieve-treated DMSO and added to DOTA–MNP in 100

mM PBS (pH 7.3) at a 1000:1 molar ratio. The reaction proceeded for 30 min at room temperature with constant mixing, followed by purification using spin columns equilibrated with 100 mM PBS (pH 6.9) containing 10 mM EDTA. c(RGDyC) was dissolved in DMSO and added to the maleimide-activated nanoparticles (DOTA-MNP_{PEG}-Mal) or methoxy-nanoparticles (DOTA-MNP_{mPEG}) at a molar ratio of 250:1 and reacted at room temperature for 2 hr. Peptide-conjugated DOTA-magnetic nanoparticles (DOTA-MNP-RGD) were purified similarly using spin columns, followed by filtration at 0.2 μ m and storage in 10 mM PBS at 4 °C. DOTA-MNP_{PEG} and DOTA-MNP_{PEG}-RGD used in live cell imaging studies were prepared using equal parts Alexa Fluor 647 succinimidyl ester and DOTA-NHS.

5.2.3 Nanoparticle Characterization

The number of integrin-targeting RGD peptides per nanoparticle was measured by reacting, in triplicate, equal amounts of c(RGDyC) with maleimide-activated nanoparticles (DOTA-MNP_{PEG}-Mal) or methoxy-nanoparticles (DOTA-MNP_{mPEG}) according to procedures outlined above. Upon completion of the reaction an aliquot of each sample was assayed for the concentration of unreacted c(RGDyC) using an Invitrogen Thiol Kit (Carlsbad, CA). The difference in thiol concentration between DOTA-MNP_{PEG}-Mal and DOTA-MNP_{mPEG} samples was used to calculate the average number of c(RGDyC) conjugated to DOTA-MNP_{PEG}-Mal.

The hydrodynamic diameter of DOTA-MNP_{PEG} and DOTA-MNP_{PEG}-RGD was measured by dynamic light scattering (DLS). DLS measurements were performed using a NICOMP 380 ZLS Submicron Particle Sizer (Particle Sizing Systems, Inc., Santa Barbara, CA) equipped with a 632.8 nm He-Ne laser and an Avalanche Photodiode detector at a fixed 90° scattering angle. Nanoparticle samples used were chelated with “cold” (i.e. stable) isotopes of copper according to the identical procedure used for radiolabeling with copper-64. Dilute nanoparticle samples

(0.4 mL) were placed in prewashed cylindrical optical cells and incident laser light was adjusted using a neutral density filter to obtain a scattering intensity of 300 KHz. Samples were measured in triplicate (5 runs each) at 23 °C for 30 min in a temperature-controlled sample chamber and data are reported as the average volume-weighted hydrodynamic diameter.

Surface potential of nanoparticle solutions was measured using the NICOMP 380 phase analysis light scattering (PALS) module. Electrophoretic mobility (μ) was measured and ξ -potential was calculated using the Smoluchowski equation. Samples were measured in triplicate (with 5 runs each) at 23 °C and data are reported as the average ξ -potential (mV).

Iron concentration of DOTA-MNP_{PEG} and DOTA-MNP_{PEG}-RGD solutions was determined using a 1,10-phenanthroline assay (12, 13). Solutions of hydroxylamine hydrochloride (10 mg/mL), sodium acetate (125 mg/mL), 1,10-phenanthroline (1 mg/mL) and hydrochloric acid (6 M) were prepared using deionized water. In a 200 μ L tube, 17 μ L of 6 M hydrochloric acid was added to 18 μ L of dilute nanoparticles and incubated in a thermocycler at 100°C for 10 minutes. The resulting solution of dissolved nanoparticles was combined with 10 μ L of hydroxylamine hydrochloride and 855 μ L of sodium acetate, followed by addition of 100 μ L 1,10-phenanthroline. The absorbance of the sample at 510 nm was measured using a microplate reader (Safire II, Tecan Group Ltd., Männedorf, Switzerland) and compared to a standard curve of ferrous ammonium sulfate hexahydrate solution.

5.2.4 Magnetic Nanoparticle Radiolabeling

In general, nanoparticles were labeled with ^{64}Cu and evaluated according to Shokeen et al (14). DOTA-MNP_{PEG} and DOTA-MNP_{PEG}-RGD were dissolved in 10 mM PBS at 1.2 and 1.5 mg Fe/mL, respectively, prior to labeling. Nanoparticles (60 μ g) were combined with 0.1 M ammonium acetate buffer (pH 5.5) to a final volume of 230 μ L. ^{64}Cu -acetate (3 mCi) was added and

nanoparticle samples were incubated at 37 °C for 1 hr with constant mixing. The solution was then challenged with 5 µL of 10 mM EDTA at 37 °C for 5 min with mixing (to remove nonspecifically bound ^{64}Cu), followed by purification using a centrifugal desalting column equilibrated with 10 mM PBS. Purity of ^{64}Cu -MNP was determined by radiochemical thin layer chromatography (radio-TLC). A small amount of the ^{64}Cu -labeled MNP solution was applied to an ITLC-SG plate (Pall Corporation, East Hills, NY) and developed using a 1:1 mixture (v/v) of 10% (w/v) ammonium acetate and methanol ($R_f = 0$ for ^{64}Cu -MNP and $R_f = 1$ for ^{64}Cu -EDTA and ^{64}Cu -acetate). The TLC plate was then measured using a Bioscan 200 imaging scanner (Bioscan Inc., Washington DC).

Radiochemical purity (RCP) of ^{64}Cu -MNP was evaluated by radio-fast protein liquid chromatography (radio-FPLC) using an Amersham Biosciences ÄKTA FLPC system (GE Healthcare, Piscataway, NJ) equipped with a UV detector (280nm) and fitted with an in-line Model 170 radioisotope detector (Beckman Coulter Inc., Fullerton, CA). A 100 µL sample of dilute ^{64}Cu -MNP (ca. 10 µCi) was applied to a Superose 12 gel filtration column (GE Healthcare, Piscataway, NJ) and eluted with 20 mM HEPES and 150 mM NaCl (pH 7.3) at a flow rate of 0.8 mL/min. The RCP of ^{64}Cu -MNP_{PEG}-RGD and ^{64}Cu -MNP_{PEG} was found to be > 98%. The nanoparticle solution was then diluted in 10 mM PBS (pH 7.4) to obtain doses (ca. 100 µCi) suitable for imaging and biodistribution studies. Serum stability of ^{64}Cu -MNP was measured by radio-TLC analysis after 0, 1, 3, 6, and 24 hr incubation in mouse serum at 37 °C with constant shaking.

5.2.5 Nanoparticle Phantom Imaging

The ability of ^{64}Cu -labeled magnetic nanoparticles to function as effective contrast agents for PET and MRI was assessed using an imaging phantom. Samples of radiolabeled nanoparticles

ranging in concentration from 0.1 to 25 $\mu\text{g Fe/mL}$ were prepared and scanned for 10 min in a Focus 120 microPET. After a period of time for sufficient ^{64}Cu decay (excess of 10 half-lives), labeled nanoparticles were reconstituted in 1% low-melting agarose and imaged in a 7.0-T Pharmascan scanner (Bruker BioSpin, Billerica, MA). T2 images were obtained using a multi-slice multi-echo sequence (2000 ms repetition time; 12 echoes ranging from 12-144 ms; 180° flip angle; 3 cm FOV; 1 mm slice thickness; 128×128 matrix; 4 averages; 234μ in-plane resolution)

5.2.6 Cellular Imaging Studies

Live cell imaging experiments were performed to determine the binding specificity of peptide-targeted dual PET/MRI nanoparticles. Human glioblastoma U87MG cells (ATCC, Manassas, VA) were cultured in low glucose DMEM (Invitrogen, Carlsbad, CA) supplemented with 10% FBS (ATCC), 100 U/mL penicillin, and 100 mg/mL streptomycin. Cell studies were performed using magnetic nanoparticles chelated with stable $^{63/65}\text{Cu}$ isotopes of copper (i.e. "cold") according to the procedure used for radiolabeling with copper-64. U87MG cells were cultured in 8-well Nunc Labtek II chambered coverslips (#1.5) (Thermo Fisher, Rochester, NY). After removal of growth medium, 65nM Alexa Fluor 647-conjugated magnetic nanoparticles in serum-free medium were added to cells and incubated for 30 minutes at 37°C . The nanoparticle/serum-free medium was removed and replaced with Opti-MEM (Invitrogen). Nanoparticle specificity was confirmed through blocking studies by incubating cells with $\text{Cu -MNP}_{\text{PEG}}\text{-RGD}$ in the presence of $5 \mu\text{M}$ c(RGDyC). Live cell images were obtained using a Zeiss Axiovert 200 epifluorescent microscope equipped with a 40X objective lens and AxioCam MRm cooled CCD camera.

5.2.7 M21/M21L Cell Uptake Assay

The M21 line ($\alpha_v\beta_3$ integrin-positive) was derived from a metastatic human melanoma lesion. The accompanying line, M21L, is an $\alpha_v\beta_3$ integrin-negative stable variant derived from the M21 that fails to synthesize α_v subunit mRNA. M21 and M21L lines were kindly provided by Dr. David Cheresh (Scripps Institute). Further details of the cell internalization assay are provided by Shokeen et al. M21 and M21L cells were maintained in RPMI 1640 supplemented with 10% FBS until reaching approximately 65-75% confluence. Uptake experiments were performed in triplicate.

Cells were detached from culture flasks using trypsin/EDTA, washed, and resuspended in PBS containing Ca and Mg. For each replicate, 1×10^6 M21 or M21L cells were incubated with 3 nM ^{64}Cu -MNP_{PEG}-RGD or ^{64}Cu -MNP_{PEG} (ca. 5 μCi). For blocking tests, cells and nanoparticles were incubated with 10 μM free c(RGDyC). Samples were incubated with nanoparticles for 30 min at 37 °C with gentle rocking using a tube rotator (Miltenyi Biotec). Samples were then pelleted (1400 rpm, 1 min) and washed 3 times with cold PBS. Cell pellets were promptly lysed using 0.5% sodium dodecyl sulfate (SDS), followed by counting in a gamma counter. After counting, protein content was determined using a BCA assay (Pierce) and counts were normalized by protein concentration.

5.2.8 Determination of Nanoparticle Biodistribution

All animal procedures were performed in compliance with guidelines set forth by the Georgia Institute of Technology Institutional Animal Care and Use Committee and the Washington University Animal Studies Committee. Female mice (BALB/c, M21/M21L tumor-bearing athymic, and U87MG tumor-bearing athymic) (Charles River Laboratories, Inc., Wilmington, MA) weighing approximately 20 g were anesthetized using 1-2 % isoflurane and given tail vein

injections of 100 μCi of ^{64}Cu –MNP_{PEG}–RGD or ^{64}Cu –MNP_{PEG} at a dose of 0.1 mg Fe/kg mouse body weight. Mice ($n = 4$ per time point) were sacrificed by cervical dislocation at 1 hr, 4 hr, and 24 hr post injection and organs of interest were collected, weighed, and activity was measured with a Gamma 8000 gamma counter (Beckman Coulter Inc., Fullerton, CA). Standard doses were prepared and measured along with the samples to allow calculation of the percentage injected dose (%ID) for the selected tissues. Data were corrected for ^{64}Cu decay and the percentage injected dose per gram of tissue (%ID/g) was calculated according to the following equation:

$$\%ID/g = \frac{(\text{cpm in sample} - \text{background}) \times 10^2}{(\text{decay correction factor}) \times (\text{sample weight}) \times (\text{cpm in standard dose})} \quad \text{Equation 5.1}$$

5.2.9 U87MG Tumor Model

Tumors were grown in female athymic *nu/nu* mice aged 3 to 4 weeks old (Charles River Laboratories). Mice received subcutaneous injections of 5×10^6 U87MG cells suspended in 100 μL PBS into the nape of the neck. Tumors were allowed to grow for approximately 3.5 weeks (200-500 mm^3 tumor volume) before use in imaging or biodistribution studies.

5.2.10 M21/M21L Tumor Model

A bilateral tumor model formed from subcutaneous inoculation with two different cell lines. The M21 line ($\alpha_v\beta_3$ integrin-positive) was derived from a metastatic human melanoma lesion. The accompanying line, M21L, is an $\alpha_v\beta_3$ integrin-negative stable variant derived from the M21 that fails to synthesize α_v subunit mRNA. M21 and M21L lines were kindly provided by Dr. David Cheresh (Scripps Institute). Tumors were grown in female athymic *nu/nu* mice aged 3 to 4 weeks old (Charles River Laboratories). Mice received subcutaneous injections of 1×10^6 M21L

and M21 cells suspended in 100 μ L PBS into the right and left rear flanks, respectively. Tumors were allowed to grow for approximately 4 – 6 weeks (0 -500 mm³ tumor volume) before use in imaging and biodistribution studies. Further details of the M21/M21L bilateral tumor model are given in chapter 4.

5.2.11 In Vivo PET/CT Imaging

MicroPET scans were performed using a microPET Focus 120 (Siemens Medical Solutions USA, Inc., Malvern, PA). U87MG tumor-bearing mice were anesthetized using 1-2 % isoflurane and given tail vein injections with 100 μ Ci of ⁶⁴Cu–MNP_{PEG}–RGD or ⁶⁴Cu–MNP_{PEG} (0.1 mg Fe/kg body weight) in 100 μ L PBS. Mice were reanesthetized and scanned in the supine position for 20 minutes at 24 hr post injection. Anatomical information was obtained from CT scans (microCAT II, Siemens Medical Solutions USA, Inc., Malvern, PA) performed immediately after completion of microPET. Analysis of microPET images was accomplished using vendor software (ASIPro, Siemens Medical Solutions USA, Inc.) on decay-corrected images. Coregistration of microPET and microCT images was performed by means of fiducial markers in the animal transfer bed and the Amira software package (Mercury Computer Systems, Inc., Chelmsford, MA). Post-PET biodistribution of tumor-bearing mice was performed as outlined above immediately following microPET imaging.

5.2.12 In Vivo MR Imaging

U87MG tumor-bearing mice underwent MR imaging immediately before and 24 hr after receiving tail vein injections of cold Cu–MNP_{PEG}–RGD or Cu–MNP_{PEG} (10 mg Fe/kg body weight) in 100 μ L PBS ($n = 4$). Animals were anesthetized using 1-2 % isoflurane and connected to an MR-compatible monitoring and gating system (Model 1025, SA Instruments, Inc., Stony Brook,

NY). Cardiac gating was performed by affixing neonatal electrodes (3M Corp., St. Paul, MN) to the forepaws using conducting electrode cream (Grass Technologies, West Warwick, RI), and respiratory gating was performed by means of a respiratory pillow (SA Instruments). Temperature was maintained using a water-filled blanket fed by a thermostatically controlled heating pump. Animals were placed in the prone position on an imaging bed and positioned in the bore of a 7.0-T Pharmascan MRI scanner (Bruker BioSpin, Billerica, MA). Tumor images were obtained using a multi-slice multi-echo sequence and a 30 mm mouse body volume coil (Bruker BioSpin) with the following parameters: SE TR/(TE), 2000 ms/(12, 24, 36, 48, 60, 72, 84, 96, 108, 120, 132, 144) ms; flip angle, 180°; matrix size, 128 × 128; field of view, 3 × 3 cm; in-plane resolution, 234 μm; slice thickness, 1 mm; slices acquired, 8; slice orientation, axial; averages, 4; scan time, 17 min 4 s. Tumor ROIs were defined using ParaVision 4 (Bruker BioSpin), and T2 colormaps were generated using MATLAB (MathWorks, Inc., Natick, MA).

5.3 Results

5.3.1 Nanoparticle Conjugation

To prepare nanoparticles for dual PET/MR imaging, cross-linked iron oxide magnetic nanoparticle were functionalized with the macrocyclic ligand DOTA to allow radiolabeling by chelation of copper-64 (Figure 5.1A). The cross-linked, aminated polysaccharide coating of the nanoparticles provides a site for attachment of DOTA and RGD peptides. DOTA-NHS was reacted with the nanoparticle coating followed by removal of any unreacted DOTA-NHS. DOTA-MNP was further modified by conjugating NHS-PEG-Maleimide to the polysaccharide coating, providing a flexible linker for attachment of integrin-targeting RGD peptides. The maleimide group on the activated intermediate product, DOTA-MNP_{PEG}-Mal, is susceptible to hydrolysis (15) and rapid purification using desalting spin columns was employed. Purified DOTA-MNP_{PEG}-

Mal was then reacted with the thiol-containing c(RGDyC). The final product, DOTA–MNP_{PEG}–RGD is shown in Figure 5.1B.

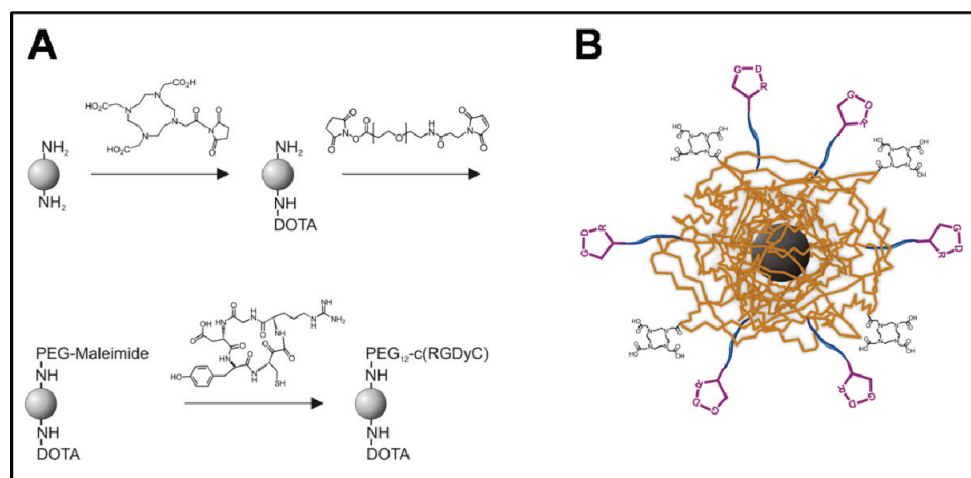


Figure 5.1: Development of $\alpha_v\beta_3$ integrin-targeted dual PET/MRI nanoparticles. (A) Conjugation scheme showing reaction of amino-CLIO with DOTA-NHS ester, followed by PEGylation and conjugation with c(RGDyC) (B) Schematic representation dual-modality ^{64}Cu -MNP_{PEG}-RGD. ^{64}Cu -MNP_{PEG} was synthesized in a similar fashion, except methoxy-terminated PEG was conjugated to the particle surface.

On average, 43 ± 9 c(RGDyC) peptides were conjugated to DOTA–MNP to allow targeting of $\alpha_v\beta_3$ integrin. The hydrodynamic diameter of nanoparticles was determined by dynamic light scattering (DLS). DOTA–MNP_{PEG}-RGD and DOTA–MNP_{PEG} were found to have diameters of 42 ± 6 nm and 34 ± 5 nm, respectively (Figure 5.2A). The ξ -potential of DOTA–MNP_{PEG}-RGD and DOTA–MNP_{PEG} was 4 mV and 7 mV. The small positive charge is attributed unreacted amine groups buried within the dextran coating.

5.3.2 Nanoparticle Radiolabeling

The positron-emitting radionuclide ^{64}Cu ($t_{1/2} = 12.7$ hr; $\beta^+ = 0.653$ MeV, 17.4%; $\beta^- = 0.578$ MeV, 39%) was used to radiolabel DOTA–MNP_{PEG}-RGD, allowing PET imaging and biodistribution

studies. Copper-64 can be produced at high specific activity and yield in biomedical cyclotrons (16, 17). Chelation of ^{64}Cu to various macrocyclic ligands provides an efficient route for radiolabeling a range of macromolecules and nanoprobe (18).

Highly efficient labeling of DOTA-MNP_{PEG}-RGD was obtained by incubation with ^{64}Cu at 37 °C for 1 hr in 0.1 M ammonium acetate buffer, pH 5.5. In this study ^{64}Cu -MNP_{PEG}-RGD was labeled to a specific activity of 45 $\mu\text{Ci}/\mu\text{g}$ (specific activity of up to 70 $\mu\text{Ci}/\mu\text{g}$ was achieved with this compound in related studies). Nonspecifically bound ^{64}Cu was removed by addition of EDTA (18) upon completion of the labeling reaction, and ^{64}Cu -EDTA was separated from ^{64}Cu -MNP_{PEG}-RGD using a desalting spin column. The radiochemical purity of the purified nanoparticles, determined by radio-FPLC, was found to be in excess 98%. The labeling yield was 82-85% by radio-TLC. ^{64}Cu -MNP_{PEG}-RGD incubated in mouse serum at 37 °C for 24 hr retained $98.2 \pm 0.2\%$ of the radioactive ^{64}Cu (decay corrected), an indication of high *in vitro* stability (Figure 5.2B).

5.3.3 Phantom Studies

The dual-modality imaging capability of ^{64}Cu -MNP_{PEG}-RGD nanoparticles was evaluated by subjecting a nanoparticle imaging phantom to standard PET and MR scans (Figure 5.2C). The T2-weighted MR image shows a clear change in contrast with iron concentration. The PET image shows corresponding concentration-dependent signal intensity. We determined the MRI detection threshold for ^{64}Cu -MNP_{PEG}-RGD in this study to be $\approx 5 \mu\text{g Fe/mL}$, while the microPET threshold was 0.1-0.5 $\mu\text{g Fe/mL}$, in agreement with previously reported values (5).

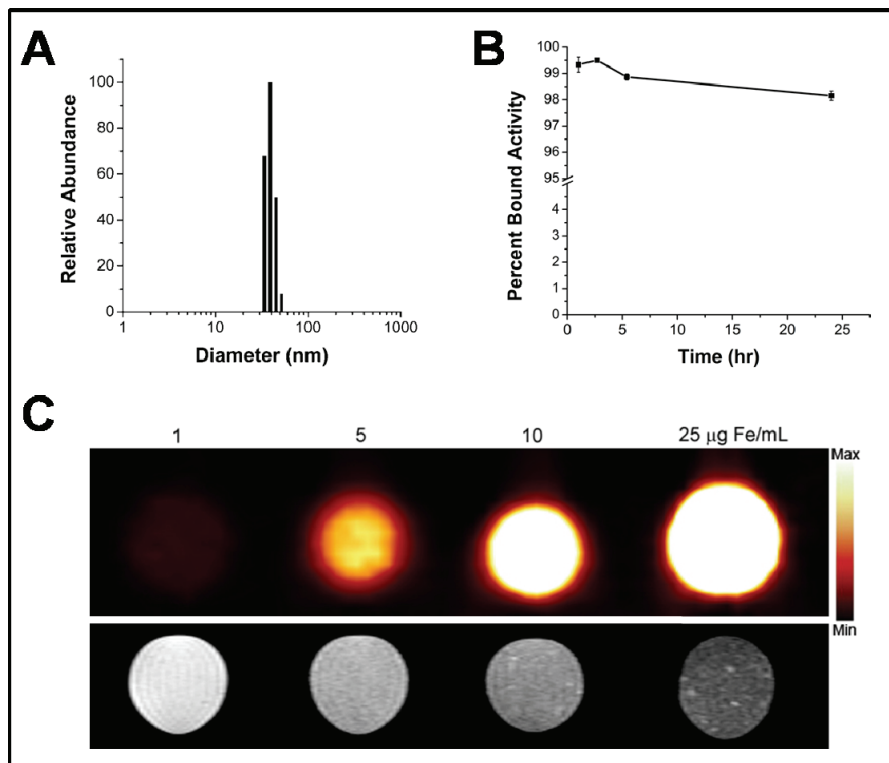


Figure 5.2: Characterization of ^{64}Cu -MNP_{PEG}-RGD. (A) Dynamic light scattering of ^{64}Cu -MNP_{PEG}-RGD showing a diameter of 42 ± 6 nm. (B) Serum stability of ^{64}Cu -MNP_{PEG}-RGD as determined by radio-TLC. (C) Phantom image of nanoparticles imaged by PET (top row) and MRI (bottom row).

5.3.4 Cellular Imaging Studies

In vitro cell binding assays were employed to evaluate the $\alpha_v\beta_3$ integrin targeting of MNP_{PEG}-RGD. U87MG human glioblastoma cells (19), known to express high levels of $\alpha_v\beta_3$ integrin (20), were incubated for 30 min at 37 °C with 65 nM of Alexa Fluor 647-labeled DOTA-MNP_{PEG}-RGD or DOTA-MNP_{PEG}. Binding of DOTA-MNP_{PEG}-RGD to U87MG cells was observed, while no significant binding of DOTA-MNP_{PEG} occurred (Figure 5.3). In the case of DOTA-MNP_{PEG}-RGD, nanoparticle binding to U87MG cells could be blocked by the addition of 5 μM c(RGDyC) to the binding medium during incubation.

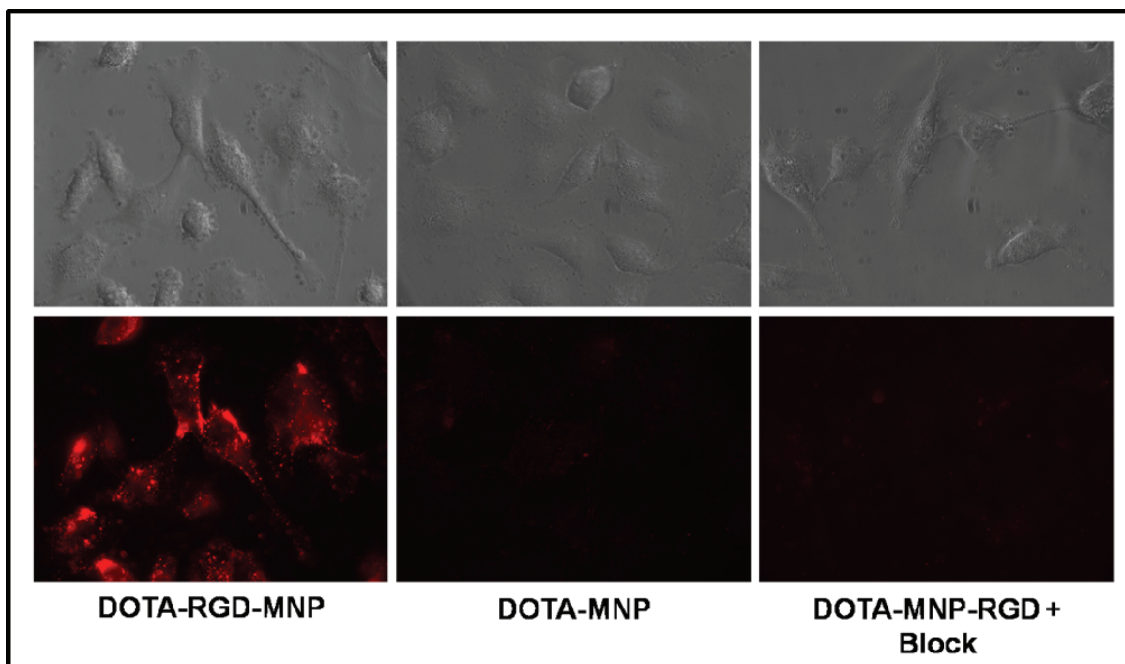


Figure 5.3: Live cell nanoparticle imaging. Bottom row shows targeting of $\alpha_v\beta_3$ integrin-expressing U87MG cells with 65 nM $^{64}\text{Cu-MNP}_{\text{PEG-RGD}}$, $^{64}\text{Cu-MNP}_{\text{PEG}}$, and $^{64}\text{Cu-MNP}_{\text{PEG-RGD}}$ in the presence of 5 μM c(RGDyC). Top row shows corresponding white light images.

5.3.5 M21/M21L Cell Uptake Assay

In vitro cell uptake assays were performed using $^{64}\text{Cu-MNP}_{\text{PEG-RGD}}$ and $^{64}\text{Cu-MNP}_{\text{PEG}}$ with and without concomitant blocking by addition of excess free c(RGDyC) peptide. M21 metastatic human melanoma cells express $\alpha_v\beta_3$ integrin with the variant line M21L is $\alpha_v\beta_3$ integrin-negative. Cells were incubated for 30 min at 37 °C with 3 nM $^{64}\text{Cu-MNP}_{\text{PEG-RGD}}$ or $^{64}\text{Cu-MNP}_{\text{PEG}}$. Blocking was accomplished by adding 10 μM free RGD peptide. Binding of $^{64}\text{Cu-MNP}_{\text{PEG-RGD}}$ to M21 cells was observed, while no significant binding of $^{64}\text{Cu-MNP}_{\text{PEG}}$ occurred (Figure 5.4). Uptake of $^{64}\text{Cu-MNP}_{\text{PEG-RGD}}$ was blocked by addition of excess RGD peptide. M21L showed no uptake of $^{64}\text{Cu-MNP}_{\text{PEG-RGD}}$ or $^{64}\text{Cu-MNP}_{\text{PEG}}$, with or without RGD blocking.

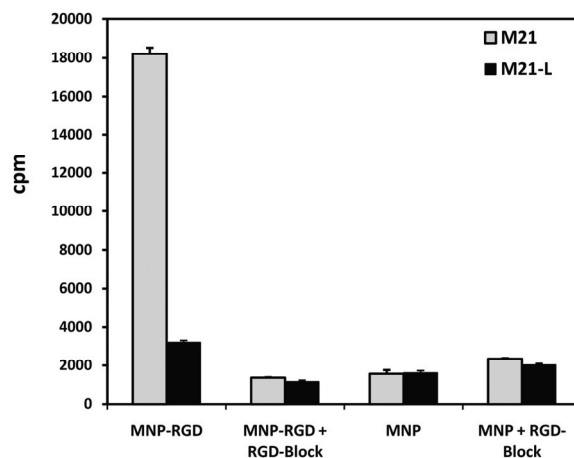


Figure 5.4: M21/M21L cell uptake of peptide-targeted magnetic nanoparticles. Binding of ^{64}Cu -MNP_{PEG}-RGD to $\alpha_v\beta_3$ integrin-positive M21 cells was observed, while no significant binding of ^{64}Cu -MNP_{PEG} occurred. Uptake of ^{64}Cu -MNP_{PEG}-RGD was blocked by addition of 10 μM RGD peptide. M21L cells ($\alpha_v\beta_3$ integrin-negative) showed no uptake of ^{64}Cu -MNP_{PEG}-RGD or ^{64}Cu -MNP_{PEG}, with or without RGD blocking.

5.3.6 Biodistribution of Peptide-targeted Dual PET/MRI Nanoparticles in BALB/c Mice

To evaluate the *in vivo* kinetics and biodistribution of RGD-functionalized dual-modality nanoparticles, BALB/c mice were injected with a low dose of nanoparticles labeled at high specific activity (100 μCi of ^{64}Cu -MNP labeled at 45 $\mu\text{Ci}/\mu\text{g}$, corresponding to 0.1 mg Fe/kg mouse body weight) and the biodistribution of selected organs was measured at 1 hr, 4hr, and 24 hr post injection (Table 5.1). RGD-functionalized nanoparticles exhibited high uptake by organs of the reticuloendothelial system (e.g. liver, spleen, bone) compared to non-functionalized nanoparticles. ^{64}Cu -MNP_{PEG}-RGD experiences rapid blood clearance after 1 hr, while ^{64}Cu -MNP_{PEG} remains at high levels at each time point. ^{64}Cu -MNP_{PEG} concentration in the heart, muscle, and fat was greater than that of ^{64}Cu -MNP_{PEG}-RGD, presumably due to the low blood concentration of ^{64}Cu -MNP_{PEG}-RGD.

Table 5.1: Biodistribution of ⁶⁴Cu-labeled, RGD-functionalized magnetic nanoparticles in female BALB/c mice

Organ	⁶⁴ Cu-RGD-MNP			⁶⁴ Cu-MNP		
	1 hr	4 hr	24 hr	1 hr	4 hr	24 hr
Blood	18.1 ± 3.50	1.1 ± 0.2	0.9 ± 0.0	46.9 ± 2.4	42.4 ± 4.1	23.5 ± 2.9
Lung	7.8 ± 1.30	4.2 ± 0.5	4.7 ± 0.4	13.2 ± 1.4	16.3 ± 2.1	9.5 ± 2.0
Liver	55.0 ± 3.10	77.9 ± 3.2	62.0 ± 6.7	11.3 ± 1.4	12.6 ± 1.0	20.5 ± 3.9
Spleen	65.6 ± 5.40	111.0 ± 10.0	135.3 ± 12.0	7.7 ± 2.4	9.0 ± 1.3	22.5 ± 5.2
Kidney	6.4 ± 1.00	5.9 ± 0.7	6.3 ± 0.5	7.0 ± 0.5	6.7 ± 1.1	6.9 ± 0.6
Muscle	0.9 ± 0.10	0.5 ± 0.1	0.5 ± 0.1	1.5 ± 0.4	1.8 ± 0.4	1.9 ± 0.2
Fat	2.2 ± 0.70	1.1 ± 0.9	0.7 ± 0.4	2.8 ± 1.1	3.5 ± 0.8	2.3 ± 0.7
Heart	3.5 ± 1.00	1.8 ± 0.2	2.2 ± 0.1	9.4 ± 2.6	8.5 ± 2.7	4.3 ± 0.5
Bone	4.9 ± 0.50	6.0 ± 0.9	5.7 ± 0.4	2.9 ± 0.5	2.9 ± 0.0	2.6 ± 0.3

Data are presented as percentage injected dose per gram (%ID/g) ± SD (n = 4).

5.3.7 Biodistribution of Peptide-targeted Dual PET/MRI Nanoparticles in U87MG Tumor-bearing Mice

The biodistribution of ⁶⁴Cu-labeled nanoparticles in U87MG tumor-bearing athymic mice at a dose of 0.1 mg Fe/kg body weight (Table 5.2) was similar to the pattern observed in BALB/c mice at 24 hr (Table 5.1). RES organ uptake of ⁶⁴Cu–MNP_{PEG}–RGD was prominent (liver, 50.4 ± 5.1; spleen, 61.1 ± 14.7; and bone, 5.8 ± 1.9 %ID/g), while blood activity was greatly diminished at 24 hr (1.0 ± 0.3 %ID/g). In the absence of peptide functionalization, ⁶⁴Cu–MNP_{PEG} nanoparticles showed reduced RES organ accumulation (liver, 22.4 ± 11.5.; spleen, 13.7 ± 7.1; and bone, 1.9 ± 0.4 %ID/g) and a ≈ 16 fold higher blood concentration relative to RGD-conjugated nanoparticles.

Table 5.2: Biodistribution of ^{64}Cu -labeled, RGD-functionalized magnetic nanoparticles in U87MG tumor-bearing mice at 24 hr post injection

Organ	%ID/g	
	^{64}Cu -RGD-MNP	^{64}Cu -MNP
Blood	1.0 ± 0.3	16.7 ± 1.5
Lung	4.6 ± 0.9	7.7 ± 1.6
Liver	50.4 ± 5.1	22.4 ± 11.5
Spleen	61.1 ± 14.7	13.7 ± 7.1
Kidney	6.4 ± 0.7	5.7 ± 0.8
Muscle	0.5 ± 0.1	2.3 ± 0.6
Fat	0.4 ± 0.2	2.2 ± 1.0
Heart	1.9 ± 0.3	4.8 ± 0.3
Brain	0.1 ± 0.0	0.8 ± 0.3
Bone	5.8 ± 1.9	1.9 ± 0.4
Tumor	3.1 ± 0.7	6.2 ± 0.8

Data are presented as percentage injected dose per gram (%ID/g) ± SD (n = 6 or 4) at 24 h post-injection.

Accumulation of ^{64}Cu -MNP_{PEG} in several non-target organs (heart, 4.8 ± 0.3; muscle, 2.3 ± 0.6; and fat, 2.2 ± 1.0 %ID/g) was greater than accumulation of ^{64}Cu -MNP_{PEG}-RGD (heart, 1.9 ± 0.3; muscle, 0.5 ± 0.1; and fat, 0.4 ± 0.2 %ID/g) due to the large difference in blood concentration between the two nanoparticles. U87MG tumor uptake of ^{64}Cu -MNP_{PEG}-RGD and ^{64}Cu -MNP_{PEG} was 3.1 ± 0.7 %ID/g and 6.2 ± 0.8 %ID/g, respectively.

To evaluate the U87MG tumor-to-background activity, and to account for the significant difference in blood concentration exhibited by ^{64}Cu -MNP_{PEG}-RGD and ^{64}Cu -MNP_{PEG}, tumor-to-tissue ratios were calculated for selected organs (Figure 5.5). In general, ratios of tissues surrounding tumors of animals administered ^{64}Cu -MNP_{PEG}-RGD (blood, 3.4 ± 1.7; muscle, 6.4 ± 2.2; and fat, 8.9 ± 4.7 %ID/g) were significantly higher than for those administered ^{64}Cu -MNP_{PEG} (blood, 0.4 ± 0.1; muscle, 2.9 ± 0.8; and fat, 3.4 ± 1.8 %ID/g).

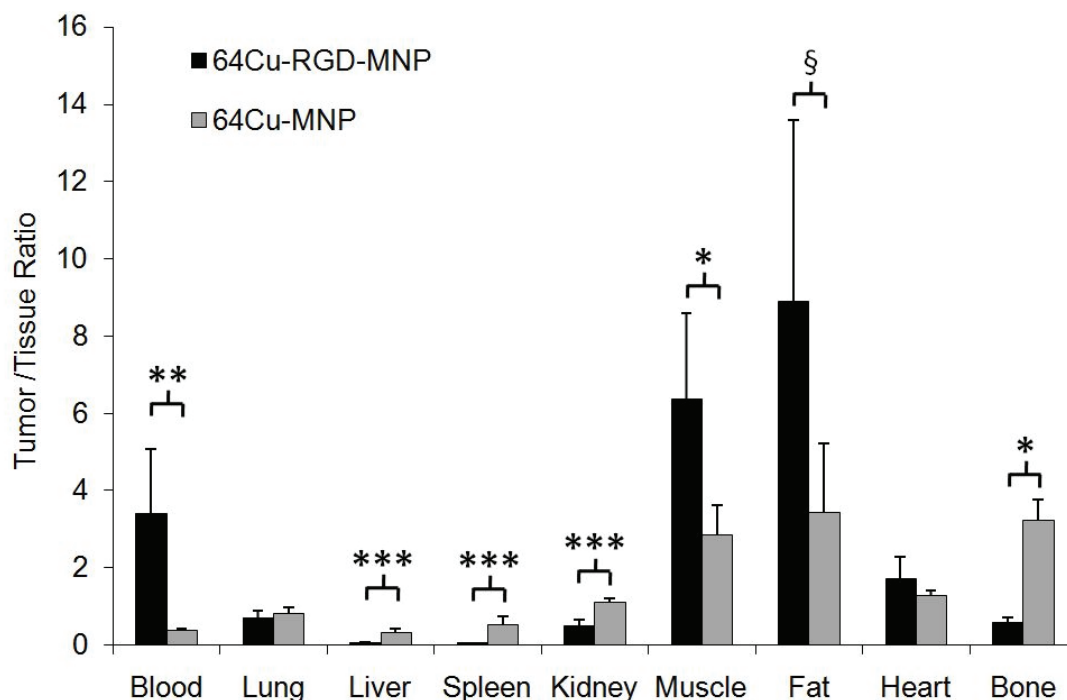


Figure 5.5: Tumor/tissue ratios. Comparison of U87MG tumor/tissue ratios for $^{64}\text{Cu-MNP}_{\text{PEG-RGD}}$ and $^{64}\text{Cu-MNP}_{\text{PEG}}$. $^{64}\text{Cu-MNP}_{\text{PEG-RGD}}$ showed a significantly higher tumor/tissue ratio for non-target tissue surrounding the tumor site (e.g. muscle, blood, fat). Error bars represent SD ($n = 4$ or 6) (* $P < 0.05$, ** $P < 0.01$, *** $P < 0.001$, § $P = 0.06$).

5.3.8 Biodistribution of Peptide-targeted Dual PET/MRI Nanoparticles in M21/M21L Tumor-bearing Mice

The biodistribution of ^{64}Cu -labeled nanoparticles in M21/M21L tumor-bearing athymic mice at a dose of 0.1 mg Fe/kg body weight (Table 5.3) was similar to the pattern observed in U87MG tumor-bearing mice at 24 hr (Table 5.2). RES organ uptake of $^{64}\text{Cu-MNP}_{\text{PEG-RGD}}$ was also prominent while blood activity was greatly diminished at 24 hr (1.0 ± 0.3 %ID/g). No difference in nanoparticle accumulation by M21 and M21L tumors was observed. Tumor-to-blood and tumor-to-muscle for $^{64}\text{Cu-MNP}_{\text{PEG-RGD}}$ remains significantly higher than that of $^{64}\text{Cu-MNP}_{\text{PEG}}$.

Table 5.3: Biodistribution of ⁶⁴Cu-labeled, RGD-functionalized magnetic nanoparticles in M21/M21L bilateral tumor-bearing mice at 24 hr post injection

Biodistribution	%ID/g		%ID/organ	
	MNP-RGD	MNP	MNP-RGD	MNP
Blood	0.93 ± 0.21	21.36 ± 1.71	1.39 ± 0.27	31.14 ± 3.37
Lung	5.41 ± 1.13	11.23 ± 1.82	0.87 ± 0.17	1.74 ± 0.49
Liver	59.02 ± 8.08	17.66 ± 7.78	49.97 ± 5.12	16.15 ± 6.13
Spleen	86.35 ± 16.36	19.86 ± 12.86	4.91 ± 1.73	1.09 ± 0.65
Kidney	6.62 ± 1.34	6.48 ± 1.25	0.98 ± 0.23	0.88 ± 0.14
Muscle	0.40 ± 0.07	2.12 ± 0.21	3.47 ± 0.63	18.16 ± 2.64
Fat	2.49 ± 3.12	2.73 ± 1.00	7.37 ± 9.60	7.73 ± 2.64
Heart	2.19 ± 0.58	4.92 ± 1.31	0.23 ± 0.07	0.50 ± 0.26
Brain	0.21 ± 0.03	1.12 ± 0.50	0.08 ± 0.02	0.43 ± 0.20
Bone	7.03 ± 2.30	2.99 ± 0.37	16.20 ± 4.73	6.78 ± 0.80
M21-L	1.55 ± 0.40	3.97 ± 1.34	0.37 ± 0.33	0.36 ± 0.20
M21	1.48 ± 0.34	4.33 ± 1.55	0.35 ± 0.39	0.47 ± 0.36

Data are presented as percentage injected dose per gram (%ID/g) and percentage injected dose per organ (%ID/organ) ± SD. (MNP, n = 7; MNP-RGD, n = 8)

5.3.9 In Vivo PET imaging of Nanoparticle Accumulation in U87MG Tumors

Tumor-bearing mice were administered a 0.1 mg Fe/kg dose (100 μCi) of ⁶⁴Cu–MNP_{PEG}–RGD (*n* = 6) or ⁶⁴Cu–MNP_{PEG} (*n* = 4) and microPET-CT images were acquired at 24 hr post injection (Figure 5.6, Figure 5.7). Both nanoparticles produced PET signal in U87MG tumors, in agreement with biodistribution studies. However, tumors were clearly visible when imaged using RGD-targeted particles due to high tumor-to-background ratios, while the high background activity exhibited by untargeted nanoparticles obscured tumor visualization. Prominent uptake of ⁶⁴Cu–MNP_{PEG}–RGD by the liver and spleen could be observed. Accumulated activity could also be seen in the bone, with marked uptake along the lumbar region of the vertebral column and the ilium. ⁶⁴Cu–MNP_{PEG} displayed low overall liver, spleen, and bone activity relative to RGD-targeted nanoparticles. A widespread, diffuse accumulation of ⁶⁴Cu–MNP_{PEG} was visible in all animals, due to its extended blood retention. ⁶⁴Cu–MNP_{PEG} was observed in the heart and carotid arteries due to the prolonged blood retention.

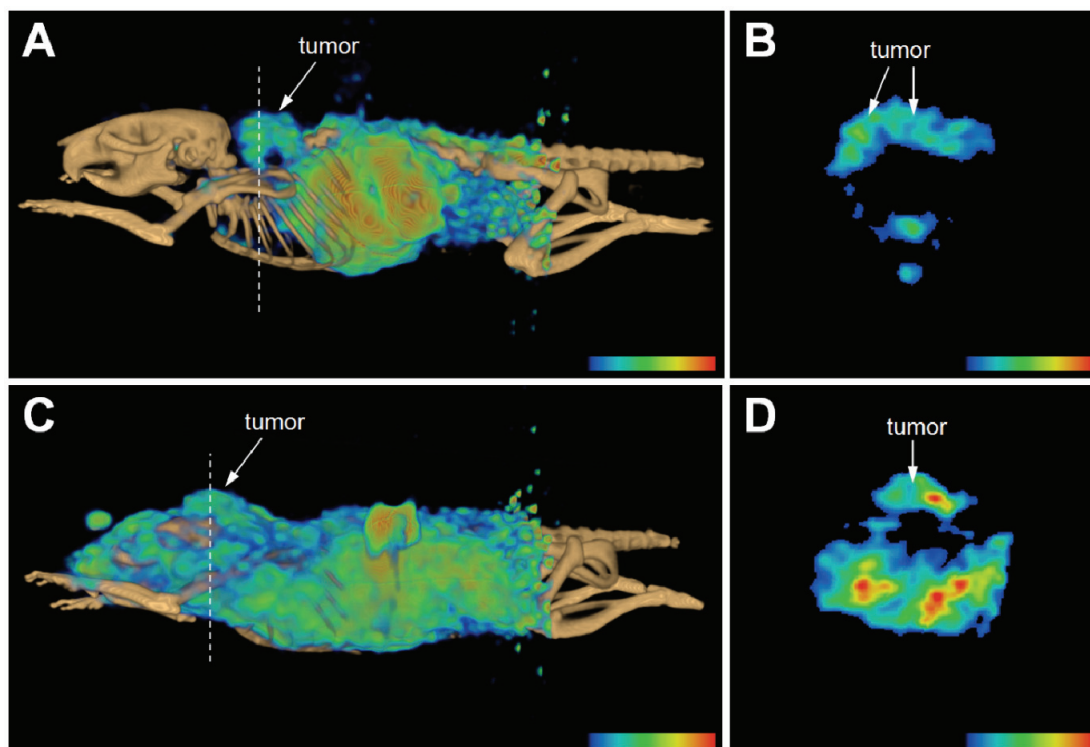


Figure 5.6: MicroPET/CT imaging $^{64}\text{Cu-MNP}_{\text{PEG-RGD}}$ (A, B) and $^{64}\text{Cu-MNP}_{\text{PEG}}$ (C, D) in U87MG tumor-bearing mice at 24 hr post-injection. (A, C) 3D PET/CT images show clear tumor delineation using RGD-targeted nanoparticles (A), while untargeted nanoparticles (C) resulted in widespread uptake. (B, D) Axial slices corresponding to dotted line in 3D PET/CT images.

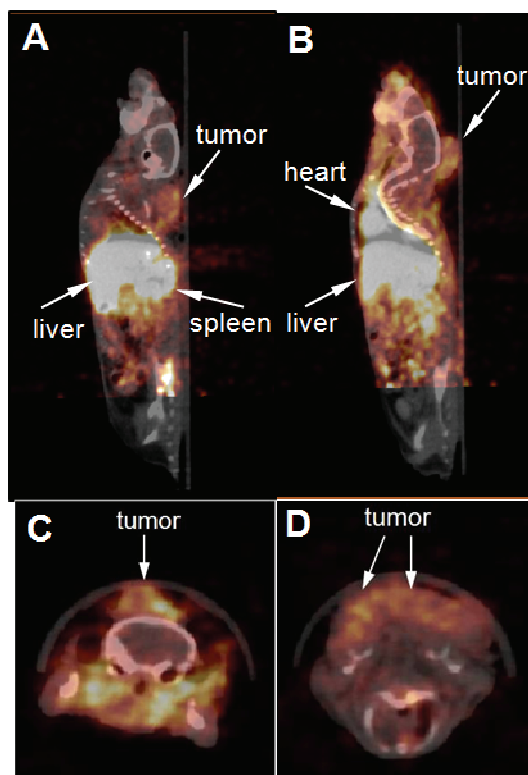


Figure 5.7: Alternate microPET/CT images of $^{64}\text{Cu-MNP}_{\text{PEG-RGD}}$ (A, C) and $^{64}\text{Cu-MNP}_{\text{PEG}}$ (B, D) in U87MG tumor-bearing mice at 24 hr post-injection. (A,B) Sagittal PET/CT images show clear tumor delineation using RGD-targeted nanoparticles (A), while untargeted nanoparticles (B) resulted in widespread uptake. (C, D) Axial slices corresponding to dotted lines in Figure 5.6.

5.3.10 In Vivo MRI of Nanoparticle Accumulation in U87MG Tumors

To examine the MR imaging potential of dual-modality nanoparticles, cold RGD-targeted magnetic nanoparticles were evaluated in tumor-bearing mice. Animals were scanned using a multi-slice multi-echo sequence to obtain T2-weighted tumor images. Animals were administered $\text{Cu-MNP}_{\text{PEG-RGD}}$ or $\text{Cu-MNP}_{\text{PEG}}$ and imaged again at 24 hr post-injection. T2 maps of tumors were generated and quantitative analysis of nanoparticle accumulation was performed.

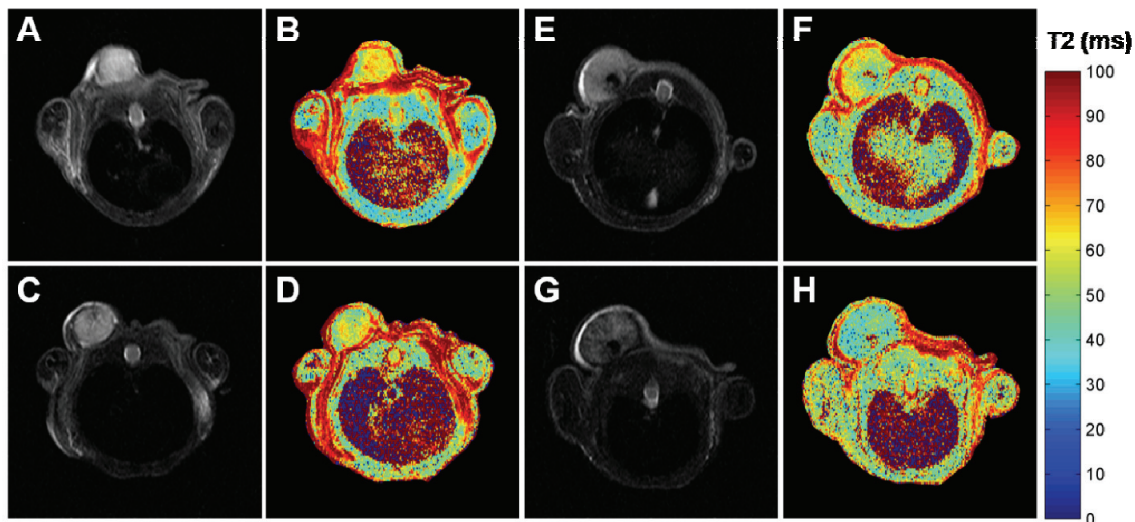


Figure 5.8: MR Imaging of Cu-MNPPEG-RGD (A-D) and Cu-MNPPEG (E-H) in tumor-bearing mice at before (top row, A-F) and 24 hr after (bottom row, C-H) injection. A decrease in mean tumor T2 resulting from administration of RGD-targeted nanoparticles can be observed in T2-weighted images (A, C) and in corresponding T2 maps (B, D). Non-targeted nanoparticles, with high blood concentration, also produced a decrease in mean tumor T2 after injection, shown in both T2-weighted images (E, G) and T2 colormaps (F, H).

MRI of U87MG tumors showed a contrast enhancement 24 hr after injection of dual-modality nanoparticles. T2-weighted images of tumors after MNP injection show a negative contrast enhancement (signal hypointensity) compared to pre-injection images (Figure 5.8). Analysis of the corresponding multi-echo T2 maps showed decrease in mean tumor T2 twenty four hours after injection of dual-modality nanoparticles.

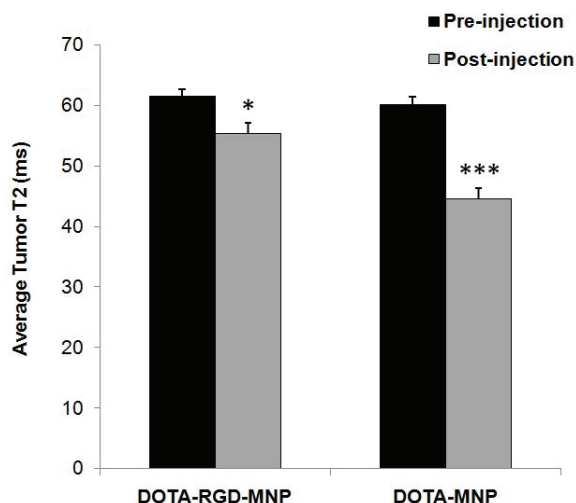


Figure 5.9: Quantitative evaluation of mean tumor T2 before and 24 hr after injection with $^{64}\text{Cu-MNP}_{\text{PEG-RGD}}$ ($n = 6$) or $^{64}\text{Cu-MNP}_{\text{PEG}}$ ($n = 4$). Error bars represent SD (* $P < 0.05$, * $P < 0.001$).**

While both $\text{Cu-MNP}_{\text{PEG-RGD}}$ and $\text{Cu-MNP}_{\text{PEG}}$ produced contrast enhancement in MRIs, the decrease in mean tumor T2 produced by $\text{Cu-MNP}_{\text{PEG-RGD}}$ (preinjection, 61.7 ± 1.2 ms; postinjection, 55.7 ± 2.1) was less than the decrease produced by $\text{Cu-MNP}_{\text{PEG}}$ (preinjection, 60.1 ± 1.4 ms; postinjection, 44.6 ± 1.8) (Figure 5.9). No measurable decrease in mean muscle or bone T2 was observed for either nanoparticle.

5.4 Discussion

Since its inception in the 1990s (21-23), PET/CT has combined the high sensitivity detection of PET with the anatomical orientation of CT, leading to improved accuracy in cancer detection (23), staging, and restaging (24, 25). Currently, PET/CT is the gold standard in general oncologic imaging (26). Unfortunately, CT scans expose patients to considerable amounts of radiation in addition to the PET tracers used in PET/CT scans. Combining PET with MRI would pair the superior resolution and soft tissue contrast as well as the functional and spectroscopic capabilities of MRI with the high sensitivity of PET (27-31). Whole-body imaging ability of PET

could aid in identification of distant lesions that could otherwise go undetected in MR scans. Interest in combining PET with MRI has surged (1, 2, 4, 6), and structured nanomaterials have emerged as possible a platform for the development of dual-PET/MR imaging agents. The unique properties of nanoparticles lend themselves to the design of PET probes. The large surface area of nanoparticles can be labeled at high specific activity, thus increasing the sensitivity of detection and payload of therapeutic isotopes and targeting ligands. To date, the majority of nanoparticles developed as PET molecular imaging agents have been polymer-based (32-34). Recently, several PET/MRI nanoparticles have been described for applications in lymph node (8), macrophage (5), and tumor imaging (6).

In this study we have combined an established magnetic nanoparticle platform (35) with a positron-emitting tracer to develop a tumor-targeted, dual-modality nanoparticle for PET/MR imaging. Magnetic nanoparticles were functionalized with polyethylene glycol to allow attachment of targeting ligands. The resulting monodisperse particles were extensively functionalized $\alpha_v\beta_3$ integrin-targeting peptides to provide multivalent enhancement of binding (36). Nanoparticles were labeled at high specific activity and exhibited strong stability in mouse serum over 24 hr, and phantom studies confirmed the dual PET/MR imaging ability of ^{64}Cu -MNP. RDG-dependent targeting of nanoparticles to $\alpha_v\beta_3$ integrin was demonstrated using a U87MG cell imaging assays showed

Biodistribution studies revealed a strong RES uptake of peptide-functionalized MNP, leading to a discrepancy in the kinetics of blood clearance and organ distribution of targeted versus non-targeted nanoparticles. The reduced blood half-life of ^{64}Cu -MNP_{PEG}-RGD may have decreased its opportunity to escape the vasculature (35) and bind to $\alpha_v\beta_3$ integrin on U87MG cells deep inside the tumor. This phenomenon would limiting nanoparticle targeting to only vascular $\alpha_v\beta_3$ integrin, thus decrease the pool of target molecules available to the nanoparticle

and reducing signal to noise. The blood concentration of $^{64}\text{Cu-MNP}_{\text{PEG}}$ at 24 hr was 16-fold higher than that of $^{64}\text{Cu-MNP}_{\text{PEG-RGD}}$, yet the tumor uptake was only 2-fold higher. Additionally, the tumor-to-background of untargeted nanoparticles was significantly lower than RGD-targeted nanoparticles (Figure 5.5). These observations indicate an RGD-dependent tumor uptake and produce substantially enhanced delineation of tumors in PET images (Figure 5.6, Figure 5.7).

The similarity in uptake by M21 and M21L tumors (Table 5.3) may be explained by the rapid blood clearance of $^{64}\text{Cu-MNP}_{\text{PEG-RGD}}$. Both M21 and M21L tumors will have angiogenic blood vessels. The endothelial cells forming the new blood vessels in both M21 and M21L tumors will express $\alpha_v\beta_3$ integrin. RGD nanoparticles may be cleared from the blood before they are able to leak into the extra-vascular space and bind to $\alpha_v\beta_3$ integrin in M21 cells. In this scenario, where particles are cleared before vascular escape, $^{64}\text{Cu-MNP}_{\text{PEG-RGD}}$ would only bind to endothelial $\alpha_v\beta_3$ integrin. Since M21 and M21L express similar amounts of vascular $\alpha_v\beta_3$ integrin the nanoparticles bind the same amount of $\alpha_v\beta_3$ integrin in each lesion. This would explain why excellent targeting was observed *in vitro* but not *in vivo*.

Magnetic resonance imaging detected the presence of nanoparticles in U87MG tumors at 24 hr post injection. A greater decrease in mean tumor T2 was produced by the $\text{Cu-MNP}_{\text{PEG}}$ (6.2 ± 2.1 ms) than by $\text{Cu-MNP}_{\text{PEG-RGD}}$ (15.5 ± 2.3 ms, $P < 0.01$) (Figure 5.9). Comparison of mean muscle T2 showed no significant decrease upon administration of either nanoparticle, precluding a tumor-to-background comparison. The inherent low T2 of muscle (26-32 ms at 7.0 T) and the use of a volume coil may have decreased the ability to detect small differences in muscle accumulation of nanoparticles.

In conclusion, we report the development of $\alpha_v\beta_3$ integrin-targeted magnetic nanoparticles for dual-PET/MR imaging. Nanoparticles were labeled with ^{64}Cu at high specific

activity and radiochemical purity. Conjugation of c(RGDyC) to magnetic nanoparticles resulted in specific targeting of $\alpha_v\beta_3$ integrin *in vitro*, as well as pronounced tumor delineation *in vivo*. MRI studies showed an accumulation of nanoparticles in tumors, however peptide-targeted nanoparticles did not show a distinct advantage over non-targeted nanoparticles. These findings provide insight into the design and development of future multimodality PET/MRI probes.

5.5 References

1. Catana, C., D. Procissi, Y. Wu, M.S. Judenhofer, J. Qi, B.J. Pichler, R.E. Jacobs, and S.R. Cherry, *Simultaneous in vivo positron emission tomography and magnetic resonance imaging*. Proc Natl Acad Sci U S A, 2008. **105**(10): p. 3705-10.
2. Judenhofer, M.S., H.F. Wehrl, D.F. Newport, C. Catana, S.B. Siegel, M. Becker, A. Thielscher, M. Kneilling, M.P. Lichy, M. Eichner, K. Klingel, G. Reischl, S. Widmaier, M. Rocken, R.E. Nutt, H.J. Machulla, K. Uludag, S.R. Cherry, C.D. Claussen, and B.J. Pichler, *Simultaneous PET-MRI: a new approach for functional and morphological imaging*. Nat Med, 2008. **14**(4): p. 459-65.
3. Pichler, B.J., M.S. Judenhofer, and H.F. Wehrl, *PET/MRI hybrid imaging: devices and initial results*. Eur Radiol, 2008. **18**(6): p. 1077-86.
4. Pichler, B.J., H.F. Wehrl, A. Kolb, and M.S. Judenhofer, *Positron emission tomography/magnetic resonance imaging: the next generation of multimodality imaging?* Semin Nucl Med, 2008. **38**(3): p. 199-208.
5. Nahrendorf, M., H. Zhang, S. Hembrador, P. Panizzi, D.E. Sosnovik, E. Aikawa, P. Libby, F.K. Swirski, and R. Weissleder, *Nanoparticle PET-CT imaging of macrophages in inflammatory atherosclerosis*. Circulation, 2008. **117**(3): p. 379-87.
6. Lee, H.Y., Z. Li, K. Chen, A.R. Hsu, C. Xu, J. Xie, S. Sun, and X. Chen, *PET/MRI dual-modality tumor imaging using arginine-glycine-aspartic (RGD)-conjugated radiolabeled iron oxide nanoparticles*. J Nucl Med, 2008. **49**(8): p. 1371-9.
7. Jarrett, B.R., B. Gustafsson, D.L. Kukis, and A.Y. Louie, *Synthesis of ⁶⁴Cu-labeled magnetic nanoparticles for multimodal imaging*. Bioconjug Chem, 2008. **19**(7): p. 1496-504.
8. Choi, J.S., J.C. Park, H. Nah, S. Woo, J. Oh, K.M. Kim, G.J. Cheon, Y. Chang, J. Yoo, and J. Cheon, *A hybrid nanoparticle probe for dual-modality positron emission tomography and magnetic resonance imaging*. Angew Chem Int Ed Engl, 2008. **47**(33): p. 6259-62.

9. Duconge', F., T. Pons, C. Pestourie, L. He'rin, B. The'ze', K. Gombert, B. Mahler, F. Hinnen, B. Kühnast, and F. Dolle', *Fluorine-18-Labeled Phospholipid Quantum Dot Micelles for in Vivo Multimodal Imaging from Whole Body to Cellular Scales*. Bioconjug Chem, 2008.
10. van Schooneveld, M., E. Vucic, R. Koole, Y. Zhou, J. Stocks, D. Cormode, C. Tang, R. Gordon, K. Nicolay, and A. Meijerink, *Improved Biocompatibility and Pharmacokinetics of Silica Nanoparticles by Means of a Lipid Coating: A Multimodality Investigation*. Nano Lett, 2008.
11. McCarthy, D.W., R.E. Shefer, R.E. Klinkowstein, L.A. Bass, W.H. Margeneau, C.S. Cutler, C.J. Anderson, and M.J. Welch, *Efficient production of high specific activity 64Cu using a biomedical cyclotron*. Nucl Med Biol, 1997. **24**(1): p. 35-43.
12. Yu, Z., *In vitro Characterization of Magnetic Resonance Imaging Contrast Agents for Molecular Imaging in Cardiology*. 2006, Charité Universitätsmedizin Berlin: Berlin. p. 60.
13. Yu, Z., M. Grafe, H. Meyborg, E. Fleck, and Y. Li, *In Vitro Characterization of Magnetic Resonance Imaging Contrast Agents for Molecular Imaging*. ASH Annual Meeting Abstracts, 2006. **108**(11): p. 3944-.
14. Shokeen, M., N. Fettig, and R. Rossin, *Synthesis, in vitro and in vivo evaluation of radiolabeled nanoparticles*. QJ Nucl Med Mol Imaging, 2008.
15. Hermanson, G., *Bioconjugate Techniques*. 2008: Academic Press.
16. McCarthy, D., R. Shefer, R. Klinkowstein, L. Bass, W. Margeneau, C. Cutler, C. Anderson, and M. Welch, *Efficient production of high specific activity 64Cu using a biomedical cyclotron*. Nuclear Medicine and Biology, 1997. **24**(1): p. 35-43.
17. McCarthy, D., L. Bass, P. Cutler, R. Shefer, R. Klinkowstein, P. Herrero, J. Lewis, C. Cutler, C. Anderson, and M. Welch, *High purity production and potential applications of copper-60 and copper-61*. Nuclear Medicine and Biology, 1999. **26**(4): p. 351-358.
18. Sun, X. and C. Anderson, *Production and applications of copper-64 radiopharmaceuticals*. Methods Enzymol, 2004. **386**: p. 237-61.
19. Ponten, J. and E. Macintyre, *Long term culture of normal and neoplastic human glia*. Acta Pathol Microbiol Scand, 1968. **74**(4): p. 465-86.
20. Guo, P., L. Xu, S. Pan, R.A. Brekken, S.-T. Yang, G.B. Whitaker, M. Nagane, P.E. Thorpe, J.S. Rosenbaum, H.-J. Su Huang, W.K. Cavenee, and S.-Y. Cheng, *Vascular Endothelial Growth Factor Isoforms Display Distinct Activities in Promoting Tumor Angiogenesis at Different Anatomic Sites*. Cancer Res, 2001. **61**(23): p. 8569-8577.
21. Beyer, T., *A combined PET/CT scanner for clinical oncology*. 2000, Soc Nuclear Med. p. 1369-1379.

22. Beyer, T., D. Townsend, and T. Blodgett, *Dual-modality PET/CT tomography for clinical oncology*. QJ Nucl Med, 2002. **46**(1): p. 24-34.
23. Martinelli, M., D. Townsend, C. Meltzer, and V. Villemagne, *7. Survey of Results of Whole Body Imaging Using the PET/CT at the University of Pittsburgh Medical Center PET Facility*. Clin Positron Imaging, 2000. **3**(4): p. 161.
24. Fukui, M., T. Blodgett, and C. Meltzer. *PET/CT imaging in recurrent head and neck cancer*. 2003: Elsevier.
25. Pannu, H., R. Bristow, C. Cohade, E. Fishman, and R. Wahl, *PET-CT in Recurrent Ovarian Cancer: Initial Observations 1*. 2004, RSNA. p. 209-223.
26. Czernin, J., M. Allen-Auerbach, and H. Schelbert, *Improvements in Cancer Staging with PET/CT: Literature-Based Evidence as of September 2006*. Journal of Nuclear Medicine, 2007. **48**(1 suppl): p. 78S.
27. Seemann, M.D., G. Meisetschlaeger, J. Gaa, and E.J. Rummeny, *Assessment of the extent of metastases of gastrointestinal carcinoid tumors using whole-body PET, CT, MRI, PET/CT and PET/MRI*. Eur J Med Res, 2006. **11**(2): p. 58-65.
28. Ruf, J., E. Lopez Hanninen, M. Bohmig, I. Koch, T. Denecke, M. Plotkin, J. Langrehr, B. Wiedenmann, R. Felix, and H. Amthauer, *Impact of FDG-PET/MRI image fusion on the detection of pancreatic cancer*. Pancreatology, 2006. **6**(6): p. 512-9.
29. Cherry, S.R., *The 2006 Henry N. Wagner Lecture: Of mice and men (and positrons)--advances in PET imaging technology*. J Nucl Med, 2006. **47**(11): p. 1735-45.
30. Catana, C., Y. Wu, M.S. Judenhofer, J. Qi, B.J. Pichler, and S.R. Cherry, *Simultaneous acquisition of multislice PET and MR images: initial results with a MR-compatible PET scanner*. J Nucl Med, 2006. **47**(12): p. 1968-76.
31. Seemann, M.D., *Whole-body PET/MRI: the future in oncological imaging*. Technol Cancer Res Treat, 2005. **4**(5): p. 577-82.
32. Sun, G., A. Hagooly, J. Xu, A. Nyström, Z. Li, R. Rossin, D. Moore, K. Wooley, and M. Welch, *Facile, Efficient Approach to Accomplish Tunable Chemistries and Variable Biodistributions for Shell Cross-Linked Nanoparticles*. Biomacromolecules, 2008. **9**(7): p. 1997-2006.
33. Rossin, R., S. Muro, M. Welch, V. Muzykantov, and D. Schuster, *In Vivo Imaging of ⁶⁴Cu-Labeled Polymer Nanoparticles Targeted to the Lung Endothelium*. Journal of Nuclear Medicine, 2008. **49**(1): p. 103.
34. XU, J., G. SUN, R. ROSSIN, A. HAGOOLY, Z. LI, K. FUKUKAWA, B. MESSMORE, D. MOORE, M. WELCH, and C. HAWKER, *Labeling of polymer nanostructures for medical imaging: Importance of cross-linking extent, spacer length, and charge density*. Macromolecules, 2007. **40**(9): p. 2971-2973.

35. Montet, X., K. Montet-Abou, F. Reynolds, R. Weissleder, and L. Josephson, *Nanoparticle imaging of integrins on tumor cells*. *Neoplasia*, 2006. **8**(3): p. 214-22.
36. Montet, X., M. Funovics, K. Montet-Abou, R. Weissleder, and L. Josephson, *Multivalent effects of RGD peptides obtained by nanoparticle display*. *J Med Chem*, 2006. **49**(20): p. 6087-93.

CHAPTER 6

SUMMARY AND FUTURE DIRECTIONS

6.1 Conclusions and Ongoing Studies

Functionalization of ^{64}Cu -MNP_{PEG} with RGD peptides dramatically altered the particle's blood clearance and biodistribution. Addition of approximately 50 peptides per produced a sharp decrease in circulation half-life as well as intense uptake by the liver and the spleen. A decrease in half-life was expected upon addition of targeting ligands, but the magnitude observed here was surprising. We feel confident in this observation, as these experiments were repeated several times and were performed on both U87MG and M21/M21L tumor-bearing mice.

The high liver and spleen uptake suggests that rapid clearance of RGD-nanoparticles is due to absorbance of plasma proteins (i.e. opsonins) and subsequent phagocytosis by Kupffer cells in the liver and monocytes in the spleen (i.e. RES system). Still, the magnitude by which the circulation half-life and biodistribution are altered is greater than reported for similar nanoparticle. While this may be the result of bias on part of some researchers when selecting "*representative data*," other parameter of ligand-dependent behavior need to be explored. Understanding how ligands affect pharmacokinetics will aid in the development of advanced nanoparticles for imaging and treating disease.

Alteration of probe pharmacokinetics due to ligand attachment is generally caused by a specific immune response to the ligand or by the absorption of plasma proteins due to ligand charge or hydrophobicity. While RGD binds to many types of cells, there is no known specific immune response to RGD. The peptide we used, cyclo(RGDyC) has two charged residues, arginine and aspartic acid. Arginine is strongly basic due to resonance stabilized positive charge

of the guanidinium chemical group ($pK_a = 12.48$) present on the sidechain (1). This also allows arginine to participate in extensive hydrogen bonding (2). Aspartic acid is an acidic residue with a β -COOH sidechain ($pK_a = 3.9$) and is negatively charged at physiologic pH. Of the remaining residues, cysteine is uncharged and the reactive thiol side chain is covalently linked to the nanoparticle PEG coating. Tyrosine is a hydrophobic, neutral residue with a phenol side chain ($pK_a = 10.5$). The hydroxyl is more acidic than that of either serine or threonine (due to resonance). The net charge on c(RGDyC) at physiologic pH would be zero, however the peptide may be somewhat basic owing to arginine. We therefore exclude charge from being the dominant factor causing the altered kinetics reported. The peptide shows little solubility in aqueous solution. DMSO was used to dissolve peptides for bioconjugation. The peptide is linked to PEG chains on the nanoparticle coating which should act to lessen the hydrophobic behavior of the peptide. However, residual hydrophobicity may be a factor contributing to the altered pharmacokinetics.

Another factor to be considered when determining the cause of ligand-dependent changes in kinetics is the binding of RGD to alternative biomolecules. That is, RGD binding to molecules other than $\alpha_v\beta_3$ integrin. RGD has high affinity for $\alpha_v\beta_3$ integrin (nanomolar) and the multivalent presentation via nanoparticles increases this affinity (3, 4). RGD also has affinity for other integrins ($\alpha_v\beta_5$, $\alpha_5\beta_1$, $\alpha_{IIb}\beta_3$, $\alpha_v\beta_3$) (5-9). The affinity for these integrins is much less than for $\alpha_v\beta_3$ integrin, however multivalent presentation of RGD on nanoparticles will increase the affinity for these integrins. The RGD sequence was discovered at an integrin binding domain present in many extracellular matrix proteins (ECM) involved in cell adhesion, such as vitronectin, fibronectin, and collagen (10-14). As such, any cell type that binds to these proteins is a potential target of RGD nanoparticles. RGD has been shown to bind to several cell types, including platelets, leukocytes, endothelial cells, and osteocytes. Thus, one factor in explaining

the marked change in nanoparticle behavior may be that particles are binding to many sites in the body and are therefore rapidly removed from circulation, while untargeted particles circulated freely.

We have already begun a series of experiments to gain understanding into the altered kinetics presented in this dissertation. The blocking of ligand binding through co-injection of excess free ligand is a common strategy to prove specificity. Here we injected U87MG tumor bearing mice with $^{64}\text{Cu-MNP}_{\text{PEG-RGD}}$ with and without concomitant block. Mice received a 15 mg/kg block of c(RGDyC) 10 minutes prior to, and 120 minutes after injection with 4 μg (100 μCi) $^{64}\text{Cu-MNP}_{\text{PEG-RGD}}$. Our observation was that blocking extended the circulation lifetime of the $^{64}\text{Cu-MNP}_{\text{PEG-RGD}}$ relative to $^{64}\text{Cu-MNP}_{\text{PEG}}$ (Table 6.2). It could be that free RGD peptide is occupying non-tumor sites of uptake (Kupffer cells in the liver, macrophages in the spleen, platelets, osteocytes, etc.). Tumor-to-blood for $^{64}\text{Cu-MNP}_{\text{PEG-RGD}}$ was higher than $^{64}\text{Cu-MNP}_{\text{PEG-RGD}}$ + RGD block at 4 hr post injection; they were equal at 24 hr post inject. Tumor-to-muscle for $^{64}\text{Cu-MNP}_{\text{PEG-RGD}}$ was also higher than $^{64}\text{Cu-MNP}_{\text{PEG-RGD}}$ + RGD block at 4 and 24 hr post injection.

The same experiments were also performed in BALB/c mice to see if the change in kinetics due to peptide conjugation was specific to nude mice (**Error! Reference source not found.**). Rapid blood clearance and high liver/spleen uptake was seen in BALB/c was well. The effect of peptide block was less evident in BALB/c mice. The uptake by the spleen at 24 hr was lower for mice receiving peptide block. Other differenced were not observed. The difference in peptide blocking between BALB/c and nude mice could be cause by the larger number of immune cells in BALB/c compare with nude mice. That is, the block may be able to saturate their phagocytic uptake of particles in nude mice but on in BALB/c because of the larger reservoir of immune cells they posses.

We also are in the process of determining the role played by enhanced permeability and retention (EPR) effect in the tumor accumulation of our probe. Specifically the role of EPR will be tested using compounds shown to modulate EPR effects (15, 16) (Table 6.2). Additionally, we have discussed using radiolabeled serum albumin to measure the blood contribution to tumor activity by circulating nanoparticles versus bound nanoparticles

We evaluated several methods to mitigate the ligand-dependent change in pharmacokinetics observed. Among the available options were (1) coinjection using blocking excess of RGD, or (2) comparing tumor uptake of ^{64}Cu -MNP_{PEG}-RGD versus nanoparticles conjugated with a non-targeting, scrambled RGD peptide. We chose the former for two reasons. One reason was because of the interest our collaborators had in this approach. While blocking with free RGD has been reported for radiolabeled RGD peptides (18), few instances of blocking long circulating, large molecular weight nanoparticles with short-circulating peptides have been reported.

The other reason for not using scrambled RGD peptides is the promiscuity shown by RGD-like peptides. RGD and RGD-like peptides bind to many members of the integrin family. For example, changing RGD to KGD destroys $\alpha_v\beta_3$ integrin affinity but does not lessen affinity for $\alpha_{IIb}\beta_3$ integrin. The glycine position can also be occupied by other individual amino acids or pairs (9). Affinity to $\alpha_v\beta_3$ integrin is retained at high levels by many substitutions to the basic cyclic RGD format (17). Many small, cyclic peptides have high affinity for other members of the integrin family (RYD, RHD, RLD, REDV, KRLDGS, KQAGDV, LDV, CREETAWAC, etc) (9). Additionally, our flow cytometry studies with fluorescent cyclic RAD peptide (Chapter 4) showed some residual binding to $\alpha_v\beta_3$ integrin-positive U87MG cells. In general, it is difficult to prepare a scrambled control peptide for RGD. Use of a less promiscuous targeting peptide is advisable.

Table 6.1: Biodistribution of ⁶⁴Cu-labeled magnetic nanoparticles in female BALB/c mice with peptide and EPR blocking

Organ	⁶⁴ Cu-MNP-RGD			⁶⁴ Cu-MNP-RGD + RGD Block			⁶⁴ Cu-MNP			⁶⁴ Cu-MNP + RGD Block		
	1 hr	4 hr	24 hr	1 hr	4 hr	24 hr	1 hr	4 hr	24 hr	1 hr	4 hr	24 hr
Blood	18.1 ± 3.48	1.1 ± 0.2	0.9 ± 0.0	26.7 ± 5.3	1.4 ± 0.7	0.7 ± 0.1	46.9 ± 2.4	42.4 ± 4.1	23.5 ± 2.9	46.3 ± 0.9	37.8 ± 6.1	17.9 ± 6.3
Lung	7.8 ± 1.32	4.2 ± 0.5	4.7 ± 0.4	9.8 ± 1.6	2.6 ± 1.2	3.5 ± 0.1	13.2 ± 1.4	16.3 ± 2.1	9.5 ± 2.0	12.7 ± 2.1	12.4 ± 2.3	8.0 ± 1.0
Liver	55.0 ± 3.12	77.9 ± 3.2	62.0 ± 6.7	38.5 ± 4.1	62.9 ± 24.2	54.6 ± 5.8	11.3 ± 1.4	12.6 ± 1.0	20.5 ± 3.9	11.5 ± 1.2	12.9 ± 2.7	18.1 ± 4.9
Spleen	65.6 ± 5.36	111.0 ± 10.0	135.3 ± 12.0	34.7 ± 3.0	74.4 ± 31.5	87.9 ± 20.8	7.7 ± 2.4	9.0 ± 1.2	22.5 ± 5.2	7.4 ± 2.5	9.8 ± 3.4	16.6 ± 5.9
Kidney	6.4 ± 1.03	5.9 ± 0.7	6.3 ± 0.5	6.1 ± 0.8	4.5 ± 2.0	5.1 ± 0.3	7.0 ± 0.5	6.7 ± 1.1	6.9 ± 0.6	6.8 ± 0.9	5.8 ± 0.9	5.0 ± 1.2
Muscle	0.9 ± 0.09	0.5 ± 0.1	0.5 ± 0.1	1.4 ± 0.6	0.4 ± 0.2	0.4 ± 0.1	1.5 ± 0.4	1.8 ± 0.4	1.9 ± 0.2	1.9 ± 0.5	1.6 ± 0.3	1.4 ± 0.2
Fat	2.2 ± 0.71	1.1 ± 0.9	0.7 ± 0.4	2.1 ± 0.8	0.6 ± 0.8	0.8 ± 0.4	2.8 ± 1.1	3.5 ± 0.8	2.3 ± 0.7	4.1 ± 2.2	2.4 ± 1.1	2.1 ± 2.0
Heart	3.5 ± 1.00	1.8 ± 0.1	2.2 ± 0.1	4.8 ± 1.5	1.5 ± 0.5	1.7 ± 0.2	9.4 ± 2.6	8.5 ± 2.7	4.3 ± 0.5	7.8 ± 0.5	6.5 ± 2.4	3.3 ± 0.8
Brain	0.4 ± 0.10	0.1 ± 0.0	0.2 ± 0.0	0.8 ± 0.2	0.1 ± 0.1	0.1 ± 0.0	1.2 ± 0.2	1.8 ± 1.3	1.0 ± 0.3	1.2 ± 0.4	1.3 ± 0.6	0.7 ± 0.2
Bone	4.9 ± 0.53	6.0 ± 0.9	5.7 ± 0.4	4.5 ± 0.9	5.1 ± 2.2	6.1 ± 0.3	2.9 ± 0.5	2.9 ± 0.1	2.6 ± 0.3	3.1 ± 0.4	2.6 ± 0.4	2.0 ± 0.5

Data are presented as percentage injected dose per gram (%ID/g) ± SD (n = 4).

Table 6.2: Biodistribution of ⁶⁴Cu-labeled magnetic nanoparticles in U87MG tumor-bearing mice with peptide and EPR blocking

Organ	⁶⁴ Cu-MNP-RGD		⁶⁴ Cu-MNP-RGD + RGD Block		⁶⁴ Cu-MNP-RGD + EPR Block		⁶⁴ Cu-MNP		⁶⁴ Cu-MNP + RGD Block		⁶⁴ Cu-MNP + EPR Block	
	4 hr	24 hr	4 hr	24 hr	4 hr	24 hr	4 hr	24 hr	4 hr	24 hr	4 hr	24 hr
Blood	1.5 ± 0.7	0.6 ± 0.1	16.8 ± 2.9	0.6 ± 0.02	X ± X	X ± X	35.2 ± 3.7	16.7 ± 1.5	30.9 ± 6.1	14.0 ± 2.1	36.5 ± 7.9	14.7 ± 4.7
Lung	3.3 ± 0.7	3.7 ± 0.3	8.8 ± 1.3	3.2 ± 0.9	X ± X	X ± X	12.6 ± 3.4	7.7 ± 1.6	13.9 ± 3.9	6.3 ± 0.3	15.4 ± 4.6	7.0 ± 1.1
Liver	52.0 ± 5.0	41.1 ± 7.2	25.6 ± 1.5	34.0 ± 3.4	X ± X	X ± X	12.5 ± 5.1	22.4 ± 11.5	12.1 ± 5.4	16.1 ± 5.5	11.0 ± 5.1	15.7 ± 7.5
Spleen	57.1 ± 6.9	74.3 ± 23.4	34.9 ± 4.5	51.7 ± 11.0	X ± X	X ± X	13.3 ± 4.7	13.7 ± 7.1	11.1 ± 6.7	27.6 ± 15.8	8.7 ± 5.1	13.8 ± 8.9
Kidney	4.3 ± 0.7	5.3 ± 1.2	6.9 ± 0.5	6.0 ± 0.4	X ± X	X ± X	6.5 ± 0.4	5.7 ± 0.8	6.1 ± 1.3	4.5 ± 1.0	6.0 ± 2.1	4.3 ± 1.4
Muscle	0.4 ± 0.2	0.3 ± 0.1	1.2 ± 0.4	0.5 ± 0.1	X ± X	X ± X	1.6 ± 0.2	2.3 ± 0.6	1.4 ± 0.2	1.4 ± 0.2	1.6 ± 0.6	1.3 ± 0.4
Fat	0.6 ± 0.2	0.3 ± 0.1	1.4 ± 1.1	0.3 ± 0.1	X ± X	X ± X	2.3 ± 1.6	2.2 ± 1.0	2.1 ± 0.6	1.1 ± 0.5	1.7 ± 1.0	0.9 ± 0.4
Heart	1.5 ± 0.3	1.7 ± 0.4	4.3 ± 1.0	2.2 ± 0.2	X ± X	X ± X	7.6 ± 2.6	4.8 ± 0.3	5.5 ± 2.1	3.4 ± 0.6	5.9 ± 2.2	3.5 ± 1.3
Brain	0.1 ± 0.03	0.1 ± 0.02	0.8 ± 0.1	0.1 ± 0.01	X ± X	X ± X	1.8 ± 0.7	0.8 ± 0.3	1.3 ± 0.8	0.7 ± 0.2	1.3 ± 0.1	0.8 ± 0.3
Bone	6.1 ± 1.0	5.3 ± 1.1	6.4 ± 0.5	6.2 ± 0.7	X ± X	X ± X	2.3 ± 0.3	1.9 ± 0.4	2.2 ± 0.4	1.8 ± 0.4	2.4 ± 0.5	1.5 ± 0.5
Tumor	2.3 ± 1.0	3.5 ± 0.7	5.1 ± 0.7	3.4 ± 2.0	X ± X	X ± X	4.5 ± 0.9	6.2 ± 0.8	3.4 ± 0.2	7.3 ± 1.1	6.8 ± 2.8	6.5 ± 1.6

Data are presented as percentage injected dose per gram (%ID/g) ± SD (n = 4).

6.2 Contributions to the Field

At the time of writing, relatively few dual-modality probes have been developed for PET/MRI. Nahrendorf et al used untargeted ^{64}Cu -labeled CLIO to image uptake by macrophages in inflammatory plaques in a mouse model of atherosclerosis (47) (Figure 1.3). PET and MRI were performed separately and the images produced were not coregistered. Also, animal groups either received ^{64}Cu -labeled magnetic nanoparticles for PET (at 1.5 mg Fe/kg body weight) or unlabeled (i.e. “cold”) versions of the same magnetic nanoparticle for MR imaging (30 mg Fe/kg body weight). No single animals underwent both PET and MRI in this study. Also of note, the chelator used to attach ^{64}Cu was the acyclic diethylene triamine pentaacetic acid (DTPA). Use of this chelator is curious, as its affinity for ^{64}Cu is lower than the more commonly used cyclic chelators (e.g. DOTA, TETA).

Choi et al used ^{124}I to label magnetic nanoparticles for combined PET/MRI (48). High temperature organometallic synthesis was used to produce monodisperse 15nm MnFe_2O_4 nanoparticles (particles are doped with manganese to enhance MR contrast effect (49)). The MnFe_2O_4 cores were coated with serum albumin to allow solubility in water (Figure 1.4). The exchange of nanoparticle surface ligands with protein is an older approach to nanoparticle coating and it is unclear why the authors chose this method. Nevertheless, ^{124}I labeling was achieved and the resultant particles produced PET and MR contrast.

To test the particles in a biological environment, untargeted particles were injected into rat forepaws. At one hour post injection PET and MR imaging was performed. Resulting images were coregistered by means of custom made fiducial markers. The injected particles gathered in the brachial and axillary lymph nodes, which were visible in post PET and MRI. The authors did not state what the circulation half-life of the nanoparticle. The early imaging time point (1 hr postinjection) indicates the nanoparticles have a short blood (ca. < 2hr) half-life. The

accumulation in brachial and axillary lymph nodes was unilateral (i.e. restricted to the side possessing the forepaw receiving the injection, in this case the right side of the body). The unilateral accumulation indicates that particles were not systemically available, presumably due to a short blood half-life. The systemic uptake of long circulating magnetic nanoparticles has been well studied (50-52).

Jarrett et al used ^{64}Cu to label anionic dextran sulfate coated iron oxide (ADIO) nanoparticles (53) (Figure 1.5). No PET or MR imaging was performed in this study. The surface of ADIO was modified to contain aldehyde groups to allow conjugation with amine-activated DOTA. Strangely, the authors reported that ADIO functionalized with DOTA could not be labeled with ^{64}Cu . The authors claimed that charge effects were the cause. Successful labeling was only reported when ^{64}Cu was chelated by DOTA prior to attachment to the nanoparticle surface. After personal discussion with the author it was determined that the author failed to use the correct pH during the labeling step. Additionally, the aldehyde particles were treated with ethylenediamine to generate amine functional groups on the particle surface. The use of bifunctional ethylenediamine will undoubtedly lead to some degree of undesired nanoparticle crosslinking.

Lee et al used ^{64}Cu to label polyaspartic acid-coated iron oxide nanoparticles (PASP-IO) (54) (Figure 1.6). The PASP-IO particles were synthesized by coprecipitation of iron salts in the presence of PASP. The nanoparticles had a 5 nm core and were 45 ± 10 nm in diameter after coating with PASP. The nanoparticles were conjugated with RGD peptide and target to integrins in a mouse tumor model. PET and MRI was performed but not coregistered. The authors failed to show pre- and post-injection MR images of the same animals. The MR images that were shown were of poor quality and low resolution. Pre- and post-injection PET images were shown and specific targeted was achieved.

Our studies evaluated two radiolabeled nanoparticles for PET/MR imaging. The first was a ^{64}Cu -labeled iron oxide nanoparticle with a PEG-lipid coating. This novel work exploited the flexibility of lipids-PEG coating which can easily be modified. Protein coatings are susceptible to immune reaction and can be bulky, whereas our work contains PEG to prevent immune reaction and is generally thinner than protein coatings. We reported detailed synthesis and radiolabeling studies. Phantom studies showing PET/MRI contrast were performed. Multi-organ, multi-time point biodistribution was performed as well as multi-time point PET imaging. This work was a systematic and rigorous investigation of a novel PET/MRI nanoparticle.

The second study we performed used RGD-targeted magnetic nanoparticles. The MNPs had a cross-linked dextran coating and were radiolabeled with ^{64}Cu . Phantom PET and MRI studies were performed. PET and MR imaging was performed in tumor-bearing mice. Specific accumulation was observed in PET images. Of the existing particles used for PET/MRI with a dextran coating, one was untargeted and an acyclic chelator was used, providing lower affinity for ^{64}Cu . Our work used targeted dextran particles with a high affinity chelator.

In summary, we have developed two novel nanoparticles as dual PET/MRI contrast agents. The particles were characterized physically, in vitro, and in vivo. Investigations were performed to study the mechanics of particle accumulation and blocking. Our work significantly contributes to the field and extends the understanding of dual PET/MRI nanoparticles.

6.3 Future Collaboration

The NHLBI sponsored Program of Excellence in Nanotechnology (PEN) provides funding to both Dr. Bao's lab and the lab of my future postdoc mentor. Our laboratories have forged a successful collaboration over the past two years and plan to continue working together. We

look forward to our continued collaboration to develop MRI, PET, and multimodal molecular imaging probes, and to apply these technologies to the aims of the NHLBI PEN.

6.4 References

1. Voet, D., J. Voet, I. Geis, J. Woolsey, B. Woolsey, and P. Lane, *Biochemistry*. 1990: Wiley New York.
2. Alberts, B., D. Bray, J. Lewis, M. Raff, K. Roberts, and J. Watson, *Molecular Biology of the Cell*. New York, 2002.
3. Montet, X., M. Funovics, K. Montet-Abou, R. Weissleder, and L. Josephson, *Multivalent effects of RGD peptides obtained by nanoparticle display*. *J Med Chem*, 2006. **49**(20): p. 6087-93.
4. Shokeen, M., Anderson, C.J., *personal communication*. 2008.
5. Cheng, S., W. Craig, D. Mullen, J. Tschopp, D. Dixon, and M. Pierschbacher, *Design and synthesis of novel cyclic RGD-containing peptides as highly potent and selective integrin. alpha. IIb. beta. 3 antagonists*. *Journal of Medicinal Chemistry*, 1994. **37**(1): p. 1-8.
6. Goodman, S.L., G. Holzemann, G.A. Sulyok, and H. Kessler, *Nanomolar small molecule inhibitors for alphav(beta)6, alphav(beta)5, and alphav(beta)3 integrins*. *J Med Chem*, 2002. **45**(5): p. 1045-51.
7. Gottschalk, K. and H. Kessler, *The Structures of Integrins and Integrin-Ligand Complexes: Implications for Drug Design and Signal Transduction*. ANGEWANDTE CHEMIE-INTERNATIONAL EDITION IN ENGLISH-, 2002. **41**(20): p. 3767-3774.
8. Kuhn, K. and J. Eble, *The structural bases of integrin-ligand interactions*. *Trends Cell Biol*, 1994. **4**(7): p. 256-61.
9. Ruoslahti, E., *RGD AND OTHER RECOGNITION SEQUENCES FOR INTEGRINS*. *Annual Reviews in Cell and Developmental Biology*, 1996. **12**(1): p. 697-715.
10. Cheresch, D. and J. Harper, *Arg-Gly-Asp recognition by a cell adhesion receptor requires its 130-kDa alpha subunit*. *Journal of Biological Chemistry*, 1987. **262**(4): p. 1434-1437.
11. CHERESH, D., J. SMITH, H. COOPER, and V. QUARANTA, *A novel vitronectin receptor integrin($\alpha_v\beta_x$) is responsible for distinct adhesive properties of carcinoma cells*. *Cell*, 1989. **57**(1): p. 59-69.

12. Pytela, R., M.D. Pierschbacher, M.H. Ginsberg, E.F. Plow, and E. Ruoslahti, *Platelet membrane glycoprotein IIb/IIIa: member of a family of Arg-Gly-Asp--specific adhesion receptors*. Science, 1986. **231**(4745): p. 1559-62.
13. Pytela, R., M.D. Pierschbacher, and E. Ruoslahti, *A 125/115-kDa cell surface receptor specific for vitronectin interacts with the arginine-glycine-aspartic acid adhesion sequence derived from fibronectin*. Proc Natl Acad Sci U S A, 1985. **82**(17): p. 5766-70.
14. Ruoslahti, E. and M.D. Pierschbacher, *New perspectives in cell adhesion: RGD and integrins*. Science, 1987. **238**(4826): p. 491-7.
15. Matsumura, Y. and H. Maeda, *A new concept for macromolecular therapeutics in cancer chemotherapy: mechanism of tumorotropic accumulation of proteins and the antitumor agent smancs*. Cancer Research, 1986. **46**(12): p. 6387-6392.
16. Wu, J., T. Akaike, and H. Maeda, *Modulation of enhanced vascular permeability in tumors by a bradykinin antagonist, a cyclooxygenase inhibitor, and a nitric oxide scavenger*. Cancer Research, 1998. **58**(1): p. 159-165.
17. Haubner, R., R. Gratias, B. Diefenbach, S. Goodman, A. Jonczyk, and H. Kessler, *Structural and functional aspects of RGD-containing cyclic pentapeptides as highly potent and selective integrin $\alpha_3\beta_3$ antagonists*. J. Am. Chem. Soc, 1996. **118**(32): p. 7461-7472.
18. Haubner, R., H.J. Wester, W.A. Weber, C. Mang, S.I. Ziegler, S.L. Goodman, R. Senekowitsch-Schmidtke, H. Kessler, and M. Schwaiger, *Noninvasive imaging of $\alpha(v)\beta_3$ integrin expression using ^{18}F -labeled RGD-containing glycopeptide and positron emission tomography*. Cancer Res, 2001. **61**(5): p. 1781-5.

CHARLES GLAUS

2645 Cecelia Avenue, Brentwood, MO 63144 | (314) 422-6941 | gtg464j@mail.gatech.edu

EDUCATION

Georgia Institute of Technology and Emory University

PhD in Biomedical Engineering

Oct. 2008

Minor: Molecular Biology

Advisor: Professor Gang Bao

GPA: 3.6

University of Missouri – Rolla

BS in Physics

2002

GPA: 3.8

HONORS and AWARDS

- North American Finalist: UK BBRC Young Entrepreneur Competition, Edinburgh, Scotland **2004**
- Georgia Tech Nanoscience and Technology Graduate Fellowship **2003-2004**
- 1st Place, Harold Q. Fuller Research Competition, University of Missouri – Rolla Dept. of Physics: *Neutron irradiation of ceramic and rare earth magnetic materials: effects on hysteresis, magnetization and Curie temperature* **2002**
- Charles M. Rice Scholarship, University of Missouri – Rolla, Dept. of Physics **2000**

TEACHING EXPERIENCE

- Georgia Institute of Technology
- **Laboratory Instructor** **2005**
- BMED 4500: Cell and Tissue Engineering Laboratory
- **Teaching Assistant** **2004**
- BMED 2100: Principles and Calculations in Chemical Engineering
- University of Missouri – Rolla
- **Laboratory Instructor** **2001 – 2002**
- Phys 26 Laboratory: Optics and Electromagnetics

RESEARCH and WORK EXPERIENCE

Georgia Institute of Technology

Graduate Research Assistant

2003-2008

- Functionalization and bioconjugation of nanoparticles (iron oxide, quantum dots, polymer, gold) with antibodies, peptides, fluorescent dyes, crosslinkers (PEG), and bifunctional chelators
- Nanoparticle Characterization: dynamic light scattering (DLS), surface charge measurements (Zeta potential), FPLC, HPLC
- Magnetic Resonance Techniques: Bruker Minispec, Bruker PharmaScan 7T MRI, ParaVision 4
- *In vitro* assays including mammalian cell culture, flow cytometry, PCR, MTT, DNA and protein analysis
- Small Animal Surgery: ovariectomy, carotid artery ligation, polymer scaffold placement, necropsy, suturing

- Histology: paraffin embedded and frozen tissue techniques, immunohistochemistry, immunofluorescence
- Microscopy: confocal, two-photon, epifluorescent, 2- and 3-D deconvolution, image analysis
- Optical imaging using Xenogen IVUS and Kodak *in vivo* imaging systems
- Radiolabeling magnetic nanoparticles with Copper-64

University of Missouri – Rolla, Department of Physics

Undergraduate Research Assistant

1998 – 2000

Computational Physics: Investigated electron-electron ionization and scattering inter-actions of electrons, positrons and protons with both light and heavy atoms.

Corrigan Company Mechanical Contractors

Database Designer, Consultant

1999 – 2002

- Optimized device testing for Boeing, Monsanto, and Daimler-Chrysler accounts
- Automated the tracking of refrigerant usage for EPA compliance

PUBLICATIONS

- Glaus, C., Bao, G., Multimodal nanoparticles for PET/MR molecular imaging. *Nanomedicine. (in preparation)*
- Glaus, C., Rossin, R., Welch, M.J., Bao, G., In vivo evaluation of ⁶⁴Cu-labeled Magnetic Nanoparticles: A Novel Probe for Dual-Modality PET/MR Imaging (*in submission*)
- Glaus, C., Hagooley, A., Welch, M.J., Bao, G., PET/MR Imaging of RGD-targeted ⁶⁴Cu-labeled Magnetic Nanoparticles (*in submission*)
- Ferrara, D.E., Glaus, C., Taylor, W.R., “Targeting Vascular Epitopes Using Quantum Dots.” In: *Nanoparticles in Biomedical Imaging*, J.W.M. Bulte and M.M.J. Modo, Springer, New York, USA, 2007

POSTERS AND PRESENTATIONS

Glaus, C., Bao, G., “PET/MR Imaging of RGD-targeted ⁶⁴Cu-labeled Magnetic Nanoparticles.” Presentation at the BMES Fall Meeting, St. Louis, MO, USA, October 1-4, 2008

Glaus, C., Bao, G., “Dual-Modality Nanoparticles for PET/MR Imaging In Vivo.” Poster presentation at the 7th Society for Molecular Imaging Meeting, Nice, France, September 10-13, 2008

Glaus, C., Bao, G., “Biodistribution of Micelle-coated Superparamagnetic Iron Oxide Nanoparticles.” Poster presentation at the BMES Fall Meeting, Los Angeles, CA, USA, September 26-29, 2007

Glaus, C., Bao, G., “In Vivo evaluation of Micelle-coated Superparamagnetic Iron Oxide Nanoparticles.” Poster presentation at the 6th Society for Molecular Imaging Meeting, Providence, RI, USA, September 8-11, 2007

Glaus, C., Ferrara D.E., Taylor, W.R., Bao, G., “Micelle-coated Superparamagnetic Iron Oxide Nanoparticles as an MRI Contrast Agent for Plaque Detection.” Poster presentation at the 5th Society for Molecular Imaging Meeting, Waikoloa Village, HI, USA, August 30-September 2, 2006

Bao, G., Nitin, N., LaConte, L., Glaus, C., “Magnetic Nanoparticle Probes as a Contrast Agent for Molecular Imaging Using MRI.” Poster presentation at the MRS Spring Meeting, San Francisco, CA, USA, April 17-21, 2006.

Nitin, N., Glaus, C., Bao, G., "Functionalization and peptide-based delivery of magnetic nanoparticles as an intracellular MRI contrast agent." Poster presentation at the 4th Society for Molecular Imaging Meeting, Cologne, Germany, September 7-10, 2005.

Nitin, N., Glaus, C., Bao, G., "Analysis Of Cytoplasmic And Nuclear RNA In Living Cells Using Peptide-Linked Molecular Beacons." Poster presentation at the ASME Summer Bioengineering Conference, Vail, CO, USA, June 22-26, 2005

LEADERSHIP

- Mentor for Georgia Tech undergraduate research assistants **2005 - 2008**
- Assisted in the planning and organization of a workshop focused on submitting a proposal for the NIH Nanomedicine Center Roadmap Initiative
- Coordinated information gathering in support of a site visit to the NSF-sponsored Georgia Tech-Emory Engineering Research Center (ERC)
- Vice President, Society of Physics Students, University of Missouri – Rolla Chapter

MEMBERSHIP

Biomedical Engineering Society	2007 - present
Society for Molecular Imaging	2005 - present
Sigma Pi Sigma, National Physics Honor Society	1999 - 2002